People's Democratic Republic of Algeria
Ministry of Higher Education and Scientific Research

Higher Normal School of Technological Education of Skikda



Department of : Physics and Chemistry

THESIS

Submitted in fulfillment of the requirements for the degree of

Doctorate

Domain:	Materials Sciences
Field of study :	Physics
Speciality:	Condensed Matter Physics

Presented by :

Mr. Gouasmia Wissem

Title:

Study of The Fundamental Properties of II-VI and III-V Semiconductor Alloys in The Framework of The DFT

Publicly defended on: / /

before the Jury composed of:

Full name	**Academic rank**	**Establishment**	**Role**
Mme. Ouarda Nemiri	MCA	ENSET Skikda	Chair
Mr. Djamel Boudjaadar	MCA	ENSET Skikda	Supervisor
Mr. Faycal Oumelaz	MCA	ENSET Skikda	Co-supervisor
Mr. Boubekri Hani	MCA	ENSET Skikda	Examiner
Mme. Rahima Boulechfar	Prof	University August,20 1955 Skikda	Examiner
Mr. Kamel Khounfais	Prof	University August,20 1955 Skikda	Examiner

Academic Year : 2025/2026

République Algérienne Démocratique et Populaire
Ministère de l'Enseignement Supérieur et de la Recherche Scientifique

École Normale Supérieure de l'Enseignement Technologique de Skikda



Département de : Physique et chimie

THÈSE

Présentée en vue de l'obtention du diplôme de

Doctorat

Domaine :	Sciences de la matière
Filière :	Physique
Spécialité :	Physique de la matière condensée

Présentée par

M^r : Gouasmia Wissem

Thème :

Étude des Propriétés Fondamentales des Alliages Semi-conducteurs II-VI et III-V dans le Cadre de la Théorie de la Fonctionnelle de la Densité (DFT)

Soutenue publiquement le : / /

devant le jury composé de :

Nom	Grade	Établissement	Qualité
Mme. Ouarda Nemiri	MCA	ENSET Skikda	Président
Mr. Djamel Boudjaadar	MCA	ENSET Skikda	Directeur de thèse
Mr. Faycal Oumelaz	MCA	ENSET Skikda	Co-directeur
Mr. Boubekri Hani	MCA	ENSET Skikda	Examinateur
Mme. Rahima Boulechfar	Prof	Université 20 Août 1955 Skikda	Examinateur
Mr. Kamel Khounfais	Prof	Université 20 Août 1955 Skikda	Examinateur

Année Universitaire : 2025/2026

Acknowledgements

First and foremost, I would like to express my deepest gratitude to my advisor, **Dr. Boudjaadar Djamal**, for his guidance, unwavering support, and invaluable scientific insight throughout the course of this work. His dedication, patience, and high standards have profoundly shaped this research.

I am equally grateful to my co-advisor **Dr. Oumelaz Fayçal,** and **Dr. Nemiri Ouarda**, for their constant continuous guidance, encouragement, constructive discussions, and meaningful contributions that significantly enriched this thesis and my published work. Their support and expertise have been instrumental at every stage of this journey.

I would also like to extend my sincere appreciation to my family for their unconditional support, understanding, and encouragement.

I would like to express my sincere appreciation to the members of the jury for accepting the evaluation of this work. I am honored by their presence and grateful for their time, expertise, and valuable feedback, which contributes to improving the quality of this thesis.

Abstract

Abstract

This thesis presents a first‑principles study of structural, stability, electronic, optical, elastic and thermal properties for four ternary alloys, the zinc-blende $AlSb_{1-x}As_x$, $AlSb_{1-x}Bi_x$, and the rock‑salt $BaO_{1-x}S_x$ and $BaO_{1-x}Se_x$ at x = 0, 0.25, 0.50, 0.75, and 1. Energy-Volume data were fitted to Murnaghan E(V) establishing zinc‑blende and NaCl as the most stable phases. The enthalpy versus pressure study provides quantitative insight into the critical pressures associated with the phase transitions. The band structure and DOS calculations were carried out using the mBJ potential developed by Koller, Tran, and Blaha. $AlSb_{1-x}As_x$ ternary alloys exhibit a direct band gap Γ–Γ at x = 0.25 – 0.75. $AlSb_{1-x}Bi_x$ have direct band gaps for all compositions with a nonzero concentration, the band gap decreases and extends from the near-infrared to the mid-infrared spectral range.The elastic constants were obtained using WC GGA/IRElast and Voigt-Reuss-Hill approaches. The optical spectra include the real and imaginary parts of the dielectric function, the refractive index, the absorption coefficient, and the reflectivity was investigated and discussed in detail. Thermal properties obtained from the Debye model reveal consistent trends linking atomic mass, chemical bonding, and lattice stiffness. Heat capacity shows the expected low-temperature rise and high-temperature saturation, the Debye temperature tracks lattice rigidity, the bulk modulus decreases with temperature, and the thermal expansion increases with temperature. The sodium chloride to cesium chloride transition pressures decrease with increasing chalcogen content and approach reported binary limits. Agreement with theoretical and experimental data for the binaries, together with consistency across properties, validates the used approaches. The thesis delivers a dataset of material properties across the compositions (x). With newly reported elastic, optical, and thermal properties for compositions (x= 0.25, 0.5 and 0.75),in addition to identifying potential applications of these compounds, including light-emitting devices and photodetectors, as well as coatings and near-ultraviolet sensing devices.

Keywords:

DFT, KTB - mBJ; WC - GGA, optical properties, band gap, Debye temperature.

Abstract

الملخص

تعرض هذه الاطروحة دراسة نظرية للخصائص البنيوية، تحولات الطور، الالكترونية، الضوئية، المرونية و الخصائص الحرارية للسبائك شبه الناقلة ($BaO_{1-x}Se_x$ و$AlSb_{1-x}As_x$ $AlSb_{1-x}Bi_x$, $BaO_{1-x}S_x$) باستعمال نظرية الكثافة الدالية وذلك عند التراكيب 0، 0,25، 0,5، 0,75 و 1 . أظهرت دراسة الخصائص البنيوية ان البنية زنك بلاند هي الأكثر استقرار بالنسبة للسبائك $BaO_{1-x}S_x$ ،$AlSb_{1-x}As_x$, $AlSb_{1-x}Bi_x$ وان طور الملح الصخري (NaCl) هو الأكثر الاستقرار بالنسبة للسبائك $BaO_{1-x}Se_x$, كما تم حسابيا انشاء منحنيات الإنثالبي بدلالة الضغط لتحديد قيم ضغوط التحول بين مختلف الأطوار المدروسة. حسِبت البنى الالكترونية وكثافات الحالات باستخدام كمون mBJ المحسن من طرف "كولر" ، "تران" و "بلاها" . كما تم حساب ثوابت المرونة باستخدام برنامج IRelast وتوظيف كمونWC−GGA ،وأيضا تم استعمال طريقة متوسط فوغت−رويس−هيل لحساب معاملات المرونة. قمن بحساب للخواص البصرية والتي تتضمن $\varepsilon_1(\omega)$ ، $\varepsilon_2(\omega)$، $n(\omega)$، $\alpha(\omega)$، $R(\omega)$.بالنسبة للخواص الحرارية فقد تم استنباطها في اطار نموذج ديباي وتم حساب المقادير التالية :$C_v(T)$ ، $\theta_D(T)$ ، $B(T)$، $\alpha(T)$.

تُظهر سبائك $AlSb_{1-x}As_x$ فجوات طاقة مباشرة من النوع Γ−Γ في المجال $0.25 \le x \approx 0.75$ ، بينما تكون فجوات طاقة $AlSb_{1-x}Bi_x$ مباشرة للتراكيب من 0,25 الى 1 مع تناقص منتظم لطاقة الفجوة يشمل المجال الطيفي من القريب من تحت−الأحمر إلى تحت−الأحمر المتوسط. ان سلوك الثوابت البصرية يتوافق مع القيم المتحصل عليها للفجوات الطاقوية Eg ينخفض $n(0)$ مع زيادة As ويزداد مع زيادة Bi أمّا في سبائك BaO ، إن استبدال الأكسجين بالكبريت ثم بالسيلينيوم يؤدّي إلى زيادة في ثابت الشبكة البلورية، ويُخفض معامل الانضغاط الحجمي B ودرجة حرارة ديباي، كما يزيد من قيم معامل التمدد الحراري $\alpha(T)$.كذلك تنخفض ضغوط الانتقال البنيوي NaCl→CsCl مع ازدياد قيمة التركيز ، وذلك في توافق جيّد مع القيم المرجعية المستخلصة من الحسابات السابقة والبيانات التجريبية المتوفّرة للمواد الثنائية. ويؤكّد هذا التطابق موثوقية طرائق الحساب المعتمدة.

قدّمت هذه الأطروحة قاعدة بيانات مفصّلة بحسب التركيب تشمل قيماً حسابية جديدة للخواص المرونية والبصرية والحرارية عند التراكيب المتوسطة $(x = 0.25–0.75)$، إلى جانب استنباط بعض التطبيقات المحتلمة لهذه المركبات و التي تشمل أجهزة منتجة للضوء وكواشف ضوئية بالإضافة الى عوازل و أجهزة استشعار الأشعة فوق البنفسجية.

.الكلمات المفتاحية:

نظرية الكثافة الدالية , الخواص الضوئية، فجوة الطاقة ، KTB−mBJ، WC−GGA، ودرجة ديباي

Abstract

Résumé

Cette thèse présente une étude ab initio des propriétés structurelles, de stabilité, électroniques, optiques, élastiques et thermiques de quatre systèmes d'alliages : $AlSb_{1-x}As_x$ et $AlSb_{1-x}Bi_x$ de structure zinc-blende, ainsi que $BaO_{1-x}S_x$ et $BaO_{1-x}Se_x$ de structure sel gemme (NaCl), pour x = 0, 0,25, 0,50, 0,75 et 1. Les courbe des énergie en fonction du volume ont été ajustées à l'équation d'état de Murnaghan, établissant les phases zinc-blende et NaCl comme phases plus stables; l'étude de l'enthalpie en fonction de la pression fournit des informations sur les transitions de phase induites par la pression. Les structures de bandes et les densités d'états ont été calculées à l'aide du potentiel mBJ développé par Koller, Tran et Blaha. $AlSb_{1-x}Bi_x$ présentent des gaps directs pour tout $x > 0$, avec une réduction du gap couvrant la gamme spectrale du proche infrarouge au moyen infrarouge (NIR–MWIR) et les alliages $AlSb_{1-x}As_x$ présentent un gap direct Γ–Γ pour $0,25 \leq x \leq 0,75$, tandis que les alliages Les constantes élastiques ont été obtenues dans le cadre de la WC-GGA en utilisant la méthode IRelast et l'approximation de Voigt–Reuss–Hill. Les spectres optiques, incluant $\varepsilon_1(\omega)$, $\varepsilon_2(\omega)$, $n(\omega)$, $\alpha(\omega)$ et $R(\omega)$, ont été évalués. Les constantes optiques suivent la tendance du gap, avec une diminution de n(0) lors de l'incorporation de l'As et une augmentation avec l'incorporation du Bi. Les propriétés thermiques ont été étudiées par le modèle de Debye afin d'obtenir la capacité calorifique, la température de Debye, le module de compressibilité et le coefficient de dilatation thermique. Dans les alliages à base de BaO, la substitution O → S → Se induit une expansion du réseau cristallin, une diminution de B et de θ^D, ainsi qu'une augmentation de $\alpha(T)$. Les pressions de transition NaCl → CsCl diminuent avec la teneur en chalcogène et tendent vers les limites binaires rapportées dans la littérature. La concordance avec les références théoriques et expérimentales disponibles pour l'ensemble des composés, ainsi que la cohérence globale des résultats obtenus, confirment la validité des méthodes employées.
La thèse fournit un ensemble de données des propriétés des matériaux pour déférente compositions (x) tels que les propriétés élastiques, optiques et thermiques, en plus d'identifier des applications potentielles de ces composés, notamment les dispositifs émetteurs de lumière et les photodétecteurs, ainsi que des revêtements et les dispositifs de détection dans le proche ultraviolet.

Mots-clés
DFT ; KTB-mBJ ; WC-GGA ; propriétés optiques , gap d'énergie , température de Debye

Contents

Liste of figures……..……i

List of table……..……ii

General introduction…….…….……1

Chapter I: Theoretical Elements in Semiconductor Physics

I.1. Basic concepts in crystallography 8

I.1.1. Lattice and Basis 8

I.1.2. Unit Cells and Bravais Lattices (e.g: Cubic Family) 9

I.1.3. Crystallographic Directions and Planes (Miller Indices) 9

I.1.4. Reciprocal Lattice and First Brillouin Zone 10

I.1.5. Common Crystal Structures 12

I.1.5.1. Zinc Blende (ZB) Structure.....12

I.1.5.2. Sodium chloride structure 12

I.1.5.3. Cesium Chloride (CsCl) structure.....14

I.1.5.4. The Wurtzite structure.....14

I.2. Binary II–V and II–VI Semiconductors: Parent Compounds for Ternary Alloy Design 15

I.3. Alloying & Vegard's Law in Ternary Semiconductor Alloys 18

I.3.1. Vegard's Law for Lattice Parameter.....18

I.3.2. Electronic-Structure Bowing.....18

I.4. First Brillouin zone and irreducible Brillouin zone.....19

I.4.1. High symmetry points.....20

I.4.2. High symmetry lines 21

I.4.3. Band structure formation 21

I.5. Theoretical background of optical properties 22
I.5.1. Dielectric function ε(ω) 23
I.5.2. Optical constants derived from ε(ω) 23
I.5.3. Interband and Intraband Transitions 25
I.5.3.1. Interband Transitions 25
I.5.1.2. Intraband Transitions 26
I.6. Elastic Properties of Crystalline Semiconductors 27
I.6.1. Elastic Constants Cij 27
I.6.2. The mechanical moduli 28
I.6.3. Ductility and Elastic Anisotropy 29
I.7. Thermal Properties in the Quasi-Harmonic Approximation (QHA) 30
I.7.1. Physical context and scope 30
I.7.2. Full-phonon QHA: thermodynamic potentials and basic responses 31
I.7.3. Fundamental QHA identities 32
I.7.4. Debye-QHA specialization 32
I.7.5. Limitations and extensions 33
References of Chapter I 34

Chapter II: Theoretical framework of DFT

II.1. Introduction to Density Functional Theory 38
II.1.1. The many-body Schrodinger equation 38
II.1.2. The Born-Oppenheimer approximation. 40
II.1.3. Independent electrons approximation 41
II.1.4. Hartree-Fock approximation 42
II.1.5. Electron correlation 44
II.2. Density Functional Theory 45

II.2.1. Thomas Fermi model 45
II.2.2 Hohenberg-Kohn theorems 48
II.2.3. The Kohn-Sham's scheme 52
II.2.3.1. The decomposition of the universal Functional 52
II.2.3.2. The Kohn-Sham's equations 54
II.3. Exchange-correlation approximations. 56
II.3.1. Local density approximation (LDA/LSDA) 57
II.3.2. Gradient expansion approximation -GEA 59
II.3.3. Generalized Gradient Functionals -GGA 61
II.3.3.1. Becke88 (B88) Exchange potential 62
II.3.3.2 Lee-Yang-Parr (LYP) Correlation functional 63
II.3.3.3. PW91 Exchange-Correlation Functional 64
II.3.3.4. PBE-GGA Exchange-Correlation Functional 65
II.3.3.5. The B97-GGA Functional 67
II.3.3.6. WC-GGA Exchange-Correlation Functional 68
II.3.3.7. The PBEsol Functional 70
II.3.3.8. EV-GGA Exchange Functional 71
II.3.4. The modified Becke-Johnson (mBJ) potential 73
II.3.5. Meta-Generalized-Gradient Approximations 76
II.3.6. Hybrid Functionals 76
II.4. Solving Kohn-Sham equations and SCF calculations 78
References of Chapter II……..……..…….....81

Chapter III: Computational methods

III.1. Bloch's Theorem and Plane-wave basis set 88
III.2.Brillouin Zone Sampling, and k-Points 89

III.3. APW method 91

III.4. The LAPW Method 94

III.5. The FP-LAPW Method 95

III.6. Basis Set Size in FP-LAPW Method 98

III.7. LAPW+lo and APW+lo Methods and the Wien2k code 99

III.7.1. LAPW+lo Method 99

III.7.2. APW+lo method 100

III.7.3. WIEN2k Electronic Structure Package and Its Components 101

III.7.3.1. Overview of Properties and approximations supported in WIEN2k 101

III.7.3.2. Essential WIEN2k modules 102

III.7.3.3. Self-Consistent Field (SCF) Cycle in WIEN2k 109

III.7.3.4. Advantages and limitations of Wien2k code 113

References of Chapter III 116

Chapter IV: Results and discussion

IV.I. Computational methods details 120

IV.II. Convergence tests for chosen global settings 121

IV.III. Structural properties 123

IV.III.1. Phase Stability 123

IV.III.2. Pressure induced phase transitions 127

IV.III.3. Equilibrium Lattice Parameters (a_0) and Bulk Moduli (B_0) 135

IV.IV. Electronic properties 136

IV.IV.1. Band structure 136

IV.IV.2. Density of states 146

IV.IV.3. Cross-Family Comparison of Electronic Structure (Bands & DOS) 154

IV.V. Optical properties 155

IV.VI. Elastic Properties 171

IV.VII. Thermal Properties 183

References of Chapter IV 196

Conclusions 198

List of figures

Figure	Title	Page
Chapter I		
Figure I.1	Lattice (crosses) with a two-atom basis (squares)	08
Figure I.2	the cubic family	09
Figure I.3	Directions [100], [110], and [111]	10
Figure I.4	(100), (110) and (111) planes	10
Figure I.5	2D square reciprocal lattice with the first Brillouin zone (square)	11
Figure I.6	The Zinc Blende Structure	13
Figure I.7	The NaCl Structure	13
Figure I.8	Cesium Chloride (CsCl) structure	14
Figure I.9	(a) the Wurtzite conventional cell structure (b)the Wurtzite unit cell structure	15
Figure I.10	The AlSb Zinc Blende Structure	16
Figure I.11	The NaCl Structure of BaS	17
Figure I.12	Illustration of the first Brillouin zones for simple cubic, face-centered cubic (fcc), and body-centered cubic (bcc) lattices, highlighting key high-symmetry points commonly used in band structure plots	19
Figure I.13	First Brillouin zone of ZB structure (F-43m)	20
Figure I.14	Schematic showing the evolution from atomic orbitals to energy bands in solids	21

Figure I.15	Band structure of gallium arsenide (GaAs)	22
Figure I.16	Schematic of an Interband Transition	26
Chapter II		
Figure II.1	Potential curves of the H_2 molecule	44
Figure II.2	Graphical illustration of the Kohn–Sham approach	55
Figure II.3	Schematic representation of Jacob's ladder of DFT	57
Figure II.4	Illustration of regions of uniform electron gas density in LDA approach	58
Figure II.5	Flow schematic chart of the SCF cycle	80
Chapter III		
Figure III.1	Truncation of the plane wave development in reciprocal space	88
Figure III.2	Employed approaches for the treatment of periodic solids materials	89
Figure III.3	The dual representation of the APW and LAPW methods	91
Figure III.4	Initialization with wien2k w2web interface	103
Figure III.5	Chart of optical properties calculation procedure in Wien2k	107
Figure III.6	Program flow in *WIEN2k (scf)*	110
Figure III.7	Execution of the SCF cycle in WIEN2k (single/parallel modes)	111
Chapter IV		
Figure IV.1	Total-energy convergence with RK_{max} density for AlAs, $AlSb_{0.75}As_{0.25}$, BaO, and $BaO_{0.25}Se_{0.75}$	122

Figure IV.2	Total-energy convergence with RK_{max} density for AlAs, $AlSb_{0.75}As_{0.25}$, BaO, and $BaO_{0.25}Se_{0.75}$	123
Figure IV.3	Total-energy vs volume datasets, fitted with a Murnaghan EOS, for ZB(B3), NaCl (B1), CsCl (B2) , and WZ for $AlSb_{1-x}Bi_x$ alloys .	124
Figure IV.4	Energy–volume points fitted with a Murnaghan EOS for the ZB, NaCl, CsCl, and WZ polymorphs of $AlSb_{1-x}As_x$ alloys .	125
Figure IV.5	Energy–volume points fitted with a Murnaghan EOS for the ZB, NaCl, CsCl, and WZ polymorphs for $BaO_{1-x}AS_x$ for $(x = 0,0.25,0.5,0.75\ and\ 1)$ alloys	126
Figure IV.6	Energy–volume points fitted with a Murnaghan EOS for the ZB, NaCl, CsCl, and WZ polymorphs of $BaO_{1-x}AS_x$ for$(x = 0,0.25,0.5,0.75 and 1)$ alloys using WC-GGA approximation.	127
Figure IV.7	Calculated enthalpy versus pressure (0 K) for the ZB, NaCl, CsCl, and WZ (wurtzite) geometries for $AlSb_{1-x}Bi_x$ alloys.	129
Figure IV.8	Computed enthalpies as a function of pressure at T=0K for the ZB, NaCl, CsCl, and WZ geometries for $AlSb_{1-x}As_x$ alloys for (x=0.25, 0.5, 0.75 and 1)	130
Figure IV.9	Computed enthalpies as a function of pressure at T=0K for the ZB, NaCl, CsCl, and WZ geometries for $BaO_{1-x}S_x$ alloys for (x=0, 0.25, 0.5, 0.75 and 1)	132
Figure IV.10	Computed enthalpies as a function of pressure at T=0K for the ZB, NaCl, CsCl, and WZ geometries for $BaO_{1-x}Se_x$ alloys for (x=0.25, 0.5, 0.75 and 1)	133
Figure IV.11	ZB $AlSb_{1-x}As_x$: Band structures (KTB-mBJ) (x=0.25,0.5,0.75 and 1)	139
Figure IV.12	ZB $AlSb_{1-x}Bi_x$: Band structures (KTB-mBJ+SoC)	140
Figure IV.13	$BaO_{1-x}S_x$ (NaCl): Band structures (KTB-mBJ).	142
Figure IV.14	$BaO_{1-x}Se_x$ (NaCl): Band structures (KTB-mBJ)	143

Figure IV.15	AlSb: Total DOS and PDOS vs energy (eV) (KTB-mBJ)	148
Figure IV.16	$AlSb_{0.5}As_{0.5}$: Total DOS and PDOS vs energy (eV) (KTB-mBJ).	148
Figure IV.17	AlBi: Total DOS and PDOS vs energy (eV) (KTB-mBJ)	149
Figure IV.18	$AlSb_{0.75}Bi_{0.25}$: Total DOS and PDOS vs energy (eV) (KTB-mBJ)	149
Figure IV.19	BaO: Total DOS and PDOS vs energy (eV) (KTB-mBJ).	152
Figure IV.20	$BaO_{0.25}S_{0.75}$: Total DOS and PDOS vs energy (eV) (KTB-mBJ).	152
Figure IV.21	BaSe: Total DOS and PDOS vs energy (eV) (KTB-mBJ).	153
Figure IV.22	$BaO_{0.5}Se_{0.5}$: Total DOS and PDOS vs energy (eV) (KTB-mBJ).	153
Figure IV.23	III-V Selected alloys' $\varepsilon_1(\omega)$ and $\varepsilon_2(\omega)$ spectra	157
Figure IV.24	III-V Selected alloys' absorption coefficients	159
Figure IV.25	III-V Selected alloys' Refractive indices	161
Figure IV.26	Reflectivities of selected III-V alloys	162
Figure IV.27	The dielectric functions of II-VI selected alloys	165
Figure IV.28	The absorption coefficients of II-VI alloys	167
Figure IV.29	The refractive indices of selected II-VI alloys	169
Figure IV.30	The reflectivities of II-VI selected alloys	170
Figure IV.31	Constant-volume heat capacity of III-V selected alloys	184
Figure IV.32	Debye temperature $\theta_D(T)$ versus temperature of III-V selected alloys	185

Figure IV.33	The temperature-dependent bulk modulus B(T) of our III-V selected alloys	186
Figure IV.34	Linear thermal expansion α(T) of our III-V selected alloys	187
Figure IV.35	Constant-volume heat capacity $C_v(T)$ of our II-VI alloys.	190
Figure IV.36	Debye temperature $\theta_D(T)$ versus temperature of II-VI selected alloys	191
Figure IV.37	The temperature-dependent bulk modulus B(T) of our II-VI selected alloys	193
Figure IV.38	Linear thermal expansion coefficients α(T) of II-VI selected alloys	193

List of tables

Table	Title	Page
Chapter I		
Table I.1	Key Characteristics of the Wurtzite structure	15
Table I.2	Structural Properties of Selected Binary Semiconductors and Electronic Configuration for their cations and anions	18
Table I.3	Comparative Analysis of Interband vs Intraband Transitions	26
Table I.4	Independent elastic constants depending on crystal system	27
Table I.5	Elastic moduli and their description	28
Table I.6	Ductility criteria and their interpretation	29
Table I.7	Elastic anisotropy indicators and interpretation	29
Chapter II		
Table II.1	TB-mBJ Parameter Variants	76
Chapter III		
Table III.1	Calculated Properties in WIEN2k	100
Table III.2	Some supported functionals in WIEN2k	101
Chapter IV		
Table IV.1	Calculated transition pressures Pc of the selected III-V alloys at 0K temperature	131

Table IV.2	Calculated transition pressures P_c of the selected II-VI alloys at 0K temperature	134
Table IV.3	Estimated computational values of lattice parameters *a* (in Å) and bulk modulus *B* (in GPa) of selected III-V ternary alloys in ZB phase via the Wu–Cohen (WC–GGA) approximation, compared with other calculations and experimental data.	135
Table IV.4	Estimated computational values of lattice parameters *a* (in Å) and bulk modulus *B* (in GPa) of selected II-VI ternary alloys in NaCl phase via the Wu–Cohen (WC–GGA) approximation, compared with other calculations and experimental data.	137
Table IV.5	Estimated computational values of Band Gaps $E_g(eV)$ of selected III-V ternary alloys in ZB phase via the PBE-KTB-mBJ+SoC approximation, compared with other calculations and experimental data.	141
Table IV.6	Estimated computational values of Band Gaps $E_g(eV)$ of selected II-VI ternary alloys in NaCl phase via the PBE-KTB-mBJ approximation, compared with other calculations and experimental data.	144
Table IV.7	III-V Selected alloys' Critical-Point Energies of $\varepsilon_2(\omega)$ and Static Dielectric Constant $\varepsilon_1(0)$	156
Table IV.8	Estimated static refractive index *n(0)* of III–V selected alloys in ZB phase via KTB-mBJ, compared with other theoretical calculations and available experimental data.	160
Table IV.9	II-VI Selected alloys' Critical-Point Energies of $\varepsilon_2(\omega)$ and Static Dielectric Constant $\varepsilon_1(0)$	166
Table IV.10	n(0) computed values II–VI selected alloys in NaCl phase via KTB-mBJ along With Benchmarks (Exp [71], GGA [51],[40], TB-mBJ[35])	168
Table IV.11	Single-Crystal Stiffness (C_{11}, C_{12}, C_{44}) and Polycrystalline Bulk Modulus (GPa), Shear Modulus (GPa), Young's Modulus (GPa), Poisson's Ratio, Vickers Hardness (GPa), Pugh Ratio, and Cauchy Pressure (GPa) for $AlSb_{1-x}As_x$ via WC-GGA with available other calculations and existing experimental values	172
Table IV.12	Computational results of Zener anisotropic index A, percentage anisotropic indices (A_G) and (A_B) ,the universal	173

	anisotropic factor (A^U) are in GPa, of $AlSb_{1-x}As_x$ alloys via WC-GGA with other available calculations.	
Table IV.13	Single-Crystal Stiffness (C_{11}, C_{12}, C_{44}) and Polycrystalline Bulk Modulus (GPa), Shear Modulus (GPa), Young's Modulus (GPa), Poisson's Ratio, Vickers Hardness (GPa), Pugh Ratio, and Cauchy Pressure (GPa) for $AlSb_{1-x}Bi_x$ via WC-GGA with available other calculations and existing experimental values	175
Table IV.14	Computational results of Zener anisotropic index A, percentage anisotropic indices (A_G) and (A_B) ,the universal anisotropic factor (A^U) in GPa of $AlSb_{1-x}Bi_x$ alloys via WC-GGA with other available calculations.	176
Table IV.15	Single-Crystal Stiffness (C_{11}, C_{12}, C_{44}) and Polycrystalline Bulk Modulus (GPa), Shear Modulus (GPa), Young's Modulus (GPa), Poisson's Ratio, Vickers Hardness (GPa), Pugh Ratio, and Cauchy Pressure (GPa) for $BaO_{1-x}S_x$ via WC-GGA with available other calculations and existing experimental values	178
Table IV.16	Computational results of Zener anisotropic index A, percentage anisotropic indices (A_G) and (A_B) ,the universal anisotropic factor (A^U) are in GPa, of $BaO_{1-x}S_x$ alloys via WC-GGA with other available calculations.	178
Table IV.17	Single-Crystal Stiffness (C_{11}, C_{12}, C_{44}) and Polycrystalline Bulk Modulus (GPa), Shear Modulus (GPa), Young's Modulus (GPa), Poisson's Ratio, Vickers Hardness (GPa), Pugh Ratio, and Cauchy Pressure (GPa) for $BaO_{1-x}Se_x$ via WC-GGA with available other calculations and existing experimental values	180
Table IV.18	Computational results of Zener anisotropic index A, percentage anisotropic indices (A_G) and (A_B) ,the universal anisotropic factor (A^U) are in GPa, of $BaO_{1-x}Se_x$ alloys via WC-GGA with other available calculations.	181
Table IV.19	Computational results of thermal properties of III-V Selected alloys at 300 K	189
Table IV.20	Computational results of thermal properties of II-VI Selected alloys at 300 K	194

General Introduction

General Introduction

Crystalline inorganic semiconductors, form the backbone of modern solid-state electronics, serves as the essential materials behind a vast array of technological devices. These semiconductors can be elemental like silicon and germanium or compounds and alloys comprising multiple elements. This thesis centers around III–V and II–VI semiconductor alloys: compound semiconductors created by combining elements from groups III and V or II and VI of the periodic table. These substitutional alloys are especially significant because of their outstanding electronic and optoelectronic properties, which make them highly valuable for a wide range of contemporary applications [1]. Over the years, III–V and II–VI alloys have played pivotal roles in advancing electronic and optoelectronic devices—such as high-electron-mobility transistors (HEMTs), semiconductor lasers, solar cells, light-emitting diodes (LEDs), and photodetectors. Devices that emit in the visible range, like LEDs and semiconductor lasers, have become indispensable in optical data storage, full-color displays, and high-speed communications. These technologies not only power high-brightness displays but also enhance HDMI interfaces, often relying on semiconductor laser-based light sources [2]. The relentless push for higher data rates and broader bandwidths-driven by the rapid evolution of wireless communication systems—has intensified the demand for faster, more efficient electronic components. Meeting this demand requires materials that can support high-speed operation, low power consumption, and minimal signal distortion. Owing to their high electron mobilities and direct band gaps, III–V and II–VI semiconductors offer an ideal platform for manufacturing such high-performance devices, thereby enabling quicker and more reliable data transmission [3]. One of the most compelling features of these alloys is their tunable electronic and optical properties. By carefully adjusting their composition and lattice parameters—through band gap engineering and strain modulation researchers can tailor these materials for specific applications. This flexibility paves the way for innovations like multi-junction solar cells with superior efficiencies or lasers designed to emit at precise wavelengths. To fully leverage this potential, a deep understanding of the intrinsic physical properties such as structural stability, electronic band structure, and optical behavior is crucial. In this context, first-principles computational methods, particularly Density Functional Theory (DFT), have emerged as

indispensable tools for investigating semiconductor materials. These ab initio approaches allow researchers to predict material properties with high accuracy, without relying on experimental data. As a result, they offer powerful insights into atomic-scale interactions, electronic structures, and mechanical properties, enabling the rational design of semiconductors with tailored functionalities [4,5]. This thesis employs ab initio methods to systematically explore the structural, electronic, and optical properties of III-V and II-VI semiconductor alloys. By integrating theoretical modeling with experimental validation, it aims to advance our understanding of these materials and contribute to their development for next-generation electronic and optoelectronic applications.

This study is motivated by the structural compatibility, tunable electronic properties, and technological interest of these binary compounds. Specifically, we are motivated by the III-V compounds AlSb, AlAs, as well as theoretically predicted AlBi, which exhibit a common zinc-blende lattice with tetrahedral coordination. Such structural compatibility allows for smooth alloying, as well as precise engineering of their band gaps. These compounds are thus interesting for opto-electronic and infrared device technologies. On the other hand, the II-VI compounds BaO, BaS, and BaSe exhibit rocksalt-type lattices, thus ensuring both chemical and crystallographic compatibility. These compounds are characterized by large band gaps, as well as ionic-type bonding. In this work , we thus investigate the III-V alloys AlSb1-xBix, AlSb1-xAsx, as well as the II-VI oxide alloys BaO1-xSx, BaO1-xSex. Specifically, we focus on these compounds for x = 0, 0.25, 0.5, 0.75, 1. We thus establish a representative model for understanding how gradual composition changes affect these compounds. We are also motivated by the fact that these compounds exhibit largely unexplored potential, especially for discovering new compound functionalities in the case of the BaO1-xSx alloy.

This work consists of four chapters:

- **Chapter I** is titled as **"Fundamentals of Crystalline Semiconductors"** it provides the essential theoretical background on crystalline semiconductors. It begins with the basic principles of crystallography introducing atomic lattices, unit cells, Miller indices, reciprocal space, and the common crystal structures found in semiconductor materials. The chapter then discusses binary II–V and II–VI compounds and explains how alloying principles such as

Vegard's law and band-gap bowing govern the behavior of ternary alloys. It also outlines the role of the Brillouin zone and its symmetry points in shaping electronic band structures. The optical response of semiconductors is reviewed through the dielectric function and the mechanisms of interband and intraband transitions. Mechanical behavior is introduced via elastic constants and moduli, followed by an overview of thermal properties using the quasi-harmonic approximation. Altogether, the chapter builds a compact but comprehensive foundation for understanding the structural, electronic, optical, mechanical, and thermal properties of the semiconductor systems explored later in the thesis.

- **Chapter II** is titled as " **Theoretical framework of DFT" ,** it presents the theoretical foundation of Density Functional Theory (DFT), the principal computational framework used throughout this work. It begins by outlining the quantum-mechanical challenge of solving the many-body Schrödinger equation and introduces key approximations including the Born–Oppenheimer, independent-electron, Hartree–Fock, and electron-correlation concepts that motivated the development of modern electronic-structure methods. The chapter then transitions to the formalism of DFT, starting with early models such as the Thomas–Fermi approximation and progressing to the Hohenberg–Kohn theorems, which establish electron density as the central variable of the theory. A detailed discussion of the Kohn–Sham scheme follows, describing the decomposition of the total energy functional, the resulting Kohn–Sham equations, and the crucial role of exchange–correlation approximations. Various functional families including LDA, GGA, meta-GGA, hybrid approaches, and specialized forms such as PBE, B88, LYP, WC-GGA, PBESol, EV-GGA, and the modified Becke–Johnson potential are reviewed to highlight their strengths and typical applications. The chapter concludes with an overview of how Kohn–Sham equations are solved in practice through self-consistent field (SCF) iterations. Overall, Chapter II provides a comprehensive yet accessible framework for understanding the methodological tools used to compute the electronic and structural properties of the materials studied in this thesis.

- **Chapter III** is titled as " **Computational methods"** which introduces the computational techniques and numerical methods used to solve the Kohn–Sham equations within the Density Functional Theory framework. It begins with a review of Bloch's theorem, which justifies the use of plane-wave basis sets and sets the foundation for representing electronic states in periodic solids. The chapter then discusses Brillouin-zone sampling and the role of k-points in achieving accurate integrations over reciprocal space. Building on these fundamentals, several all-electron methods are presented, including the Augmented Plane Wave (APW), Linearized APW (LAPW), and Full-Potential LAPW (FP-LAPW) schemes, with explanations of how they improve accuracy by treating core and valence electrons without shape approximations. The discussion extends to the LAPW+lo and APW+lo formulations, which enhance variational flexibility and computational efficiency. A substantial part of the chapter is devoted to the WIEN2k package, describing its structure, supported approximations, essential modules, and the steps involved in a typical self-consistent field (SCF) cycle. The chapter concludes by outlining the strengths and limitations of WIEN2k, emphasizing why it is widely used for precise electronic-structure calculations. Overall, Chapter III provides the methodological and practical background necessary for performing accurate first-principles simulations of crystalline materials.

- **Chapter IV** is titled as "**Results and Discussion**" presents the core computational results obtained in this work, beginning with the numerical details and convergence tests required to ensure reliable first-principles calculations. Once the global parameters were optimized, the chapter examines the structural properties of the studied compounds, including their phase stability, pressure-induced structural transitions, and the extraction of equilibrium lattice constants and bulk moduli from equation-of-state fitting. The electronic properties are then analyzed through calculated band structures and densities of states, followed by a cross-family comparison to highlight trends in electronic behavior across different material phases. The optical response of the materials is subsequently explored using frequency-dependent dielectric functions, enabling the derivation of key optical constants and the identification of characteristic absorption features. Mechanical

behavior is assessed through a full set of elastic constants and related moduli, providing insights into ductility, anisotropy, and mechanical stability. The chapter concludes with the evaluation of thermal properties within the quasi-harmonic approximation, including heat capacity, thermal expansion, and Debye temperature, to complete a comprehensive understanding of the materials' behavior under realistic conditions. Altogether, Chapter IV delivers a systematic and interconnected analysis of structural, electronic, optical, elastic, and thermal properties, forming the central scientific contribution of this thesis.

Refrences

1. S. Adachi, *Properties of Semiconductor Alloys: Group-IV, III-V and II-VI Semiconductors*, 1. ed (Wiley, Chichester, 2009).

2. S. M. Sze and K. K. Ng, Physics of Semiconductor Devices **3**, 601 (2006).

3. I. Vurgaftman, J. Meyer, and L. R. Ram-Mohan, Journal of Applied Physics **89**, 5815 (2001).

4. Hafner, Ab-initio simulations of materials using VASP: Density-functional theory and beyond, J. Comput. Chem. 29, 2044 (2008).

5. R. M. Martin, *Electronic Structure: Basic Theory and Practical Methods*, 2nd ed. (Cambridge University Press, 2020).

Chapter I

CHAPTER I

Chapter I: Fundamentals of Crystalline Semiconductors

Semiconductors which are the cornerstone of modern technology enable the function of transistors, light-emitting diodes (LEDs), lasers, and photovoltaic devices. What distinguishes semiconductors from insulators and metals is their moderate band gap and the ability to manipulate their electrical and optical behavior via doping, external fields, and alloying [1]. In particular, III–V and II–VI compound semiconductors have garnered significant attention due to their favorable optoelectronic properties, high carrier mobilities, and wide tunability in band structure [2,3] .The performance of semiconductors is deeply rooted in their crystal structure and symmetry. Common structures include zinc blende (ZB) , wurtzite (WZ), often observed in III–V and II–VI compounds, as well as rocksalt (NaCl) and cesium chloride (CsCl), which appear under specific thermodynamic conditions or in certain binary alloys [4–6]. These crystal frameworks define the electronic band topology and phonon dispersion, influencing the material's transport and optical responses.

To fully understand semiconductor behavior, it is essential to explore the band theory of solids, particularly the distinction between direct and indirect band gaps, the application of Bloch's theorem, and the concept of effective mass [7]. These ideas explain how electrons and holes move in a periodic potential and how their dynamics determine current flow, recombination rates, and optical transitions [8,9] .This chapter also outlines the optical properties of semiconductors, such as interband absorption, photoluminescence, and excitonic effects, which are fundamental to applications in photodetectors and light sources [10–12].

Moreover, the Brillouin zone (BZ) and irreducible Brillouin zone (IBZ) are introduced, as they are key to interpreting band structures, especially along high-symmetry directions defined by space group symmetry [13,14] .A central theme in modern semiconductor research is alloying, where binary compounds such as GaAs or CdTe are mixed to form ternary or quaternary alloys like $In_xGa_{1-x}As$ or $Cd_{1-x}Zn_xTe$. Alloying enables band gap engineering, strain tuning.

Finally, this chapter introduces real-world applications of III–V and II–VI semiconductors, including high-electron-mobility transistors (HEMTs), multi-junction solar cells, infrared sensors, and UV LEDs, laying the groundwork for the computational and theoretical analysis presented in the following chapters.

This chapter presents the fundamental concepts and essential physical principles underlying the behavior of III–V and II–VI semiconductor alloys. It lays the groundwork for understanding their crystal structures, electronic band properties, optical responses, and alloying effects, providing a comprehensive basis for the theoretical and computational investigations in the subsequent chapters.

I.1. Basic concepts in crystallography

I.1.1. Lattice and Basis

A crystal is constructed by placing a basis (motif) on every point of a periodic lattice. The lattice governs translational symmetry, whereas the basis sets the chemistry and local bonding environment. Primitive and conventional cells describe the same periodic solid; the latter is often chosen to display symmetry clearly as shown in Figure I.1 [1,15].

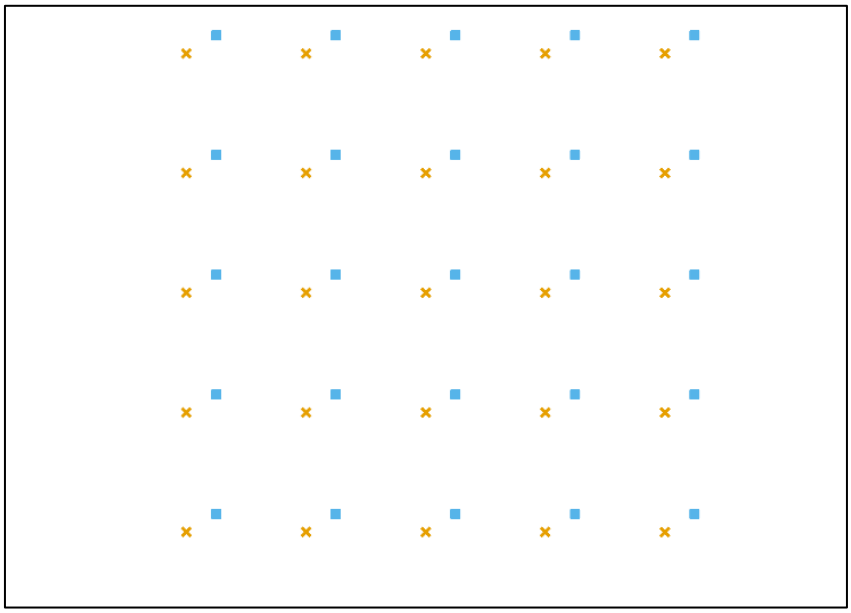


Figure. I.1 . Lattice (crosses) with a two-atom basis (squares)

I.1.2. Unit Cells and Bravais Lattices (e.g: Cubic Family)

A unit cell tiles space under lattice translations. A primitive cell contains one lattice point, while a conventional cell is chosen for symmetry. There are 14 Bravais lattices; the cubic family comprises P (primitive), I (body-centered), and F (face-centered) as shown in Figure I.2 [1,16].

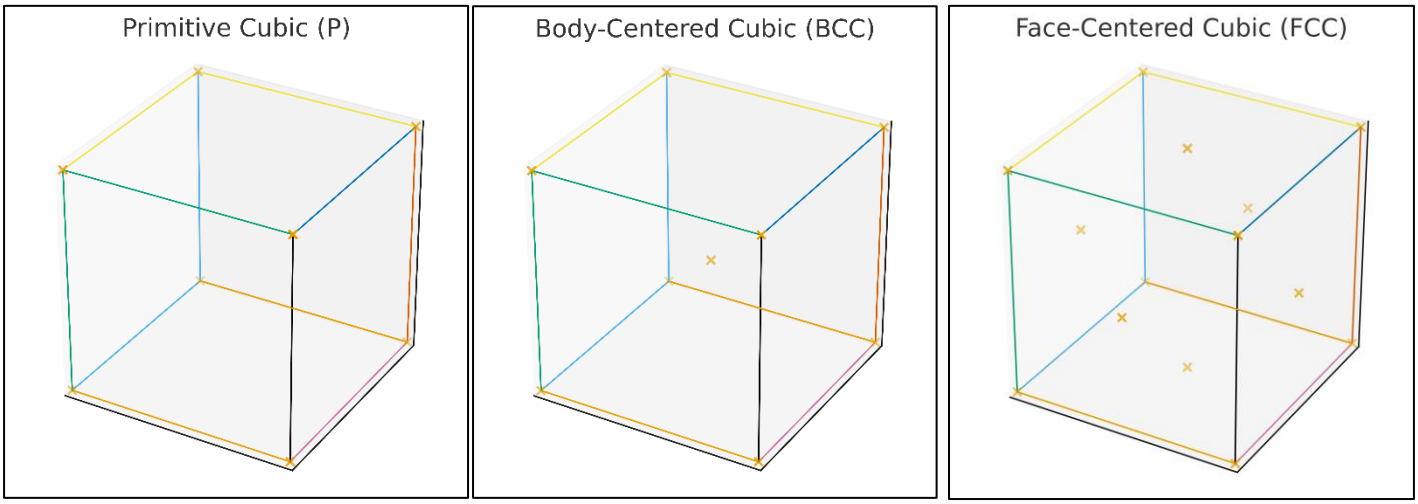


Figure I.2. The cubic family

I.1.3. Crystallographic Directions and Planes (Miller Indices)

Crystallographic directions describe how vectors are oriented inside a crystal lattice. They are expressed by Miller indices written in square brackets, for example [100], [111].To obtain them, the vector is written relative to the crystal axes, simplified to the smallest integers, and negatives are marked with a bar.While Planes inside crystals are indexed using Miller indices written in parentheses, such as (100), (110), or (111). They are determined by identifying how a plane cuts the crystallographic axes, taking the reciprocals of those intercepts, and reducing to whole numbers. Families of symmetry-equivalent planes are denoted by curly brackets, for example {111} for all octahedral planes in a cubic lattice. These planes are central in diffraction studies since they represent sets of atomic layers that scatter X-rays. In summary; Directions are denoted [hkl] (families ⟨hkl⟩); planes use (hkl) ({hkl}). Miller indices for planes are derived from the reciprocals of axis intercepts expressed in lattice-parameter units [15,17]. Figure I.3 shows Directions [100], [110], and [111] while Figure I.4 illustrates (100), (110) and (111) planes in cubic structure.

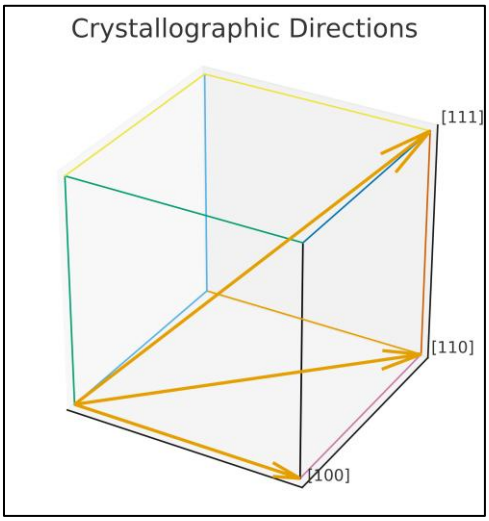


Figure I.3. Directions [100], [110], and [111].

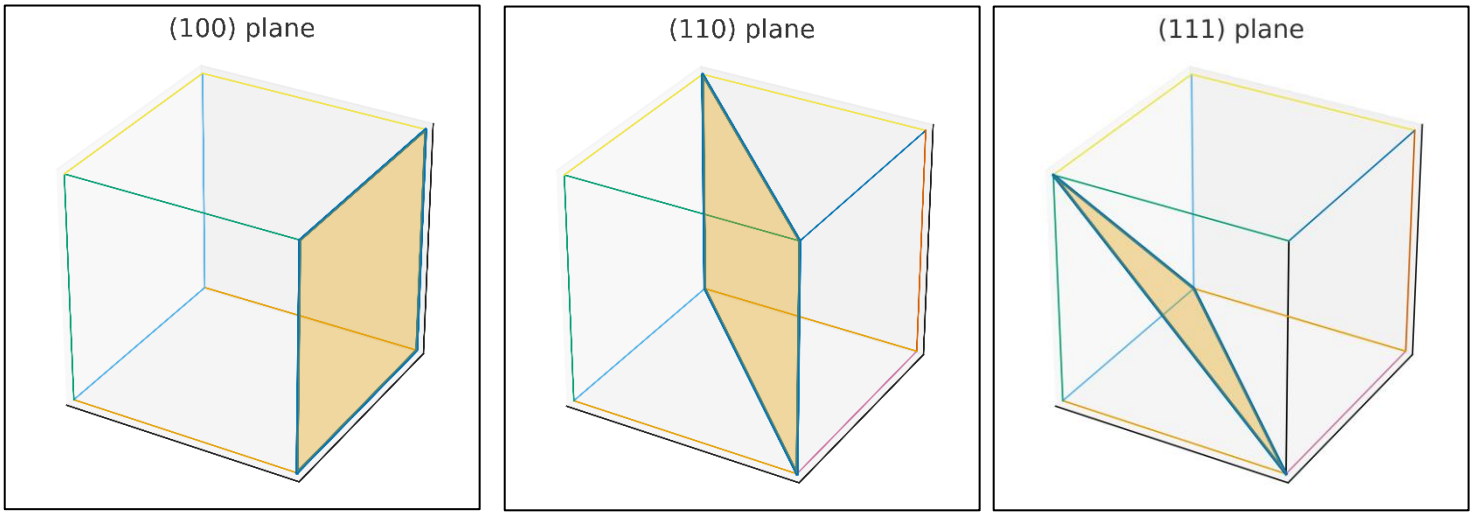


Figure I.4. (100), (110) and (111) planes.

I.1.4. Reciprocal Lattice and First Brillouin Zone

The reciprocal lattice is the natural framework for wave phenomena in crystals: each lattice point corresponds to a plane wave compatible with the crystal periodicity, so diffraction patterns map directly onto this lattice and are most transparently interpreted there. Classic treatments show how electron, phonon, and X-ray scattering are organized in reciprocal space, making it the standard language for band structures and dispersion relations. The first Brillouin zone is the Wigner–Seitz cell of the reciprocal lattice; its boundaries are defined by Bragg planes that bisect lines from the origin to neighboring reciprocal points. Restricting wavevectors to this zone avoids double

counting because crossing a boundary carries you to an equivalent description in an adjacent zone; symmetry then allows focus on an *irreducible* wedge and on designated high-symmetry points and lines used in band-structure paths.So, The reciprocal lattice encodes the periodicity of waves [7].

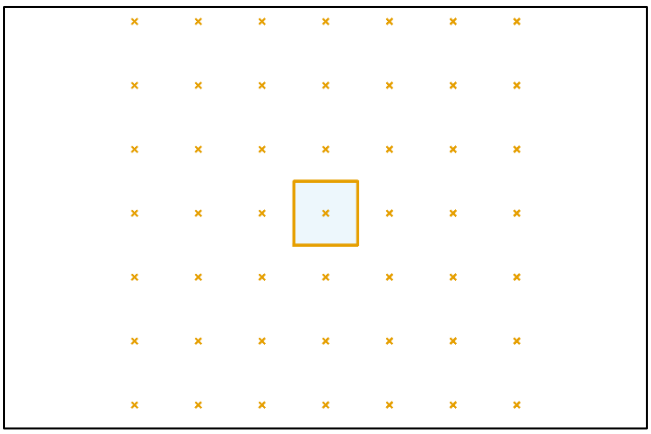


Figure. I.5. 2D square reciprocal lattice with the first Brillouin zone (square).

So, In crystalline solids, it is often convenient to work in reciprocal (Fourier) space, which naturally describes wave vectors, Bragg diffraction, and electronic band structures. The reciprocal lattice provides a mathematical representation of the periodicity of the crystal in momentum space.

A vector G belongs to the reciprocal lattice if and only if:

$$e^{iG\cdot R} = 1, \quad \forall R \in \text{direct lattice}. \tag{I. 1}$$

Equivalently:

$$G \cdot R = 2\pi m, \quad m \in Z. \tag{I. 2}$$

The real-space lattice points are written as:

$$R = n_1 a_1 + n_2 a_2 + n_3 a_3, \quad n_i \in Z. \tag{I. 3}$$

The reciprocal lattice is generated by the primitive reciprocal vectors b_1, b_2, b_3, defined by:

$$a_i \cdot b_j = 2\pi\delta_{ij}. \tag{I. 4}$$

An explicit construction is:

$$b_1 = \frac{2\pi(a_2 \times a_3)}{a_1 \cdot (a_2 \times a_3)} \tag{I. 5}$$

$$b_2 = \frac{2\pi(a_3 \times a_1)}{a_1 \cdot (a_2 \times a_3)} \tag{I. 6}$$

$$b_3 = \frac{2\pi(a_1 \times a_2)}{a_1 \cdot (a_2 \times a_3)} \quad (\mathbf{I.7})$$

Any reciprocal lattice vector can be written as:

$$G = m_1 b_1 + m_2 b_2 + m_3 b_3, \quad m_i \in Z. \quad (\mathbf{I.8})$$

The reciprocal lattice provides a fundamental representation of crystal periodicity in momentum space. Its definition ensures a direct connection between real-space translations and wave-vector quantization, which is essential for describing Bragg diffraction, electronic band structures, and phonon dispersion. This framework underpins most k-space formulations used in first-principles and solid-state calculations.

I.1.5. Common Crystal Structures

I.1.5.1. Zinc Blende (ZB) Structure

The zinc blende structure (as shown in Figure I.1) comprises of an FCC crystal lattice with a two-atom basis at (0, 0, 0) and (1/4 , 1/4 , 1/4), in distinguish to the diamond structure, the basis consists of two different atoms (ions), e.g. Zn and S. So each Zn atom is tetrahedrally surrounded by 4 S atoms and vice versa. Where The S^{2-} ions are present in FCC (Face Centered Cubic) layout. i.e The S^{2-} ions are present at the corner of the cube and at the center of each face and The Zn^{2+} ions are located in the alternative tetrahedral void and Each Zn^{2+} ion is encircled tetrahedrally by four S^{2-} ions and each S^{2-} ion is encircled tetrahedrally by four Zn^{2+} ions. Thus the structure has 4:4 coordination. In addition to ZnS many of the (most technologically important) III-V and II-VI semiconductors crystallize In the ZnS structure, in particular AlSb, AlAs, ZnSe, CdS, etc [18].This structure has space group F-43m (No. 216).The unit cell contains four Zn^{2+} and four S^{2-} ions, maintaining electrical neutrality and stoichiometry. Its tetrahedral bonding leads to significant covalent character and influences the electronic and optical properties of the material. Unlike the Dimond Structure the Zinc Blende (ZnS) structure lacks the inversion symmetry [1].

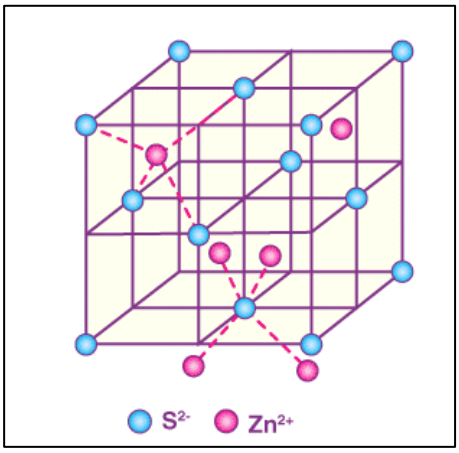


Figure I.6. The Zinc Blende Structure [19]

I.1.5.2. Sodium chloride structure

The Sodium Chloride (NaCl) structure (as presented in figure I.7) is consisted of a face centered cubic (FCC) structure with a two-atom basis (e.g., NaCl) with one atom (or ion, e.g., Na+) at site (0, 0, 0) and the other atom (ion, e.g., Cl−) at (1/2, 1/2, 1/2) [1,18].There are four units of NaCl in each unit cube, with atomic positions of (Cl: 0 0 0; ½ ½ 0 , ½ 0 ½ ; 0 ½ ½) and (Na: ½ ½ ½ ; 0 0 ½ ; 0 ½ ; ½ 0 0) with every atom has as nearest neighbors six atoms of the opposite type [1].Very few (if any) III–V semiconductors crystallizes in NaCl structure even under pressure. However, some II–VI compounds can adopt the NaCl structure like BaO, BaS and BaSe [20,21]

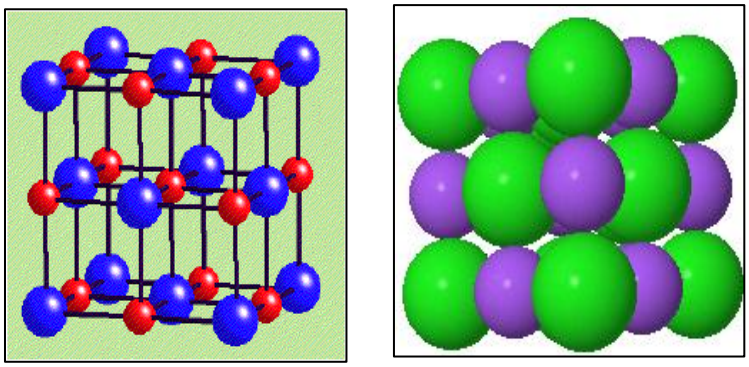


Figure I.7. The NaCl Structure [22]

I.1.5.3. Cesium Chloride (CsCl) structure

This structure is presented in figure I.8. In it there is one CsCl unit per primitive cell with the two-atom basis consisting of one atom/ion (e.g. Cs^+) at the position (0,0,0) and another atom/ion (e.g. Cl^-) at (1/2, 1/2, 1/2).

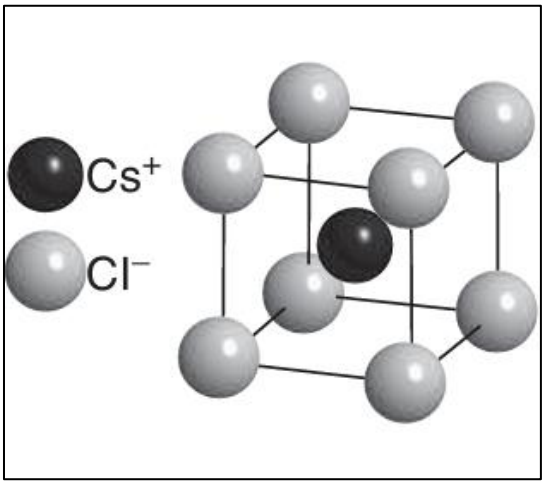


Figure I.8. Cesium Chloride (CsCl) structure [23]

This Structure can be escribed as a primitive cubic lattice of anions with cations in alternating cube body centers. In this structure, all body-center positions are occupied. Solids crystallizing in this structure can be classified into two main groups: halides of large monovalent elements and several intermetallic compounds, including CsCl, CsBr, TlCl, CuZn, and LiAg [24].

I.1.5.4. The Wurtzite structure

The wurtzite structure is a hexagonal crystal lattice that is thermodynamically stable for several III-V and II-VI binary semiconductors, such as nitrides like GaN, AlN, InN, and ZnO. This structure is characterized by its hexagonal symmetry, differing from the cubic symmetry of the zinc-blende structure. The wurtzite lattice plays an important role in several applications such as high-power microwave transistors and light-emitting diodes because of its special electronic and phonon characteristics. The unique features of the structure are a result of its hexagonal close-packed nature and the stacking order of its tetrahedrally bonded atoms.the Key Characteristics of this structure are listed in table I.1 below [1,24]:

Table I.1. Key Characteristics of the Wurtzite structure.

Property	Value/Description
Crystal system	Hexagonal (space group: $P6_3mc$, No. 186)
Lattice constants	Typically: $a \neq c$; $c/a \approx 1.633$ (ideal)
Coordination	Tetrahedral (each atom bonded to 4 neighbors)
Stacking sequence	ABAB (same as hcp anion lattice)
Atoms per unit cell	4 (2 cations + 2 anions)
Polarity	Polar structure (spontaneous polarization)

The Wurtzite structure has four atoms per unit cell in a hexagonal lattice. Two of these are cations (such as Zn in ZnO or Ga in GaN) and two are anions (such as O or N). The cations occupy fractional coordinates (1/3, 2/3, 0) and (2/3, 1/3, 1/2), and the anions are at (1/3, 2/3, u) and (2/3, 1/3, u + 1/2), where u is an internal parameter generally close to 0.375 [24].This structure is demonstrated in figure I.9 below.

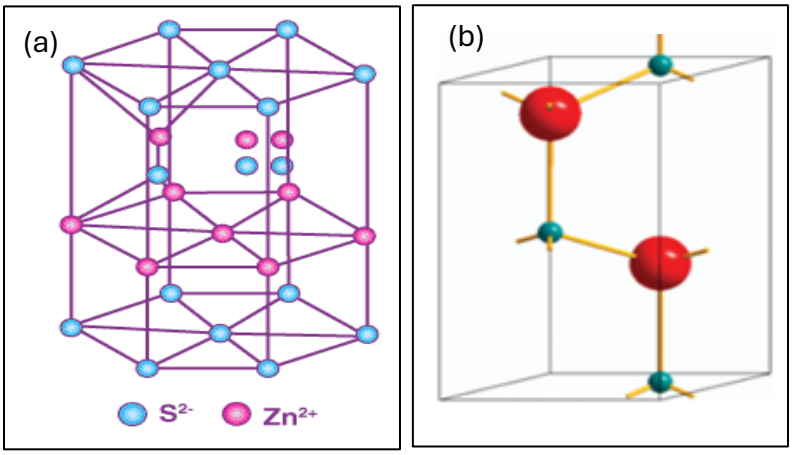


Figure I.9. (a) the Wurtzite conventional cell structure (b)the Wurtzite unit cell structure [19,25].

I.2. Binary II–V and II–VI Semiconductors: Parent Compounds for Ternary Alloy Design

In this study, the choice of binary semiconductor compounds was guided by their structural compatibility, tunable electronic properties, and relevance to optoelectronic and electronic

applications. Binary systems from the III–V and II–VI families were chosen as the foundational materials for the design and study of ternary alloys. The III–V compounds considered include aluminum antimonide (AlSb), aluminum arsenide (AlAs), and aluminum bismuthide (AlBi), all of which crystallize in the zinc blende (ZB) structure and exhibit tetrahedral coordination with direct or indirect band gaps for AlSb, AlAs and direct band gap for AlBi [1,5] . This structure, illustrated in Figure I.10 (for AlSb as example), consists of a face-centered cubic (FCC) Bravais lattice with a two-atom basis. Each atom is tetrahedrally coordinated, making it ideal for covalently bonded semiconductors like AlSb. The symmetry and short-range order of the ZB structure are important for maintaining direct or nearly direct band gaps in III–V systems [1,5] . Among the III–V materials, AlBi is a theoretically proposed compound, and first-principles calculations suggest that it could be suitable for infrared applications due to its band structure characteristics [26]. Alloys such as $AlSb_{1-x}Bi_x$ and $AlSb_{1-x}As_x$ are of interest for tailoring electronic and structural properties in optoelectronic devices [12,27] .

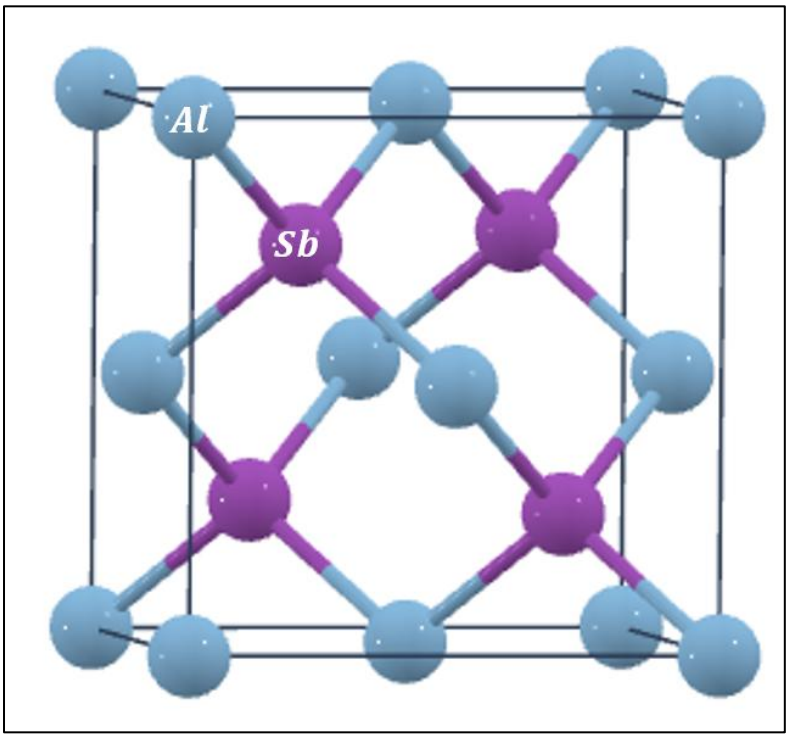


Figure I.10. The AlSb Zinc Blende Structure [28].

For the II–VI compounds, barium oxide (BaO), barium sulfide (BaS), and barium selenide (BaSe) were selected. These materials share the same rocksalt (NaCl-type) cubic structure and exhibit wide band gaps with a high degree of ionic bonding [4,21] . The rocksalt structure of BaS (as example) , shown in Figure I.11 , is characterized by octahedral coordination in a highly symmetric cubic lattice, which promotes strong ionic bonding. This structural compatibility makes BaS, along with BaO and BaSe, well suited for alloy formation. For instance, $BaO_{1-x}Se_x$ alloys have been shown to retain their structural and electronic characteristics across a range of compositions [29]. Additionally, BaS and BaSe exhibit a pressure-induced phase transition from the NaCl-type (B1) to the CsCl-type (B2) structure, which is relevant when considering their behavior under external constraints [30].

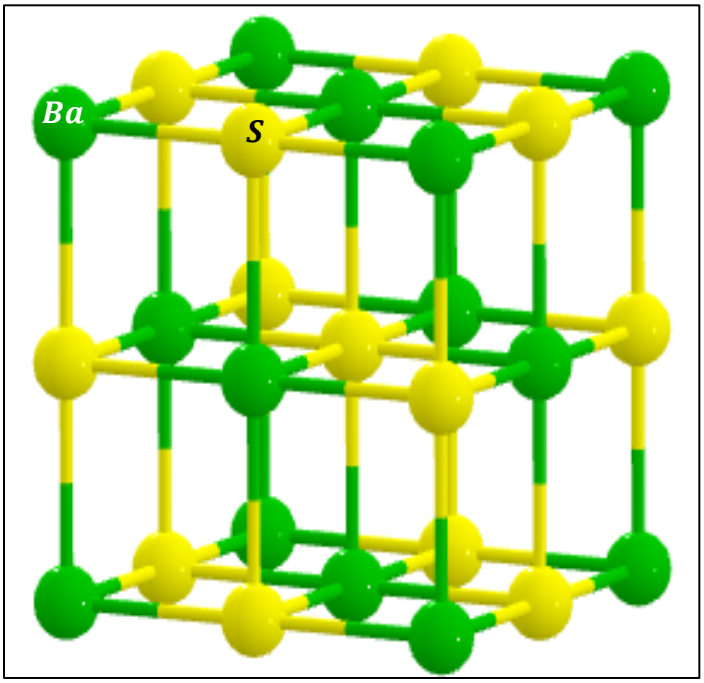


Figure I.11. The NaCl Structure of BaS [28]

Table I.2 summarizes the key crystal structure properties of the binaries selected in this work. The $BaO_{1-x}S_x$ alloys system is explored in this study due to its structural compatibility and chemical similarity between BaO and BaS, both of which crystallize in the rocksalt structure. Despite this, no dedicated experimental or theoretical work has been found on $BaO_{1-x}S_x$ in existing literature, making it a relatively unexplored system. Its investigation offers a promising opportunity to understand and tailor the structural and dielectric properties of IIa–VI oxide-sulfide alloys within the II–VI semiconductor family.

Table I.2: Structural Properties of Selected Binary Semiconductors and Electronic Configuration for their cations and anions

Compound	Group	Crystal Structure	Electronic Configuration (cation/anion)
AlSb	III–V	Zinc Blende (ZB)	Al: [Ne] $3s^2$ $3p^1$ / Sb: [Kr] $4d^{10}$ $5s^2$ $5p^3$
AlAs	III–V	Zinc Blende (ZB)	Al: [Ne] $3s^2$ $3p^1$ / As: [Ar] $3d^{10}$ $4s^2$ $4p^3$
AlBi	III–V	Zinc Blende (ZB)	Al: [Ne] $3s^2$ $3p^1$ / Bi: [Xe] $4f^{14}$ $5d^{10}$ $6s^2$ $6p^3$
BaO	II–VI	Rocksalt (NaCl)	Ba^{2+}: [Xe] / O^{2-}: [He] $2s^2$ $2p^6$
BaS	II–VI	Rocksalt (NaCl)	Ba^{2+}: [Xe] / S^{2-}: [Ne] $3s^2$ $3p^6$
BaSe	II–VI	Rocksalt (NaCl)	Ba^{2+}: [Xe] / Se^{2-}: [Ar] $3d^{10}$ $4s^2$ $4p^6$

I.3. Alloying & Vegard's Law in Ternary Semiconductor Alloys

A ternary semiconductor alloy $A_{1-x}B_xC/AB_{1-x}C_x$ (e.g., $In_xGa_{1-x}As$, $AlSb_{1-x}As_x$) forms when two isostructural binaries share the same sublattice and mix substitutionally. At fixed T and P, the alloy usually adopts the structure of the end members (e.g., zinc blende or wurtzite). Key problems are how lattice parameter (or volume), electronic band gap, and thermodynamic stability vary with composition x, and what governs linear vs. nonlinear trends [31–33] .

I.3.1. Vegard's Law for Lattice Parameter

For many semiconductor alloys, a small but systematic deviation from linearity is observed. A practical refinement is a quadratic "lattice bowing" correction [27,31–34] :$a(x) = (1-x)a_A + xa_B - \delta x(1-x)$. Linearity is favored when atomic size and bonding character are similar and local relaxations remain small. Deviations arise from size mismatch, charge transfer, and short-range order/clustering. First-principles supercell studies (SQS) reveal positive or negative bowing depending on the cation/anion combination and local relaxation patterns.

I.3.2. Electronic-Structure Bowing

Band gaps in alloys often show pronounced nonlinearity independent of lattice bowing. A standard interpolation is [27,31–34]: $E_g(x) = (1-x)E_g(A) + xE_g(B) - bx(1-x)$. Large b arises from chemical/electronic mismatch, band-edge anticrossings (e.g., dilute nitrides/bismides), and

disorder. Notably, b need not track δ. Comprehensive parameter sets (III–V, nitride-containing, and IV–IV GeSn) quantify strong bowing even when a(x) is nearly Vegard-like.

I.4. First Brillouin zone and irreducible Brillouin zone

Another prominent cell in crystal lattices is the Wigner-Seitz cell. It is centered at a lattice point and can be described as the collection of all points whose distance to this lattice point is less than to any other lattice point. The Wigner-Seitz cell can be geometrically created as the following:
Draw connecting lines from the specified lattice point to other lattice points (beyond only the nearest neighbors) and construct the perpendicular bisector planes to these lines. The smallest volume contained by the several planes constitutes the Wigner-Seitz cell. Only the simple cubic lattice yields a Wigner-Seitz cell in the form of a cube; in other cases, more complex geometries arise. The first Brillouin zone is simply the reciprocal lattice's Wigner-Seitz cell [18].

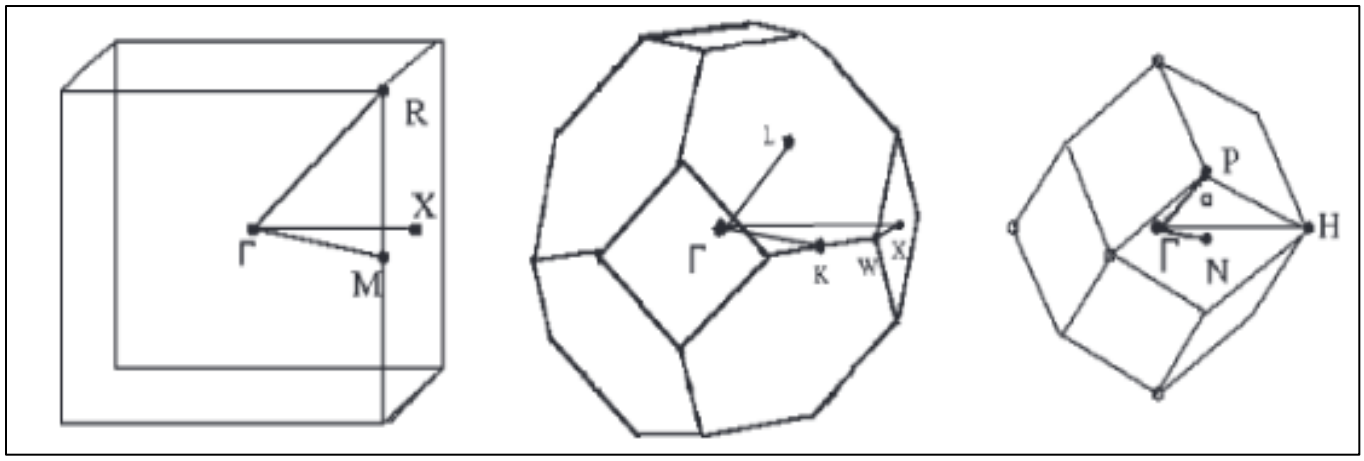


Figure I.12. Illustration of the first Brillouin zones for simple cubic, face-centered cubic (fcc), and body-centered cubic (bcc) lattices, highlighting key high-symmetry points commonly used in band structure plots [1].

The irreducible Brillouin zone (IBZ) represents the smallest portion of the first Brillouin zone (FBZ) that remains after applying all relevant symmetry operations of the crystal, such as rotational, mirror, and time-reversal symmetries. It is commonly used in electronic structure calculations, including band structure and density of states, to reduce computational effort while preserving accuracy [7].

I.4.1. High symmetry points

Figure I.13 shows the First Brillouin zone of ZB structure illustrating its High-symmetry points. High-symmetry points are important in the first Brillouin zone (BZ). Band dispersion is often traced along standard paths using these unique k-points, which correlate to locations of high crystallographic symmetry in reciprocal space. The most crucial high-symmetry points for cubic structures, such as those of Zinc Blende and NaCl, are Γ, X, L, W, and Z. Each of these points represents a distinct location within the Brillouin zone. These points and their coordinates are briefly described below [1]:

Γ (Gamma): This point represents the center of the first Brillouin zone, with coordinates **k_Γ = (0, 0, 0)**.

X: This point is situated in the middle of one of the octahedron's square faces. One of the reciprocal space axes (k_x, ky, or kz) is in line with it. X's coordinates are:

$k_x = (\pm 1, 0, 0) \times (2\pi / a)$

$k_y = (0, \pm 1, 0) \times (2\pi / a)$

$k_z = (0, 0, \pm 1) \times (2\pi / a)$

L: This point is equivalent to the middle of one of the octahedron's hexagonal faces. Here are its coordinates:

$k_L = (1, 1, 1) \times (2\pi / a)$

W: This point is located at a corner of the square faces. Its coordinates are:

$k_W = (0, ½, 1) \times (2\pi / a)$

Z: This point lies on the line connecting the center of a square face to one of the corners of the octahedron. Its coordinates are: $k_Z = (1, ½, 1) \times (2\pi / a)$

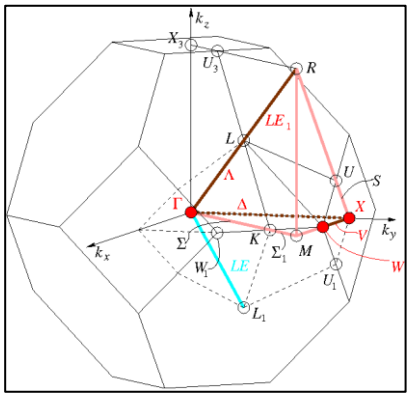


Figure I.13. First Brillouin zone of ZB structure (F-43m) [35]

I.4.2. High symmetry lines

In computing the electronic band structure of crystalline solids, not only the high-symmetry points of the Brillouin zone are important, but also the lines connecting them. These lines describe the evolution of electronic bands in reciprocal space and are chosen according to the symmetry of the crystal. In cubic systems such as the zinc blende or rocksalt (NaCl) structures, a standard set of directions is typically followed, each corresponding to a high-symmetry path in reciprocal space:

Δ (Delta): This direction takes the ⟨100⟩ crystallographic direction. It runs from the center of the Brillouin zone Γ to the X point, which is at the center of a square face.

Σ (Sigma): Lying in one of the mirror symmetry planes of the crystal (such as $k_x = k_y$, $k_y = k_z$, or $k_x = k_z$), this direction connects Γ to K or equivalent points, depending on the symmetry of the material.

Λ (Lambda): Along the ⟨111⟩ direction, this line links Γ to the L point, which is in the middle of a hexagonal face of the Brillouin zone.

I.4.3. Band structure formation

The formation of energy bands in semiconductors stems from the interaction of atomic orbitals in a periodic crystalline environment. When atoms are isolated, their electrons occupy discrete orbitals (s, p, etc.). However, as atoms are brought together in a crystal, these orbitals overlap, forming

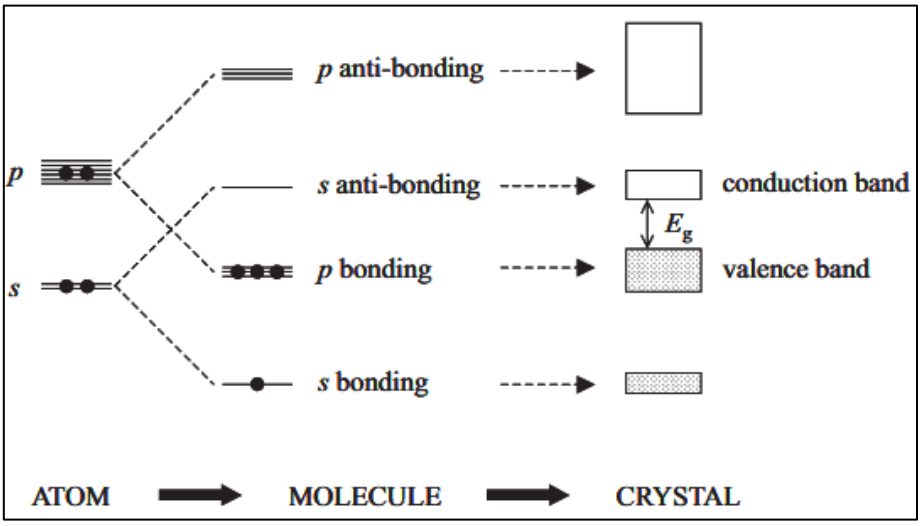


Figure I.14. Schematic showing the evolution from atomic orbitals to energy bands in solids [36].

bonding and antibonding states. In solids, the interaction among many atoms broadens these discrete levels into continuous energy bands, with forbidden regions known as bandgaps [36].

A textbook example is gallium arsenide (GaAs) (Figure I.15), a III–V semiconductor with the zinc-blende crystal structure. Its electronic band structure features a direct bandgap at the Γ point (center

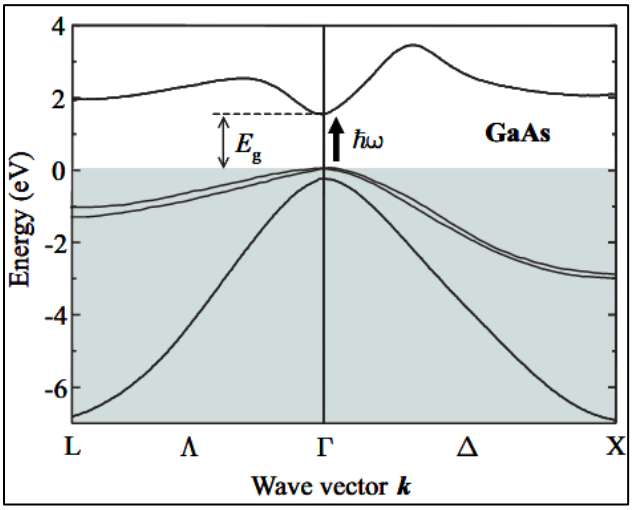


Figure I.15. Band structure of gallium arsenide (GaAs)

of the Brillouin zone) as shown in figure I.13, where both the conduction band minimum and valence band maximum are located. The conduction band in GaAs primarily originates from Ga 4s orbitals, whereas the valence band is mainly derived from As 4p orbitals. To contrast this typical III–V behavior, we consider BaSe, a II–VI compound crystallizing in the rocksalt (NaCl-type) structure. Despite its different chemical nature, BaSe also exhibits a direct band gap at the Γ point, as confirmed by first-principles calculations performed using the GGA-PBEsol and TB-mBJ functionals within the WIEN2k framework [29].

I.5.Theoretical background of optical properties

The intrinsic energy gaps of most semiconductors range from zero to approximately 6 eV. High-energy photons can elevate electrons from the occupied valence bands to the unoccupied conduction bands. The optical spectra of semiconductors yield extensive insights into their electronic characteristics. In numerous semiconductors, photons can interact with lattice vibrations and electrons localized at defects, rendering optical computations valuable for investigating these

excitations. Their optical characteristics underpin numerous significant applications of semiconductors, including lasers, light-emitting diodes, and photodetectors [37].

I.5.1. Dielectric function ε(ω)

The dielectric function ε(ω) is a complex quantity that describes the linear response of a material to an oscillating electric field. As defined by Yu and Cardona, the real part $\varepsilon_1(\omega)$ represents the dispersive properties of the material, while the imaginary part $\varepsilon_2(\omega)$ is directly related to optical absorption via interband transitions [5]. Similarly, Dressel and Grüner describe ε(ω) as encoding the polarization and energy dissipation response of the electron system to an external field [38]. Wooten further clarifies that ε(ω) characterizes how an electric field induces a displacement field, with ε_2 indicating absorption and ε_1 responsible for refractive effects [39].The dielectric function ε(ω) is a complex quantity defined as [5]:

$$\varepsilon(\omega) = \varepsilon_1(\omega) + i\varepsilon_2(\omega) \qquad (\mathbf{I.9})$$

Where $\varepsilon_1(\omega)$ refers to the real part of dielectric functions and $\varepsilon_2(\omega)$ is its imaginary part. Which are expressed by the following:

$$\varepsilon_1(\omega) = 1 + \frac{2}{\pi} P \int_0^{\infty} \frac{\omega' \varepsilon_2(\omega')}{(\omega'^2 - \omega^2)} d\omega' \qquad (\mathbf{I.10})$$

$$\varepsilon_2(\omega) = -\frac{2\omega}{\pi} P \int_0^{\infty} \frac{\varepsilon_2(\omega') - 1}{(\omega'^2 - \omega^2)} d\omega' \qquad (\mathbf{I.11})$$

Where P denotes the principal value of the integral.

I.5.2. Optical constants derived from ε(ω)

Equations (I.10) and (I.11) enable the evaluation of several key optical parameters, such as the refractive index n(ω) ,extinction coefficient K(ω), absorption coefficient α(ω) and the optical conductivity σ(ω), over the relevant spectral domain:

a) **Complex refractive index N(ω):** defined as $N = n(\omega) + ik(\omega)$ where $n(\omega)$ is the real refractive index which determines the phase velocity of light in the material compared to in a vacuum, $k(\omega)$ is the extinction coefficient, representing the exponential attenuation n both n and k are give by the expression below [40]:

$$n(\omega) = \frac{1}{\sqrt{2}}\left[\varepsilon_1(\omega) + \sqrt{\varepsilon_1^2(\omega) + \varepsilon_2^2(\omega)}\right]^{\frac{1}{2}} \quad (\mathbf{I.12})$$

$$k(\omega) = \frac{1}{\sqrt{2}}\left[\sqrt{\varepsilon_1^2(\omega) + \varepsilon_2^2(\omega)} - \varepsilon_1(\omega)\right]^{\frac{1}{2}} \quad (\mathbf{I.13})$$

b) Absorption Coefficient α(ω) : The absorption coefficient measures how deeply light can penetrate a material before being absorbed. It's directly related to the extinction coefficient and given by [39]:

$$\alpha(\omega) = \frac{4\pi k(\omega)}{\lambda} \quad (\mathbf{I.14})$$

With ω is the angular frequency, λ: the vacuum's wavelength of light.

c) Optical Conductivity σ(ω): Optical conductivity describes how much current a material can conduct in response to an oscillating electric field (light). It's connected to the imaginary part of the dielectric function:

$$\sigma(w) = \frac{-i\omega}{4\pi}\varepsilon(\omega) \quad (\mathbf{I.15})$$

This property is especially important when studying metals, semiconductors, and plasmonic materials [38].

d) Energy Loss Function (ELF): The energy loss function tells us how much energy a fast electron loses as it passes through a material. It's defined as:

$$\mathrm{ELF}(\omega) = \frac{\varepsilon_2}{\varepsilon_1^2 + \varepsilon_2^2} \quad (\mathbf{I.16})$$

Peaks in the ELF correspond to collective electron excitations known as plasmons, and this function is widely used in electron energy loss spectroscopy (EELS) [1].

Understanding optical constants, including the refractive index, extinction coefficient, absorption coefficient, dielectric function, optical conductivity, and energy loss function, is essential for characterizing material interactions with light. Each parameter delineates a distinct aspect of this response specifically, the mechanisms by which light is attenuated or absorbed, or how it stimulates

electronic behavior within the material. These constants collectively provide a comprehensive understanding of a material's optical properties, essential for the design and analysis of optical devices, semiconductors, and photonic materials.

I.5.3. Interband and Intraband Transitions

Optical transitions in solids are governed by the interaction between photons and electrons, leading to changes in electronic states. These transitions are broadly categorized into interband and intraband processes, each with distinct physical mechanisms and implications for material properties.Figure I.16 illustrates this concept: the photon energy ($h\omega$) promotes an electron from its initial state (E_i) below the Fermi level (E_f) to a higher energy state in the conduction band, bridging the band gap (E_g) between the two electronic bands.

I.5.3.1. Interband Transitions

Interband transitions involve the excitation of electrons from one energy band to another, typically from the **valence band to the conduction band** in semiconductors and insulators. These transitions are central to the optical absorption edge and are responsible for the onset of strong absorption in materials with a band gap [36]:

- **Mechanism**: A photon with energy equal to or greater than the band gap excites an electron across the gap, leaving behind a hole.
- **Selection Rules**: Governed by momentum and symmetry considerations; direct transitions occur without phonon assistance, while indirect transitions require phonon interaction.
- **Spectral Features**: Sharp absorption onset at the band edge, often accompanied by excitonic peaks in high-purity crystals.
- **Applications**: Fundamental to the operation of optoelectronic devices such as solar cells, photodetectors, and light-emitting diodes.

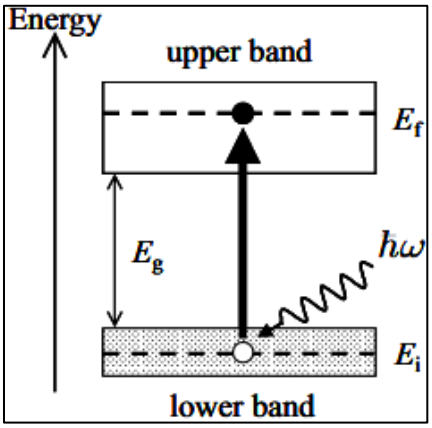


Figure I.16. Schematic of an Interband Transition [36].

I.5.1.2. Intraband Transitions

Intraband transitions occur within the same energy band, typically in the conduction band of metals or heavily doped semiconductors. These transitions are associated with free-carrier absorption and are described by the Drude model [36]: (Table I.3 below shows Comparative Analysis of Interband vs Intraband Transitions.)

- **Mechanism**: Electrons absorb low-energy photons and transition to higher energy states within the same band.
- **Spectral Features**: Broad absorption in the infrared and microwave regions, with a characteristic frequency-dependent conductivity.
- **Scattering Effects**: Strongly influenced by electron-phonon and electron-defect scattering, which determine the relaxation time and mobility.
- **Applications**: Relevant in plasmonics, terahertz technologies, and infrared sensing.

Table I.3 Comparative Analysis of Interband vs Intraband Transitions

Aspect	Interband Transition	Intraband Transition
Electron Movement	Between different energy bands	the same energy band
Photon Energy	High (equal to or greater than band gap)	Low (IR/ microwave range)
Spectral Behavior	Sharp absorption onset	Broad, smooth absorption
Typical Materials	Semiconductors, insulators	Metals/doped semiconductors

Interband transitions directly influence the optical band gap and are critical for understanding the electronic structure of materials. Intraband transitions, on the other hand, provide insight into

carrier dynamics, mobility, and conductivity. Together, these processes define the full optical response of a material across the electromagnetic spectrum.

I.6. Elastic Properties of Crystalline Semiconductors

Investigating elastic constants and moduli is essential for predicting a material's mechanical stability, stiffness, and performance in various applications. These parameters describe a material's response to external forces and provide an average measure of its resistance to deformation. This section introduces the fundamental theoretical background of elasticity in crystalline solids.

I.6.1. Elastic Constants C_{ij}

Elastic constants C_{ij} represent the components of the second-order elastic stiffness tensor that links stress σ and strain ε through the generalized Hooke's law [1]:

$$\sigma_i = \Sigma_j C_{ij} \varepsilon_j \qquad (\mathbf{I.17})$$

The number of independent elastic constants depends on the symmetry of the crystal system as shown in table I.4 :

Table I.4. Independent elastic constants depending on crystal system.

Crystal System	Number of Independent C_{ij} Constants
Cubic	3
Hexagonal	5
Tetragonal	6 or 7 (depending on class)
Orthorhombic	9
Monoclinic	13
Triclinic	21

Mechanical stability of a crystal requires the elastic constants to satisfy certain inequalities known as the Born stability criteria, which are specific to the crystal symmetry. For example, the criteria for cubic crystals are:

$C_{11} - C_{12} > 0, \quad C_{11} + 2C_{12} > 0, \quad C_{44} > 0$ **(I.18)**

Violation of these conditions suggests mechanical instability under small deformations [41,42].

I.6.2. The mechanical moduli

The mechanical moduli are scalar quantities derived from the elastic constants, providing useful insights into a material's bulk behavior. These moduli along there description are tabulated in table I.5 below:

Table I.5. Elastic moduli and their description

Modulus	Symbol	Description
Bulk Modulus	B	Resistance to uniform volume compression
Shear Modulus	G	Resistance to shear deformation
Young's Modulus	Y	Ratio of tensile stress to tensile strain
Poisson's Ratio	ν	Ratio of lateral to axial strain
Anisotropy Index	A	Indicator of elastic anisotropy in cubic crystals
Hardness	H_v	measures a material's resistance to permanent deformation

For polycrystalline aggregates, moduli are typically calculated using Voigt (uniform strain), Reuss (uniform stress), and Hill (arithmetic average) approximations [43] . These provide upper and lower bounds and their average:

$$G_v = \frac{1}{5}(C_{11} - C_{12} + 3C_{44}) \quad \textbf{(I.19)}$$

$$G_R = \frac{5(C_{11} - C_{12})C_{44}}{4C_{44} + 3(C_{12} - C_{12})} \quad \textbf{(I.20)}$$

$$B = B_v = B_R = \frac{1}{3}(C_{11} + 2C_{12}) \quad \textbf{(I.21)}$$

The bulk (B), the shear (G) , Young's (Y) , Poisson's ratio , Pugh ratio Hardness and Anisotropy Index are given -respectively- by the following expressions:

$$G = \frac{1}{2}(G_v + G_R) \quad \textbf{(I.22)}$$

$$G_v = \frac{1}{5}(C_{11} - C_{12} + 3C_{44}) \quad \textbf{(I.23)}$$

$$G_R = \frac{5(C_{11} - C_{12})C_{44}}{4C_{44} + 3(C_{12} - C_{12})} \quad \textbf{(I.24)}$$

$$E = \frac{9BG}{3B + G} \quad \textbf{(1.25)}$$

$$\nu = \frac{3B - 2G}{2(3B + G)} \quad \textbf{(1.26)}$$

$$Pugh\ ratio = B/G \quad \textbf{(I.27)}$$

$$H_v = 0.92\left(\frac{G}{B}\right)^{1.137} \times G^{0.708} \quad (\mathbf{I.28})$$

$$A = \frac{2C_{44}}{C_{11} - C_{12}} \quad (\mathbf{I.29})$$

I.6.3.Ductility and Elastic Anisotropy

Several theoretical criteria can be used to evaluate the mechanical response of a material under stress, including its tendency to behave in a ductile or brittle manner and the degree to which this behavior is directionally dependent.

a) Ductility

Ductility describes a material's ability to deform plastically before fracturing. It can be assessed using Pugh's ratio, Cauchy pressure, and Poisson's ratio. These criteria are summarized in the table I.6 below:

Table I.6. Ductility criteria and their interpretation.

Criterion	Condition	Interpretation	Reference
Pugh's Ratio	B/G > 1.75	Ductile	Pugh (1954) [44]
	B/G < 1.75	Brittle	
Cauchy Pressure	Cp = $C_{12} - C_{44} > 0$	Ductile (metallic bonding)	Pettifor (1992) [45]
	Cp = $C_{12} - C_{44} < 0$	Brittle (covalent bonding)	
Poisson's Ratio (ν)	ν > 0.26	Ductile	Frantsevich et al.[46]
	ν < 0.26	Brittle	

b) Elastic Anisotropy

Elastic anisotropy describes the directional variation of elastic behavior. For cubic systems, it is typically evaluated using the Zener factor (A), while Voigt-Reuss-based anisotropic indices, such as A_G and A_B, provide deeper insight. These values are presented in Table I.7.

Table I.7. Elastic anisotropy indicators and interpretation

Indicator	Formula	Interpretation	Reference
Zener Factor A	$A = \frac{2C_{44}}{C_{11} - C_{12}}$	A = 1: Isotropic; A ≠ 1: Anisotropic	Zener (1948) [47]
Shear Anisotropy A_G	$A_G = \frac{G_v - G_R}{G_v + G_R}$	$A_G = 0$: G is Isotropic; $A_G > 0\%$: G is anisotropic	
Bulk Anisotropy A_B	$A_B = \frac{B_v - B_R}{B_v + B_R}$	$A_B = 0$: B is Isotropic; $A_B > 0\%$: B is anisotropic	

Universal Index (A^U)	$A^U = 5\frac{G_V}{G_R} + \frac{B_v}{B_R} - 6$	$A^U = 0$: Isotropic $A^U > 0$: Anisotropic	Ranganathan & Ostoja-Starzewski (2008) [48]

I.7. Thermal Properties in the Quasi-Harmonic Approximation (QHA)

This section provides a comprehensive, equation-oriented review of the quasi-harmonic approximation (QHA) for crystalline solids.

Beginning from a variational statement of the Gibbs free energy, we derive the equilibrium volume as a function of temperature and pressure. From this, we obtain consistent expressions for the constant-volume and constant-pressure heat capacities (Cv and Cp), the Debye temperature, entropy, and the volumetric thermal expansion coefficient. We first outline the full phonon formalism with mode-resolved contributions, then specialize to the Debye-QHA model commonly implemented in GIBBS, GIBBS2, and related workflows. Throughout the discussion, we emphasize practical identities particularly those linking the average Grüneisen parameter to α, Cv, Cp and elastic moduli and provide guidance for reporting results along with recommended sanity checks[7,49–58].

I.7.1. Physical context and scope

The quasi-harmonic approximation extends harmonic lattice dynamics by allowing phonon frequencies to depend on crystal volume V while maintaining harmonic statistics at each fixed volume. Temperature enters only through Bose–Einstein occupations; explicit anharmonic phonon–phonon interactions are omitted except through their volume dependence.

QHA is reliable up to a sizable fraction of the melting temperature for many close-packed or moderately anisotropic crystals and under pressures where the structure remains mechanically stable. Breakdown occurs near structural instabilities, at very high temperatures where phonon lifetimes shorten dramatically, or in frameworks with strong anharmonic soft modes. Within its domain of validity, QHA supplies internally consistent thermoelastic properties over wide (T,p) ranges with modest computational cost [7,49–51].

I.7.2. Full-phonon QHA: thermodynamic potentials and basic responses

At fixed (T,V), the vibrational Helmholtz free energy, internal energy, entropy, and constant-volume heat capacity can be written in mode-resolved form. Let $\omega_{qs}(V)$ be the phonon frequencies (branch s at wavevector q) and $x_{qs} \equiv \hbar \cdot \omega_{qs}(V)/(k_B \cdot T)$.

$$F_{vib}(T,V) = k_B \cdot T \cdot \Sigma_{q,s} ln\left[2 \cdot sinh\left(\hbar \cdot \omega_{qs}(V)/(2 \cdot k_B \cdot T)\right)\right] \quad (\mathbf{I.30})$$

$$U_{vib}(T,V) = \Sigma_{q,s}\left[(1/2) \cdot \hbar \cdot \omega_{qs}(V) + \hbar \cdot \omega_{qs}(V)/\left(e^{\hbar \cdot \omega_{qs}(V)/(k_B \cdot T)} - 1\right)\right] \quad (\mathbf{I.31})$$

$$C_V(T,V) = k_B \cdot \Sigma_{q,s}\left[{x_{qs}}^2 \cdot e^{x_{qs}}/(e^{x_{qs}} - 1)^2\right], x_{qs} = \hbar \cdot \omega_{qs}(V)/(k_B \cdot T) \quad (\mathbf{I.32})$$

The total Helmholtz free energy is $F(T,V) = E_{static}(V) + F_{vib}(T,V)$, where $E_{static}(V)$ is the 0-K electronic (Born–Oppenheimer) energy. At imposed pressure P, equilibrium follows from minimizing the non-equilibrium Gibbs function with respect to V:

$$G^*(V,P,T) = E(V) + P \cdot V + F_{vib}(V;T) \quad (\mathbf{I.33})$$

The minimum over V at fixed (P,T) defines the equilibrium volume V*(T,P) and thereby all derived properties [1–4,18].

Stationarity of G* implies an equation of state that separates static and thermal contributions to pressure. Differentiating with respect to V gives $P = P_{static}(V) + P_{th}(T,V)$, with $P_{static}(V) = -dE/dV$ and $P_{th}(T,V) = -(\partial F_{vib}/\partial V)_T$. Differentiating the stationarity condition with respect to T at fixed P yields an exact QHA identity connecting the thermal pressure derivative to the expansion coefficient. Defining the isothermal bulk modulus $B_T \equiv -V(\partial P/\partial V)_T$ and $\alpha \equiv (1/V)(\partial V/\partial T)_P$ leads to the standard relations below.

$$(\partial G^*/\partial V)_{P,T} = 0 \Rightarrow P = P_{static}(V) + P_{th}(T,V) \quad (\mathbf{I.34})$$

$$P_{th}(T,V) = (1/V) \cdot \Sigma_{q,s}\gamma_{qS}(V) \cdot \left[U_{qS}(T,V) - (1/2) \cdot \hbar \cdot \omega_{qs}(V)\right] \quad (\mathbf{I.35})$$

$$P_{th}(T,V) \approx \gamma(T,V) \cdot U_{vib'}(T,V)/V, U_{vib'} = U_{vib} - (1/2) \cdot \Sigma_{q,s}\hbar \cdot \omega_{qS} \quad (\mathbf{I.36})$$

Equations (**I. 34**)–(**I. 36**) introduce the mode Grüneisen parameters $\gamma_{qs}(V) \equiv -\partial ln\omega_{qs}(V)/\partial lnV$ and their heat-capacity-weighted average γ(T,V). They provide a compact Mie–Grüneisen form for the thermal pressure and underpin the α–Cv–Cp identities that follow [49–51,54–56].

I.7.3. Fundamental QHA identities

Evaluated at the equilibrium volume V*(T,P), the key identities used in practice are:[49–51,54–56]

$$\alpha(T,P) = \gamma(T,P) \cdot C_V(T,P)/[B_T(T,P) \cdot V^*(T,P)] \quad (\mathbf{I.37})$$

$$C_P - C_V = \alpha^2 \cdot B_T \cdot V^* \cdot T \quad (\mathbf{I.38})$$

$$B_S/B_T = C_P/C_V \quad (\mathbf{I.39})$$

Equation (**I. 37**) shows that expansion grows with heat capacity and anharmonicity (γ) but is suppressed by stiffness and volume. Equation (**I. 38**) expresses the C_p–C_v difference as the product of thermoelastic couplings, and Eq. (**I. 39**) links the adiabatic/isothermal modulus ratio to the heat-capacity ratio. Together, these relations provide stringent internal consistency checks for any QHA dataset.

I.7.4. Debye-QHA specialization

Replacing the full phonon spectrum by a Debye model yields compact expressions driven by the Debye function $D_3(y)$ with $y = \theta_D/T$. The Debye vibrational free energy (per cell with n atoms) reads [59]:

$$F_{Vib}(T,V) = n \cdot k_B \cdot T\left[(9 \cdot \theta_D)/(8 \cdot T) + 3 \cdot ln\left(1 - e^{-\theta_D/T}\right) - 3 \cdot D_3(\theta_D/T)\right] \quad (\mathbf{I.40})$$

A widely used elastic proxy for the volume dependence of θ_D is the Anderson-type relation:

$$\theta_D(V) = (\hbar/k_B) \cdot (6\pi^2 n/V)^{(1/3)} \cdot f(\sigma) \cdot \sqrt{(B_S/\rho)} \quad (\mathbf{I.41})$$

Here f(σ) is a weak function of Poisson's ratio σ, ρ is the density, and B_S is the adiabatic bulk modulus (close to the static curvature for many solids). A convenient curvature estimate used in static calculations is:

$$B(V) \approx V \cdot d^2E(V)/dV^2 \quad (\mathbf{I.42})$$

And $f(\sigma)$ function is extracted from reference [59] where σ is Poisson's ratio, the Entropy (S) and thermal expansion coefficient α we use the following expressions [59]:

$$C_V = 3nk\left[4D\left(\frac{\boldsymbol{\theta_D}}{T}\right) - \frac{3\theta_D/T}{e^{\theta_D/T}-1}\right] \quad (\mathbf{I.43})$$

$$S = nk\left[4D\left(\frac{\theta_D}{T}\right) - 3\,ln\left(1 - e^{-\theta_D/T}\right)\right] \quad (\mathbf{I.44})$$

$$B(P,V) = V\left(\frac{d^2G^*(P,V)}{dV^2}\right) \quad (\mathbf{I.45})$$

$$\alpha = \frac{\gamma C_V}{B_T V} \quad (\mathbf{I.46})$$

With γ representing the Grüneisen parameter:

$$\gamma = -\frac{d\,ln\,\theta(V)}{d\,ln\,V} \quad (\mathbf{I.47})$$

Note: Low- and high-temperature limits (sanity checks)

• As T → 0, $Cv \propto T^3$ and $S \propto T^3$ for non-metallic crystals; α(T) typically vanishes as T^3 due to the acoustic-mode density of states. • As T → ∞ (well below melting), $C_v \to 3n \cdot k_B$ (Dulong–Petit) while α(T) often saturates ; significant deviations in computed curves usually indicate an inconsistent $\theta_D(V)$ mapping, an overly narrow E(V) fit region, or numerical differentiation noise [50,51,60]

I.7.5. Limitations and extensions

QHA neglects explicit temperature-driven phonon renormalization beyond volume effects. In materials with strong anharmonicity, soft modes, or near phase transitions, full phonon calculations at multiple volumes (and, if needed, temperature-dependent effective potentials) are preferable. Anisotropic QHA generalizations treat linear expansion along crystallographic axes and couple to the full elastic tensor; negative thermal expansion and layered crystals often require this tensorial treatment. Under very high pressures, ensure mechanical stability (positive elastic eigenvalues) for all volumes used [50,51,53] .

References of Chapter I

[1] C. Kittel, Introduction to solid state physics, 8. ed., [repr.], Wiley, Hoboken, NJ, 20.
[2] S. Adachi, Properties of semiconductor alloys: group-IV, III-V and II-VI semiconductors, 1. ed, Wiley, Chichester, 2009.
[3] S.M. Sze, K.K. Ng, LEDs and lasers, Physics of Semiconductor Devices 3 (2006) 601–657.
[4] O. Madelung, Semiconductors: Data Handbook, Springer, Berlin, Heidelberg, 2004. https://doi.org/10.1007/978-3-642-18865-7.
[5] P. YU, M. Cardona, Fundamentals of Semiconductors: Physics and Materials Properties, Springer Science & Business Media, 2010.
[6] T. Hahn, International Tables for Crystallography: Brief Teaching Edition of Volume A. Vol. 1. Springer, 1996.
[7] N.W. Ashcroft, N.D. Mermin, Solid state physics Brooks, Cole, Cengage Learning 10 (1976).
[8] J. Singh, Semiconductor devices: basic principles, John Wiley & Sons, 2007.
[9] Neamen, Donald A., and Dhrubes Biswas. Semiconductor physics and devices. New York: McGraw-Hill higher education, 2011.
[10] Pankove, Jacques I. Optical processes in semiconductors. Courier Corporation, 2012.
[11] S. Adachi, Optical properties of crystalline and amorphous semiconductors: Materials and fundamental principles. Springer Science & Business Media, 2012.
[12] P. Bhattacharya, Semiconductor optoelectronic devices. Prentice-Hall, Inc., 1997.
[13] C. Bradley, A. Cracknell, The mathematical theory of symmetry in solids: representation theory for point groups and space groups, Oxford University Press, 2009.
[14] W. Setyawan, S. Curtarolo, High-throughput electronic band structure calculations: Challenges and tools, Computational Materials Science 49 (2010) 299–312.
[15] C. Hammond, The basics of crystallography and diffraction. Vol. 21. Oxford university press, 2015.
[16] P. Paufler, International tables for crystallography. Vol. A. Edited by Th. Hahn. Pp. xx+ 911. Dordrecht: Kluwer Academic Publishers, 2002. Price EUR 242, GBP 142, USD 225. ISBN 0-7923-6590-9., Foundations of Crystallography 60 (2004) 641–642.
[17] N.W. Gregory, Elements of X-Ray Diffraction., J. Am. Chem. Soc. 79 (1957) 1773–1774. https://doi.org/10.1021/ja01564a077.
[18] G. Czycholl, Solid State Theory, Volume 1: Basics: Phonons and Electrons in Crystals, Springer Berlin Heidelberg, Berlin, Heidelberg, 2023. https://doi.org/10.1007/978-3-662-66135-2.
[19] YJU'S (n.d.), Zinc blende structure, BYJU'S. Available at: https://byjus.com/chemistry/zinc-blende-structure/ (accessed July 5, 2025).
[20] R. Kumar, B.K. Sharma, G. Sharma, Electronic Structure and Momentum Density of BaO and BaS, Advances in Condensed Matter Physics 2013 (2013) 415726. https://doi.org/10.1155/2013/415726.
[21] X. Zhou, J.L. Roehl, C. Lind, S.V. Khare, Study of B1 (NaCl-type) to B2 (CsCl-type) pressure-induced structural phase transition in BaS, BaSe and BaTe using ab initio computations, J Phys Condens Matter 25 (2013) 075401. https://doi.org/10.1088/0953-8984/25/7/075401.

[22] La structure NaCl . Available at: https://ressources.univ-lemans.fr/AccesLibre/UM/Pedago/chimie/01/06-Etat_solide/deug/nacl.html (accessed July 9, 2025).
[23] Hofmann, Philip. Solid state physics: an introduction. John Wiley & Sons, 2022.
[24] M.E. Wieser, T.B. Coplen, Atomic weights of the elements 2009 (IUPAC Technical Report), Pure and Applied Chemistry 83 (2010) 359–396. https://doi.org/10.1351/pac-rep-10-09-14.
[25] L. Sun, L. Shi, C. Wang, L. Sun, L. Shi, C. Wang, Investigations of Phonons in Zinc Blende and Wurtzite by Raman Spectroscopy, in: Applications of Molecular Spectroscopy to Current Research in the Chemical and Biological Sciences, IntechOpen, 2016. https://doi.org/10.5772/64194.
[26] B. Amrani, H. Achour, S. Louhibi, A. Tebboune, N. Sekkal, First principles study of AlBi, Solid State Communications 148 (2008) 59–62. https://doi.org/10.1016/j.ssc.2008.07.016.
[27] I. Vurgaftman, J. Meyer, L.R. Ram-Mohan, Band parameters for III–V compound semiconductors and their alloys, Journal of Applied Physics 89 (2001) 5815–5875.
[28] Materials Project, Materials Project (n.d.). https://next-gen.materialsproject.org/materials/mp-2624?chemsys=Al-Sb (accessed July 9, 2025).
[29] Khalfallah, B.; Driss Khodja, F. Z.; Marbouh, N.; Saidi, Y., Predictive study of structural, electronic and optical properties of the ternary alloys $BaO_{1-x}Se_x$ (x = 0.25, 0.50 and 0.75), Journal of Optoelectronics and Communication 3 (3) (2021).
[30] A.R. West, Solid state chemistry and its applications, John Wiley & Sons, 2022.
[31] L. Vegard, Die Konstitution der Mischkristalle und die Raumf□llung der Atome, Z. Physik 5 (1921) 17–26. https://doi.org/10.1007/BF01349680.
[32] A.R. Denton, N.W. Ashcroft, Vegard's law, Phys. Rev. A 43 (1991) 3161–3164. https://doi.org/10.1103/PhysRevA.43.3161.
[33] A. Zunger, S.-H. Wei, L.G. Ferreira, J.E. Bernard, Special quasirandom structures, Phys. Rev. Lett. 65 (1990) 353–356. https://doi.org/10.1103/PhysRevLett.65.353.
[34] M.N. Magomedov, On the deviation from the Vegard's law for the solid solutions, Solid State Communications 322 (2020) 114060.
[35] The k-vector Types of Space Groups, (n.d.). https://www.cryst.ehu.es/cgi-bin/cryst/programs/nph-kv-list?gnum=216&fig=f4q3mf&what=data (accessed July 10, 2025).
[36] M. Fox, Optical properties of solids, 2nd ed, Oxford University Press, Oxford ; New York, 2010.
[37] D.W. Snoke, Solid State Physics: Essential Concepts, 2nd ed., Cambridge University Press, 2020. https://doi.org/10.1017/9781108123815.
[38] M. Dressel, Electrodynamics of solids: optical properties of electrons in matter, Cambridge University Press, Cambridge, 2002.
[39] F. Wooten, Optical properties of solids. Academic Press, 1972.
[40] Tsymbal, E. Y. "Optical properties of solids." PHYS927 University of Nebraska-Lincoln (2008).
[41] F. Mouhat, F.-X. Coudert, Necessary and sufficient elastic stability conditions in various crystal systems, Phys. Rev. B 90 (2014) 224104. https://doi.org/10.1103/PhysRevB.90.224104.
[42] M. Born, K. Huang, Dynamical theory of crystal lattices, Oxford university press, 1996.

[43] R. Hill, The Elastic Behaviour of a Crystalline Aggregate, Proc. Phys. Soc. A 65 (1952) 349. https://doi.org/10.1088/0370-1298/65/5/307.
[44] S.F. Pugh, XCII. Relations between the elastic moduli and the plastic properties of polycrystalline pure metals, The London, Edinburgh, and Dublin Philosophical Magazine and Journal of Science 45 (1954) 823–843. https://doi.org/10.1080/14786440808520496.
[45] D.G. Pettifor, Theoretical predictions of structure and related properties of intermetallics, Materials Science and Technology 8 (1992) 345–349. https://doi.org/10.1179/mst.1992.8.4.345.
[46] F.F.V. I. N. Frantsevich S.A. Bakuta, Elastic Constants and Elastic Moduli of Metals and Insulators Handbook, Naukova Dumka, Kiev, 1983.
[47] Zener, Clarence M., and Sidney Siegel. "Elasticity and Anelasticity of Metals." The Journal of Physical Chemistry 53, no. 9 (1949): 1468-1468.
[48] S.I. Ranganathan, M. Ostoja-Starzewski, Universal Elastic Anisotropy Index, Phys. Rev. Lett. 101 (2008) 055504. https://doi.org/10.1103/PhysRevLett.101.055504.
[49] C.G. Sammis, Thermodynamics of crystals by DC Wallace, Foundations of Crystallography 29 (1973) 582–583.
[50] G. Grimvall, Thermophysical properties of materials, Elsevier, 1999.
[51] B. Fultz, Vibrational thermodynamics of materials, Progress in Materials Science 55 (2010) 247–352.
[52] H.B. Callen, Thermodynamics and an Introduction to Thermostatistics, John Wiley& Sons 2 (1993).
[53] A. Togo, I. Tanaka, First principles phonon calculations in materials science, Scripta Materialia 108 (2015) 1–5.
[54] Nabarro, F. R. N., Theory of Crystal Dislocations, Oxford University Press, Oxford, 1967.
[55] Ganguly, Jibamitra. Thermodynamics in earth and planetary sciences. Berlin: Springer, 2008.
[56] E. Grüneisen, Theorie des festen Zustandes einatomiger Elemente, Annalen Der Physik 344 (1912) 257–306. https://doi.org/10.1002/andp.19123441202.
[57] P. Debye, Zur Theorie der spezifischen Wärmen, Annalen Der Physik 344 (1912) 789–839. https://doi.org/10.1002/andp.19123441404.
[58] S. Baroni, S. De Gironcoli, A. Dal Corso, P. Giannozzi, Phonons and related crystal properties from density-functional perturbation theory, Rev. Mod. Phys. 73 (2001) 515–562. https://doi.org/10.1103/RevModPhys.73.515.
[59] A. Otero-de-la-Roza, D. Abbasi-Pérez, V. Luaña, Gibbs2: A new version of the quasiharmonic model code. II. Models for solid-state thermodynamics, features and implementation, Computer Physics Communications 182 (2011) 2232–2248. https://doi.org/10.1016/j.cpc.2011.05.009.
[60] M.A. Blanco, E. Francisco, V. Luaña, GIBBS: isothermal-isobaric thermodynamics of solids from energy curves using a quasi-harmonic Debye model, Computer Physics Communications 158 (2004) 57–72. https://doi.org/10.1016/j.comphy.2003.12.001.

Contents

I.1. Basic concepts in crystallography 8
I.1.1. Lattice and Basis 8
I.1.2. Unit Cells and Bravais Lattices (e.g: Cubic Family) 9
I.1.3. Crystallographic Directions and Planes (Miller Indices) 9
I.1.4. Reciprocal Lattice and First Brillouin Zone 10
I.1.5. Common Crystal Structures 12
I.1.5.1. Zinc Blende (ZB) Structure 12
I.1.5.2. Sodium chloride structure 13
I.1.5.3. Cesium Chloride (CsCl) structure 14
I.1.5.4. The Wurtzite structure 14
I.2. Binary II–V and II–VI Semiconductors: Parent Compounds for Ternary Alloy Design 15
I.3. Alloying & Vegard's Law in Ternary Semiconductor Alloys 18
I.3.1. Vegard's Law for Lattice Parameter 18
I.3.2. Electronic-Structure Bowing 18
I.4. First Brillouin zone and irreducible Brillouin zone 19
I.4.1. High symmetry points 20
I.4.2. High symmetry lines 21
I.4.3. Band structure formation 21
I.5. Theoretical background of optical properties 22
I.5.1. Dielectric function ε(ω) 23
I.5.2. Optical constants derived from ε(ω) 23
I.5.3. Interband and Intraband Transitions 25
I.5.3.1. Interband Transitions 25
I.5.1.2. Intraband Transitions 26
I.6. Elastic Properties of Crystalline Semiconductors 27
I.6.1. Elastic Constants Cij 27
I.6.2. The mechanical moduli 28

I.6.3. Ductility and Elastic Anisotropy..... 29
I.7. Thermal Properties in the Quasi-Harmonic Approximation (QHA)..... 30
I.7.1. Physical context and scope..... 30
I.7.2. Full-phonon QHA: thermodynamic potentials and basic responses..... 31
I.7.3. Fundamental QHA identities 32
I.7.4. Debye-QHA specialization 32
I.7.5. Limitations and extensions 33
References of Chapter I 34

Chapter II

CHAPTER II

Theoretical framework of DFT

This chapter presents the fundamental theoretical aspects of Density Functional Theory (DFT), with the aim of understanding and mastering DFT-based theoretical methods to enable the calculation and analysis of the physical properties of selected semiconductor materials. Over time, DFT has evolved into a "standard tool" for modeling a wide range of materials in physics, chemistry, and materials science [1]. Its major strength lies in being a powerful modeling approach, originating from the seminal work of Hohenberg and Kohn in 1964, and continuously advancing toward higher accuracy and shorter computational times [2] **.** In this chapter, we discuss the theoretical foundations of DFT, covering its historical development, the fundamental concepts of electronic structure theories, and the main challenges associated with DFT.

II.1. Introduction to Density Functional Theory

II.1.1. The many-body Schrodinger equation

To describe the behavior of a quantum system, it is necessary to determine its wavefunction Ψ(r) for every radius r, this procedure incorporates the solving of Schrodinger equation [3] which takes the following symbolic expression:

$$\left(\hat{T} + \hat{V}\right)\psi = E\psi \qquad \textbf{(II. 1)}$$

Where $\hat{T}$ denotes the kinetic energy operator, $\hat{V}$ is the potential energy operator and E is the total energy of the system's stationary state described by the wavefunction Ψ.

To develop a realistic approach to appropriately describe the systems containing many electrons and many nuclei using this Schrodinger equation we need to introduce the many-body wavefunction $\Psi(r_1, r_2, \ldots\ldots, r_N; R_1, R_2, \ldots\ldots, R_M)$ where N is the the number of electrons with their coordinates $(r_1, r_2, \ldots\ldots, r_N)$ and M the number of nuclei with their coordinates $(R_1, R_2, \ldots\ldots, R_M)$

[2]. In the same way we represent the total electronic charge density n(r) in terms of induvial electron wavefunctions [1] :

$$n(r) = 2\sum_{i} \psi^{*}(r_1, r_2, \ldots\ldots, r_N;\ R_1, R_2, .., R_M).\psi(r_1, r_2, \ldots\ldots, r_N; R_1, R_2, .., R_M) \qquad (\mathbf{II.2})$$

As for the many-body kinetic energy operator, this operator consists of kinetic energy of electrons and the nuclei and given by the following symbolic expression:

$$T = -\sum_i \frac{\hbar^2}{2m_e}\boldsymbol{\nabla_i^2} - \sum_I \frac{\hbar^2}{2M_I}\boldsymbol{\nabla_I^2} \qquad (\mathbf{II.3})$$

With $\hbar$ the plank's constant, m_e: electron mass and MI the nucleus mass, The index **i** runs from 1 to the total number of electrons **N**, and the index **I** runs from 1 to the total number of nuclei **M**.

The potential energy operator consists of three terms, the first term is the electron-electron repulsion potential (V_{ee}), the second term is nucleus-nucleus repulsion V_{nn} and the third one is the nucleus-electron attraction potential V_{en}; these three terms are given as follows [2]:

$$V_{ee} = \frac{1}{2}\sum_{i\neq j} \frac{e^2}{4\pi\epsilon_0|\boldsymbol{r_i} - \boldsymbol{r_j}|} \qquad (\mathbf{II.4})$$

$$V_{nn} = \frac{1}{2}\sum_{I\neq J} \frac{e^2 Z_I Z_J}{4\pi\epsilon_0|\boldsymbol{R_I} - \boldsymbol{R_J}|} \qquad (\mathbf{II.5})$$

$$V_{en} = -\sum_{i,I} \frac{e^2 Z_I}{4\pi\epsilon_0|\boldsymbol{r_i} - \boldsymbol{R_I}|} \qquad (\mathbf{II.6})$$

So, the potential energy operator is defined as [2]:

$$\hat{\mathrm{V}} = V_{ee} + V_{nn} + V_{en} \qquad (\mathbf{II.7})$$

With Z_I denotes the atomic numbers, r_i, r_j are positions of electron **I** and electron **J** respectively. And $\boldsymbol{R_I}, \boldsymbol{R_J}$ are positions of neuclus i and nucleus j respectively.

Thus, combining equation from II.3 to II.7 the many body Schrodinger equation can be written as follows [2] :

$$\left[-\sum_i \frac{\hbar^2}{2m_e}\nabla_i^2 - \sum_I \frac{\hbar^2}{2M_I}\nabla_I^2 + \frac{1}{2}\sum_{i\neq j}\frac{e^2}{4\pi\epsilon_0|r_i - r_j|} + \frac{1}{2}\sum_{I\neq J}\frac{e^2 Z_I Z_J}{4\pi\epsilon_0|R_I - R_J|} - \sum_{I,i}\frac{e^2 Z_I}{4\pi\epsilon_0|r_i - R_I|}\right]\psi = E_{\text{tot}}\psi \quad (\mathbf{II.8})$$

This equation is too complex to be solved analytically, so approximations must be employed [4]. In the following we discuss the historical development of various approximations and models including density functional theory.

II.1.2. The Born-Oppenheimer approximation.

Among the various methods used to simplify the description of molecular systems, one widely adopted approach is the Born-Oppenheimer approximation. In which the nuclei are considered much heavier than the electrons and can be treated as fixed in space, allowing their kinetic energy to be neglected. We can assume that the electrons are in instantaneous equilibrium with the nuclei. In other words the electronic cloud is kept as the only player in the many body Schrodinger equation while the nuclei are reduce to only a source of external field created with their positives charges [4]. This approach partially decouples the electrons from the nuclei motion, it amounts to a factorization of the many-body wavefunction $\Psi(r_1, r_2, .., r_N; R_1, R_2, ., R_M)$ into two parts, the first part is the electronic wavefunction ψ_{iN}^e and the second part is the nuclear wave function ψ_{iM}^n [5]

$$\Psi(r_1, r_2, \ldots.., r_N; R_1, R_2, \ldots.., R_M) = \Psi_{iM}^n(R_1, \ldots, R_M).\ \Psi_{iN}^e(r_1, \ldots, r_N) \quad (\mathbf{II.9})$$

The wave function depends parametrically on the nuclei positions, and since we considered the nuclei is kinetic energy this case the many body Schrodinger equation is written as [2]:

$$\left[-\sum_i \frac{\hbar^2}{2m_e}\nabla_i^2 + \sum_i V_n(r_i; R) + \frac{1}{2}\sum_{i\neq j}\frac{e^2}{4\pi\epsilon_0|r_i - r_j|}\right]\psi_{iM}^n.\ \psi_{iN}^e = E\psi_{iM}^n.\ \psi_{iN}^e \quad (\mathbf{II.10})$$

with $V_n(r_i; R)$ the potential of static nuclei influencing the i^{th}electron . this equation can be separated into and electronic equation and nuclear equation shown respectively in equations (II.11) and (II.13) bellow:

$$H_{el}(r; R)\psi_{iN}^e(r; R) = E_{el}\psi_{iN}^e(r; R) \quad (\mathbf{II.11})$$

H_{el} and E_{el} are respectively the electronic Hamiltonian and the electronic energy with:

$$H_{el}(r;R) = -\sum_i \frac{\hbar^2}{2m}\nabla_i{}^2 + V_n(r;R) + \frac{1}{2}\sum_{i<j}\frac{e^2}{4\pi\epsilon_0|r_i - r_j|} \quad (\mathbf{II.12})$$

$$H_N(R)\psi_{iM}^N(R) = E_N\psi_{iM}^N(R) \quad (\mathbf{II.13})$$

H_N and E_N are respectively the nuclear Hamiltonian and the nuclei total energy with:

$$H_N = V_n(R) + E_{el}(R) \quad (\mathbf{II.14})$$

$V_n(R)$ and $E_{el}(R)$ are the potential energy of the nucleus-nucleus interactions and the electronic energy consequently.

This approach disregards the motion of atomic nuclei, treating electrons as if they are moving in a medium with stationary nuclei. The rationale for this is that electrons possess significantly less mass than nuclei, resulting in their considerably higher velocity. This approximation is very accurate for most materials. Now, we can concentrate only on electrons. However, it presents a significant challenge. The electrons interact with the atomic nuclei and with each another through Coulomb forces. While the electron-nucleus interaction can be treated accurately, electron-electron interactions are generally intractable and therefore require approximations, such as DFT[6].

II.1.3. Independent electrons approximation

In effort of solving the equation II.11 scientist developed numerous approximation approaches, since the 1920s Thomas (1927); Fermi (1928) ; Hartree (1928); Pauling (1928); Slater (1929) and Fock (1930). The first step to simplify this problem was to suppose that electrons don't interact with each other, thus eliminating the coulomb interaction between them. This approximation is called Independent electrons approximation. Using this method, the electronic wave function can be written as a product of single particle functions ϕ_i so Many-Body Schrödinger Equation become a single particle equation which are both shown the following equations [2]:

$$\Psi_e(r_1, r_2, \dots, r_N) \approx \prod \phi_i(r_i) = \phi_1(r_1)\phi_2(r_2)\cdots\phi_N(r_N) \quad (\mathbf{II.15})$$

$$\left[\sum_i \widehat{H}_0(r_i)\right]\phi_1(r_1)\cdots\phi_N(r_N) = E\phi_1(r_1)\phi_2(r_2)\cdots\phi_N(r_N) \quad \textbf{(II. 16)}$$

$\widehat{H}_0(r_i) = -\sum_i \frac{\hbar^2}{2m}\boldsymbol{\nabla}_i{}^2 + V_n(r;R)$ is the single electron Hamiltonian. The single electron wave functions $\phi_i(r_i)$ are obtained by solving single-electron Schrodinger equation [2]:

$$\widehat{H}_0(r)\phi_i(r) = \varepsilon_i\phi_i(r) \quad \textbf{(II.17)}$$

ε_i represents the eigenvalue associated with the iii-th single-particle wavefunction.

II.1.4. Hartree-Fock approximation

The Hartree approach was first developed by Hartree Douglas in 1928.However, this approximation did not include the antisymmetric of electronic wave functions regarding to exchange energy, this method was further extended by Fock to include the wave function's antisymmetry [6]. Both Slater and Fock demonstrated that to ensure this antisymmetry and thus ensure that electron obey the Pauli's exclusion principle by establishing a Slater determinant consisted of single electron wave functions, this determinant is antisymmetric [7]

$$\Psi_{HF}(r_1, r_2, r_3, \dots \dots r_N) = \frac{1}{\sqrt{N!}}\begin{vmatrix} \psi_1(r_1) & \psi_2(r_1) & \cdots & \psi_N(r_1) \\ \psi_1(r_2) & \psi_2(r_2) & \cdots & \psi_N(r_2) \\ \vdots & \vdots & \vdots & \vdots \\ \psi(r_N) & \psi_2(r_N) & \cdots & \psi_N(r_N) \end{vmatrix} \quad \textbf{(II.18)}$$

The term $\frac{1}{\sqrt{N!}}$ serves as the normalization factor for a system with N electrons.

$$\psi_i(r) = \phi_i(r)\chi_i(\zeta) \quad \textbf{(II.19)}$$

Where, $\phi_i(r)$ is the spatial orbital and $\chi_i(\zeta)$ denote the spin wavefunction. Here, r represents the spatial and ζ shows to the spin coordinates of the electron.

incorporating the Slater determinant and variational principle Fock introduced and additional term to the electronic Hamiltonian, this term is called Fock exchange. Consequently the Hartree-Fock equation is written as follows [7]:

$$-\frac{\hbar^2}{2m}\nabla^2\phi_i(r) + U^{ion}(r)\phi_i(r) + U^{el}(r)\phi_i(r) + U^{ex}(r)\phi_i(r) = \epsilon_i\phi_i(r) \qquad \textbf{(II. 20)}$$

U^{ion} is the ion-electron interaction potential, U^{el} represents the electrons interactions potential and U^{ex} represents the potential of exchange correlation .

ϵ_i represents the eigenvalue associated with the iii-th single-particle wavefunction.

This equation can be written in the form of single-particle Schrodinger equations [8]:

$$\hat{F}\phi_i(r) = \epsilon_i\phi_i(r) \qquad \textbf{(II. 21)}$$

With $\hat{F} = -\frac{\hbar^2}{2m}\nabla^2 + V_n + V_H + V_X$ is called the Fock operator ,V_H is the Hartree potential and $V_X = U^{ex}$ is the Fock exchange potential which arises from the quantum mechanical effect of the electrons being indistinguishable particles that have to obey the Pauli exclusion principle with V_H is written in terms of electronic density n(r) using atomic units [2]:

$$V_{\mathrm{H}}(\vec{r}) = \int d\overrightarrow{r'}\,\frac{n(\overrightarrow{r'})}{\left|\vec{r} - \overrightarrow{r'}\right|} \qquad \textbf{(II. 22)}$$

The exchange potential V_X is as function of electronic density using atomic units as follows:

$$V_{\mathrm{X}}(\vec{r}, \overrightarrow{r'}) = -\sum_j \frac{\phi_j^*(\overrightarrow{r'})\,\phi_j(\vec{r})}{\left|\vec{r} - \overrightarrow{r'}\right|} \qquad \textbf{(II. 23)}$$

The total energy (E_{HF}) of the system is defined as: $E_{HF} = \sum\langle\phi_i(r)\left|\hat{F}\right|\phi_i(r)\rangle$.

Furthermore, the Hartree–Fock equations represent a significant advancement by transitioning from a classical mean-field approximation to a quantum mechanical treatment of electrons. However, this approach has limitations, as it fails to accurately describe systems where electron correlation is significant. Consequently, more advanced methods, such as DFT are required [9].

II.1.5. Electron correlation

Electron correlation in physics refers to the interaction between electrons in a system, where the state of each electron depends on the positions and spins of its neighbors [10]. In the Hartree-Fock approximation, the Slater determinant provides an approximate wave function that captures much of the physics of many-electron systems. However, it does not represent the exact wave function. Consequently, according to the variational principle, the resulting Hartree-Fock energy is always higher than the exact ground-state energy calculated within the Born-Oppenheimer approximation (neglecting relativistic effects). The difference between these two energies is defined as the correlation energy , a concept introduced by Löwdin in 1959 [11]:

$$E_C = E_0 - E_{HF} \qquad \textbf{(II. 24)}$$

As the correlation energy E_C is a negative since E_0 and E_{HF} are both negative and $|E_0| < |E_{HF}|$. E_C accounts for the error introduced in the Hartree Fock approach. For example, as shown in Figure II.1, the Hartree–Fock potential for the molecule lies above the exact ground-state curve due to the neglect of electron correlation. The development of approximation methods to assess the correlation energy accurately is still an active research area in quantum mechanics. Electron correlation arises from the instantaneous repulsion between electrons, which is not fully accounted for in the Hartree–Fock methodology. Qualitatively, in the Hartree–Fock scheme, electrons can approach one another too closely because their electrostatic interaction is treated in a mean-field manner. Consequently, the electron repulsion energy is overestimated, making the Hartree–Fock energy higher than the exact ground-state energy. This component is related to the term

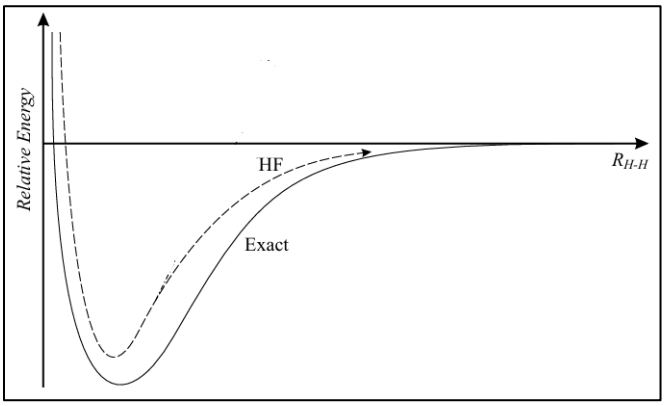


Figure II.1. Potential curves of the H_2 molecule [11]

$\frac{e^2}{4\pi\epsilon_0|r_i-r_j|}$ in the system's Hamiltonian and so related to the movements of individual electrons and it called the short-range correlation effect.The second part of the correlation energy is the non-dynamical or static correlation it came as the result of the ground state Slater determinant is not a reliable approximation n to the exact ground state [11]. This missing correlation is clearly evidenced in Fig. II.1 by the systematic overestimation of the H_2 ground-state energy at the Hartree–Fock level.

II.2. Density Functional Theory

II.2.1. Thomas Fermi model

Developed by Llewellyn Thomas and Enrico Fermi, the Thomas-Fermi (TF) model is considered as the first type of density functional theory (DFT). Its basic idea is to model the electrons cloud as zero temperature Fermi-Dirac fluid that is negatively charged. In other words, it is a statistical model that considers the electrons around the nucleus as a gas of particles, all obeying the Pauli exclusion principle [12]. This model incorporates electron density as a key ingredient to solve many-body problems. It uses a semiclassical approximation for electrons in an external potential, (V_ext), expressing the total energy as a functional of the electron density (n(r). Dirac later improved the theory by including a term describing the exchange energy[13]:

$$E^{TFD}[n] = C_1 \int d^3\, r\, n(\boldsymbol{r})^{5/3} + \int d^3\, r\, V_{\text{ext}}(\boldsymbol{r}) n(\boldsymbol{r}) + C_2 \int d^3\, r\, n(\boldsymbol{r})^{4/3} + \frac{1}{2}\int d^3\, r\, d^3 r'\, \frac{n(\boldsymbol{r}) n(\boldsymbol{r}')}{|\boldsymbol{r}-\boldsymbol{r}'|} \qquad (\mathbf{II.25})$$

This expression represents the Thomas-Fermi energy functional of atoms. For molecules With $C_1 = \left(\frac{3}{10}\right)(3\pi^2)^{2/3}$ and $C_2 = -\frac{3}{4}\left(\frac{3}{\pi}\right)^{\frac{1}{3}}$. The first term represents the kinetic energy of the electrons within the homogeneous electron gas (HEG) approximation. It is followed by the electron-nucleus interaction, the Hartree energy, and finally the exchange energy. The HEG approach is fundamental to Density Functional Theory (DFT); consequently, the HEG density is defined as follows[13]:

$$n = \frac{N}{\Omega} \qquad (\mathbf{II.26})$$

where N is the total number of electrons in the volume Ω. The electronic density is usually expressed using the parameter r_s defined as :

$$r_s = \left(\frac{3}{4\pi n}\right)^{\frac{1}{3}} \qquad (\mathbf{II.27})$$

Here, r_s is the radius of a sphere containing exactly one electron (the Wigner-Seitz radius). The larger the rs is, the lower is the electron density, and n is the number of electrons per unit volume.

Thomas and Fermi individually realized that the Fermi Thomas potential energy $(-eV)$ fulfilled a second order nonuniform differential equation with a term relative to $(V^{3/2})$ [14]:

$$\boldsymbol{\nabla}^2 V = \frac{4e}{3\pi}\left(\frac{2m}{\hbar^2}\right)^{\frac{3}{2}}(eV)^{\frac{3}{2}} \qquad (\mathbf{II.28})$$

This equation can be used to evaluate the atomic potential by applying boundary conditions: as the radius approaches zero, the potential tends toward the Coulomb potential of the nucleus. Conversely, as the potential vanishes. To simplify equation (II.28), Fermi introduced an appropriate change of variables:

$$r = \mu x, \quad \mu = \frac{1}{2}\left(\frac{3\pi}{4}\right)^{2/3}\frac{\hbar^2}{me^2}Z^{-1/3} \qquad (\mathbf{II.29})$$

$$V(r) = \frac{Ze}{r}\varphi(r) \qquad (\mathbf{II.30})$$

In terms of equation(becomes (for $\varphi(r)$>0): $\varphi''(r) = \frac{\varphi^{3/2}}{\sqrt{x}}$ with the prime depicts differentiation reltive to (x). with the boundary conditions of $\varphi(0) = 1\ and\ \varphi(\infty) = 0$.

With $\varphi(r)$ is a screening function that accounts for the reduction in effective nuclear charge because of the existence of other electrons. Equation (II.29) is a universal equation because it isn't depending on the atomic number or the $(m, e, \hbar)$ constants.Fermi immediately realized that its solution describes a screened Coulomb potential generated by an effective charge of $Ze\varphi(r/\mu)$. Because of the independence of the equation from Z, the potential could be easily adapted to any

atom by using the appropriate scaling factor. To extend this procedure to positive ions, Fermi and Rasetti suggested treating an ion with nuclear charge (Ze) as a neutral atom with nuclear charge (Z−1)e possessing an additional proton. This finally allowed them to approximate the potential energy for an additional electron in an ionized atom and simplify the calculation of ionization energies and other properties of atoms. Their approach gave a lot of flexibility in their modeling of neutral atoms and ions within a statistical model. The potential energy of an additional electron were determined as [14]:

$$-eV = -\frac{e^2}{r}\left[1 + (Z-1)\varphi\left(\frac{r}{\mu}\right)\right] \qquad (\mathbf{II.31})$$

Equation (II.31) illustrates how the collective interaction of many electrons can be represented through an effective screened potential, reducing the many-body problem to a single-particle equation within a statistical approximation. This method was generalized by B.Baker (1930) to include positively charged ions and it was revised By Eugene Guth and Peierls after months later. For atoms and molecules, the electron density typically varies strongly from being homogeneous. Therefore, the homogeneous electron gas, HEG, model that assumes an even distribution of electrons has been seen as too crude and insufficient to capture the complexity of real systems. The first attempts at improving this model, like Thomas–Fermi theory, were found to be far from quantitatively predictive for atomic and molecular systems. Nonetheless, the theory introduced a novel revolutionary concept: taking the electron charge density as the fundamental variable, instead of the wave function, to describe electronic properties. This shift in perspective has since become one of the cornerstones of modern electronic structure theory. The concept of concentrating on the electron density, rather than on wave functions, finally resulted in the formulation of density functional theory (DFT). In DFT, electron density is arguably simpler three-dimensional function than a complicated, high-dimensional wave function- is taken as the primary variable. The basis for this is provided by the Hohenberg–Kohn theorems, which state that the ground-state properties of a many-electron system are uniquely determined by its electron density.

By allowing a description of the energy and other electronic properties in terms of functionals of the electron density, DFT has enabled calculations of properties of complex materials at a fraction

of the computational cost of wave function-based methods. In this formalism, each term is an integral over the charge density, meaning that these terms are functionals of the electron density.

II.2.2 Hohenberg-Kohn theorems

The Hohenberg-Kohn (HK) theorems ensures that the stationary many-body system can be full described via the ground state density [5].the entire field of DFT depends on these two fundamental mathematical proved theorems the first theorem is demonstrated by Hohenberg and Kohn which states that:

Theorem (II.1): "The ground state density n(r) determines the external potential energy V(r) to within a trivial additive constant C" [15].

this means that there is a one to one mapping linking the ground state density and the ground state wave function. An additional way to iterate Hohenberg and Kohn's result is that the ground-state density exclusively establishes all physical properties, involving the energy and wave function, of the ground state [1].In order to prove this theorem Hohenberg and Kohn considered an amount of electrons moving in a large closed box under the influence of an external potential $v(\boldsymbol{r})$ and the Coulomb interaction U [16]. As a result, the Hamiltonian is expressed as :

$$H = T + V_{ext} + U \qquad (\mathbf{II.32})$$

Where:

$$T = \frac{1}{2}\int \boldsymbol{\nabla}\Phi^*(r)\boldsymbol{\nabla}\Phi(r)\ dr \qquad (\mathbf{II.33})$$

$$V_{ext} = \int v(r)\Phi^*(r)\Phi(r)\ dr \qquad (\mathbf{II.34})$$

$$U = \frac{1}{2}\int \frac{1}{|r-r'|}\Phi^*(r)\Phi^*(r')\Phi(r')\Phi(r)\, drdr' \qquad (\mathbf{II.35})$$

After that, to simplify we assume that the ground state density n(r)is nondegenerate, we now show that $v(\boldsymbol{r})$ is uniquely a functional of n(r). The proof is performed using "reductio ad absurdum" by adopting that there is another external potential $v'(r)$ with ground state Ψ' leading to same ground density n(r). Therefore, we express the Hamiltonian and ground-state energies related to Φ and

$\Phi'$by H, H' and E, E' respectively. Employing the minimal characteristic of the ground state we find [16] :

$$E' = \langle \Phi' | H' | \Phi' \rangle < \langle \Phi | H' | \Phi \rangle = \langle \Phi | (H + V' - V) | \Phi \rangle \quad \textbf{(II.36)}$$

Hence that:

$$E' < E + \int [v'(\boldsymbol{r}) - v(\boldsymbol{r})] n(\boldsymbol{r}) \, d\boldsymbol{r} \quad \textbf{(II.37)}$$

The same way we find that:

$$E < E' + \int [v(\boldsymbol{r}) - v'(\boldsymbol{r})] n(\boldsymbol{r}) \, d\boldsymbol{r} \quad \textbf{(II.38)}$$

Adding eq (I.35) with eq (I.36) leads to a contradiction:

$$E + E' < E + E' \quad \textbf{(II.39)}$$

Therefore, the external potential v(r) is uniquely determined by the ground-state density n(r). As a result, the many-electron ground state is uniquely identified as a functional of the ground-state density.

The following are outcomes of Theorem (II.1) [15] :

a) The ground state density n(r) exclusively determines the system's Hamiltonian H. Therefore, the density n(r) completely characterizes the system.

b) Once the Hamiltonian is uniquely determined , may be solved to determine the many-body wave function and the corresponding total energies of the ground and excited states. Therefore, knowledge of the ground-state density enables the determination of the system's physical properties.

c) The total energy eigenvalue derived from Eq. (I.8) is a functional of the ground-state density n(r).

$$E = E[n(r)] \quad \textbf{(II.40)}$$

d) By splitting out the external potential energy component $V_{ext}(r)$, the energy functional $E[n(r)]$ may be written as:

$$E[\mathrm{n(r)}] = \int \mathrm{n}(r)V_{ext}(r)\,\mathrm{d}r + F_{HK}[\mathrm{n(r)}] \qquad \textbf{(II.41)}$$

Where:

$$F_{HK}[\mathrm{n(r)}] = \langle \Phi[\mathrm{n(r)}]\,|T + V\,|\Phi[\mathrm{n(r)}]\,\rangle \qquad (\mathbf{II.42})$$

Is the Hohenberg-Kohn functional which depends only on the kinetic energy T and electron interaction V operators. This functional is universal for all Coulomb systems like atoms, molecules and solids. However, it is an unknown functional.

The second Hohenberg and Kohn's statement is the following:

Theorem II.2: "The ground state density n(r) is determined by application of the variational principle for the energy by variation only of the density."

This theorem provides the ground state energy E_0 as a functional of the density n(r) of the ground state:

$$E_0 = E[n(r)] = \langle \Phi[\mathrm{n(r)}]\,|H\,|\,\Phi[\mathrm{n(r)}]\,\rangle \qquad (\mathbf{II.43})$$

According to the second Hohenberg and Kohn theorem the ground state energy can be assessed employing the variational minimization of the functional of energy $E[n(r)]$. For a trial density $\tilde{n}(r)$ such that $\tilde{n}(r) > 0$ and $\int \tilde{n}(r).dr = N$ Where N is the total number of electrons we shall have [17] :

$$E_0 < E[\tilde{n}(r)] \qquad (\mathbf{II.44})$$

Where E[ñ(r)] is the energy functional from (II.41), which is analogous to the variational principle for wave functions. It provides the proper justification for the Thomas–Fermi variational principle, in the sense that $E^{TF}[n]$ in equation (II.25) approximates the exact energy functional E[n(r)]. To prove this theorem, note that the first Hohenberg–Kohn theorem implies that ñ(r) determines its own external potential ṽ(r), Hamiltonian (H), and wave function Φ(r). The latter can then be used

as a trial wave function for the system of interest, which is characterized by the external potential *v(r)*. Therefore:

$$\langle \Phi | \widehat{H} | \Phi \rangle = \int \tilde{n}(\boldsymbol{r}) v(\boldsymbol{r})\, d\boldsymbol{r} + F_{HK}[\tilde{n}] = E[\tilde{n}] \geq E[n] \qquad (\mathbf{II.45})$$

By assuming the differentiability of $E[n]$, the variational principle demands that the ground state density satisfies the stationary condition:

$$\delta\{E[\mathrm{n}] - \mu[\int \mathrm{n}(r)\,.\, dr - N]\} = 0 \qquad \textbf{(II.46)}$$

Which yields to the Euler langrage equation:

$$\mu = \frac{\delta E[\mathrm{n}]}{\delta \mathrm{n}(r)} = v(r) + \frac{\delta F_{\mathrm{HK}}[\mathrm{n}]}{\delta \mathrm{n}(r)} \qquad \textbf{(II.47)}$$

With μ is the chemical potential.

If the Hohenberg-Kohn functional $F_{\mathrm{HK}}[\mathrm{n}]$ were known and sufficiently a simple functional of the density n , determining This would simply require minimizing a functional of the three-dimensional density. However, the main difficulty in many-electron problems lies in determining the universal functional $F_{\mathrm{HK}}[\mathrm{n}]$, due to the long-range nature of the Coulomb interaction embodied in Hartree energy functional $E_H[n] = \frac{1}{2}\int\int \frac{n(r)n(r')}{|r-r'|}\, dr\, dr'$ Hohenberg and Kohn have proposed to separate this contribution form the expression of the universal functional $F_{HK}[\mathrm{n(r)}]$ and write is as [16]:

$$F[n] = \frac{1}{2}\int \frac{n(r)n(r')}{|r-r'|}\, dr\, dr' + G[n] \qquad \textbf{(II.48)}$$

So, the universal energy functional expression is now written as:

$$E[n] = \int v(r)n(r)\ dr + \frac{1}{2}\int \frac{n(r)n(r')}{|r-r'|}\, dr\, dr' + G[n] \qquad \textbf{(II.49)}$$

Where $G[n]$ is a universal functional like the functional $F_{HK}[\mathrm{n(r)}]$. which is also uknown

The exact ground state energy is expressed as :

$$E_0 = min\left\{\int v(r)n(r)\ dr + \frac{1}{2}\int \frac{n(r)n(r')}{|r-r'|}\ dr\, dr' + G[n]\right\} = min\{V_{ext} + E_H[n] + G[n]\}\ \textbf{(II. 50)}$$

II.2.3. The Kohn-Sham's scheme

II.2.3.1. The decomposition of the universal Functional

As stated earlier, the universal functional $G[n]$ in equation (II.49) is unknown. The Hohenberg-Kohn theorems establish that the ground-state total energy of a many-electron system depends on the electron density n(r), and that the Hohenberg–Kohn functional $F_{HK}[\mathrm{n(r)}]$ is a functional of $\mathrm{n(r)}$.However, as noted, these theorems provide no guidance on how to actually construct this functional. Since the original work, a number of practical approximations have been developed. In their 1965 paper, Kohn and Sham proposed the first approximation to the functional G[n], using a scheme analogous to Hartree's method. Importantly, it captures the main part of the exchange and correlation effects by decomposing G[n] as in the following expression[18] :

$$G[n] = T[n] + E_{xc}[n] \quad \textbf{(II.51)}$$

Where $T[n]$ dictate the kinetic energy of the system of non-interacting electrons with density n(r), and $E_{xc}[n]$ is the echange-correlation energy functional of an interacting system within the definition of Kohn and Sham. This latter energy has no simple known expression. However, Khon and sham stated that if the density n(r) varies adequately slow, one can show that [18]:

$$E_{xc}[n] = \int n(r).\epsilon_{xc}\big(n(r)\big).dr \quad \textbf{(II.52)}$$

With $\epsilon_{xc}\big(n(r)\big)$ is the exchange-correlation energy per electron of the system.

The non-interacting kinetic energy functional of the system is expressed as[19] :

$$T[n] = min\langle\Phi|\hat{T}|\Phi\rangle = \langle\Phi[n]|\hat{T}|\Phi[n]\rangle \quad \textbf{(II.53)}$$

The minimizing is carried out over the set of the many-electron single-determinant wave function. The exchange-correlation energy functional accounts for all the complex many-electron interactions that are not included in the non-interacting kinetic energy and the Hartree energy. The Kohn–Sham approach enables more accurate calculations of electronic structures because the

kinetic energy of non-interacting electrons can be computed exactly, while the remaining exchange-correlation energy although the most challenging part to approximate can be treated with suitable approximations. The idea behind the Kohn–Sham scheme is to use the exact expression for the non-interacting kinetic energy functional T[n] by reformulating the minimization in equation (II.50) as a minimization carried out over the set of Φ:

$$E_0 = min\{V_{ext} + E_H[n] + T[n] + E_{xc}[n]\} \quad \textbf{(II.54)}$$

The classical electrostatic repulsion energy for the charge distribution is computed exactly. The exchange-correlation energy functional, however, must be approximated. If there is a unique Kohn-Sham (KS) wave function , we can further decompose $E_{xc}[n]$ [19]:

$$E_{xc}[n] = E_x[n] + E_c[n] \quad \textbf{(II.55)}$$

$E_x[n]$ is the exchange energy functional which is defined by:

$$E_x[n] = \langle \Phi[n] | \hat{V}_{ee} | \Phi[n] \rangle - E_H[n] \quad \textbf{(II.56)}$$

$E_c[n]$ is the correlation energy functional which is defined by:

$$E_c[n] = T_c[n] + V_c[n] \quad \textbf{(II.57)}$$

With $T_c[n]$ and $V_c[n]$ denotes the kinetic energy and potential correlation contributions respectively. Outline illustration of the Kohn–Sham is presented in Figure II.2:

The same definition of the Kohn-Sham exchange correlation potential v_{xc} is given by [15]:

$$v_{xc}(r) = v_x(r) + v_c(r) \quad \textbf{(II.58)}$$

With the definition of the Kohn-Sham exchange potential $v_x(r)$ is:

$$v_x(r) = \frac{\delta E_x[n]}{\delta n(r)} \quad \textbf{(II.59)}$$

With the define the Kohn-Sham correlation potential $v_c(r)$ is:

$$v_c(r) = \frac{\delta E_c[n]}{\delta n(r)} \quad \textbf{(II.60)}$$

II.2.3.2. The Kohn-Sham's equations

The fundamental concept of the Kohn–Sham scheme is to transform the many-particle problem into a system of non-interacting particles that possesses the same ground state density n(r) as the original many-particle system [13] .The single determinant wave function is formed from a set of N orthonormal spin-orbitals $\Phi_{i_{i=1,\dots,N}}$. To enforce spin symmetry, each spin-orbital is factorized as $\Phi_i(r) = \phi_i(r).\chi_{\sigma i}(\sigma)$, where ϕ_i is a spatial orbital and $\chi_{\sigma i}$ is a spin orbital (σ_i is the spin of the spin-orbital i). Rewriting the total electronic ground-state energy in equation (II.54) in terms of spin orbitals and integrating over the spin variables yields [19]:

$$E_0 = \min_{\Phi}\left\{\sum_{i=1}^{N}\int \phi_i{}^*(\mathrm{r})\left(-\frac{1}{2}\boldsymbol{\nabla}^2 + \hat{V}_{ext}(\mathrm{r})\right)\phi_i(r)\ d^3\mathrm{r} + E_H[n] + E_{xc}[n]\right\} \quad \textbf{(II.61)}$$

With the electron density defined as :

$$n(\mathrm{r}) = \sum_{i=1}^{N}|\phi_i(\mathrm{r})|^2 \quad \textbf{(II.62)}$$

Applying the method of Lagrange multipliers subject to the normalization condition:

$$\int \phi_i^*(\mathrm{r})\phi_i(\mathrm{r})\ d^3\mathrm{r} = 1 \quad \textbf{(II.63)}$$

Kohn and sham constructed the Kohn-Sham orbital equations given by [17] :

$$\left(-\frac{1}{2}\boldsymbol{\nabla}^2 + V_{\text{eff}}(r)\right)\phi_i(\mathrm{r}) = \varepsilon_i\phi_i(r) \quad \textbf{(II.64)}$$

With:

$$V_{\text{eff}}(r) = \hat{V}_{ext}(\mathrm{r}) + \hat{V}_H(\mathrm{r}) + \hat{V}_{xc}(\mathrm{r}) = \hat{V}_{ext}(\mathrm{r}) + \int d^3\mathrm{r}'\ \frac{\boldsymbol{n(r)}}{|\boldsymbol{r}-\boldsymbol{r}'|} + \frac{\boldsymbol{\delta E_{xc}[n]}}{\boldsymbol{\delta n(r)}} \quad \textbf{(II.65)}$$

Here $\hat{V}_{ext}(\mathrm{r})$ is the external nuclear potential operator. $\hat{V}_H(\mathrm{r})$, the Hartree potential operator, $\hat{V}_{xc}(\mathrm{r})$ is the exchange-correlation potential operator. The Lagrange multiplier associated to the normalization condition is denoted ε_i which actually is the Kohn-Sham orbital energies.φ_i are referred to as the Kohn-Sham orbitals.

$V_{\mathrm{eff}}(r)$ is called The Kohn-Sham potential, or effective potential, is a local external field in which non-interacting fermions move.

Note: In the presence of a magnetic field, density functional theory has been extended from spin-unpolarized to spin-polarized densities. This dependence on spin densities allows for the construction of more accurate exchange-correlation functional approximations and is therefore routinely used in practice for open-shell systems. The spin density $n_\sigma(r)$ is define as [19] :

$$n(r) = n(r,\uparrow) + n(r,\downarrow) \qquad \textbf{(II. 66)}$$

within this approach the KS equations are written as:

$$\left(-\frac{1}{2}\boldsymbol{\nabla}^2 + \hat{V}_{ext}(\mathrm{r}) + \hat{V}_H(\mathrm{r}) + \hat{V}_{\mathrm{xc},\sigma}(\boldsymbol{r})\right)\phi_{i\sigma}(\boldsymbol{r}) = \varepsilon_{i\sigma}\phi_{i\sigma}(\boldsymbol{r}) \qquad \textbf{(II. 67)}$$

The exchange-correlation potential's dependence on the spin-resolved density is as follows :

$$v_{\mathrm{xc},\sigma}(r) = \frac{\delta E_{\mathrm{xc}}[\mathrm{n}_\uparrow, \mathrm{n}_\downarrow]}{\delta \mathrm{n}_\sigma(r)} \qquad \textbf{(II. 68)}$$

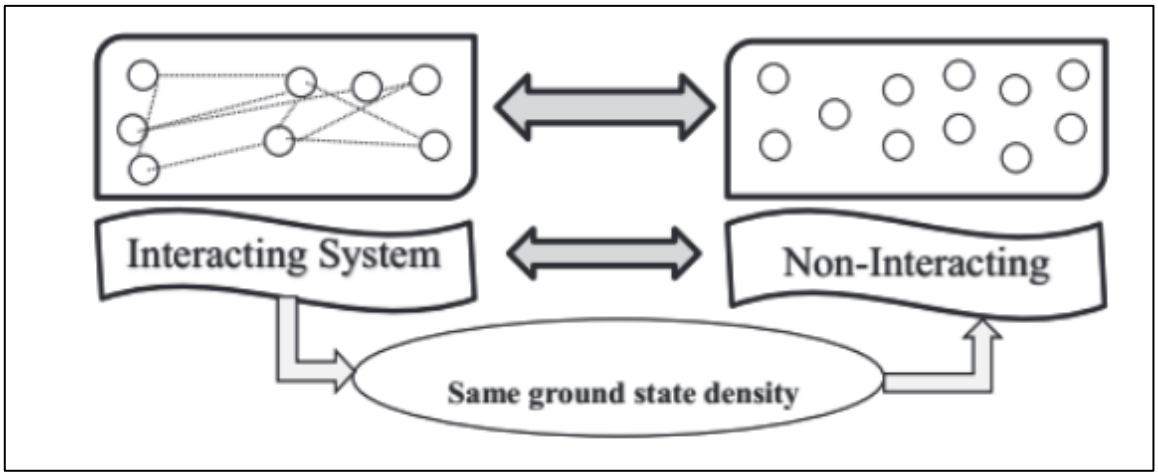


Figure II.2. Graphical illustration of the Kohn–Sham approach [20]

and the spin density,

$$\mathrm{n}_\sigma(r) = \sum_{i=1}^{N_\sigma} |\phi_{i\sigma}(r)|^2 \qquad (\mathbf{II.69})$$

The Kohn-Sham scheme in Density Functional Theory (DFT) is a powerful computational approach that simplifies the study of many-electron systems. It introduces a fictitious system of non-interacting particles that remarkably produces the same ground-state electron density as the actual, interacting system (as shown in Figure II.2**)**. This allows for the calculation of key properties, such as the total energy and electron distribution, by solving a set of equations for these non-interacting particles, although approximations are necessary, particularly in describing the complex interactions between electrons, the Kohn-Sham scheme provides a robust and efficient framework for investigating the electronic structure of a wide range of systems, from atoms and molecules to solids and materials. For instance, Imagine you have a bustling crowd of people, all interacting and moving around. Understanding their collective behavior can be incredibly complex. The Kohn-Sham method in Density Functional Theory is like creating a simplified model of this crowd. Instead of directly tracking every individual's movement and interaction, we imagine a more orderly scenario where everyone moves independently, but the overall distribution of people in space remains the same as in the real, chaotic crowd. This simplified model, while not perfectly realistic, allows us to make accurate predictions about the overall behavior of the crowd. Similarly, the Kohn-Sham method allows scientists to predict the electronic behavior of complex molecules and materials by simplifying the electrons interactions.

II.3. Exchange-correlation approximations.

The exchange-correlation energy $E_{xc}[n]$ appearing in the total energy functional represents a major challenge. Because its accurate determination relies on approximations, the strict validity of the variational principle is compromised.

This means that minimizing the approximate energy functional does not ensure that the calculated energy will be an upper bound to the true ground state energy. Moreover, the exact ground state charge density may not be the one that minimizes the approximate functional. Despite these

limitations, the variational principle is still applied, and the resulting density is typically accepted as the ground state density [13].

In Kohn-sham equations effective potential all terms are known and exact expect for the exchange-correlation energy which had to be approximated. The quality of a given approximation is determined by how closely it reproduces the exact exchange-correlation energy. In this section, we examine various exchange-correlation approximations in terms of their advantages and limitations.

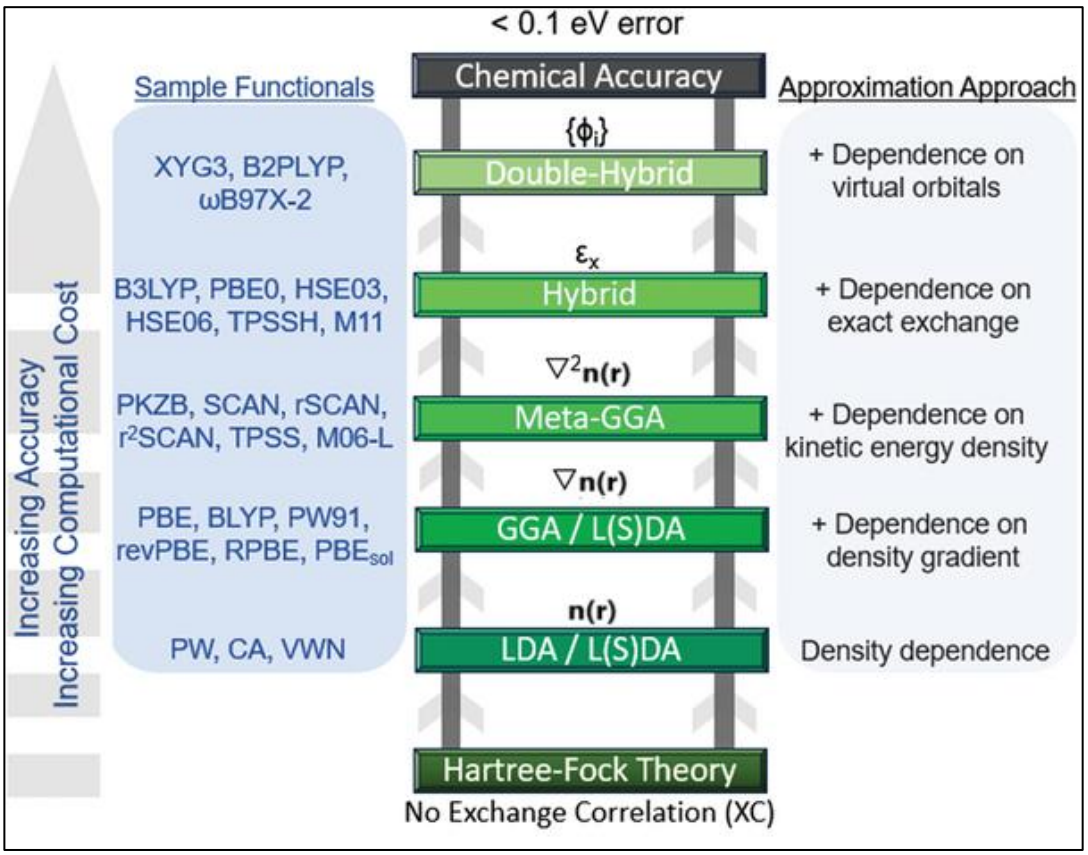


Fig II.3. Schematic representation of Jacob's ladder of DFT [21]

II.3.1. Local density approximation (LDA/LSDA)

The LDA/LSDA [22] is the simplest DFT approximation to exchange-correlation . The fundamental point behind this approach is the assumption that XC energy density at given position

relies solely on the electron density. Therefore, LDA treats the real system as it is made of infinitesimally small regions of uniform electron gas density. Which can be described as dividing

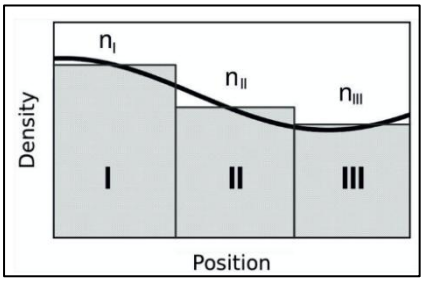


Fig. II.4. Illustration of regions of uniform electron gas density in LDA approach [2]

the system into tiny-connected boxes (regions), each with a constant electron density. And for each box, the XC energy can be estimated employing the known XC energy of a uniformelectron gas with the same density (as demonstrated in Figure II.4**)**. Thus, By summing up the XC energies of all these boxes, we obtain an approximation to the total XC energy of the system [23].

In this approach the exchange-correlation energy is described by the following relation:

$$E_{xc} = \int_V \frac{E_{xc}^{HEG}[n(r)]}{V} dr \qquad (\mathbf{II.70})$$

With $E_{xc}^{HEG}[n(\boldsymbol{r})]$ is homogeneous electron gas exchange-correlation energy functional. with its exchange part is known and given by Dirac exchange-energy functional [2]:

$$E_x^{LDA} = -\frac{3}{4}\left(\frac{3}{\pi}\right)^{\frac{1}{3}} \int_V n^{4/3}(r) d^3r \qquad (\mathbf{II.71})$$

Using equation (II.60) we can get the exchange potential in the LDA framework as :

$$v_x^{LDA}(r) = -\left(\frac{3}{\pi}\right)^{\frac{1}{3}} n^{\frac{1}{3}} \qquad (\mathbf{II.72})$$

The correlation part E_c does not have an exact analytical expression. Instead, it is estimated using various parameterizations, such as the one by Ceperley and Alder [24] based on quantum Monte Carlo simulations, which was later parameterized by Perdew and Zunger [22] as follows [2]:

$$E_c^{LDA} = nV.\begin{cases} -0.048 + 0.03111\, ln\, r_s - 0.0116 r_s + 0.002 r_s\, ln\, r_s\,, & r_s < 1 \\ \dfrac{-0.1423}{1 + 1.0529\sqrt{r_s} + 0.3334 r_s}, & r_s > 1 \end{cases} \quad (\mathbf{II.73})$$

Here, r_s denotes the Wigner–Seitz radius, which measures the average distance between electrons in a system. It is commonly used in DFT for simplicity and is related to the electron density at position r via the following expression:

$$r_s = \left(\frac{3}{4\pi n(r)}\right)^{1/3} \quad (\mathbf{II.74})$$

Note: There are other parameterizations for the correlation energy of a homogeneous electron gas including those of Kohen and Sham [18], Hedin and Lundqvist [25], Perdew and Wang [26], Wigner, Noziére and Pines [27].

The LDA has been extended to deal with spin-polarized systems as the local spin-polarized density approximation (LSDA) [23]:

$$E_{xc}^{\mathrm{LSDA}}[\mathrm{n}_\uparrow(r), n(r)] = \int_V \mathrm{n(r)}\, \mathrm{E}_{xc}^{\mathrm{UEG}}[\mathrm{n}_\uparrow(r), \mathrm{n}_\downarrow(r)]\, d^3r \quad (\mathbf{II.75})$$

However, this approach assumes a spherical average for the exchange-correlation hole, completely neglecting any angular dependence which leads to inaccuracies, especially in systems with degenerate orbitals or complex electron distributions. Moreover, LDA/LSDA fails to capture the long-range behavior of exchange-correlation, particularly in systems with delocalized electron density[23].

Moreover, LDA tends to overbind, as it typically predicts bond lengths that are too short, along with underestimated lattice parameters, band gaps, and spin and orbital moments [28].

II.3.2. Gradient expansion approximation -GEA

The gradient expansion approximation approach gives the density corrected to order $|\boldsymbol{\nabla}|^2$ for a system tha has a slowly varying electron density n(r) as derived by kohn and sham [18]. This approximation was designed to improve upon LDA/LSDA. While LDA assumes a uniform electron density, the gradient expansion approximation (GEA) incorporates terms that depend on the gradient of the electron density, thereby accounting for its non-uniformity in real systems.

$$E_x^{\mathrm{GEA4}}[n] = E_x^{\mathrm{LDA}}[n] + C_x^{(2)} \int_{R^3} \frac{|\boldsymbol{\nabla} n(r)|^2}{n(r)^{4/3}} dr + C_{x,1}^{(4)} \int_{R^3} \frac{|\boldsymbol{\nabla}^2 n(r)|^2}{n(r)^2} dr + C_{x,2}^{(4)} \int_{R^3} \frac{|\boldsymbol{\nabla} n(r)|^2 \boldsymbol{\nabla}^2 n(r)}{n(r)^3} dr \qquad (\mathbf{II.76})$$

Including the gradient of electron density $\boldsymbol{\nabla} n(\boldsymbol{r})$ and the Laplacian $\boldsymbol{\nabla}^2 n(\boldsymbol{r})$. Employing the the screened Yukawa interaction L.J. Sham [29] estimated the second order correction coefficient $C_x^{(2)} \approx -0.001667$. known as the Coulombic second-order coefficient it was later found that the correct $C_x^{(2)} \approx -0.002382$ [19]. P. S. Svendsen and U. von Barth [30] estimated The fourth-order coefficients $C_{x,1}^{(4)} \approx -0.000036$ and $C_{x,2}^{(4)} \approx 0.00009$.

The GEA correlation energy functional $E_c^{\mathrm{GEA4}}[n]$ was obtained by S.MA and A. BRUECKNER [31] expressed as :

$$E_c^{\mathrm{GEA2}}[n] = E_c^{\mathrm{LDA}}[n] + \int_{R^3} C_c^{(2)}\big(r_s(r)\big) \frac{|\boldsymbol{\nabla} n(r)|^2}{n(r)^{4/3}}\, dr \qquad (\mathbf{II.77})$$

With $C_c^{(2)}\big(r_s(r)\big)$ is a second-order coefficient depending on the Wigner-Seitz radius. For higher-density limit ($r_s \to 0$) this coefficient is estimated by MA and BRUECKNER to be about 0.004235. However, this result suffers from an order-of-limits issue—meaning that the way the limits were taken in the derivation (e.g., in treating high-density limits or interaction terms) introduced inaccuracies. Upon correcting for the exchange coefficient $C_x^{(2)}$, the correct second-order coefficient becomes:

$$C_c^{(2)}(r_s \to 0) = C_{xc}^{(2)}(r_s \to 0) - C_x^{(2)} = 0.004950 \quad \textbf{(II. 78)}$$

The exchange-correlation second-order coefficient $C_{xc}^{(2)}$ had been parametrized by Rasolt and Geldart in reference [32] :

$$C_{xc}(r_s) = 10^{-3}\frac{2.568 + ar_s + br_s^2}{1 + cr_s + dr_s^2 + 10br_s^3} \quad \textbf{(II. 79)}$$

With $a = 23.266$, $b = 7.389.10^{-3}$, $c = 8.723$, and $d = 0.472$.

The gradient expansion approximation (GEA) was intended to improve upon LDA/LSDA for slowly varying electron densities. In practice, however, this approach turned out to be less accurate than LDA itself. Moreover, GEA can sometimes violate known physical constraints, such as the negativity of the exchange-correlation hole or the sum rule for the exchange-correlation hole. These violations can lead to unphysical results. The GEA, especially at elevated orders, contravenes essential physical principles such as positivity and charge neutrality. For example, expansions to O(∇^2) significantly contravene the principle of charge neutrality, which is essential for precisely characterizing electron correlations in atoms [33] . Notwithstanding these limitations, GEA remains an invaluable tool in computational chemistry, particularly when used in conjunction with other techniques or adaptations. The advancement of the (GGAs) such as PBE has mitigated certain deficiencies of GEA by integrating supplementary constraints and refining parameters for enhanced performance across many properties [34] . These developments underscore the persistent efforts to enhance and elevate the fundamental principles of GEA, guaranteeing its sustained significance in the discipline.

II.3.3. Generalized Gradient Functionals -GGA

Generalized gradient approximation (GGA) was developed due the failure of GEA starting in the 1980s GGAs were constructed as improvement over LDA/ LSDA The improvement is based on the density distribution by adding the gradient term $|\nabla n(r)|$, which allows us to represent the heterogeneity of the electronic density. Thus, the exchange-correlation functional $E_{xc}[n(r)]$ is written as [35]:

$$E_{xc}^{\mathrm{GGA}}[n(r)] = \int f(n(r), |\nabla n(r)|).d^3r \qquad (\mathbf{II.80})$$

The use of GGAs have improved the accuracy of calculations compared to LDA [2] In the following we discuss some of the well-known Generalized Gradient (GGA) functionals. GGAs have been widely utilized in solid-state applications and have demonstrated the capacity to rectify certain deficiencies of LDA. The issues encompass the calculation of bond lengths, molecular binding energies, and lattice constants in crystalline structures. GGAs have also proven capable of addressing these deficiencies. Nonetheless, there are instances where GGA excessively compensates for the LDA outcomes in ionic crystals. This transpires when the lattice constants derived from LDA simulations closely align with the empirical evidence present. Despite the several GGA functionals developed thus far, there is no consensus on which formulation is the most accurate, and the selection is depends upon the specific case under examination [36].

II.3.3.1. Becke88 (B88) Exchange potential

Axel Becke [37] proposed this exchange functional, a big step to GGA. It was a gradient correction to the LDA exchange, carefully designed to reproduce the exact exchange energy of atoms. And thus, it formed a basis for many subsequent functionals. The B88 exchange energy functional is written as:

$$E_x = E_x^{LDA} - \beta \sum_{\sigma} \int n_{\sigma}^{4/3} \frac{x_{\sigma}^2}{(1 + 6\beta x_{\sigma} \sinh^{-1} x_{\sigma})} d^3 r \qquad (\mathbf{II.81})$$

With $x_{\sigma} = \frac{|\nabla n_{\sigma}|}{n_{\sigma}^{4/3}}$. $\beta = 0.0042$ is constant which was determined by least squares fit to exact Hartree-Fock exchange of rare gases atoms.

The B88 potential generates the exact asymptotic behavior of the exchange energy density given by [19]:

$$\mathrm{E}_x[n(r)] \sim_{|r|\to+\infty} -\frac{1}{2|r|} \qquad (\mathbf{II.82})$$

This can be proved using Taylor series the expansion of B88.Howerver, this potential does not fulfill the $(-1/r)$ asymptotic conduct. There are alternative ways to estimate β, based on theoretical considerations on is the Large atomic number Asymptotic Expansion involving the consideration the asymptotic behavior of the exchange energy for atoms with a very large nuclear charge (Z) which was done by P.Elliott and K.Burke [38] this led to a very close value of β to at deduced by Beck . For spin-polarized systems the B88 is given by the following expression [19]:

$$E_x^{B88}(\mathrm{n}_\uparrow, \mathrm{n}_\downarrow, \boldsymbol{\nabla}\mathrm{n}_\uparrow, \boldsymbol{\nabla}\mathrm{n}_\downarrow) = E_x^{LDA}(\mathrm{n}_\uparrow, \mathrm{n}_\downarrow) - \sum_\sigma \int n_\sigma^{4/3} \frac{x_\sigma^2}{(1 + 6\beta x_\sigma \sinh^{-1} x_\sigma)} d\,r \qquad (\mathbf{II.83})$$

II.3.3.2 Lee-Yang-Parr (LYP) Correlation functional

In their paper, Lee, Yang, and Parr [39] introduces advancements to the Colle-Salvetti [40] formula for correlation energy by reformulation its correlation-energy expression into a density-functional theory (DFT) framework the original Colle-Salvetti by :

$$E_c = -a \int \frac{n(r)^{4/3}}{1 + bn(r)} \exp\left[-cn(r)^{1/3}\right] dr \qquad (\mathbf{II.84})$$

a, b, and c are empirical constants derived from fitting the formula to helium atom data with a=0.04918, b=0.132 and c=0.2533.

To enhance this formula Lee, Yang, and Parr introduced local kinetic-energy densities resulting a modified formula incorporates the Hartree-Fock kinetic $T_{HF}(r)$ energy density and the Thomas-Fermi kinetic energy density $T_{HF}(r)$ [39]:

$$E_c = -a \int \frac{n(r)^{4/3}}{1 + bn(r)} [t_{\mathrm{HF}}(r) - 2t_{\mathrm{TF}}(r)] \exp\left[-cn(r)^{1/3}\right] dr \qquad (\mathbf{II.85})$$

a, b, and c are empirical constants derived from fitting the formula to helium atom data with a=0.04918, b=0.132 and c=0.2533. With Hartree-Fock Kinetic-Energy Density:

$$t_{\mathrm{HF}}(r) = -\frac{1}{2}\sum_i \psi_i^*(r)\boldsymbol{\nabla}^2\psi_i(r) \qquad (\mathbf{II.86})$$

Thomas-Fermi Kinetic-Energy Density:

$$t_{\mathrm{TF}}(r) = C_F n(r)^{5/3}, \quad C_F = \frac{3}{10}(3\pi^2)^{2/3} \qquad (\mathbf{II.87})$$

For open-shell systems, the correlation energy formula is extended to account for spin-dependent densities $n_\uparrow$ and $n_\downarrow$ [39]:

$$E_c = -a \int \frac{n(r)^{4/3}\left[n_\uparrow t_{\mathrm{HF},\uparrow} + n_\downarrow t_{\mathrm{HF},\downarrow}\right]}{1 + bn(r)} \exp\left[-cn(r)^{1/3}\right] dr \qquad (\mathbf{II.88})$$

$t_{\mathrm{HF},\uparrow}$ and $t_{\mathrm{HF},\downarrow}$ are Hartree-Fock Kinetic-Energy spin-dependent densities.

this reformulated expression enables efficient and accurate calculation of correlation energy relying solely on the electron density n(r) making it computationally practical while maintaining high accuracy. This formulation serves as the foundation for later developments in density-functional approximations, such as the BLYP functional .

II.3.3.3. PW91 Exchange-Correlation Functional

The Perdew–Wang 91 (PW91) [41] exchange-correlation functional aimed to fulfill exact constraints and was a significant step in GGA development, this functional is based on the LDA /LSDA . this functional is written as :

$$E_{XC}^{PW91}[n] = \int \varepsilon_{XC}^{PW91}\big(n(r), \boldsymbol{\nabla} n(r)\big) n(r) dr \qquad (\mathbf{II.89})$$

With $\varepsilon_{XC}^{PW91} = \varepsilon_x^{PW91} + \varepsilon_C^{PW91}$ is the exchange-correlation energy per electron.

The PW91 exchange energy density $\varepsilon_x\big(n(r)\big)$ is expressed as follows :

$$\varepsilon_x^{PW91}(n, s) = \varepsilon_X^{LDA}(n) F_X(s) \qquad (\mathbf{II.90})$$

With s is the Reduced Gradient, This dimensionless quantity simplifies the expressions:

$$s = \frac{|\boldsymbol{\nabla} n|}{2(3\pi^2 n)^{1/3} n} \qquad (\mathbf{II.91})$$

And $F_X(s)$ the PW91 exchange enhancement factor to account for gradient corrections is expressed as :

$$F_x^{PW91}(s) = \frac{1 + 0.19645s\,\sinh^{-1}(7.7956s) + [0.2743 - 0.1508\exp(-100s^2)]s^2}{1 + 0.19645s\,\sinh^{-1}(7.7956s) + 0.004s^4} \qquad (\mathbf{II.92})$$

For spin-dependent systems the PW91 exchange energy density is:

$$e_x^{PW91}(n_\uparrow, n_\downarrow, \boldsymbol{\nabla} n_\uparrow, \boldsymbol{\nabla} n_\downarrow) = \frac{e_x^{PW91}(2n_\uparrow, 2\boldsymbol{\nabla} n_\uparrow) + e_x^{PW91}(2n_\downarrow, 2\boldsymbol{\nabla} n_\downarrow)}{2} \qquad (\mathbf{II.93})$$

The PW91 correlation energy density $\varepsilon_c\big(n(r)\big)$ is given as [19] :

$$\varepsilon_c^{PW91} = \varepsilon_c^{LDA}(r_s, \zeta) + H(r_s, \zeta, t) \qquad (\mathbf{II.94})$$

Where t is reduced density gradient as adapted to correlation $H(r_s, \zeta, t)$ is the gradient correction expressed as : $H(r_s, \zeta, t) = e^2 \frac{\beta^{PW} t^2}{1+\beta^{PW} t^2/(1-\zeta^2)} D(r_s, \zeta)$ .With $\beta^{PW} = 0.066725$ is a constant, and $D(r_s, \zeta)$ is a spin-dependent function that depends on the Wigner-Seitz radius and the spin polarization ζ.

II.3.3.4. PBE-GGA Exchange-Correlation Functional

PBE [42] exchange-correlation functional is a modification over PW91 approximation. It is expressed as :

$$E_{\mathrm{xc}}^{\mathrm{PBE}}[\mathrm{n(r)}] = \int \mathrm{n}(r)\ \varepsilon_{\mathrm{xc}}^{\mathrm{PBE}}\big(\mathrm{n}(r), \boldsymbol{\nabla}\mathrm{n}(r)\big)\, dr \qquad (\mathbf{II.95})$$

With $\varepsilon_{XC}^{PBE} = \varepsilon_x^{PBE} + \varepsilon_C^{PBE}$ is the PBE exchange-correlation energy per electron.

The spin-independent PBE exchange energy density (exchange energy per electron) is expressed as [19]:

$$\varepsilon_{\mathrm{x}}^{\mathrm{PBE}}(\mathrm{n}, \boldsymbol{\nabla}\mathrm{n}) = \varepsilon_{\mathrm{x}}^{\mathrm{LDA}}(\mathrm{n})\, F_{\mathrm{x}}^{\mathrm{PBE}}(s) \qquad (\mathbf{II.96})$$

Where $F_{\mathrm{x}}^{\mathrm{PBE}}(s)$ the enhancement factor is [43]:

$$F_{\mathrm{x}}^{\mathrm{PBE}}(s) = F_{\mathrm{x}}^{\mathrm{PBE}}(s) = 1 + \kappa - \frac{\kappa}{1 + \mu s^2/\kappa} \qquad (\mathbf{II.97})$$

with empirical parameters $\kappa = 0.804$ and $\mu = 0.21951$.

In fact, a similar exchange functional form was suggested in the B86 [44] approximation with parameters (μ = 0.235, .κ = 0.967).

The $F_{\mathrm{x}}^{\mathrm{PBE}}(s)$ enhancement factor is designed to simplify to the Local Density Approximation (LDA) when the parameter ss is zero and to match the gradient expansion form for small values of s. For large values of s, the enhancement factor becomes a constant, which is determined by the parameter κ. Both κ and μ are chosen to meet specific exact conditions. The parameter μ is selected to maintain the good linear response of LDA for a uniform electron gas under weak perturbation, while κ is set according to the Lieb–Oxford bound on the exchange-correlation energy [38].Another reworked version of PBE-GGA exchange is the revPBE which stands for Revised Perdew-Burke-Ernzerhof. It is a modified version of the PBE exchange functional, which is used in density functional theory (DFT) to improve the accuracy of calculations involving electron exchange interactions The local Lieb-Oxford bound is a theoretical limit on the exchange-correlation energy density. revPBE was designed to enforce this bound, ensuring that the calculated exchange-correlation energy does not exceed this limit. The enhancement factor is a function that modifies the exchange energy density. For revPBE, the enhancement factor is given by the equation [45] :

$$F_X^{\mathrm{revPBE}}(s) = 1 + \kappa(1 - \exp(-\mu s^2/\kappa)) \qquad (\mathbf{II.98})$$

with $\kappa = 0.804$ and $\mu = 0.21951$ similar to PBE.

The main advantage of this approximation is that PBE is aa "parameter-free" functional that is structured based in way that it stratifies universal exact physical constraints, this improves its reliability and reduces the need for empirical fitting . Which make it performs well for different applications such as molecular properties and solid-state physics as it provides a good description of short-range exchange–correlation .However, like some other DFT functionals, PBE includes self-interaction errors, which can affect the accuracy of certain calculations. Also,

PBE approximation cannot accurately treat the non-local correlation effects important for long-range interactions, like van der Waals forces [46].

II.3.3.5. The B97-GGA Functional

B97-GGA functional is a fragment of B97-hybrid functional [47].The B97 functional is a type of density functional used in quantum chemistry it is widely used in studying organic molecules, reaction mechanisms, and intermolecular interactions .It is designed to be a semi-local functional, which means it uses information from the local environment of each electron, making it computationally efficient [48] .Its exchange energy is:

$$E_x^{\mathrm{B97}} \int n_\sigma(r)\ \varepsilon_{\mathrm{x}}^{\mathrm{B97}}(n_\uparrow, n_\downarrow, \boldsymbol{\nabla} n_\uparrow, \boldsymbol{\nabla} n_\downarrow)\, dr \qquad (\mathbf{II.99})$$

(The arrows indicate the two spin channels: ↑ **means spin-up electrons, and ↓ means spin-down electrons).**With $\varepsilon_{\mathrm{x}}^{\mathrm{B97}}$ is exchange energy density (exchange energy per electron) of B97:

$$e_x^{\text{B97-GGA}}(n_\uparrow, n_\downarrow, \boldsymbol{\nabla} n_\uparrow, \boldsymbol{\nabla} n_\downarrow) = \sum_{\sigma\in\{\uparrow,\downarrow\}} e_{x,\sigma}^{\mathrm{UEG}}(n_\sigma) g_x(x_\sigma) \qquad (\mathbf{II.100})$$

$e_{x,\sigma}^{\mathrm{UEG}}$ is the spin part of the uniform electron gas exchange density and $g_x(x_\sigma)$ is a gradient correnction function in termes of $x_\sigma = \frac{|\boldsymbol{\nabla} n_\sigma|}{n_\sigma^{4/3}}$

$$g_x(x_\sigma) = \sum_{i=0}^{m} c_{x,i} u_x(x_\sigma)^i \qquad (\mathbf{II.101})$$

With:

$$u_x(x_\sigma) = \frac{\gamma_x x_\sigma^2}{1+\gamma_x x_\sigma^2} \qquad (\mathbf{II.102})$$

With γ_x is a fitting parameter determined empirically to improve the functional's performance.

The B97 correlation energy density is [19]:

$$e_c^{\text{B97-GGA}}(n_\uparrow, n_\downarrow, \boldsymbol{\nabla} n_\uparrow, \boldsymbol{\nabla} n_\downarrow) = e_{c,\uparrow\downarrow}^{\text{B97-GGA}}(n_\uparrow, n_\downarrow, \boldsymbol{\nabla} n_\uparrow, \boldsymbol{\nabla} n_\downarrow) + \sum_{\sigma\in\{\uparrow,\downarrow\}} e_{c,\sigma\sigma}^{\text{B97-GGA}}(n_\sigma, \boldsymbol{\nabla} n_\sigma) \qquad (\mathbf{II.103})$$

With:

$$e_{c,\uparrow\downarrow}^{\text{B97-GGA}}(n_\uparrow, n_\downarrow, \boldsymbol{\nabla} n_\uparrow, \boldsymbol{\nabla} n_\downarrow) = e_{c,\uparrow\downarrow}^{\text{UEG}}(\rho_\uparrow, \rho_\downarrow) g_{c,\uparrow\downarrow}(x_{\uparrow\downarrow}) \qquad (\mathbf{II.104})$$

And:

$$e_{c,\sigma\sigma}^{\text{B97-GGA}}(n_\sigma, \boldsymbol{\nabla} n_\sigma) = e_{c,\sigma\sigma}^{\text{UEG}}(n_\sigma) g_{c,\sigma\sigma}(x_\sigma) \qquad (\mathbf{II.105})$$

Where $e_{c,\uparrow\downarrow}^{\text{UEG}}(n_\uparrow, n_\downarrow) = e_c^{\text{UEG}}(n_\uparrow, n_\downarrow) - e_c^{\text{UEG}}(n_\uparrow, 0) - e_c^{\text{UEG}}(n_\downarrow, 0)$ and $e_{c,\sigma\sigma}^{\text{UEG}}(n_\sigma) = e_c^{\text{UEG}}(n_\sigma, 0)$ are the estimated of the opposite- and same-spin contributions to the uniform electron gas correlation energy density [49,50] and $x_{\uparrow\downarrow} = \sqrt{\frac{x_\uparrow^2 + x_\downarrow^2}{2}}$.

$$g_{c,\uparrow\downarrow}(x_{\uparrow\downarrow}) = \sum_{i=0}^{m} c_{c,i}^{\uparrow\downarrow} u_c^{\uparrow\downarrow}(x_{\uparrow\downarrow})^i \qquad (\mathbf{II.106})$$

With $u_c^{\uparrow\downarrow}(x_{\uparrow\downarrow}) = \frac{\gamma_c^{\uparrow\downarrow} x_{\uparrow\downarrow}^2}{1+\gamma_c^{\uparrow\downarrow} x_{\uparrow\downarrow}^2}$. Here $\gamma_c^{\uparrow\downarrow} = 0.006$.

The B97 approach can accurately predict non-bonded interactions which essential for molecular geometries and interactions in complex systems. Also, it provides fairly accurate results regarding thermochemical properties making it adequate for a wide a range chemistry applications [51].Whereas, one of the notable limitation of this approximation requires empirical dispersion corrections to improve accuracy for certain systems, which can complicate its application [52]. Additionally, like many GGA-type functionals, B97-GGA suffers from self-interaction errors, which can affect the accuracy of calculations involving strongly correlated electron systems [53].

While the functional B97-GGA balances between accuracy and computational cost, attention must be given to the limitations of this functional. The fact that one must add empirical corrections and possible self-interaction errors may be a concern in the selection of the functional for certain applications.

II.3.3.6. WC-GGA Exchange-Correlation Functional

The Wu-Cohen [54] GGA (WC-GGA) is a variant of Generalized Gradient Approximation that was developed to improve accuracy in the calculation of exchange correlation energy within DFT. In more detail, WC-GGA has been widely applied in studying the electronic, magnetic, and structural properties of a broad range of materials, offering a favorable balance between efficiency and accuracy particularly for the structural properties of solids. Comparisons with other GGA functionals and hybrid functionals are frequently made to assess its performance across various contexts.The key features of the WCGGA will be discussed: the mathematical formulation, applications, and performances. This approach is based on the Perdew-Burke-Ernzerhof (PBE) GGA but includes adjustments to improve the description of certain properties [55]. The WC-GGA exchange part is [54] :

$$\epsilon_x^{\text{WC-GGA}}(n,x) = \epsilon_x^{\text{LDA}}(n) F_s^{WC}(x) \qquad (\mathbf{II.107})$$

With $F_s^{WC}(x)$ is the enhancement factor, which is the defining characteristic of WC-GGA's exchange part and given by:

$$F_s^{WC}(x) = 1 + \kappa - \frac{\kappa}{1 + \frac{x}{\kappa}} \qquad (\mathbf{II.108})$$

With $\kappa = 0.804$ was taken to satisfy the Lieb-Oxford bound and Wu and Cohen took $\mu = 0.21951$ to include the LSDA/LDA linear response and they posed the following ansatz for x:

$$x^{WC} = \left(\frac{10}{81}\right) s^2 + \left[\mu - \frac{10}{81}\right] s^2 \exp(-s^2) + \ln(1 + cs^4) \qquad (\mathbf{II.109})$$

With $c = 0.0079325$ is a parameter .For WC-GGA, the correlation energy is often taken as like that in PBE.

The main advantage of WC-GGA is that it is practically exceptionally good in the estimation of lattice constants of solids. It presents better results than most GGA-based functionals and hence is preferred in studies whose focus is on the properties of solids. Moreover, A combination of WC-GGA with other functionals like RPBE allows for a balanced approach which can handle molecular

and solid-state systems quite nicely [56].In the other hand, WC-GGA has certain limitations including the underestimation of band gaps which make not suitable for optoelectronic applications [57]. Although the WC-GGA is a sophisticated GGA functional presents incredibly reliable performance regarding structural properties, electronic, optical, and magnetic ones depend strongly on the material system. Hence, there are some problems concerning the underestimation of the gap of bands. On that account, WC-GGA is used in conjunction with other approximations to obtain a good prediction of materials properties.

II.3.3.7. The PBEsol Functional

The PBEsol (PBE for solids) [58] approximation is alternate to PBE which used in density functional theory (DFT) calculations. In their paper P. Perdew et al proposed a revised version of the PBE functional tailored for surfaces and solids. This approximation modifies some parameters in PBE to better with the gradient expansion for slowly varying densities. The PBEsol exchange energy is given by the following [58]:

$$E_x^{PBEsol}[n] = \int d^3\, r\, \epsilon_x^{\text{unif}}\big(n(r)\big) F_x^{PBEsol}\big(s(r)\big) \qquad \textbf{(II. 110)}$$

Where s is a dimensionless density gradient $s = \frac{|\nabla n|}{2k_F n}$, $k_F = (3\pi^2 n)^{1/3}$ and $F_x^{PBEsol}\big(s(r)\big)$ is Gradient Expansion for Exchange (the enhancement factor) of the PBEsol approximation expressed as :

$$F_x(s) = 1 + \mu s^2 + \cdots \qquad \text{,as (s} \rightarrow 0\text{)} \qquad \textbf{(II.111)}$$

With the gradient expansion coefficient $\mu = 10/81 \approx 0.1234$ which is specifically tailored for solids and surfaces.

The correlation Energy part of PBEsol is expressed by the following expression [58]:

$$E_c[n] = \int d^3\, r\, n(r)\big[\epsilon_c^{\text{unif}}\big(n(r)\big) + \beta t^2(r) + \cdots\big] \qquad \textbf{(II.112)}$$

Where t is a dimensionless density gradient $t = \frac{|\nabla n|}{2k_{\mathrm{TF}}n}$, $k_{\mathrm{TF}} = \sqrt{\frac{4k_F}{\pi}}$ is called the Thomas-Fermi screening wavevector and $\beta = 0.066725$ is a coefficient for the second-order term in the gradient expansion.

The PBEsol approximation offers enhanced structural predictions by providing better geometric predictions compared to standard PBE approach and hence, more accurate lattice parameters and bond lengths this is crucial for materials properties estimations [59,60]. Another key advantage of this approximation is that PBEsol can be efficiently implemented in hybrid functional such as HSE06 to improve electronic properties calculations ,this combination yields an accurate model for materials with complex electronic properties, such as vanadium dioxide [61].Moreover, this approach works effectively for a so many systems involving rare gas crystals, bulk solids, layered solids making it useful for various applications in solid-state physics and materials science. However, like most other GGAs, PBEsol approximation tends to underestimate the bad gaps of semiconductors, hence affecting the accuracy of optoelectronic properties calculations [62]. The PBEsol functional may not describe many systems with correlation effects involving d and f electrons; for these systems, additional corrections such as the Hubbard-U term must be used in conjunction with PBEsol, i.e., PBEsol+U to obtain the proper electronic structure [63].

While PBEsol makes greater improvements in structure predictions concerning solid-state systems, its limitations to the accuracy of electronic structure prediction, especially concerning materials with strong correlation effects or dynamic instabilities, must be overcame. Normally, Researchers often use PBEsol with other functionals or corrections to overcome such problems and get more complete results.

II.3.3.8. EV-GGA Exchange Functional

The term "EV-GGA" refers to the Engel-Vosko Generalized Gradient Approximation [64], is computational physics and materials science approach aimed at precise analysis of electronic structure. This is particularly pertinent for DFT, where this approach is utilized to enhance the exchange-correlation potential, resulting in superior band structure predictions. EV-GGA is recognized for providing more accurate band gap estimates than other methods, including LDA

and conventional GGAs. It is particularly used in materials science for predicting the electronic properties of compounds. The EV-GGA is particularly employed in materials science for predicting the electronic characteristics of compounds. In the context of the Engel and Vosko (1993) article, the discussion focuses primarily on the exchange-only properties of GGA. The EV-GGA exchange functional is given by the following expression [64]:

$$E_x^{EV(93)}[n_\sigma] = \int \varepsilon_x^{LDA}[n_\sigma] F^{EV(93)}(\xi_\sigma) dr \qquad (\mathbf{II.113})$$

Where $F^{EV(93)}(\xi_\sigma)$ is a GGA enhancement factor that ensures the exchange energy does not diverge for exponentially decaying densities and incorporates nonlocal corrections, Vaosnko and Engel proposed the following form of $F^{EV(93)}(x_\sigma)$:

$$F^{EV(93)}(\xi_\sigma) = \frac{1 + a_1\xi_\sigma + a_2{\xi_\sigma}^2 + a_3{\xi_\sigma}^3}{1 + b_1\xi_\sigma + b_2{\xi_\sigma}^2 + b_3{\xi_\sigma}^3} \qquad (\mathbf{II.114})$$

Where $\xi_\sigma \equiv \left(\frac{|\nabla n_\sigma(r)|}{2k_{F\sigma}(r)n_\sigma(r)}\right)^2$ is reduced spin density gradient . and $k_{F\sigma}(r) = \left(3\pi^2 n_\sigma(r)\right)^{1/3}$ is the Fermi wavevector for spin σ at position r.

EV-GGA focuses uniquely on approximating the exchange energy. For the correlation part EV-GGA is coupled with other GGA correlation functionals such LYP to form the complete exchange-correlation functional (EV-LYP).

***Advantages of EV-GGA:**

- **Improved Band Gap Predictions**: the EV-GGA is known for yielding near experimental band gap values compared to other approximations such as the local density approximation and even the standard GGA. For instance, it estimated a band gap of 2.8 eV in very good agreement with the experimental value of 2.84 eV in the chalcopyrite compound HgGa2S4 and outperforming the LDA and GGA [65].Also, in the studies: Zhenbao Feng et al [66] , Berrezoug et al [67], Bakhtiar et al [68] where EV-GGA performed better than other GAAs like PBE compared to experimental results.

- **Optimized Exchange Potential and Applicability to Complex Systems:** The primary objective of EV-GGA is the variational optimization of the exchange-correlation potential; however, achieving realistic band structure calculations is crucial for aligning theoretical results with experimental data in systems where electronic properties are highly dependent on the specifics of the potential. Effective applications of EV-GGA to complex systems like non centrosymmetric compounds provide dependable insights into electronic structure, serving as a valuable resource in the examination of materials with sophisticated bonding and electronic characteristics[65].

***Drawbacks of EV-GGA**

- **Limited Applicability to Energetic Properties:** EV-GGA works well in band structure for a wide range of materials. However, it may not perform as well for other properties such as total energies or reaction barriers [69].

- **Electron self-interaction:** Since the EV-GGA is a GGA, it inherits the restrictions of this approximation, which includes the fact that the self-interaction is not completely cancelled out during the process [70].

EV-GGA provides notable enhancements in band structure accuracy; however, its limitations primarily stem from energetic properties and computational requirements. The researcher's selection is frequently determined by a trade-off among the aforementioned properties in relation to a specific application.

II.3.4. The modified Becke-Johnson (mBJ) potential

The modified Becke-Johnson (mBJ) or (TB-mBJ) potential [71] is used within DFT to improve the computational results for the electronic structure, mainly for the effective mass of electrons in the conduction band and the optical properties of materials. Because of its balanced profile about computational efficiency versus accuracy, it became exceedingly popular among researchers. With each passing day, the mBJ potential is applied within a wide range of studies covering electronics, magnetism, and optics for different studies of materials. It is an exchange only potential. The

mBJ potential is based on the Becke-Johnson (BJ) [72] exchange potential by introducing modifications that enhance its performance in solid-state calculations.

The Becke-Johnson (BJ) was primarily designed to treat exact exchange potential for atoms by combining the Becke-Roussel (BR)potential with the kinetic energy density $t(r)$ [73] :

$$v_x^{BJ}(r) = v_x^{BR}(r) + \sqrt{\frac{5}{12}}\sqrt{\frac{2t(r)}{n(r)}} \qquad (\mathbf{II.115})$$

This potential works well for atoms and improves band gap predictions compared to LDA and GGAs but underestimates band gaps for solids falling far from experimental accuracy. Thus, Blaha and Tran were motivated to improve this approach via introducing a tunable empirical parameter c that adjusts the weight of the terms in the potential to match experimental band gaps more closely yielding to the mBJ potential [71]:

$$v_x^{mBJ}(r) = c \cdot v_x^{BR}(r) + (3c-2)\sqrt{\frac{5}{12}}\sqrt{\frac{2t(r)}{n(r)}} \qquad (\mathbf{II.116})$$

Trana and Blaha proposed the following expression for parameter c :

$$c = \alpha + \beta\sqrt{\frac{1}{V_{cell}}\int_{cell}\frac{|\boldsymbol{\nabla} n(r)|}{n(r)}\,d^3r} \qquad (\mathbf{II.117})$$

With $\alpha = -0.012$ and $\beta = 1.023\ bohr^{1/2}$ are fitting parameters determined to minimize the mean absolute relative error of band gaps across a test set of solids. V_{cell} is The volume of the unit cell which The integral is normalized by to account for the size of the system.

And the kinetic energy density is given by:

$$t(r) = \frac{1}{2}\sum_{i=1}^{N}|\boldsymbol{\nabla}\varphi_i(r)|^2 \qquad (\mathbf{II.118})$$

$v_x^{BR}(r)$ is the Becke-Roussel (BR) Potential [72] :

$$v_x^{BR}(r) = -\frac{1}{b(r)}\left(1 - e^{-x(r)} - \frac{1}{2}x(r)e^{-x(r)}\right) \quad (\mathbf{II.119})$$

$b(r)$and $x(r)$ are parameters interdependent, requiring iterative or numerical methods to solve.

The modified Becke-Johnson potential improves an earlier exchange potential, which was developed by Becke and Johnson. It was consciously designed to strongly enhance the predictive capability of band gap calculations on solids. The mBJ method revises the traditional exchange potential in a manner that the electronic interactions responsible for band gaps are more accurately represented. Tran and Blaha showed that this mBJ potential yields an exceptionally good accord with experiment for an unprecedentedly wide variety of solids ranging from wide gap insulators via sp-semiconductors to strongly correlated 3d transition-metal oxides. This accuracy is comparable to the far more sophisticated techniques-hybrid functional (like HSE) and G_0W_0/GW methods-which are considerably computationally expansive [74] [71].On the other hand, despite these strengths, the major limit of mBJ is its inability to compute forces which makes it not suitable for geometry optimization. Also, for ferromagnetic metals like Iron, mBJ tend to overestimate magnetic moments, This drawback may be partially overcome by combining mBJ with other approaches for instance, the inclusion of on-site Coulomb U (Hubbard) to improve its predictions. Nevertheless, these challenges do exist, the TB-mBJ potential has proved to be an immensely powerful tool in computational materials science, enabling exciting new insights into the electronic and optical properties of an enormous variety of materials.

Later in 2012 Koller, Tran, and Blaha [75] worked on the improving the modified Becke-Johnson (mBJ) potential by primary tuning the c parameter :

$$c = A + B\bar{g}^e \quad (\mathbf{II.120})$$

With Exponent controlling the dependence of c on $\bar{g} = \frac{1}{V_{\text{cell}}}\int_{\text{cell}} \frac{|\nabla n(r)|}{n(r)}\, d^3r$ The new A and B parameters have been optimized using a larger test set of solid material yielding to different parametrizations for the parameter c [75] as shown in Table II.1 bellow:

Table II.1: TB-mBJ Parameter Variants.

Variant name	A	β (bohr^1/2)	e
P-original (TB-mBJ)	-0.012	1.023	0.5
P-present	0.488	0.500	1.0
P-semiconductor	0.267	0.656	1.0

Koller, Tran and Blaha proposed alternative definitions for g to calculate the parameter c including reduced density gradient Weizsäcker kinetic energy density , Thomas-Fermi kinetic energy density and Local ccc Approaches, however none of this approaches produced significant accuracy improvements [75].

II.3.5. Meta-Generalized-Gradient Approximations

Meta-GGAs are extensions to GGAs through including not only the density n(r) and it gradient but also the Kohn-Sham orbital ($\varphi_i(\boldsymbol{r})$) kinetic energy $\tau(r)$ these functionals have a generalized form expressed as follows [19] :

$$E_{xc}^{MGGA}[n,\tau] = \int_{R^3} e_{xc}^{MGGA}\big(n(r), \boldsymbol{\nabla} n(r), \boldsymbol{\nabla}^2 n(r), \tau(r)\big) dr \qquad (\mathbf{II.121})$$

Where the Kohn-Sham orbital kinetic energy $\tau(r)$ is :

$$\tau(r) = \frac{1}{2}\sum_{i=1}^{N} |\boldsymbol{\nabla}\varphi_i(r)|^2 \qquad (\mathbf{II.122})$$

Meta-GGAs are a type of semi-local approximations that have numerous variants such as SCAN, TPSS and M06-L [76] , these functionals provide highly improved accuracy for both crystalline solids and molecular systems. They even outperform GGAs in many cases due to their ability to incorporate detailed information about the electronic structure—such as orbital kinetic energy proving successful in predicting the structural, magnetic, and electronic properties of materials [77,78]. However this improvement came with a cost that is they are computationally expansive compared to traditional GGAs.

II.3.6. Hybrid Functionals

In 1993, based on the adiabatic connection theory, Becke proposed mixing a fraction of exact exchange E_x^{HF} from the Hartree–Fock model with the GGA exchange-correlation formalism, resulting in a three-parameter functional of the form [19]:

$$E_{xc}^{3H} = aE_x^{HF} + bE_x^{GGA} + (1-a-b)E_x^{LSDA} + cE_c^{GGA} + (1-c)E_c^{LSDA} \qquad (\mathbf{II.123})$$

Where is a, b and c are empirical parameters. Later in 1996 Becke constructed a much simpler single parameter hybrid functional :

$$E_{xc}^{1H} = aE_x^{\text{exact}} + (1-a)E_x^{\text{GGA}} + E_c^{\text{GGA}} \qquad (\mathbf{II.124})$$

Where the parameter a is a fraction of Hartree-Fock exchange that has to be determined and it was fitted empirically to be 0.25 for molecules [43]. The addition of portion of the E_x^{HF} exact exchange turned out to be beneficial for decreasing the self-interaction error also this makes Hybrid functionals a set of the most accurate density functionals in DFT [19,43].in the following We now discuss some of the well-known and most used hybrid functionals:

a) B3LYP:

B3LYP functional [79] is commonly employed, it incorporates both B88 exchange and LYP correlation functional [19] :

$$E_{xc}^{\text{B3LYP}} = aE_x^{\text{HF}} + bE_x^{\text{B88}} + (1-a-b)E_x^{\text{LSDA}} + cE_c^{\text{LYP}} + (1-c)E_c^{\text{LSDA}} \qquad (\mathbf{II.125})$$

Where the parameters a, b and c are 0.20, 0.72, and 0.81 respectively were determined through optimizing on ionization and atomization energies, proton affinities of small molecules and the total atomic energies of the periodic table's first row atoms .

b) PBE0:

Known also as PBE1PBE the PBE0 functional that is constructed incorporating the PBE-GGA functional [19] :

$$E_{xc}^{PBE0} = \frac{1}{4}E_x^{HF} + \frac{3}{4}E_x^{PBE} + E_c^{PBE} \quad (\mathbf{II.126})$$

c) M06 and M06-2X:

M06/M06-2X [80] are both M-GGA hybrids employing the M06-L meta-GGA exchange ($E_x^{\text{M06-L}}$) and correlation ($E_c^{\text{M06-L}}$) functional :

$$E_{xc}^{\text{M06}}[\Phi] = aE_x^{\text{HF}} + (1-a)E_x^{\text{M06-L}} + E_c^{\text{M06-L}} \quad (\mathbf{II.127})$$

With the parameter $a = 0.27$ for M06 and $a = 0.54$ for M06-2X.

d) HSE :

HSE is a commonly employed hybrid functional , it incorporates short range Hartree-Fock functional ($E_x^{SR,HF}$) PBE exchange (E_x^{PBE}) correlation (E_c^{PBE}) functionals and long-range/short range PBE exchange functionals (noted as $E_x^{SR,PBE}$and $E_x^{lR,PBE}$ respectively):

$$E_{xc}^{\text{HSE}} = \frac{1}{4}E_x^{\text{SR,HF}} + \frac{3}{4}E_x^{\text{SR,PBE}} + E_x^{\text{lR,PBE}} + E_c^{\text{PBE}} \quad (\mathbf{II.128})$$

In their paper Furio Corà and others conducted a study that systematically applies hybrids to a range of systems (for instance: main group oxides, perovskites, and transition metal oxides) concluded that the use of Hybrid functionals grants more accurate structural, electronic (such as band gap) and Phonon properties (e.g.: In NiO, B3LYP provides magnetic coupling constants closer to experimental values rather than LDA or HF methods) [81].

II.4. Solving Kohn-Sham equations and SCF calculations

In previous sections we discussed the basic concepts of DFT and the Kohn-sham scheme but yet a question to answer which is : how do we actually solve the Kohn–Sham equations and get the total ground state energy**?** [2]

The first step the expansion of the Kohn-Sham orbitals $\phi_i(\boldsymbol{r})$ in generic basis set functions $\{\varphi_\beta(\boldsymbol{r}); \beta = 1,2,\ldots\ldots,M\}$ as follows:

$$\phi_i(r) = \sum_{\beta=1}^{M} C_{i\beta}\varphi_\beta(r) \qquad (\mathbf{II.129})$$

Where $C_{i\beta}$ are the expansion coefficients, and M is the total number of basis functions.

The second step is to substitute the expanded orbitals in the Kohn-Sham equations then multiply on the left by $\varphi_\alpha^*(r)$ and integrate over (r) as to get:

$$\int \varphi_\alpha^*(r)\hat{h}(r)\sum_{\beta=1}^{M} C_{i\beta}\varphi_\beta(r)\ dr = \varepsilon_i \int \varphi_\alpha^*(r)\sum_{\beta=1}^{M} C_{i\beta}\varphi_\beta(r)\ dr \qquad (\mathbf{II.130})$$

With $\hat{h}(r) = \left(-\frac{1}{2}\boldsymbol{\nabla}^2 + \hat{V}_{ext}(\mathrm{r}) + \hat{V}_H(\mathrm{r}) + \hat{V}_{\mathrm{xc},\sigma}(\boldsymbol{r})\right)$ is Kohn-Sham Hamiltonian matrix.

Now we define the elements of the Kohn-Sham Hamiltonian matrix as:

$$h_{\alpha\beta} = \langle\varphi_\alpha|\hat{h}|\varphi_\beta\rangle = \int \varphi_\alpha^*(r)\hat{h}(r)\varphi_\beta(r)\ dr \qquad (\mathbf{II.131})$$

Also, we define the elements of the overlap matrix as follows:

$$S_{\alpha\beta} = \langle\varphi_\alpha|\varphi_\beta\rangle = \int \varphi_\alpha^*(r)\varphi_\beta(r)\ dr \qquad (\mathbf{II.132})$$

Substituting equation (II.131) and (II.132) in equation (II.133) we get the following :

$$\sum_{\beta=1}^{M} h_{\alpha\beta}C_{i\beta} = \varepsilon_i \sum_{\beta=1}^{M} S_{\alpha\beta}C_{i\beta} \qquad (\mathbf{II.133})$$

With $\sum_{\beta=1}^{M} h_{\alpha\beta}$ is the Kohn-Sham Hamiltonian matrix $\boldsymbol{h}$ and $\sum_{\beta=1}^{M} S_{\alpha\beta}C_{i\beta}$ is the overlap matrix $\boldsymbol{S}$ .Also we define are the expansion coefficients matrix $\boldsymbol{C}$**.** The equation (II. 133) becomes the eigenvalue problem :

$$\boldsymbol{hC} = \varepsilon_i \boldsymbol{SC} \qquad (\mathbf{II.134})$$

To simplify the calculations, we solve the II(I. 134) for the symmetry points in the first Brillouin zone. This resolution is done, in an iterative manner using a self-consistent iteration cycle

schematized by the flowchart in figure (II.5). We start by injecting an initial charge density n_{in} to diagonalize the eigenvalue problem **:**

$$(\boldsymbol{h} - \varepsilon_i \boldsymbol{S})\boldsymbol{C_i} = 0 \qquad \textbf{(II. 135)}$$

Then the new charge density n_{out} is constructed with the eigenvectors of this secular equation using the total charge density which can be obtained by a summation over Kohn-Sham orbitals (eq. I.60).If the ne density is not the same as the initial one (the calculations are not converged) the same process is repeated iteratively till the Then the new charge density n_{out} is the same as the old one injected before it and so one until the convergence happen. The initial density is predicted thorough the summing the densities of completely isolated atoms consisting the system but positioned in the same positions as in the studied material [2].

In case of no convergence the old density $n_{in}^{(i)}$ and the new are mixed $n_{out}^{(i)}$ as follows:

$$n_{in}^{(i+1)} = (1 - \alpha)n_{in}^{(i)} + \alpha n_{out}^{(i)} \qquad \textbf{(II. 136)}$$

i represents the ith iteration and α a mixing parameter. the iterative procedure can be continued until convergence is achieved (see Figure II.5.)

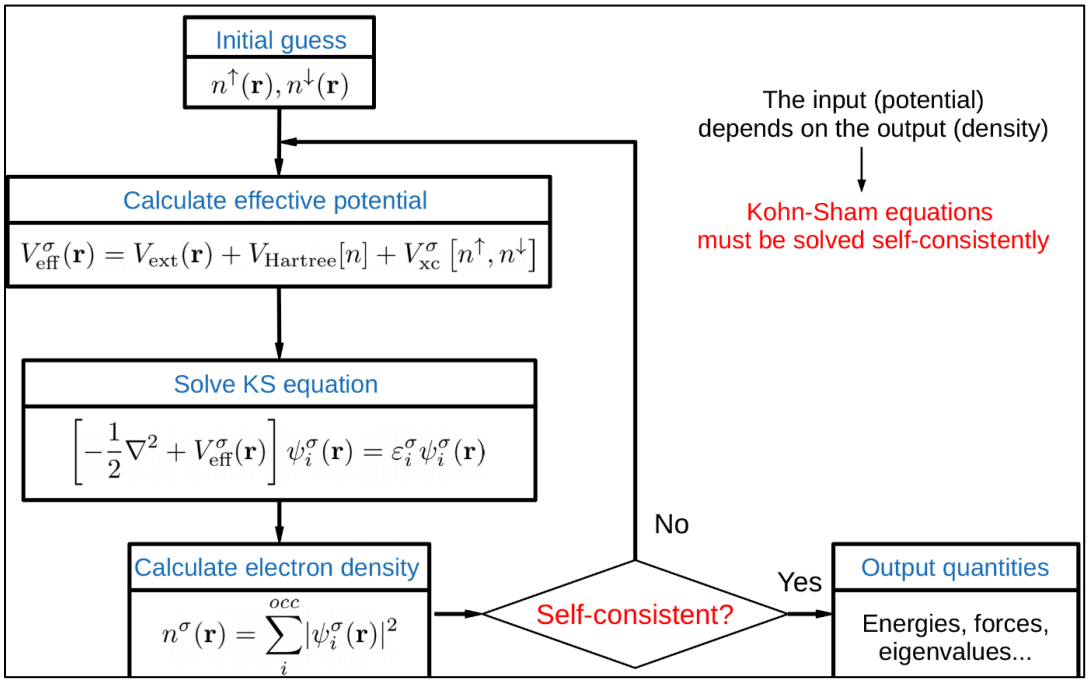


Figure. II.5. Flow schematic chart of the SCF cycle [82].

References

[1] D.S. Sholl, J.A. Steckel, Density Functional Theory: A Practical Introduction, 1st ed., Wiley, 2009. https://doi.org/10.1002/9780470447710.

[2] F. Giustino, Materials modelling using density functional theory: properties and predictions, 1st ed, Oxford University Press, Oxford, 2014.

[3] E. Schrödinger, Quantisierung als Eigenwertproblem, Ann. Phys. 384 (1926) 361–376. https://doi.org/10.1002/andp.19263840404.

[4] S. Cottenier, . "Density Functional Theory and the family of (L) APW-methods: a step-by-step introduction." Instituut voor Kern-en Stralingsfysica, KU Leuven, Belgium 4, no. 0 (2002): 41.

[5] E. Engel, R.M. Dreizler, Density Functional Theory: An Advanced Course, Springer Berlin Heidelberg, Berlin, Heidelberg, 2011. https://doi.org/10.1007/978-3-642-14090-7.

[6] Y.B. Band, Y. Avishai, 10 - Electronic Structure of Multielectron Systems, in: Y.B. Band, Y. Avishai (Eds.), Quantum Mech. Appl. Nanotechnol. Inf. Sci., Academic Press, Amsterdam, 2013: pp. 545–578. https://doi.org/10.1016/B978-0-444-53786-7.00010-1.

[7] P.K. Misra, Chapter 7 - Electron–Electron Interaction, in: P.K. Misra (Ed.), Phys. Condens. Matter, Academic Press, Boston, 2012: pp. 199–242. https://doi.org/10.1016/B978-0-12-384954-0.00007-4.

[8] H. Eschrig, The Fundamentals of Density Functional Theoryy. Vol. 32. Stuttgart: Teubner, 1996.

[9] S. Gulania, J.D. Whitfield, Limitations of Hartree–Fock with quantum resources, J. Chem. Phys. 154 (2021) 044112. https://doi.org/10.1063/5.0018415.

[10] A.F. Silva, L.J. Duarte, P.L.A. Popelier, Contributions of IQA electron correlation in understanding the chemical bond and non-covalent interactions, Struct. Chem. 31 (2020) 507–519. https://doi.org/10.1007/s11224-020-01495-y.

[11] W. Koch, M.C. Holthausen, A Chemist's Guide to Density Functional Theory, 1st ed., Wiley, 2001. https://doi.org/10.1002/3527600043.

[12] Esposito S. The Physics of Ettore Majorana: Theoretical, Mathematical, and Phenomenological. Cambridge University Press; 2014.

[13] J.M. Wills, O. Eriksson, P. Andersson, A. Delin, O. Grechnyev, M. Alouani, Full-Potential Electronic Structure Method: Energy and Force Calculations with Density Functional and Dynamical Mean Field Theory, Springer Berlin Heidelberg, Berlin, Heidelberg, 2010. https://doi.org/10.1007/978-3-642-15144-6.

[14] S. Esposito, ed., Thomas–Fermi model, in: Phys. Ettore Majorana Theor. Math. Phenomenol., Cambridge University Press, Cambridge, 2014: pp. 83–106. https://doi.org/10.1017/CBO9781107358362.004.

[15] V. Sahni, Quantal Density Functional Theory II: Approximation Methods and Applications, Springer Berlin Heidelberg, Berlin, Heidelberg, 2009. https://doi.org/10.1007/978-3-540-92229-2.

[16] P. Hohenberg, W. Kohn, Inhomogeneous Electron Gas, Phys. Rev. 136 (1964) B864–B871. https://doi.org/10.1103/PhysRev.136.B864.

[17] R.G. Parr, W. Yang, Density-functional theory of atoms and molecules, Oxford University Press, New York, 2020. https://doi.org/10.1093/oso/9780195092769.001.0001.

[18] W. Kohn, L.J. Sham, Self-Consistent Equations Including Exchange and Correlation Effects, Phys. Rev. 140 (1965) A1133–A1138. https://doi.org/10.1103/PhysRev.140.A1133.

[19] E. Cancès, G. Friesecke, eds., Density Functional Theory: Modeling, Mathematical Analysis, Computational Methods, and Applications, Springer International Publishing, Cham, 2023. https://doi.org/10.1007/978-3-031-22340-2.

[20] M. Aamir Iqbal, N. Ashraf, W. Shahid, D. Afzal, F. Idrees, R. Ahmad, Fundamentals of Density Functional Theory: Recent Developments, Challenges and Future Horizons, in: D. Glossman-Mitnik

(Ed.), Density Funct. Theory - Recent Adv. New Perspect. Appl., IntechOpen, 2022. https://doi.org/10.5772/intechopen.99019.
[21] Schematic representation of Jacob's ladder of DFT with the different rungs, ResearchGate , accessed January 1, 2025. Available at: https://www.researchgate.net/figure/Schematic-representation-of-Jacobs-ladder-of-DFT-with-the-different-functional_fig8_376448828
[22] J.P. Perdew, A. Zunger, Self-interaction correction to density-functional approximations for many-electron systems, Phys. Rev. B 23 (1981) 5048–5079. https://doi.org/10.1103/PhysRevB.23.5048.
[23] J.G. Lee, Computational materials science: an introduction, Second edition, CRC Press, Taylor & Francis Group, CRC Press is an imprint or the Taylor & Francis Group, an informa business, Boca Raton, 2017.
[24] D.M. Ceperley, B.J. Alder, Ground State of the Electron Gas by a Stochastic Method, Phys. Rev. Lett. 45 (1980) 566–569. https://doi.org/10.1103/PhysRevLett.45.566.
[25] L. Hedin, B.I. Lundqvist, Explicit local exchange-correlation potentials, J. Phys. C Solid State Phys. 4 (1971) 2064. https://doi.org/10.1088/0022-3719/4/14/022.
[26] J.P. Perdew, Y. Wang, Accurate and simple analytic representation of the electron-gas correlation energy, Phys. Rev. B 45 (1992) 13244–13249. https://doi.org/10.1103/PhysRevB.45.13244.
[27] P. Nozières, D. Pines, Correlation Energy of a Free Electron Gas, Phys. Rev. 111 (1958) 442–454. https://doi.org/10.1103/PhysRev.111.442.
[28] M. MARQUES, A. Castro, A. Rubio, Assessment of exchange-correlation functionals for the calculation of dynamical properties of small clusters in time-dependent density functional theory, J. Chem. Phys. 115 (2001) 3006–3014. https://doi.org/10.1063/1.1385368.
[29] L.J. Sham, Approximations of the Exchange and Correlation Potentials, in: P.M. Marcus, J.F. Janak, A.R. Williams (Eds.), Comput. Methods Band Theory Proc. Conf. Held IBM Thomas J Watson Res. Cent. Yorktown Heights N. Y. May 14–15 1970 Jt. Spons. IBM Am. Phys. Soc., Springer US, Boston, MA, 1971: pp. 458–468. https://doi.org/10.1007/978-1-4684-1890-3_36.
[30] P.S. Svendsen, U. Von Barth, Gradient expansion of the exchange energy from second-order density response theory, Phys. Rev. B 54 (1996) 17402–17413. https://doi.org/10.1103/PhysRevB.54.17402.
[31] S. Ma, K.A. Brueckner, Correlation Energy of an Electron Gas with a Slowly Varying High Density, Phys. Rev. 165 (1968) 18–31. https://doi.org/10.1103/PhysRev.165.18.
[32] M. Rasolt, D.J.W. Geldart, Exchange and correlation energy in a nonuniform fermion fluid, Phys. Rev. B 34 (1986) 1325–1328. https://doi.org/10.1103/PhysRevB.34.1325.
[33] M. Slamet, V. Sahni, Analysis of the density-gradient-expansion approximation for the exchange-correlation energy of density-functional theory, Int. J. Quantum Chem. 40 (1991) 235–248. https://doi.org/10.1002/qua.560400824.
[34] R. Peverati, Y. Zhao, D.G. Truhlar, Generalized Gradient Approximation That Recovers the Second-Order Density-Gradient Expansion with Optimized Across-the-Board Performance, J. Phys. Chem. Lett. 2 (2011) 1991–1997. https://doi.org/10.1021/jz200616w.
[35] J.P. Perdew, K. Burke, Y. Wang, Generalized gradient approximation for the exchange-correlation hole of a many-electron system, Phys. Rev. B 54 (1996) 16533–16539. https://doi.org/10.1103/PhysRevB.54.16533.
[36] P.G. Jambrina, J. Aldegunde, Chapter 20 - Computational Tools for the Study of Biomolecules, in: M. Martín, M.R. Eden, N.G. Chemmangattuvalappil (Eds.), Comput. Aided Chem. Eng., Elsevier, 2016: pp. 583–648. https://doi.org/10.1016/B978-0-444-63683-6.00020-4.
[37] A.D. Becke, Density-functional exchange-energy approximation with correct asymptotic behavior, Phys. Rev. A 38 (1988) 3098–3100. https://doi.org/10.1103/PhysRevA.38.3098.
[38] P. Elliott, K. Burke, Non-empirical derivation of the parameter in the B88 exchange functional, Can. J. Chem. 87 (2009) 1485–1491. https://doi.org/10.1139/V09-095.

[39] C. Lee, W. Yang, R.G. Parr, Development of the Colle-Salvetti correlation-energy formula into a functional of the electron density, Phys. Rev. B 37 (1988) 785–789. https://doi.org/10.1103/PhysRevB.37.785.
[40] Approximate calculation of the correlation energy for the closed and open shells | Theoretical Chemistry Accounts, (n.d.). https://link-springer-com.sndl1.arn.dz/article/10.1007/BF00547606 (accessed December 25, 2024).
[41] J.P. Perdew, Y. Wang, Accurate and simple analytic representation of the electron-gas correlation energy, Phys. Rev. B 45 (1992) 13244–13249. https://doi.org/10.1103/PhysRevB.45.13244.
[42] J.P. Perdew, K. Burke, M. Ernzerhof, Generalized Gradient Approximation Made Simple, Phys. Rev. Lett. 77 (1996) 3865–3868. https://doi.org/10.1103/PhysRevLett.77.3865.
[43] Perdew, John P., and Stefan Kurth. "Density functionals for non-relativistic Coulomb systems in the new century." In A primer in density functional theory, pp. 1-55. Berlin, Heidelberg: Springer Berlin Heidelberg, 2003.
[44] A.D. Becke, Density functional calculations of molecular bond energies, J. Chem. Phys. 84 (1986) 4524–4529. https://doi.org/10.1063/1.450025.
[45] B. Hammer, L.B. Hansen, J.K. Nørskov, Improved adsorption energetics within density-functional theory using revised Perdew-Burke-Ernzerhof functionals, Phys. Rev. B 59 (1999) 7413–7421. https://doi.org/10.1103/PhysRevB.59.7413.
[46] J.-D. Chai, S.-P. Mao, Seeking for reliable double-hybrid density functionals without fitting parameters: The PBE0-2 functional, Chem. Phys. Lett. 538 (2012) 121–125. https://doi.org/10.1016/j.cplett.2012.04.045.
[47] A.D. Becke, Density-functional thermochemistry. V. Systematic optimization of exchange-correlation functionals, J. Chem. Phys. 107 (1997) 8554–8560. https://doi.org/10.1063/1.475007.
[48] R.M. Martin, Electronic Structure: Basic Theory and Practical Methods, 2nd ed., Cambridge University Press, 2020. https://doi.org/10.1017/9781108555586.
[49] H. Stoll, E. Golka, H. Preuß, Correlation energies in the spin-density functional formalism, Theor. Chim. Acta 55 (1980) 29–41. https://doi.org/10.1007/BF00551408.
[50] H. Stoll, C.M.E. Pavlidou, H. Preuß, On the calculation of correlation energies in the spin-density functional formalism, Theor. Chim. Acta 49 (1978) 143–149. https://doi.org/10.1007/PL00020511.
[51] N. Mardirossian, M. Head-Gordon, Mapping the genome of meta-generalized gradient approximation density functionals: The search for B97M-V, J. Chem. Phys. 142 (2015) 074111. https://doi.org/10.1063/1.4907719.
[52] L.A. Constantin, E. Fabiano, F. Della Sala, Meta-GGA Exchange-Correlation Functional with a Balanced Treatment of Nonlocality, J. Chem. Theory Comput. 9 (2013) 2256–2263. https://doi.org/10.1021/ct400148r.
[53] Jana, Subrata, Szymon Smiga, Lucian A. Constantin, and Prasanjit Samal. "Semilocal meta-GGA exchange–correlation approximation from adiabatic connection formalism: Extent and limitations." The Journal of Physical Chemistry A 127, no. 41 (2023): 8685-8697.
[54] Z. Wu, R.E. Cohen, More accurate generalized gradient approximation for solids, Phys. Rev. B 73 (2006) 235116. https://doi.org/10.1103/PhysRevB.73.235116.
[55] M. Siddique, A.U. Rahman, A. Iqbal, B.U. Haq, S. Azam, A. Nadeem, A. Qayyum, A Systematic First-Principles Investigation of Structural, Electronic, Magnetic, and Thermoelectric Properties of Thorium Monopnictides ThPn (Pn = N, P, As): A Comparative Analysis of Theoretical Predictions of LDA, PBEsol, PBE-GGA, WC-GGA, and LDA + U Methods, Int. J. Thermophys. 40 (2019) 104. https://doi.org/10.1007/s10765-019-2572-7.
[56] P. Haas, F. Tran, P. Blaha, K. Schwarz, Construction of an optimal GGA functional for molecules and solids, Phys. Rev. B 83 (2011) 205117. https://doi.org/10.1103/PhysRevB.83.205117.
[57] G. Kadim, R. Masrour, A. Jabar, A comparative study between GGA, WC-GGA, TB-mBJ and GGA + U approximations on magnetocaloric effect, electronic, optic and magnetic properties of BaMnS2

compound: DFT calculations and Monte Carlo simulations, Phys. Scr. 96 (2021) 045804. https://doi.org/10.1088/1402-4896/abe00d.
[58] J.P. Perdew, A. Ruzsinszky, G.I. Csonka, O.A. Vydrov, G.E. Scuseria, L.A. Constantin, X. Zhou, K. Burke, Generalized gradient approximation for solids and their surfaces, Phys. Rev. Lett. 100 (2008) 136406. https://doi.org/10.1103/PhysRevLett.100.136406.
[59] J. Schmidt, H.-C. Wang, T.F.T. Cerqueira, S. Botti, M.A.L. Marques, A dataset of 175k stable and metastable materials calculated with the PBEsol and SCAN functionals, Sci. Data 9 (2022) 64. https://doi.org/10.1038/s41597-022-01177-w.
[60] G.M. Dongho Nguimdo, D.P. Joubert, A density functional (PBE, PBEsol, HSE06) study of the structural, electronic and optical properties of the ternary compounds AgAlX2 (X = S, Se, Te), Eur. Phys. J. B 88 (2015) 113. https://doi.org/10.1140/epjb/e2015-50478-x.
[61] E. Mohebbi, E. Pavoni, D. Mencarelli, P. Stipa, L. Pierantoni, E. Laudadio, PBEsol/HSE functional: a promising candidate for vanadium dioxide (B) characterization, RSC Adv. 12 (2022) 31255–31263. https://doi.org/10.1039/D2RA04322J.
[62] A.V. Terentjev, L.A. Constantin, J.M. Pitarke, Dispersion-corrected PBEsol exchange-correlation functional, Phys. Rev. B 98 (2018) 214108. https://doi.org/10.1103/PhysRevB.98.214108.
[63] Portugal, Guilherme Ribeiro, and Jeverson Teodoro Arantes. "Polar NaTaO3/LaAlO3 (001) superlattices: A comparison of PBEsol and PBEsol+ U first-principles calculations." Computational Materials Science 233 (2024): 112747.
[64] E. Engel, S.H. Vosko, Exact exchange-only potentials and the virial relation as microscopic criteria for generalized gradient approximations, Phys. Rev. B 47 (1993) 13164–13174. https://doi.org/10.1103/PhysRevB.47.13164.
[65] A.H. Reshak, R. Khenata, I.V. Kityk, K.J. Plucinski, S. Auluck, X-ray photoelectron spectrum and electronic properties of a noncentrosymmetric chalcopyrite compound HgGa(2)S(4): LDA, GGA, and EV-GGA, J. Phys. Chem. B 113 (2009) 5803–5808. https://doi.org/10.1021/jp901142q.
[66] Feng, Zhenbao, Haiquan Hu, Zengtao Lv, and Shouxin Cui. "First-principles study of electronic and optical properties of BaS, BaSe and BaTe." Central European Journal of Physics 8, no. 5 (2010): 782-788.
[67] H.I. Berrezoug, A.E. Merad, A. Zerga, Z.S. Hassoun, Ab-initio calculations of structural, electronic, and dielectric properties of ZnO, in: 2014 North Afr. Workshop Dielectic Mater. Photovolt. Syst. NAWDMPV, IEEE, Tlemcen, 2014: pp. 1–5. https://doi.org/10.1109/NAWDMPV.2014.6997621.
[68] U.H. Bakhtiar, R. Ahmed, R. Khenata, M. Ahmed, R. Hussain, A first-principles comparative study of exchange and correlation potentials for ZnO, Mater. Sci. Semicond. Process. 16 (2013) 1162–1169. https://doi.org/10.1016/j.mssp.2012.11.012.
[69] R. Peverati, D.G. Truhlar, Exchange–Correlation Functional with Good Accuracy for Both Structural and Energetic Properties while Depending Only on the Density and Its Gradient, J. Chem. Theory Comput. 8 (2012) 2310–2319. https://doi.org/10.1021/ct3002656.
[70] P. Mori-Sánchez, A.J. Cohen, W. Yang, Many-electron self-interaction error in approximate density functionals, J. Chem. Phys. 125 (2006) 201102. https://doi.org/10.1063/1.2403848.
[71] F. Tran, P. Blaha, Accurate Band Gaps of Semiconductors and Insulators with a Semilocal Exchange-Correlation Potential, Phys. Rev. Lett. 102 (2009) 226401. https://doi.org/10.1103/PhysRevLett.102.226401.
[72] A.D. Becke, E.R. Johnson, A simple effective potential for exchange, J. Chem. Phys. 124 (2006) 221101. https://doi.org/10.1063/1.2213970.
[73] A.D. Becke, M.R. Roussel, Exchange holes in inhomogeneous systems: A coordinate-space model, Phys. Rev. A 39 (1989) 3761–3767. https://doi.org/10.1103/PhysRevA.39.3761.
[74] D. Koller, F. Tran, P. Blaha, Merits and limits of the modified Becke-Johnson exchange potential, Phys. Rev. B 83 (2011) 195134. https://doi.org/10.1103/PhysRevB.83.195134.

[75] D. Koller, F. Tran, P. Blaha, Improving the modified Becke-Johnson exchange potential, Phys. Rev. B 85 (2012) 155109. https://doi.org/10.1103/PhysRevB.85.155109.
[76] Y. Zhao, D.G. Truhlar, A new local density functional for main-group thermochemistry, transition metal bonding, thermochemical kinetics, and noncovalent interactions, J. Chem. Phys. 125 (2006) 194101. https://doi.org/10.1063/1.2370993.
[77] R. Liu, D. Zheng, X. Liang, X. Ren, M. Chen, W. Li, Implementation of the meta-GGA exchange-correlation functional in numerical atomic orbital basis: With systematic testing on SCAN, rSCAN, and r2SCAN functionals, J. Chem. Phys. 159 (2023) 074109. https://doi.org/10.1063/5.0160726.
[78] Desmarais, Jacques K., Alessandro Erba, Giovanni Vignale, and Stefano Pittalis. "Meta-Generalized Gradient Approximation Made Magnetic." Physical Review Letters 134, no. 10 (2025): 106402.
[79] P.J. Stephens, F.J. Devlin, C.F. Chabalowski, M.J. Frisch, Ab Initio Calculation of Vibrational Absorption and Circular Dichroism Spectra Using Density Functional Force Fields, J. Phys. Chem. 98 (1994) 11623–11627. https://doi.org/10.1021/j100096a001.
[80] Y. Zhao, D.G. Truhlar, The M06 suite of density functionals for main group thermochemistry, thermochemical kinetics, noncovalent interactions, excited states, and transition elements: two new functionals and systematic testing of four M06-class functionals and 12 other functionals, Theor. Chem. Acc. 120 (2008) 215–241. https://doi.org/10.1007/s00214-007-0310-x.
[81] F. Corà, M. Alfredsson, G. Mallia, D.S. Middlemiss, W.C. Mackrodt, R. Dovesi, R. Orlando, The Performance of Hybrid Density Functionals in Solid State Chemistry, in: Princ. Appl. Density Funct. Theory Inorg. Chem. II, Springer Berlin Heidelberg, Berlin, Heidelberg, 2004: pp. 171–232. https://doi.org/10.1007/b97944.
[82] SIESTA Developers, The self-consistent-field cycle, SIESTA Documentation, The SIESTA Project (accessed January 1, 2025). Available at: https://docs.siesta-project.org/projects/siesta/en/stable/tutorials/basic/scf-convergence/index.html

Chapter III

CHAPTER III

Chapter III: Computational methods

The Full Potential Linearized Augmented Plane Wave (FP-LAPW) method is one of the most accurate and widely applied computational techniques in solid-state physics and materials science. The technique is employed to investigate a wide range of physical properties, including electronic structure, magnetic properties, optical properties, and mechanical properties of materials. The method is based on Density Functional Theory (DFT), which offers a conceptual framework for explaining the quantum-mechanical many-body behavior of electrons in different materials. Owing to its high accuracy and flexibility, the Full-Potential Linearized Augmented Plane Wave (FP-LAPW) method has been implemented in a large number of DFT computer programs, of which the WIEN2k package is among the most popular [1] .The FP-LAPW approach developed from the initial Augmented Plane Wave (APW) approach, which was among the initial approaches to solving the Kohn-Sham equations of DFT. APW did, however, have some limitations, particularly regarding its efficiency and convergence properties. It was due to these issues that several improvements were introduced, thereby resulting in the (LAPW) approach, where linearization was employed for the purpose of improving computational efficiency. The Full-Potential LAPW method was developed through additional improvements which eliminated shape approximations of the potential to allow for more reliable calculations of complicated systems. Other additional extensions like APW with local orbitals (APW+lo) and LAPW with local orbitals (LAPW+lo) were developed to enhance the basis set completeness and treatment of semi core and high-energy states. In this chapter, a detailed account of these methodological improvements is given, how they evolved from the analysis by APW to the modern FP-LAPW-based approaches. This study discusses the principles behind every approach, along with their strengths and weaknesses, and the reasons why they have been adapted. Furthermore, we introduce the WIEN2k code, a popular computer program package designed for FP-LAPW calculations.

III.1. Bloch's Theorem and Plane-wave basis set

The Bloch's theorem is applies to the quantum states of a periodic solid to in z lttice periodic potential. It states that the wave-functions of an electron can be expanded to a function that has the same periodicity as the lattice's. So, the eigen functions of a lattice's periodic Hamiltonian can be expanded using plane waves basis set (PW) in the following form [2]:

$$\psi_{n,k}(r) = \frac{1}{\sqrt{V}} e^{ik\cdot r} u_k(r) \qquad \textbf{(III. 1)}$$

Where $u_k(r)$ is a function that has the same periodicity of the lattice, thus $u_k(r+R) = u_k(r)$ for any lattice vector R. k is the crystal momentum associated with the wavefunction.V is the volume of the unit cell which is implemented to satisfy the normalization of the wave-function. Employing Fourier transform theory the periodic function $u_k(\boldsymbol{r})$ can expanded in terms of the reciprocal space vectors G to the following formula:

$$u_k = \sum_G C_{nk}(G) e^{iG\cdot r} \qquad \textbf{(III. 2)}$$

with $C_{nk}(G)$ are the Fourier coefficients, n labels the band index, distinguishing different energy eigenstates for a given k and $e^{iG\cdot r} = 1$ for any lattice vector R. So, the electronic wave-function (eq III. 1**)** can be expressed the as [3] :

$$\psi_{n,k}(r) = \frac{1}{\sqrt{V}} \sum_G C_{nk}(G) e^{i\mathrm{K}\cdot r} \qquad \textbf{(III. 3)}$$

With $K = k + G$ is the total wave vector .The plane wave basis set is depending on the wave vector K, so all eigen states $\psi_{n,k}(r)$ that posses the same n and k will be expanded using the same basis set while for eigen states with another wave vector K a new PW basis set must be used. However, In Computational applications, it is impossible to employ an infinite basis set; therefore some sort of restriction must be enforced . For plane waves, this can be achieved by restricting the set to all K for which K is less than or equal to K_{max}. This corresponds to a sphere of radius K_{max} centered at the origin of reciprocal space. The basis set contains all reciprocal lattice vectors which fall within

this sphere. Instead of referring to K_{max}, it is common to refer to the free electron energy corresponding to K_{max} which is called the cut-off energy E_{cut} (Figure. III.1) [4]:

$$E_{cut} = \frac{\hbar^2}{2m} K_{max}^2 \qquad \textbf{(III. 4)}$$

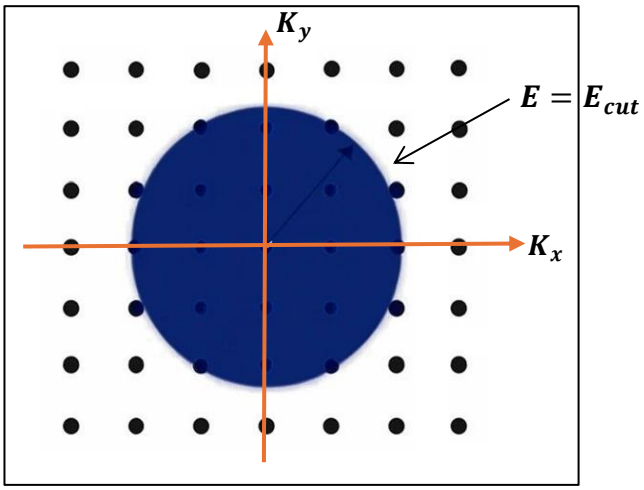


Figure. III.1 .Truncation of the plane wave development in reciprocal space.

III.2. Brillouin Zone Sampling, and k-Points

Those who try to describe a wave function in real (direct) space soon learn that this is a very challenging task. In reciprocal space, the problem is much simpler because it just consists of constructing a mesh, provided we define the unit of the reciprocal lattice to match with that of wave vectors(1/length). The points of this mesh represent the permitted wave vectors. This is the basis of the logic behind the construction of a new structure known as the reciprocal lattice, constructed on the real lattice. Most solids are characterized by a structural periodicity, which is missing in the amorphous or liquid phases .Therefore, if one crystal cell contains two atoms, another will also contain two atoms in the identical pattern. In the computational analysis of materials, we endeavor to minimize the system size for calculations, this methodology is significantly dependent on the periodicity of solids .The general process of this reduction maneuver is outlined in Figure III.2 , which encompasses the following : A solid is initially converted to a supercell composed of many unit cells. The constructed supercell is extended to infinity by the periodic boundary conditions. The supercell is converted into reciprocal space and situated within

the first Brillouin zone .In this context, all electronic wave functions are accurately represented by the wave vector k and the reciprocal lattice vector G, hence allowing all attributes to be successfully described by the Bloch equations. The initial Brillouin zone is then condensed into an irreducible

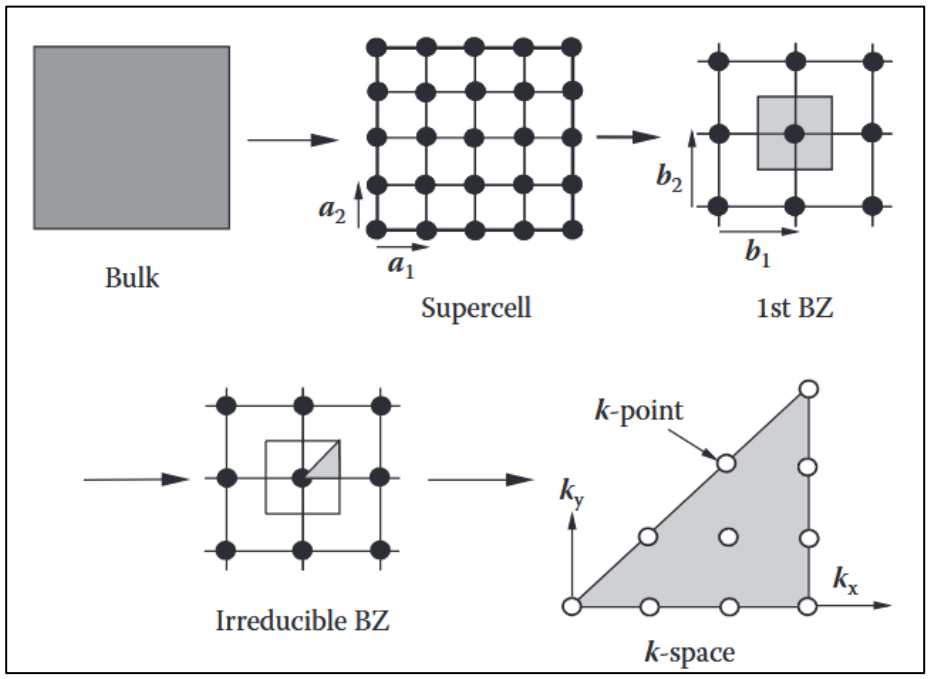


Figure. III.2 Employed approaches for the treatment of periodic solids materials

Brillouin zone (IBZ) using symmetry procedures, preserving all information. The IBZ is mapped using discrete k-points, and all requisite quantities are derived through integration, summation, or extrapolation at these points. Consequently, addressing a solid is analogous to managing a finite number of k-points within a reduced volume of the irreducible Brillouin zone due to the periodicity of solids and their Symmetry operations (for instance: rotation and inversion) [5]. For example, a 10x10x10 mesh in the first BZ of an FCC unit cell is made of 1000 k-points that it is equivalent to 35 characteristic k-points in the IBZ. K-points are utilized to sample the Brillouin Zone for numerical integration, and their effective selection is essential for computational efficiency. Algorithms for producing k-point grids concentrate on minimizing them to symmetrically different points, thereafter mapped onto the Brillouin Zone (BZ). This procedure is refined to reduce the quantity of irreducible k-points, hence improving computational efficiency [6]. The tetrahedron method is an example of an approach that uses a translational grid of k-points and tetrahedra to improve integration accuracy [7]. Also, The Monkhorst–Pack approach (Monkhorst and Pack,

1976) is widely used, this method produces a grid of k-points evenly distributed over the IBZ. It offers an efficient method for integrating periodic functions of the wave vector. The integration may extend over the whole Brillouin zone or over any designated parts of it. The same procedure may be applied to spectral and density-of-states calculations [8]. The majority of DFT packages provide algorithms to generate the k-points automatically once grid information is provided [5]. The reduction to k-points within the irreducible Brillouin zone enhances computational efficiency. However, it may result in the loss of information due to symmetry reduction. In systems where the complete Brillouin zone may be necessary (such as extremely asymmetric photonic crystals) to investigate all relevant physical phenomena [9,10].

III.3. APW method

In his 1937 paper, Slater introduced the augmented plane wave (APW) method, clearly stating that near an atomic nucleus, the potential and wavefunctions resemble those of an isolated atom: they vary rapidly while remaining nearly spherically symmetric. In contrast, in the interstitial region between atoms, both the potential and wavefunctions are relatively smooth. Accordingly, space is divided into distinct regions, each described by a different basis set expansion. Radial solutions of Schrödinger's equation within non-overlapping atom-centered spheres (muffin-tin) and plane waves in the intervening interstitial area (Figure III.3) [11]:

$$\varphi(r) = \begin{cases} \Omega^{-1/2} \sum_G c_G e^{i(G-k)\cdot r} & r \in I \\ \sum_{lm} A_{lm} u_l(r) Y_{lm}(\hat{r}) & r \in S \end{cases} \quad \textbf{(III.5)}$$

With $\varphi(r)$ KS orbital, Ω is the unit cell volume, A_{lm} and c_G coefficients and u_l is the solution of the radial Schrodinger equation:

$$\left[-\frac{d^2}{dr^2} + \frac{l(l+1)}{r^2} + V(r) - E_l\right] r u_l(r) = 0 \quad (\textbf{III. 6})$$

Where : V(r) is spherical part of the potential and E_l is a parmeter.

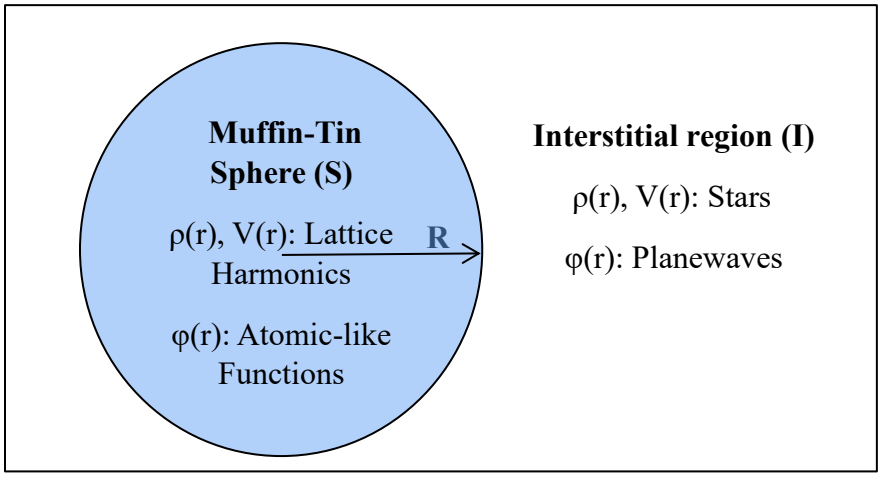


Figure. III.3. The dual representation of the APW and LAPW methods

Slater justifies this specific choice of basis functions by noting that plane waves are solutions to the Schrödinger equation in a constant potential, whereas the radial functions are solutions in a spherical potential, provided that E_l corresponds to the eigenvalue. One point remains. The dual representation specified by Equation 4.1 is not assured to be continuous at the sphere boundaries, which is a requisite for the proper definition of kinetic energy. Therefore, it is essential to implement this requirement. In the APW approach, this is accomplished by expressing the coefficients A_{lm} in relation to the c_G via the spherical harmonic expansion of the plane waves. The coefficient of each lm component is aligned at the sphere boundary [11].So, At the boundary of the muffin-tin sphere (radius R), the wavefunction from both regions must match continuously and differentially, the values of $\varphi(r)$ must much and also the derivative $\frac{\partial\varphi(r)}{\partial r}$. these conditions link the plane wave expansion coefficients c_G to atomic like orbitals expansion coefficients A_{lm}.

The plane wave can be expanded into spherical harmonics and spherical Bessel functions [11]:

$$e^{i(k+G)\cdot r} = 4\pi \sum_{l=0}^{\infty} \sum_{m=-l}^{l} i^l j_l(|k+G|r) Y_{lm}^*\big(\widehat{k+G}\big) Y_{lm}(\hat{r}) \qquad \textbf{(III. 7)}$$

We Substitute this into the plane wave expansion of $\varphi(r)$:

$$\varphi(r) = \frac{4\pi}{\sqrt{\Omega}} \sum_{G} c_G \sum_{l=0}^{\infty} \sum_{m=-l}^{l} i^l j_l(|k+G|r) Y_{lm}^*\big(\widehat{k+G}\big) Y_{lm}(\hat{r}) \qquad \textbf{(III. 8)}$$

By Matching at the Muffin-Tin Boundary (r = R) we get:

$$\sum_{l,m} A_{lm} u_l(R) Y_{lm}(\hat{r}) = \frac{4\pi}{\sqrt{\Omega}} \sum_G c_G \sum_{l,m} i^l j_l(|k+G|R) Y_{lm}^*\big(\widehat{k+G}\big) Y_{lm}(\hat{r}) \qquad (\mathbf{III.9})$$

Using Orthogonality of Spherical Harmonics ($\int Y_{l'm'}^*(\hat{\boldsymbol{r}}) Y_{lm}(\hat{\boldsymbol{r}})\ d\Omega = \delta_{ll'}\delta_{mm'}$) yields to:

$$\sum_{l,m} A_{lm} u_l(R) \int Y_{l'm'}^*(\hat{r}) Y_{lm}(\hat{r})\ d\Omega = \frac{4\pi}{\sqrt{\Omega}} \sum_G c_G \sum_{l,m} i^l j_l(|k+G|R) Y_{lm}^*\big(\widehat{k+G}\big) \int Y_{l'm'}^*(\hat{r}) Y_{lm}(\hat{r})\ d\Omega \qquad (\mathbf{III.10})$$

Due to orthogonality, the integrals give Kronecker deltas, simplifying the equation:

$$A_{lm} u_l(R) = \frac{4\pi}{\sqrt{\Omega}} \sum_G c_G i^l j_l(|k+G|R) Y_{lm}^*\big(\widehat{k+G}\big) \qquad (\mathbf{III.11})$$

Finally, we solve for the coefficients

$$A_{lm} = \frac{4\pi i^l}{\Omega^{1/2} u_l(R)} \sum_G c_G j_l(|k+G|R) Y_{lm}^*\big(\widehat{k+G}\big) \qquad (\mathbf{III.12})$$

Although powerful for computations of electronic structure, the Augmented Plane Waves (APW) approach has limitations. Its computational needs and difficulties in precisely modelling certain processes generate these limitations . An further challenge with the APW technique is its difficulty, though not impossibility, in extending to a general crystal potential, beyond the warped muffin-tin approximation (generic potential in the interstitial region, but a spherical potential inside the spheres). In this scenario, the optimal variational choice of E_l is no longer determined by setting E_l equal to the band energy. Specifically, various bands often exhibit distinct orbital characteristics inside the sphere. In a non-spherical potential, these orbitals encounter distinct effective potentials that deviate from the spherical average used to ascertain the radial function [11]. Furthermore, The APW approach complicates the mathematical process and causes errors in certain computations by using continuous basis functions but discontinuous derivatives of those functions [12].

The APW (augmented plane wave) method is an advanced electronic structure calculation method but one lacking in basis set flexibility and computational efficiency. LAPW (Linearized Augmented Plane Wave) and APW+lo (Augmented Plane Wave plus local orbitals) are methods designed to address such shortcomings by incorporating an enhanced basis set and enhancing computational

efficiency. These extensions are designed to enable more precise and effective solutions to the Kohn-Sham equations for density functional theory (DFT) calculations.

III.4. The LAPW Method

In 1975 Anderson [13] introduced the concept of a linearized APW by expanding the radial wave function inside the muffin-tin (MT) spheres around a fixed energy E_0:

$$ul(E,r) \approx u_l(E_0,r) + (E - E_0)\dot{u}_l(E_0,r) \qquad (\mathbf{III.13})$$

Where $u_l(E,r)$is the radial solution of Kohn Sham equations and $\dot{u}_l(E_0,r)$ is its first energy derivative.

Although Andersen's contributions are mostly associated with the LMTO approach, he also developed a linearization of the APW method, achieving favorable results. The technological obstacles of the canonical APW method that we have just discussed are removed. Koelling and Arbman promptly adopted the notion, enhancing it mainly by eliminating an expansion approach used by Andersen to closely align with what is now referred to as the linearized APW (LAPW) method, and implemented it by updating Koelling's pre-existing APW code. The LAPW and APW bases differ just inside the spherical regions. Within atomic sphere S, with radius R_S, each orbital is a linear combination of radial functions multiplied by spherical harmonics [14]:

$$\varphi(r) = \begin{cases} \Omega^{-1/2} \sum_G c_G e^{i(G+k)\cdot r} & r \in I \\ \sum_{lm} (A_{lm} u_l(r) + B_{lm} \dot{u}_l(r)) Y_{lm}(\hat{r}) & r \in S \end{cases} \qquad \mathbf{(III.14)}$$

The determination of A_{lm} and B_{lm}coefficients requires that the orbitals inside the sphere must match the plane wave in Interstitial region for both tin value and the slope at the sphere boundary.

N.B: The augmented wave functions u_l and $\dot{u}_l$ must satisfy the condition of being orthogonal to the core states within the MT sphere. However, this condition is only fulfilled when there are no core states with the same *l*. As a result, there is a risk of confusing semi core states with valence states. The issue of non-orthogonality of some core states is not addressed by the APW method, and using the FP-LAPW method requires careful selection of the energy E_0. Therefore, for the calculation to be accurate, E_0 must be adjusted. In this case, the ideal solution is to use a local

orbital expansion. However, this option is not available in all programs, so we must select the largest possible MT sphere radius. Finally, the different energies E_0 should be defined independently of each other. The energy bands have different orbitals. For an accurate calculation of the electronic structure, E_0 should be chosen as close as possible to the energy of the band if the latter has the same l [15].

III.5. The FP-LAPW Method

The primary distinction between the Full-Potential Linearized Augmented Plane Wave (FP-LAPW) method and LAPW method is in the treatment of the potential and the electron density within the system. While in the LAPW method, the potential is treated in general by a spherical potential within the muffin-tin (MT) spheres with a constant or uniform assumption in the interstitial region. This simplification in the approximation streamlines the calculation process, making LAPW less computationally demanding though at the cost of reduced accuracy, particularly in systems with complex electronic structures or non-spherical charge distributions [16]. In contrast, FP-LAPW treats the full potential without relying on such approximations. The potential is examined in a systematic manner over the whole system, both in the interstitial spaces as well as in the MT spheres , hence giving an improved description of the electronic structure of the material. The careful examination of the potential leads to greater accuracy in computing properties such as the density of states (DOS) and band structure, particularly for systems characterized by localized electronic states or non-spherical symmetries [17].The enhanced accuracy of FP-LAPW comes at the cost of higher computational complexity. Because the full potential is used, FP-LAPW requires more computer resources and time than the LAPW approach, and this can be a limiting factor for larger or more complex systems. While LAPW is generally sufficient for bulk systems with simple electronic structures, FP-LAPW is preferable for systems where very high accuracy is required, e.g., materials with surface or interface effects or those with complex bonding arrangements [16,17]. So, while LAPW offers a faster, less computationally intensive approach, FP-LAPW yields a more detailed and accurate description and is consequently essential for high-accuracy studies in materials science.In FP-LAPW the orbitals are expanded as follows:

$$\varphi(r) = \begin{cases} \sum_{\mathrm{l,m}} R_{l\mathrm{m}}(r) Y_l^m(\theta,\phi) & r \in S \\ \sum_{\vec{k}} \sum_{l,m} c_{\vec{k},lm} e^{i(\vec{k}+\vec{G})\cdot\vec{r}} & r \in I \end{cases} \qquad \textbf{(III.15)}$$

The same way the potential $V(r)$ (Eq 16) and the electron density $n(r)$ (Eq 17) are written as :

$$V(r) = \begin{cases} \sum_{lm} V_{lm}(r) Y_{lm}(r) & r \in S \\ \sum_{k} V_k e^{ikr} & \text{r} \in I \end{cases} \quad \textbf{(III. 16)}$$

$$n(r) = \begin{cases} \sum_{lm} n_{lm}(r) Y_{lm}(r) & r \in S \\ \sum_{k} n_k e^{i(\vec{k}+\vec{G})r} & \text{r} \in I \end{cases} \quad \textbf{(III. 17)}$$

The mathematical formulations in equations (III.15) to (III.17) highlight the strength of the FP-LAPW method in accurately modeling both spherical and non-spherical components of the potential and electron density. Unlike conventional approximations that oversimplify the potential within the crystal, FP-LAPW treats it without shape constraints across both muffin-tin spheres and interstitial regions. This results in more precise evaluations of critical electronic quantities, such as the band structure, density of states (DOS), and charge distribution [18,19]

Compared to pseudopotential-based plane-wave methods, FP-LAPW is an all-electron technique and does not neglect the core region, making it especially suitable for systems with transition metals, rare-earth elements, or strong relativistic effects [20]. Its ability to represent the potential with full flexibility enables improved resolution in regions where localized orbitals significantly influence material behavior.

The method also supports advanced exchange-correlation functionals, such as GGA-PBEsol and the modified Becke–Johnson (mBJ) potential, which further enhance the accuracy of band gap predictions and optical property calculations [21,22] .This makes FP-LAPW highly effective for exploring dielectric functions, absorption coefficients, and reflectivity, ensuring high fidelity in both ground-state and excited-state analyses.

Although computationally more demanding than simplified approaches, the precision offered by FP-LAPW justifies its use in high-accuracy first-principles investigations. It remains one of the most trusted techniques in computational condensed matter physics and materials science for modeling electronic, optical, and structural behavior at the quantum level [11,23].

Despite its widely recognized accuracy, the (FP-LAPW) scheme is associated with several computational and methodological limitations. One of the most prominent drawbacks is its significant computational cost. Owing to its all-electron and full-potential formulation, FP-LAPW requires dense k-point sampling and large basis sets to achieve convergence, which can be computationally prohibitive for systems with large unit cells or reduced symmetry [11,24]. This makes it less practical for high-throughput studies or large-scale simulations when compared to pseudopotential-based methods. Moreover, the method introduces linearization errors due to the energy dependence of the radial basis functions, which can become significant for unoccupied states far from the linearization energy. Such inaccuracies may affect the reliability of optical and excited-state calculations. To address this, the inclusion of local orbitals (LOs) has been proposed and widely adopted to improve the description of semi core and high-lying conduction states [25]. Additionally, for materials containing heavy elements, relativistic effects such as spin–orbit coupling play a crucial role in the electronic structure. FP-LAPW accommodates these effects using scalar-relativistic approximations or by solving the Dirac equation for core electrons, but doing so further increases computational demands [26]. Another concern involves core leakage and sphere overlap under conditions of high pressure or in low-symmetry structures, which are typically resolved by optimizing sphere sizes and refining the atomic configuration [27].

The method also presents practical challenges. Its steep learning curve and the need for careful parameter tuning can make it less accessible to novice users. However, recent developments in user interfaces, notably within the WIEN2k package, have improved its usability through graphical front-ends and detailed documentation . While these enhancements ease the setup process, mastering the theoretical background and technical details of FP-LAPW remains essential for obtaining reliable results. Despite these drawbacks, the method's precision in treating both core and valence electrons, its flexible potential representation, and its support for advanced exchange–correlation functionals continue to make it one of the most trusted approaches for electronic structure calculations in condensed matter physics and materials science.

III.6. Basis Set Size in FP-LAPW Method

In the (FP-LAPW) method, the basis set plays a critical role in determining the accuracy and efficiency of electronic structure calculations. The FP-LAPW approach divides the unit cell into two regions: non-overlapping muffin-tin (MT) spheres around each atomic nucleus and the

interstitial region between these spheres. Within the MT spheres, the wavefunctions are expanded in terms of radial functions multiplied by spherical harmonics, while in the interstitial region, they are represented as plane waves [1,11]. The size of the basis set in the interstitial region is controlled by the cutoff parameter RK_{max}, defined as:

$$RK_{max} = R_{MTmin} \times K_{max} \quad (\mathbf{III.18})$$

where R_{MTmin} is the smallest muffin-tin radius in the system, and $K_{max}$is the maximum magnitude of the reciprocal lattice vector included in the plane-wave expansion. The number of plane waves N scales approximately with the cube of K_{max}, i.e.,

$$N \propto K^3{}_{\max} \propto (R_{MTmin} \times K_{max})^3 \quad (\mathbf{III.19})$$

Therefore, increasing the value of RK_{max} leads to a larger number of basis functions, enhancing the completeness of the basis set and thereby improving the accuracy of the total energy, electronic eigenvalues, and derived quantities such as the density of states (DOS). However, this increase also comes with a higher computational cost, due to the diagonalization of larger Hamiltonian matrices. Choosing an appropriate value of RK_{max} is thus a trade-off between computational expense and numerical precision. In most practical calculations, values of RK_{max} between 6.0 and 9.0 are commonly used. Higher values (e.g., $RK_{max}\geq$ 8.0) are typically required for systems with rapidly varying charge densities or when highly localized orbitals are present, such as in d- or f-electron systems [1,21].Moreover, the muffin-tin radii R_MT must be chosen carefully to avoid sphere overlap while ensuring that the interstitial region remains as small as possible.

A small interstitial volume reduces the number of required plane waves, thereby improving computational efficiency without sacrificing accuracy [11]. Overall, the RK_{max} parameter directly controls the quality of the wavefunction in the interstitial region and is a crucial convergence parameter in FP-LAPW-based calculations. Which makes a cutoff parameter that its careful selection is necessary to guarantee reliable and reproducible results in first-principles simulations.

III.7. LAPW+lo and APW+lo Methods and the Wien2k code

Density Functional Theory (DFT) is a cornerstone of modern computational materials science. Among its many formulations, all-electron full-potential methods like the Linearized Augmented Plane Wave (LAPW) and Augmented Plane Wave (APW) methods stand out for their accuracy.

These techniques partition the unit cell into non-overlapping muffin-tin (MT) spheres and an interstitial region. The LAPW and APW methods treat the electronic structure using different radial and angular expansions in these regions. However, difficulties arise when dealing with semicore and unoccupied states. This led to the introduction of 'local orbitals' (lo), which when combined with APW or LAPW, form the highly efficient APW+lo and LAPW+lo methods [1,19,25].The LAPW method uses a linear approximation around an energy parameter E_l. While effective near E_l, this approach breaks down when the actual eigenvalue E_n deviates substantially. Semicore states often located well below the valence bandsas well as high-energy conduction states, require greater flexibility. The APW method uses energy-dependent basis functions, resulting in nonlinear eigenvalue problems. Local orbitals (lo), designed to be non-zero only inside the muffin-tin spheres, solve these issues by providing an additional variational degree of freedom without increasing the plane wave cutoff [19,28]. Inside the muffin-tin sphere, local orbitals are constructed from radial solutions of the Schrödinger equation. A typical lo function $\varphi^{Lo}(r)$ for angular momentum l and magnetic quantum number m is:

$$\varphi^{Lo}(r) = \begin{cases} 0 & r \in I \\ \sum_{lm} [A_{lm} u_l(r, E_{1l}) + B_{lm} \dot{u}_l(r, E_{1l}) + C_{lm} u_l(r, E_{2l})]\, Y_m^l(\hat{r}) & r \in MT \end{cases} \quad \textbf{(III. 20)}$$

The coefficients A, B, C are determined to ensure that the local orbital and its derivative vanish at the sphere boundary. This guarantees no overlap with interstitial basis functions, maintaining orthogonality and numerical stability.

III.7.1. LAPW+lo Method

The (LAPW) method is one of the most precise techniques for solving the Kohn–Sham equations within density functional theory (DFT), particularly for periodic solids The LAPW method uses a linearized basis set expanded around a fixed energy E_l. By augmenting this with local orbitals, LAPW+lo effectively improves representation for semicore states and corrects linearization errors. To overcome the linearization error and improve the description of semi core and localized states (e.g., 3s, 3p in 3d metals), the LAPW method is augmented by local orbitals (lo) [25].

The full Kohn–Sham wavefunction $\psi^k(r)$ is written as a linear combination of LAPW and LO basis functions:

$$\psi^k(r) = \sum_G C_G . \phi_{k+G}^{LAPW} + \sum_{lm} d_{lm} . \phi_{lm}^{lo} \quad (\mathbf{III.21})$$

The LAPW+lo method has several significant advantages:

All-electron, full-potential treatment without shape approximation to the potential [19] .

Accurate treatment of core, semicore, and valence electrons; particularly well suited for materials with localized d- and f-electrons, such as transition metals, lanthanides, and actinides. Systematic convergence via plane wave cutoff and addition of local orbitals. For these reasons, LAPW+lo is the standard implementation in modern codes like WIEN2k, which remains a benchmark for precision in electronic structure calculations.

III.7.2. APW+lo method

The Augmented Plane Wave plus local orbitals (APW+lo) method is a highly accurate all-electron technique derived from the traditional Augmented Plane Wave (APW) approach. It was developed to overcome limitations in the convergence properties of the original APW method by combining the energy-accurate formulation of APW with the variational flexibility of LAPW , while maintaining a more compact and efficient basis set [25].The resulting basis provides high accuracy and fast convergence even with fewer plane waves:

$$\psi^k(r) = \sum_G C_G . \phi_{k+G}^{APW} + \sum_{lm} d_{lm} . \phi_{lm}^{lo} \quad (\mathbf{III.22})$$

LAPW+lo and APW+lo have been successfully used to study electronic, magnetic, optical, and thermoelectric properties of various materials. APW+lo typically offers faster convergence with fewer basis functions, whereas LAPW+lo provides more flexibility for semi core treatment. In both cases, lo's dramatically improve precision and reduce computational cost.

III.7.3. WIEN2k Electronic Structure Package and Its Components

WIEN2k is one of the most powerful first-principles simulation packages for solving the electronic structure of crystalline solids using Density Functional Theory (DFT). It employs the full-potential (linearized) augmented plane wave plus local orbitals (FP-LAPW+lo) method, which is widely regarded as one of the most accurate schemes for solid-state calculations [1]. It treats all electrons

(core and valence) explicitly and avoids shape approximations to the potential or charge density. The code is written in Fortran and is optimized for UNIX/Linux environments. Its accuracy, modular structure, and wide applicability have made it a cornerstone tool in computational materials science.

III.7.3.1.Overview of Properties and approximations supported in WIEN2k

WIEN2k enables the computation of a broad spectrum of physical properties from first principles, including structural, electronic, optical, magnetic, and thermoelectric characteristics. Some major categories are listed in Table III.1.

Table III.1. Calculated Properties in WIEN2k

Property	Examples of calculated parameters
Structural	Total energy, lattice constants, bulk modulus, c/a ratio…
Electronic	Band structure, density of states (DOS), charge density.
Magnetic	Magnetic moments, spin-polarized DOS, spin density maps
Optical	Dielectric function, reflectivity, absorption coefficient…
Mechanical	Elastic constants, anisotropy index, Poisson's ratio…

Post-processing tools such as VESTA [29] and BoltzTraP [28] are commonly used to visualize results or extract properties like thermopower and conductivity.

The accuracy of DFT depends critically on the exchange-correlation (XC) approximation. WIEN2k supports several XC functionals, including (Table III.2):

Table III.2. Some supported functionals in WIEN2k

Type	Examples of functional
LDA	Depends only on local electron density like VWN, CA [30]
GGA	PBE, PW91, WC-GGA, PBEsol.
mBJ	TB-mBJ, KTB-mbj, nKTB-mBJ

m-GGA	revTPSS, Scan
Hybrid	Y-PBE0, B3LYP,

III.7.3.2. Essential WIEN2k modules

Below is a detailed breakdown of each essential WIEN2k module, including its role and usage context [31]:

init_lapw A shell script that interactively orchestrates the entire initialization (Figure III.4**)** procedure for a new case. It sequentially runs the structure setup and initial guess programs (nn, sgroup, symmetry, lstart, kgen, dstart), prompting the user for necessary inputs (such as the exchange–correlation functional and core-valence separation energy) .The script generates all initial input files (e.g. case.in0, case.in1, case.in2, etc.) and an initial electron density. In modern versions, init_lapw can be run in a batch mode with default options or step-by-step (init_lapw -b or -c for curses mode) for more control. It typically produces on the order of 50 files, including the master structural file and specific inputs for each program (). After init_lapw completes, the system is ready for the self-consistent cycle.

nn (Nearest Neighbors): This program reads the crystal structure from case.struct and computes all interatomic distances, especially each atom's nearest neighbor distances . It checks that atomic sphere radii (R_{mt}) do not overlap; if overlap is detected, a warning is issued . It also prints coordination shells up to a specified multiple of the nearest-neighbor distance in case.outputnn . Additionally, nn verifies the equivalence of atoms: if the input atomic positions labeled as equivalent do not truly have the same neighbor environment, an error is flagged and an adjusted structure file (case.struct_nn) is generated suggesting proper unique atom labeling . This ensures the space group and atomic multiplicities are consistent. By helping set optimal sphere sizes and correct equivalencies, nn guarantees a proper starting geometry for the calculation.

sgroup (Space Group Determination): sgroup analyzes the geometry in case.struct to determine the crystal space group and the point group of each atomic site . It can identify if the provided unit cell can be reduced to a smaller primitive cell or if the origin can be shifted to a more symmetric choice . Using the atomic positions and nuclear charges, it finds symmetry operations and can

output a standardized structure file case.struct_sgroup with the conventional lattice setting and proper atomic equivalences. This is especially useful for “handmade” structures to ensure the highest possible symmetry is recognized. If the user chooses to accept the suggestions, the new struct file can replace the original. sgroup thus helps validate and standardize the crystal structure before proceeding .

symmetry (Point Group and Symmetry Operations): This program uses the space group operations to generate the full symmetry of the lattice and the local symmetry at each atom . If the struct file’s symmetry information is incomplete (e.g. NSYM=0), symmetry will determine all symmetry operations of the space group and write them into an expanded struct file case.struct_st . If symmetry operations were already present in case.struct, it cross-checks them; any discrepancy results in a warning in case.outputs . symmetry also finds the point group for each inequivalent atom and prepares data needed for later steps: it writes the appropriate local rotation matrices and harmonic expansion indices to case.struct_st, and creates case.in2_st (and case.in2_sy) containing the spherical-harmonic lattice harmonics used in charge density and potential representations . This ensures the Hamiltonian will respect the crystal symmetry and reduces computational effort by using symmetry-unique points.

lstart (Atomic LSDA Initialization): lstart generates initial atomic wavefunctions and electron densities for each unique atom, which serve as the starting density for the crystal SCF cycle . It is a modified relativistic atomic solver (based on Desclaux’s code) that performs a self-consistent atomic LSDA calculation for each species . The output includes atomic radial charge densities (case.rsp for non-spin or case.rspup/dn for spin-polarized cases) and atomic potential files . Using the atomic eigenvalues, lstart also automatically generates the initial input files needed for the SCF programs: case.in0 (for potential), case.in1 (basis set), case.in2 (charge density), case.inc (core configuration), and case.inm (mixing) . These inputs are tailored so that core-valence separation and occupation are appropriate for each atom. For example, lstart asks the user for the exchange–correlation (XC) functional (with numeric codes for LSDA or various GGAs) and an energy cutoff to distinguish core and valence states . Typically, states below –6.0 Ry are treated as core . If an atomic state fails to converge (indicated by NSTOP in case.outputst), the occupancy of nearly degenerate levels may need adjustment . Warnings are given if core charge leaks outside the muffin-tin sphere, prompting the user to include those states as valence by lowering the cutoff . In

summary, lstart ensures a good starting electron density by combining superposed atomic densities, and it prepares all requisite input files for the SCF cycle.

kgen (k-Point Mesh Generator): This utility generates the set of k-points in the Brillouin zone for Brillouin-zone integrations . The user specifies either the number of k-points or the mesh subdivisions along each reciprocal axis. kgen then produces the list of points in the irreducible wedge of the Brillouin zone (using the crystal symmetry to reduce the full grid) . It implements the Monkhorst-Pack scheme (special points on a uniform grid) and can generate meshes compatible



Figure III.4. Initialization with wien2k w2web interface

with the modified tetrahedron integration method of Blöch . In essence, kgen defines the k-space sampling for integrations, balancing accuracy and cost.

dstart (Density Start): Using the output of lstart, this program builds the initial crystal electron density by superposing atomic densities . It reads each atom's radial density (case.rsp files from lstart) and places them in the crystal arrangement, summing contributions to form the total valence density case.clmsum (and spin-up/down densities case.clmup/case.clmdn for spin-polarized cases) . dstart uses information from case.in1 and case.in2 to represent the density in the mixed basis of spherical harmonics inside spheres and Fourier series in the interstitial . The initial charge density

is written in a format ready for input to lapw0. If core states are present, dstart -c will also combine core densities.

lapw0 (Poisson Solver – Potential Generation): This is the first step in each SCF iteration. lapw0 computes the total electrostatic potential from the electron density and adds the exchange–correlation potential , yielding the total potential . It takes as input the charge density (case.clmsum and spin-polarized case.clmup/dn) and produces the potential files (case.vsp for the spherical part and case.vns for the non-spherical part) for use by the eigenvalue solver . For spin-polarized cases, it outputs separate up- and down-spin potentials (case.vspup/dn and case.vnsup/dn) . lapw0 uses an efficient multipole expansion plus Fourier transform method (Weinert's method) to solve Poisson's equation.

lapw1 (Band Eigenvalue Solver): lapw1 is the main Hamiltonian eigen-solver, which constructs the Kohn–Sham Hamiltonian matrix (kinetic + potential) in the APW+lo basis and solves for eigenvalues and eigenvectors . It reads the potential from lapw0 (case.vsp/vns) and for each k-point sets up the generalized eigenvalue problem. The method follows Koelling and Arbman's relativistic APW formalism . The resulting eigenvalues (band energies) and eigenvectors are output to case.energy and case.vector files.

lapw2 (Charge Density and DOS): After eigen-solutions are obtained, lapw2 calculates the electron charge density (and related quantities) from the eigenfunctions . It reads the eigenvectors (case.vector) and eigenvalues (case.energy) from lapw1, and for each occupied state it computes the expansion of the electron density on the same mixed basis (spherical harmonics inside spheres and plane waves outside) . Summing over all occupied bands and k-points, it produces the valence charge density in the form of spherical harmonic coefficients, which is then integrated to obtain partial charges inside each atomic sphere . This yields the key output case.clmval (valence density) and associated files. . In summary, lapw2 generates the valence electron density required for the next iteration's potential and provides band-decomposed charge information. It can also be run in a special mode (-band) to prepare data for band structure plots (using a fine k-path and writing results suitable for the spaghetti program) .

lcore (Core States Solver): This program handles the deep core electrons that are treated separately from the valence in the APW method. lcore solves the radial Dirac (or Schrödinger)

equation for core orbitals using the spherical part of the potential case.vsp . It thus finds core-level eigenvalues and generates the core electron density. The output includes case.clmcor (the core charge density in each atomic sphere) and a list of core state energies, which are added to the total energy and can be reported (e.g., for X-ray spectroscopy, core level shifts) . It also calculates core contributions to forces (important if open-core pseudopotential-like approximations are used) . For relativistic effects, lcore can include spin–orbit splitting of core levels (unless run in a scalar-relativistic mode as indicated by the NREL switch in struct file) . In spin-polarized cases, it is run separately for up and down channels (lcore -up/-dn).

mixer (Density Mixing and SCF Convergence): After lapw2 and lcore, WIEN2k has new output densities (valence and core) which must be mixed with the previous density to achieve a stable self-consistency. The mixer program takes the new output charge density and spin densities and mixes them with the old input density to generate an updated electron density for the next cycle .

run_lapw / runsp_lapw (SCF Cycle Control): These are high-level job control scripts that automate the repeated execution of the above programs to achieve self-consistency. run_lapw is used for non-spin-polarized (or spin-averaged) calculations, whereas runsp_lapw handles spin-polarized cases (running two spin channels and adding spin flags where needed.The script controls the flow: calling lapw0 → lapw1 → lapw2 → (lapwso if spin–orbit is included) → lcore → mixer in a loop. It checks after each iteration if convergence criteria are met by grepping the case.scf file for indicators like :DIS (charge distance) and :ENE (energy change. The user can specify convergence thresholds via command-line switches (for example, run_lapw -ec 0.0001 -cc 0.0001).

lapwso (Spin–Orbit Coupling): This module treats spin–orbit (SO) coupling, typically after an initial SCF has been obtained (though it can be included self-consistently as well). lapwso performs a second-variational diagonalization of the spin–orbit Hamiltonian, taking as input the scalar-relativistic eigenfunctions from lapw1 . It expands the SO Hamiltonian in the basis of eigenstates from lapw1. The code then computes new eigenvalues and eigenvectors that include spin–orbit splitting, writing them to case.energyso and case.vectorso .

Eosfit: Within WIEN2k, the determination of the structural equilibrium parameters from the total-energy calculations is achieved through the internal utility program "eosfit". This tool analyzes the obtained results on the energy-volume relationship and performs a numerical least-squares fit to

the analytical equations of state that are frequently used to characterize the elastic response of solids under compression. Among the implemented equations of state, the following have been found useful: the Murnaghan model, the Birch-Murnaghan EOS, the Vinet EOS, and the Poirier-Tarantola EOS. The fitting procedure is applied to the obtained results on the energy-volume relationship that were calculated during the volume optimization procedure, which is often stored in the case.vol file. By finding the minimum of the obtained fitting curve, the equilibrium volume V is found from which the bulk modulus B and its pressure derivative B' follow naturally. The fact that this procedure is an integral part of the WIEN2k package guarantees that the obtained results are consistent with the FP-LAPW method used to perform the total-energy calculations.

Spaghetti (Band Structure Plotting): The Spaghetti module generates electronic band structure plots (so-called "spaghetti" diagrams of E vs k). After an SCF run, one typically reruns lapw1 and lapw2 in band structure mode (with a dense list of k along high-symmetry lines and the -band switch) to produce eigenvalues along a chosen path. spaghetti then reads those eigenvalues (from case.output1 for non-SO or case.outputso for SO bands) and plots them .

tetra (Density of States Integration): The tetrahedron method, as implemented in the program TETRA, computes the density of states (DOS) and related integrated properties by performing an integration over the Brillouin zone using the linear tetrahedron method. It requires as input the eigenvalues on a dense kmesh (usually the SCF mesh, found in case.energy or from an -efg switch in lapw2) and, if partial DOS are needed, the case.qtl file with projections. The file case.int specifies the energy mesh and Gaussian broadening. tetra then partitions the Brillouin zone into tetrahedra (using the mesh from kgen) and integrates the spectral function to produce the total DOS and partial DOS for each atom and orbital, resolved in up to three channels (DOS1, DOS2, DOS3) . The outputs include case.dos1/2/3 .

optic (Optical Matrix Elements): The optic program computes momentum matrix elements and optical transition probabilities between occupied and unoccupied states, enabling calculation of frequency-dependent optical properties . It reads eigenvalues and eigenvectors (from lapw1/lapw2 results) and calculates the dipole transition matrix for all band pairs at each k-point satisfying selection. The input file case.inop allows the user to specify the desired components (e.g., polarization directions) and whether to include intraband Drude terms. The optic program then produces raw transition data, output in the case.symmat (symmetric matrix elements) and

case.mommat (momentum matrix elements) files . Essentially, it enumerates all transitions from every occupied band to every empty band at each k, which is the basis for computing the frequency-dependent dielectric function. Because this can be a large number of transitions, a dense k-mesh is usually required for good convergence of optical spectra .

joint (Optical Spectra Integration): After optic, the joint program performs the Brillouin zone integration of the optical transitions to compute the joint density of states and frequency-dependent optical constants .

kram (Kramers–Kronig Transformation): This program applies the Kramers–Kronig relations to the $\epsilon_2(\omega)$ data from joint to obtain the real part of the dielectric function $\epsilon_1(\omega)$ and other derived optical constants . Together, optic, joint, and kram enable WIEN2k to predict optical properties (Figure III.5) like absorption spectra and reflective indices from first principles.

lapw5 (Electron Density and Potential Plotting): This program extracts the electron density or potential on a 2D grid (plane) through the crystal for visualization. The user specifies a crystallographic plane (by three points or Miller indices in case.in5), and lapw5 will output the charge density .

lapwdm (Density Matrix for LDA+U / Hybrid): This program computes the onsite density matrix for localized orbitals, needed in DFT+U and hybrid functional calculations. After each lapw2, which provides partial charges per . Together with orb, it enables an on-site Hartree–Fock-like term to be included. lapwdm also runs in parallel (over k) similarly to lapw2 because it processes band occupations for each k-point.

III.7.3.3. Self-Consistent Field (SCF) Cycle in WIEN2k

The self-consistent field (SCF) cycle is the core iterative loop within WIEN2k that enables the convergence of the total energy and charge density of a crystalline system. This loop solves the Kohn–Sham equations of Density Functional Theory (DFT) self-consistently, updating the potential until the system reaches its electronic ground state. A precise SCF solution is critical as it forms the basis for all subsequent calculations including band structure, density of states (DOS), optical and thermoelectric properties. The etailed SCF Workflow is as follows [1].

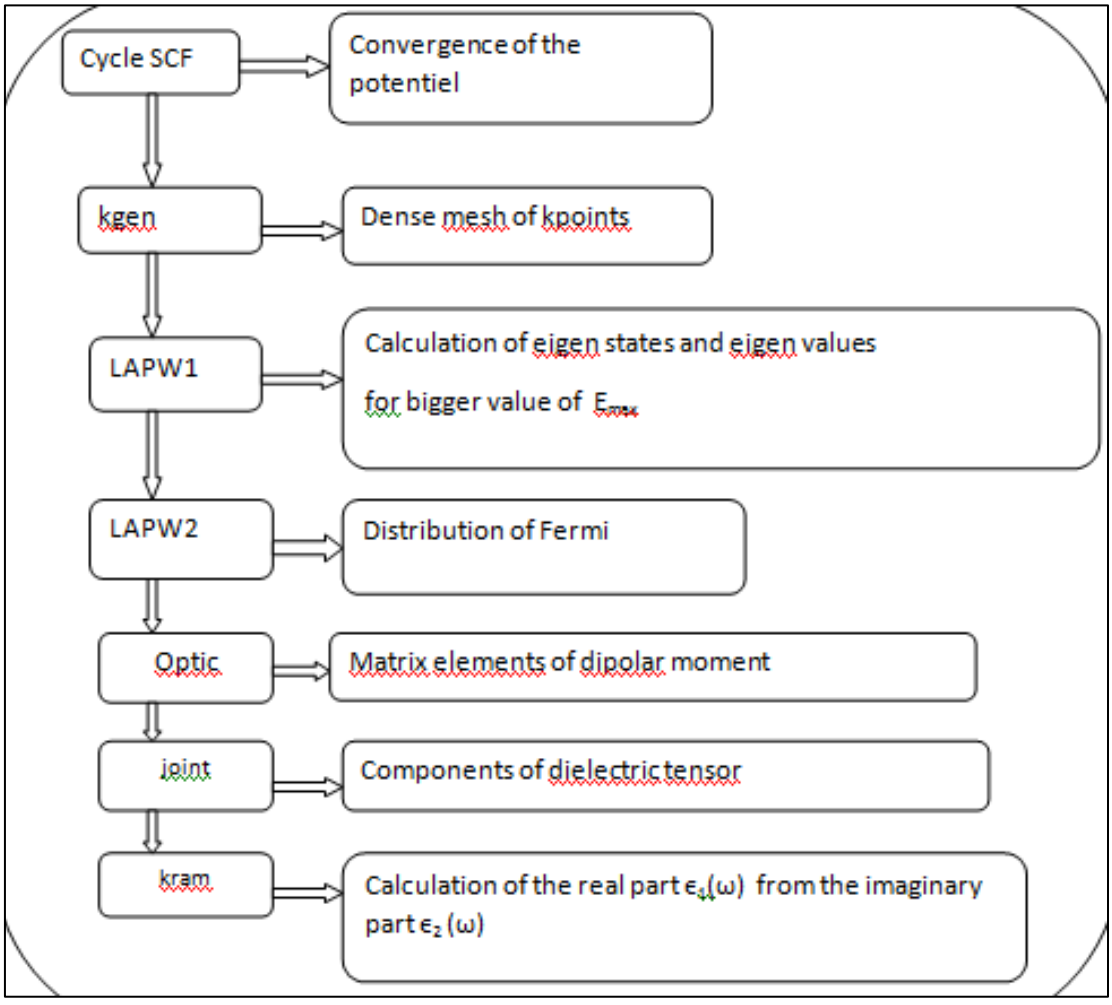


Figure III.5. Chart of optical properties calculation procedure in Wien2k [32]

Initialization of Atomic Densities and Input Files:

-`lstart` constructs atomic-like radial wavefunctions and local densities based on the atomic configuration.
-`nn` ensures non-overlapping muffin-tin spheres and defines nearest neighbors [31].
-`dstart` combines the atomic charge densities from `lstart` into a superimposed total initial density (ρ_0).

Calculation of Electrostatic and Exchange-Correlation Potentials:

`lapw0` solves Poisson's equation to obtain the Coulomb potential from the initial charge density. It then adds the exchange-correlation potential derived from the selected functional (LDA, GGA, mBJ, etc.), forming the total potential V [3].

Kohn–Sham Eigenvalue Problem (Valence States):

-`lapw1` solves the Kohn–Sham equations in reciprocal space by diagonalizing the Hamiltonian, producing eigenvalues (E_k) and eigenfunctions (ψ_k).
`lapw2` computes the valence electron density from these eigenfunctions [1].
If spin–orbit coupling is needed, `lapwso` introduces relativistic corrections after `lapw1` [4].

Core Electrons Treatment:

`lcore` solves the Dirac equation for atomic core states within the muffin-tin spheres, generating the core charge density and core energies [1].

Charge Density Mixing and Convergence Check:

The `mixer` compares the new and old densities, applies a mixing scheme, and produces an updated total charge density ρ_{new}. Convergence is assessed based on energy differences, integrated charge change ($\Delta\rho$), and optional force criteria. A typical convergence threshold is 10^{-4} Ry for energy and 10^{-3} e for charge [1,31].

Iteration Control:

If the convergence criteria are met, the SCF cycle terminates. If not, the updated ρ_new is used as input for the next iteration starting from `lapw0`, continuing until convergence is reached. This loop is controlled automatically using `run_lapw` (non-spin-polarized) or `runsp_lapw` (spin-polarized) scripts.

Figure III.6 illustrates an extended *WIEN2k's* SCF scheme that includes additional modules for advanced calculations, such as spin–orbit coupling and strongly correlated systems. The main iterative loop is centered around the traditional sequence—starting from the generation of potential and electron density, progressing through the LAPW0, LAPW1, and LAPW2 modules to solve the Kohn–Sham equations. These steps yield updated charge densities and potentials, which are assessed for convergence.

Several optional modules can be incorporated depending on the physical model:

-The **ORB** module introduces orbital-dependent potentials (e.g., LDA+U and orbital polarization corrections), allowing for better treatment of localized d or f electrons.

-The **LAPWSO** module enables spin–orbit coupling, essential for materials with heavy elements or topological behavior, and is integrated self-consistently into the Hamiltonian.

-For systems requiring density matrix calculations, the **LAPWDM** module is used, particularly in conjunction with LDA+U to extract orbital occupation and spin polarization.

The flowchart also shows post-processing steps such as charge decomposition, density of states (DOS), and band structure analysis, depending on the final converged solution. This comprehensive scheme emphasizes *WIEN2k*'s modular and adaptable architecture for advanced quantum mechanical simulations of solids, allowing users to tailor calculations based on the electronic complexity of the studied material.

Figure III.7 illustrates the self-consistent field (SCF) cycle in **WIEN2k**, comparing execution in single and parallel modes. In the single mode (left), the SCF cycle progresses sequentially through the LAPW0, LAPW1, LAPW2, LCORE, and MIXER modules, with LAPW1 consuming most of the computational time (~75%). LAPW2 and LAPW0 follow with 20% and 3% respectively, while LCORE and MIXER each contribute about 1%. After each iteration, the cycle checks for self-consistency before terminating. In contrast, the parallel mode (right) optimizes performance by distributing the LAPW1 and LAPW2 calculations across multiple processors. This parallelization significantly accelerates the SCF process without altering its logical structure. The SUMPARA utility coordinates the parallel components before feeding results to LCORE and MIXER. The loop

continues until convergence is achieved, highlighting WIEN2k's scalability for high-performance computing applications [33].

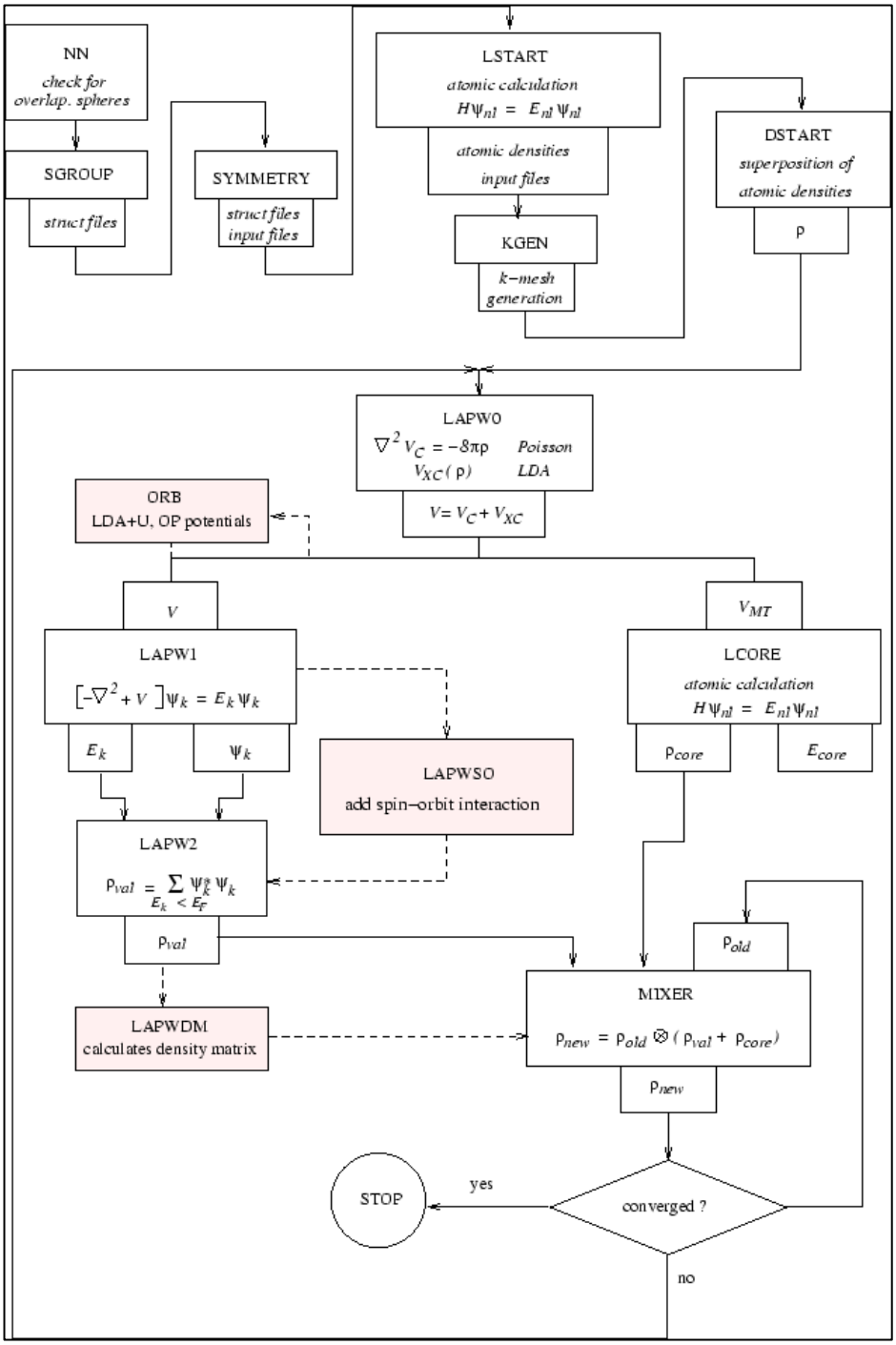


Figure III.6. Program flow in *WIEN2k (scf)* [34]

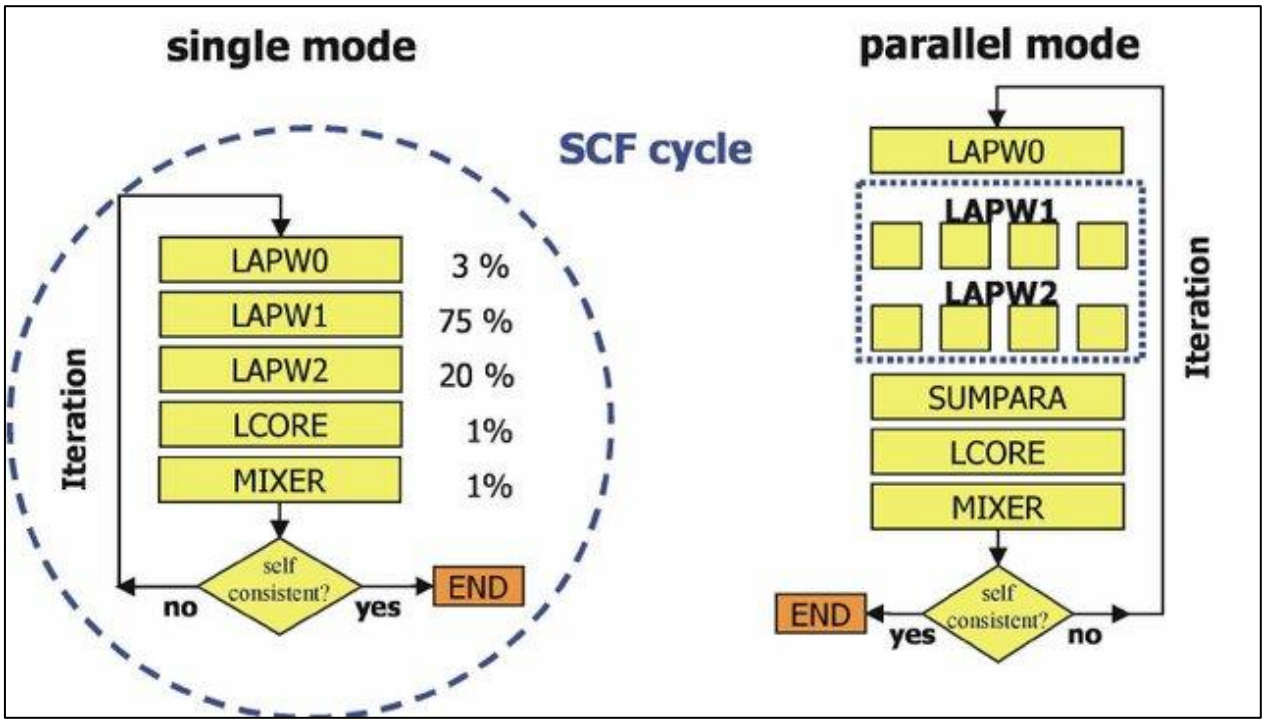


Figure III.7. Execution of the SCF cycle in WIEN2k (single/parallel modes) [33]

III.7.3.4.Advantages and limitations of Wien2k code

The WIEN2k package is a very precise and versatile full-potential DFT electronic structure code. It includes the all-electron augmented plane wave plus local orbitals (APW+lo) method, which treats both core and valence electrons correctly without making shape approximations for the potential or charge density. Listed below are the key advantages of the code:

- **All-Electron Accuracy:** WIEN2k treats both valence and core electrons on equal footing using the (FP-LAPW) method. This results in superior accuracy for total energies, electronic structures, and charge distributions, especially in heavy-element compounds, rare-earths, actinides, and systems with localized electrons where core-valence interactions play a crucial role [1].

- **No Shape Approximation:** Unlike methods that impose shape approximations (e.g., muffin-tin or pseudopotentials), WIEN2k applies no such simplification to the potential or charge density. This enables precise simulations of low-symmetry, layered, and strongly anisotropic materials, such as perovskites, superlattices, or 2D materials [1,11].

- **Wide Range of XC Functionals:** The software supports various exchange-correlation approximations, including LDA, GGA, the modified Becke–Johnson (mBJ) potential, and hybrid functionals like HSE06. This versatility allows researchers to fine-tune their calculations depending on the desired accuracy or material type. For instance, mBJ yields band gaps close to GW-level predictions with less computational cost [21].

- **Highly Modular Architecture:** Every calculation in WIEN2k is controlled by a separate module, and thus one has fine control over each computation step. This kind of modularity also allows scripting, automation, and interfacing to external packages such as BoltzTraP2 (for thermoelectric transport), Phonopy (for phonons), and VESTA (visualization)[1,35].

- **Parallel Computing Capabilities:** The code is optimized for parallel execution using both MPI and OpenMP. Computational bottlenecks such as `lapw1` and `lapw2` benefit significantly from distributed memory systems. This ensures scalability and feasibility for large-scale simulations involving dense k-meshes or hybrid functionals [35].

- **Broad Property Computation Spectrum:** WIEN2k can calculate structural, electronic, optical, magnetic, mechanical, thermoelectric, and phononic properties with high precision. Its integration with tools like Gibbs2 allows even thermodynamic modeling at finite temperatures, making it ideal for comprehensive material assessment [1,28].

-**Educational and Visualization Tools:** The graphical interface `w2web` simplifies job setup and management, especially for educational use. Visualization of charge densities, Fermi surfaces, and band structures via VESTA and spaghetti plots enhances understanding and presentation.

Despite its many strengths, WIEN2k is not flawless. Like any computational package, it possesses specific limitations derived from its methodological assumptions and target applications. Awareness of such limitations is of key importance in the choice of appropriate systems as well as correct interpretation of the results. Major limitations are discussed below:

- **Complex Learning Curve:** WIEN2k requires users to be proficient in UNIX/Linux systems, understand the physics of DFT, and have command-line experience. Manual editing of input files is common, and beginners may find the setup daunting without adequate documentation or training.

-Limited to Periodic Systems: WIEN2k is designed strictly for crystalline solids under periodic boundary conditions. It cannot model molecules, clusters, or amorphous materials, limiting its application in non-crystalline and low-dimensional systems like nanodots or liquids [1].

- Resource Intensive: Due to its all-electron, full-potential methodology, WIEN2k demands considerable computational resources. Calculations involving large unit cells, spin-orbit coupling, or hybrid functionals may require high-performance clusters and extended run times [11].

- No Native Phonon Solver: Phonon dispersion calculations require interfacing with PHONOPY. Generating displaced supercells and extracting force constants involves manual setup and scripting, and WIEN2k lacks an internal module for phonon computations.

-Lacks Molecular Dynamics: Unlike codes like VASP [36] or Quantum ESPRESSO [37], WIEN2k does not support time-dependent simulations or ab initio molecular dynamics (AIMD), making it unsuitable for kinetic studies or reaction dynamics.

- Manual Workflow Management: While modular, most input files must be edited manually. There is limited in-built support for automatic structure relaxation, high-throughput workflows, or convergence optimization, increasing the potential for user error.

Nevertheless, for precision DFT studies on periodic solids especially those requiring all-electron treatment WIEN2k continues to be one of the most trusted and powerful tools in the field of computational materials science.

References

[1] P. Blaha, K. Schwarz, F. Tran, R. Laskowski, G.K.H. Madsen, L.D. Marks, WIEN2k: An APW+lo program for calculating the properties of solids, J. Chem. Phys. 152 (2020) 074101. https://doi.org/10.1063/1.5143061.

[2] Sólyom, Jeno. Fundamentals of the Physics of Solids. Springer-Verlag New York, Inc, 2007.

[3] D.W. Snoke, Solid State Physics: Essential Concepts, 2nd ed., Cambridge University Press, 2020. https://doi.org/10.1017/9781108123815.

[4] Cottenier S. Density Functional Theory and the family of (L) APW-methods: a step-by-step introduction. Instituut voor Kern-en Stralingsfysica, KU Leuven, Belgium. 2002 Sep 18;4(0):41.

[5] Lee, June Gunn. Computational materials science: an introduction. CRC press, 2016.

[6] G.L.W. Hart, J.J. Jorgensen, W.S. Morgan, R.W. Forcade, A robust algorithm for k-point grid generation and symmetry reduction, J. Phys. Commun. 3 (2019) 065009. https://doi.org/10.1088/2399-6528/ab2937.

[7] P.E. Blöchl, O. Jepsen, O.K. Andersen, Improved tetrahedron method for Brillouin-zone integrations, Phys. Rev. B 49 (1994) 16223–16233. https://doi.org/10.1103/PhysRevB.49.16223.

[8] H.J. Monkhorst, J.D. Pack, Special points for Brillouin-zone integrations, Phys. Rev. B 13 (1976) 5188–5192. https://doi.org/10.1103/PhysRevB.13.5188.

[9] S. Nojima, Y. Kamakura, Irreducible First Brillouin-Zone for Two-Dimensional Binary-Compound Photonic Crystals, J. Phys. Soc. Jpn. - J PHYS SOC JPN 77 (2008). https://doi.org/10.1143/JPSJ.77.034403.

[10] H. Yang, G.-H. Yun, Y.-J. Cao, Irreducible first Brillouin zone for two-dimensional magnonic crystals with asymmetric complex lattices, Mod. Phys. Lett. B 35 (2021) 2150170. https://doi.org/10.1142/S0217984921501700.

[11] D.J. Singh, L. Nordström, Planewaves, pseudopotentials, and the LAPW method, 2nd ed, Springer, New York, NY, 2006.

[12] C. Brouder, Boundary conditions for augmented plane-wave methods, Phys. Rev. B 72 (2005) 085118. https://doi.org/10.1103/PhysRevB.72.085118.

[13] O.K. Andersen, Linear methods in band theory, Phys. Rev. B 12 (1975) 3060–3083. https://doi.org/10.1103/PhysRevB.12.3060.

[14] S. Cottenier, Density Functional Theory and the Family of (L)APW-methods: a step-by-step introduction, Instituut voor Kern-en Stralingsfysica, KU Leuven, Belgium, 2004.

[15] S. Bendaif, Étude des propriétés structurales, électroniques, thermodynamiques et thermiques des alliages quaternaires Zn1-xCdxSySe1-y , PhD Thesis, Université Badji Mokhtar – Annaba, Algeria, 2015.

[16] E. Wimmer, H. Krakauer, M. Weinert, A.J. Freeman, Full-potential self-consistent linearized-augmented-plane-wave method for calculating the electronic structure of molecules and surfaces: ${\mathrm{O}}_{2}$ molecule, Phys. Rev. B 24 (1981) 864–875. https://doi.org/10.1103/PhysRevB.24.864.

[17] Reggad, Abderrahmane. Étude par calcul ab initio des propriétés structurales et optoélectroniques de bismuthinite Bi_2S_3. Magister thesis, Université Ibn Khaldoun – Tiaret, 2013.

[18] Blaha, P., K. Schwarz, and Georg Madsen. "WIEN2K, An Augmented Plane Wave Plus Local Orbitals Program for Calculating Crystal Properties [Z]." Karlheinz Schwarz: Vienna University of Thechnology (2002).

[19] D. Singh, L. Nordström, Planewaves, Pseudopotentials and the LAPW Method, Second Edition, 2005. https://doi.org/10.1007/978-0-387-29684-5.

[20] Belkhiri, Lotfi, Boris Le Guennic, and Abdou Boucekkine. "DFT investigations of the magnetic properties of actinide complexes." Magnetochemistry 5, no. 1 (2019): 15.

[21] F. Tran, P. Blaha, Accurate Band Gaps of Semiconductors and Insulators with a Semilocal Exchange-Correlation Potential, Phys. Rev. Lett. 102 (2009) 226401. https://doi.org/10.1103/PhysRevLett.102.226401.

[22] Perdew, John P., Adrienn Ruzsinszky, Gabor I. Csonka, Oleg A. Vydrov, Gustavo E. Scuseria, Lucian A. Constantin, Xiaolan Zhou, and Kieron Burke. "Generalized gradient approximation for solids and their surfaces." arXiv preprint arXiv:0707.2088 (2007).

[23] Tran, F. "WIEN2k: an augmented plane wave plus local orbitals program for calculating crystal properties." (2018).

[24] K. Schwarz, P. Blaha, Solid state calculations using WIEN2k, Comput. Mater. Sci. 28 (2003) 259–273.

[25] E. Sjöstedt, L. Nordström, D.J. Singh, An alternative way of linearizing the augmented plane-wave method, Solid State Commun. 114 (2000) 15–20. https://doi.org/10.1016/S0038-1098(99)00577-3.

[26] A.H. MacDonald, W.E. Picket, D.D. Koelling, A linearised relativistic augmented-plane-wave method utilising approximate pure spin basis functions, J. Phys. C Solid State Phys. 13 (1980) 2675. https://doi.org/10.1088/0022-3719/13/14/009.

[27] J. Grotendorst, S. Blügel, John von Neumann-Institut für Computing, eds., Computational nanoscience: do it yourself! winter school, 14 - 22 February 2006, Forschungszentrum Jülich, Germany ; lecture notes, NIC-Secretariat, Research Centre Jülich, Jülich, 2006.

[28] G.K.H. Madsen, D.J. Singh, BoltzTraP. A code for calculating band-structure dependent quantities, Comput. Phys. Commun. 175 (2006) 67–71. https://doi.org/10.1016/j.cpc.2006.03.007.

[29] K. Momma, F. Izumi, VESTA 3 for three-dimensional visualization of crystal, volumetric and morphology data, J. Appl. Crystallogr. 44 (2011) 1272–1276. https://doi.org/10.1107/S0021889811038970.

[30] J.P. Perdew, Y. Wang, Accurate and simple analytic representation of the electron-gas correlation energy, Phys. Rev. B 45 (1992) 13244–13249. https://doi.org/10.1103/PhysRevB.45.13244.

[31] Blaha, P., K. Schwarz, G. K. H. Madsen, D. Kvasnicka, J. Luitz, and WIEN2K—An Augmented Plane Wave. "Local Orbital Program for Calculating Crystal Properties 2001." TU Wien.

[32] Calculation of optical properties (The case of TiC), http://wien2k-algerien1970.blogspot.com/2016/10/calculation-of-optical-properties-of.html (accessed May 9, 2025).

[34] Schweifer, Johannes Michael. "A distributed computing environment for material sciences." PhD diss., Technische Universität Wien, 2006.

[33] WIEN2k Developers. Files and Program Flow. In WIEN2k User's Guide / Documentation. Vienna University of Technology. Accessed May 9, 2025 Available at: https://euler.phys.cmu.edu/cluster/WIEN2k/4Files_Program.html

[35] K. Lejaeghere, G. Bihlmayer, T. Björkman, P. Blaha, S. Blügel, V. Blum, D. Caliste, I.E. Castelli, S.J. Clark, A. Dal Corso, S. de Gironcoli, T. Deutsch, J.K. Dewhurst, I. Di Marco, C. Draxl, M. Dułak, O. Eriksson, J.A. Flores-Livas, K.F. Garrity, L. Genovese, P. Giannozzi, M. Giantomassi, S. Goedecker, X. Gonze, O. Grånäs, E.K.U. Gross, A. Gulans, F. Gygi, D.R. Hamann, P.J. Hasnip, N.A.W. Holzwarth, D. Iuşan, D.B. Jochym, F. Jollet, D. Jones, G. Kresse, K. Koepernik, E. Küçükbenli, Y.O. Kvashnin, I.L.M. Locht, S. Lubeck, M. Marsman, N. Marzari, U. Nitzsche, L. Nordström, T. Ozaki, L. Paulatto, C.J. Pickard, W. Poelmans, M.I.J. Probert, K. Refson, M. Richter, G.-M. Rignanese, S. Saha, M. Scheffler, M. Schlipf, K. Schwarz, S. Sharma, F. Tavazza, P. Thunström, A. Tkatchenko, M. Torrent, D. Vanderbilt, M.J. van Setten, V. Van Speybroeck, J.M. Wills, J.R. Yates, G.-X. Zhang, S. Cottenier, Reproducibility in density functional theory calculations of solids, Science 351 (2016) aad3000. https://doi.org/10.1126/science.aad3000.

[36] . Hafner, Ab initio simulations of materials using VASP: Density-functional theory and beyond, J. Comput. Chem. 29 (2008) 2044–2078. https://doi.org/10.1002/jcc.21057

[37] P. Giannozzi, S. Baroni, N. Bonini, M. Calandra, R. Car, C. Cavazzoni, D. Ceresoli, G. L. Chiarotti, M. Cococcioni, I. Dabo, A. Dal Corso, S. de Gironcoli, S. Fabris, G. Fratesi, R. Gebauer, U. Gerstmann, C. Gougoussis, A. Kokalj, M. Lazzeri, L. Martin-Samos, N. Marzari, F. Mauri, R. Mazzarello, S. Paolini, A. Pasquarello, L. Paulatto, C. Sbraccia, S. Scandolo, G. Sclauzero, A. P. Seitsonen, A. Smogunov, P. Umari, R. M. Wentzcovitch, QUANTUM ESPRESSO: a modular and open-source software project for quantum simulations of materials, J. Phys.: Condens. Matter 21 (2009) 395502. https://doi.org/10.1088/0953-8984/21/39/395502

Chapter ***IV***

CHAPTER IV

Chapter IV: Results and Discussion

Alloying offers a practical means of tuning semiconductor properties without altering the underlying chemistry. In III–V systems such as $AlSb_{1-x}As_x$ and $AlSb_{1-x}Bi_x$, isovalent substitution simultaneously modifies the lattice constant and the band gap, enabling lattice matching and allowing the band gap to be adjusted across a wide spectral range. Notably, bismuth introduces strong spin–orbit coupling, which significantly affects the band edges, whereas arsenic preserves the electronic structure close to that of the parent compound.

The oxide–chalcogenide alloys $BaO_{1-x}S_x$ and $BaO_{1-x}Se_x$ on the II–VI side provide a precise control over ionicity and bond rigidity, which directly influence optical transparency, refractive index, and elastic properties.

This chapter examines how structure, phase stability, electronic bands, optical response, and elasticity vary with composition at x = 0, 0.25, 0.5, 0.75, and 1. First-principles calculations are employed to determine equilibrium parameters , energies and volumes, for stability evaluation, and the elastic constants C_{ij} required to validate the Born criteria and to derive bulk, shear, and Young's moduli, along with ductility indicators such as Pugh's ratio and Poisson's ratio. The electronic structures, including gap characteristics , are examined .When applicable, the influence of spin-orbit coupling on Bi-rich alloys. We derive the refractive index and absorption spectra from the complicated dielectric function to identify composition-dependent optical edges.

The goal is practical: to establish the composition–property relationships that balance lattice compatibility, mechanical stability, and the desired band gaps. By examining III–V and II–VI systems on an equal footing, the results identify the most promising compositions for device applications and clarify the associated trade-offs.

IV.I. Computational methods details

All the calculations presented in this work were performed using the full-potential linearized augmented plane-wave (FP-LAPW) method within density functional theory (DFT) [1] , using the WIEN2k code [2] , because FP-LAPW is an all-electron scheme that gives reliable total energies and structures in solids (especially with heavier atoms) and WIEN2k is a well-validated implementation. For structural properties, the exchange–correlation potential was treated with the generalized-gradient approximation in the Wu–Cohen form (WC-GGA) [3], chosen because WC-GGA is tailored for crystalline solids and typically improves lattice constants and bulk moduli over standard GGA (e.g., PBE). The recent modified Becke–Johnson potential (KTB-mBJ) by D.Koller et al. [4] was also used to study the band structures, since mBJ efficiently mitigates the band-gap underestimation of semi local GGAs at a fraction of the cost of hybrid or GW methods while preserving reasonable band ordering. In FP-LAPW, space is divided into non-overlapping muffin-tin (MT) spheres around atomic sites and an interstitial region (IR), the standard partition that lets us use atom-centered radial functions where they work best and plane waves elsewhere. Inside the MT spheres, the basis sets are described by radial solutions of the (scalar-relativistic) Kohn–Sham equation for the spherically averaged potential and their energy derivatives, multiplied by spherical harmonics; in the interstitial region, the basis consists of plane waves. In the present calculations, the plane-wave cutoff satisfied the condition $R_{MT}.K_{max} = 8$, a WIEN2k-standard compromise that delivers well-converged energies/forces without unnecessary cost. Accordingly, the muffin-tin radii for the four atoms were taken values ranging from 2.14–2.5 a.u., as large as possible without sphere overlap during relaxation, to capture more atomic character and keep the plane-wave part modest. The maximum angular momentum for the wave-function expansion inside the atomic spheres was limited to $l_{max} = 10$, which is sufficient to represent the angular character (including d- and higher components) .

The charge density was expanded up to $G_{max} = 14(Ryd)^{(1/2)}$, a safe, widely used value that stabilizes total energies and forces. A mesh of 47 special k-points for the binary compounds and about 64 k-points for the ternary alloys was used in the irreducible Brillouin zone, with the denser sampling for ternaries reflecting their larger cells/complexity and being sufficient to meet our

energy criterion. Convergence threshold: 0.1 mRy in total energy between consecutive SCF steps (≈ 1.36 meV), chosen to secure robust phase-energy separations, a tight threshold that ensures robust energy differences and dependable derived properties. For optical properties and the density of states (DOS), we employed a much denser k-mesh of 5000 k-points using the same KTB-mBJ potential, because optical spectra and DOS converge more slowly and require fine sampling to resolve band-edge features, van Hove singularities, and interband transitions cleanly. For elastic properties, we used 3000 k-points, since stress/strain derivatives benefit from smooth Brillouin-zone integration but do not require the extreme resolution needed by optics/DOS. The phase stability was studied employing the Gibbs2 code [5], which fits the E(V) data to an equation of state and evaluates thermodynamic functions within a quasi-harmonic Debye framework, so we can compare Gibbs free energies versus temperature and pressure in a consistent way. Spin–orbit coupling (SOC) was included in a second-variational step for $AlSb_{1-x}Bi_x$ to capture the relativistic effects of the heavy Bi.

IV.II. Convergence tests for chosen global settings

To avoid redundant convergence scans on all twenty systems, we established global numerical settings using four representatives—AlAs, $AlSb_{0.75}As_{0.25}$, BaO, and $BaO_{0.25}Se_{0.75}$—chosen to bracket our dataset across chemistry (covalent III–V ↔ oxide/chalcogenide), cell size (primitive ↔ supercell), order (binary ↔ alloy), and elemental hardness (O ↔ Se). For each, we perfomed convergence tests converged RK_{max} and the Brillouin-zone sampli ng (k-points) :

a) Total-energy convergence vs RK_{max} (AlAs, $AlSb_{0.75}As_{0.25}$, BaO, $BaO_{0.25}Se_{0.75}$)

Figure IV.1 shows total-energy convergence with Rk_{max} density for AlAs, $AlSb_{0.75}As_{0.25}$, BaO, and $BaO_{0.25}Se_{0.75}$Across all four systems, the total energy drops steeply from RKmax = 4→5 and then stabilizes; beyond RKmax ≈ 7 residual changes are at the micro-Rydberg level. We therefore adopt RKmax = 8, which sits firmly on the flat part of the curve, adds a small safety margin over the minimal converged value, and avoids the unnecessary cost of 9–10. This choice ensures consistent, production-level accuracy across compositions for derived properties (relaxations, bands, optics) without bloating runtime.

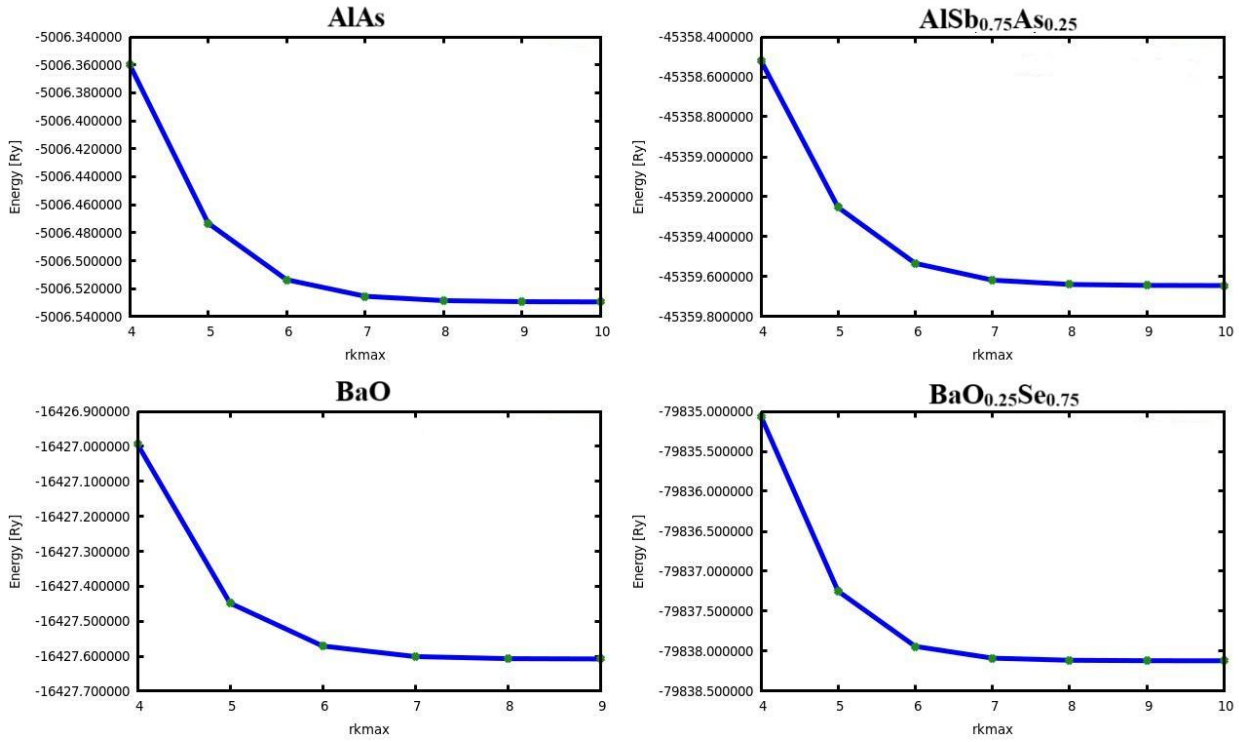


Figure IV.1. Total-energy convergence with RK_{max} density for AlAs, $AlSb_{0.75}As_{0.25}$, BaO, and $BaO_{0.25}Se_{0.75}$

b) Total-energy convergence vs k-point sampling

Figure IV.2 shows total-energy convergence with k-point density for AlAs, $AlSb_{0.75}As_{0.25}$, BaO, and $BaO_{0.25}Se_{0.75}$. In all cases the energy drops steeply at low sampling and then flattens; beyond ~400–600 k-points (binaries) or ~50–75 (ternaries) residual changes are at the μRy level. For production we therefore use 1000 k-points for binaries, which by symmetry reduce to 47 points in the IBZ, and 150 k-points for ternaries, which reduce to 64 IBZ points. This choice equalizes the effective IBZ sampling across the higher-symmetry binaries and lower-symmetry alloyed cells, places all systems on the flat part of the convergence curves, and avoids the unnecessary cost of denser meshes without compromising accuracy for derived properties.

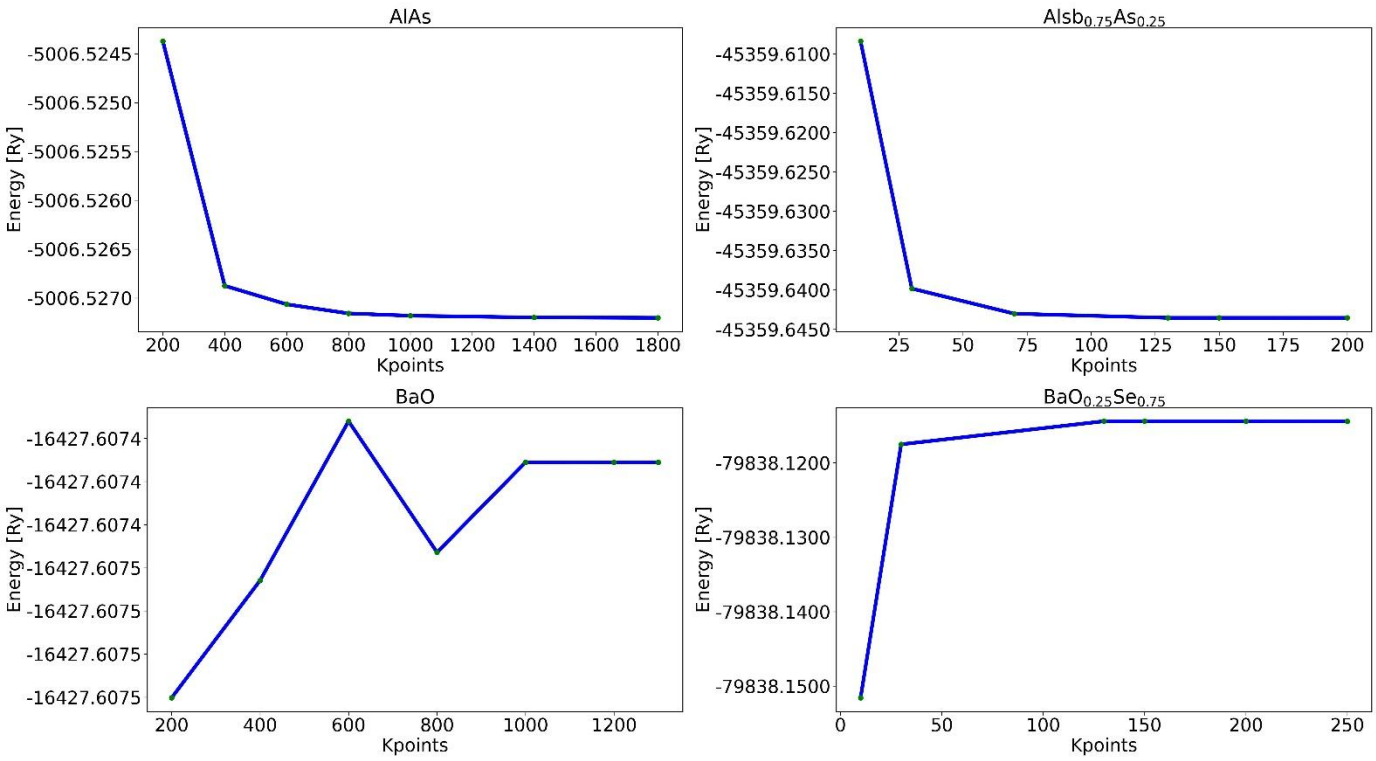


Figure IV.2. Total-energy convergence with K-points density for AlAs, $AlSb_{0.75}As_{0.25}$, BaO, and $BaO_{0.25}Se_{0.75}$

IV.III. Structural properties

IV.III.1. Phase Stability

Phase stability was determined from total-energy versus volume datasets, E(V), fitted for each candidate polymorph and composition to the Murnaghan equation of state (eq IV.1) in energy–volume form. For each composition, the ambient-pressure ground state is the phase with the lowest fitted E_0.

$$E(V) = E_0 + \frac{B_0 V}{B_0'(B_0'-1)}\left[\left(\frac{V_0}{V}\right)^{B_0'} + (B_0' - 1)\right] - \frac{B_0 V_0}{B_0'-1} \qquad (\mathbf{IV.1})$$

For $AlSb_{1-x}Bi_x$, introducing bismuth expands the lattice: V_0 increases with x and B_0 decreases toward the Bi-rich side. Zinc-blende remains lowest at P = 0 (Figure IV.3) , but the ZB–WZ energy separation narrows at high x, reflecting the effect larger and more polarizable Bi anion. Where the fitted ΔE_0 becomes small, the total energy curves constructed from the EOS indicate that any

structural crossover, if present, would occur only at finite pressure rather than at ambient conditions.

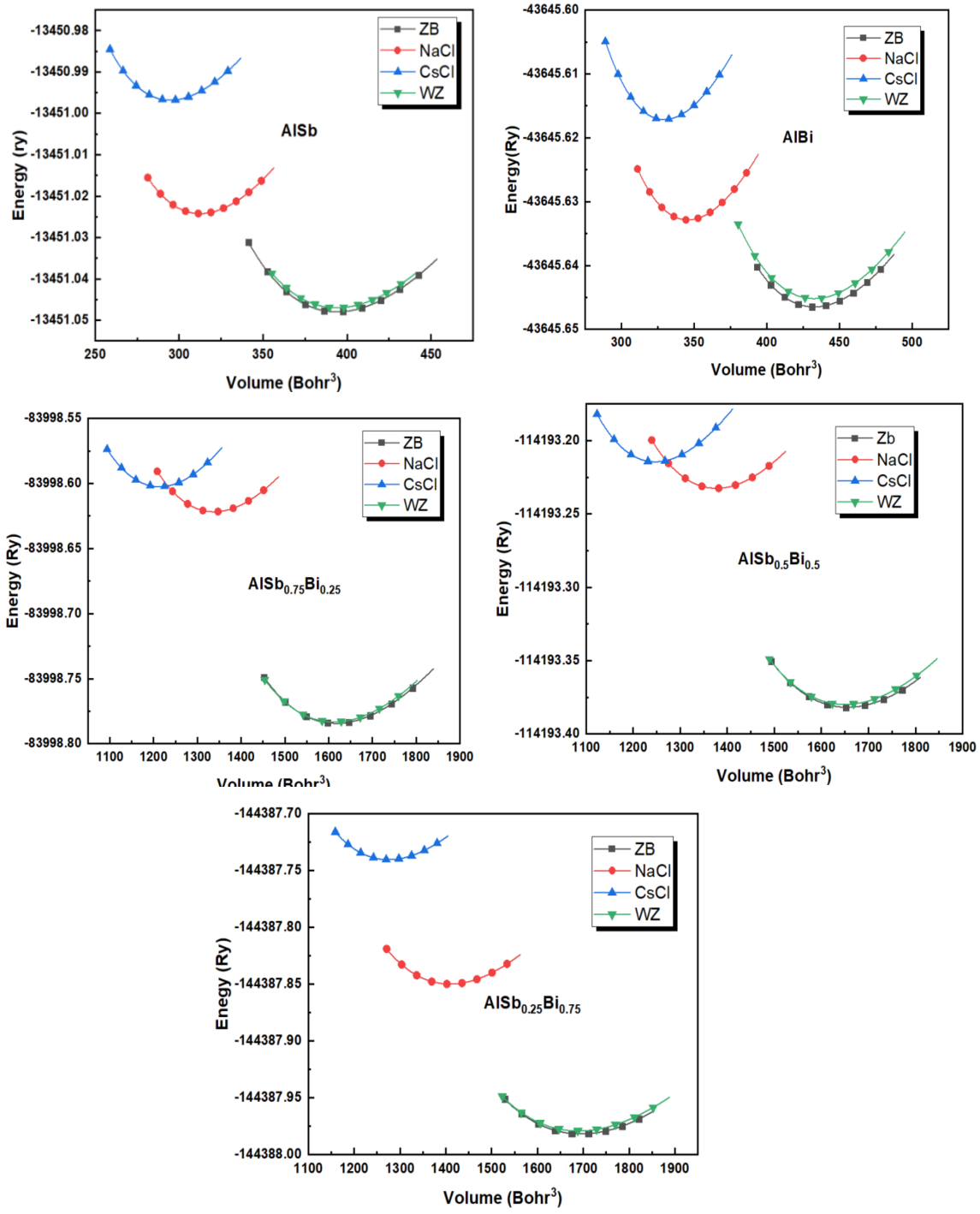


Figure. IV.3. Total-energy vs volume datasets, fitted with a Murnaghan EOS, for ZB(B3), NaCl (B1), CsCl (B2) , and WZ for $AlSb_{1-x}Bi_x$ alloys .

From Figure IV.4 we note that $AlSb_{1-x}As_x$, the zinc-blende (F-43m) well is systematically the deepest at P = 0 across the studied compositions, establishing zinc-blende as the ambient ground state. The wurtzite ($P6_3mc$) well remains higher by a small difference but consistent energy margin, and the EOS-based total energy comparison does not reveal a low-pressure crossing, indicating no spontaneous ZB to WZ transition under modest compression.

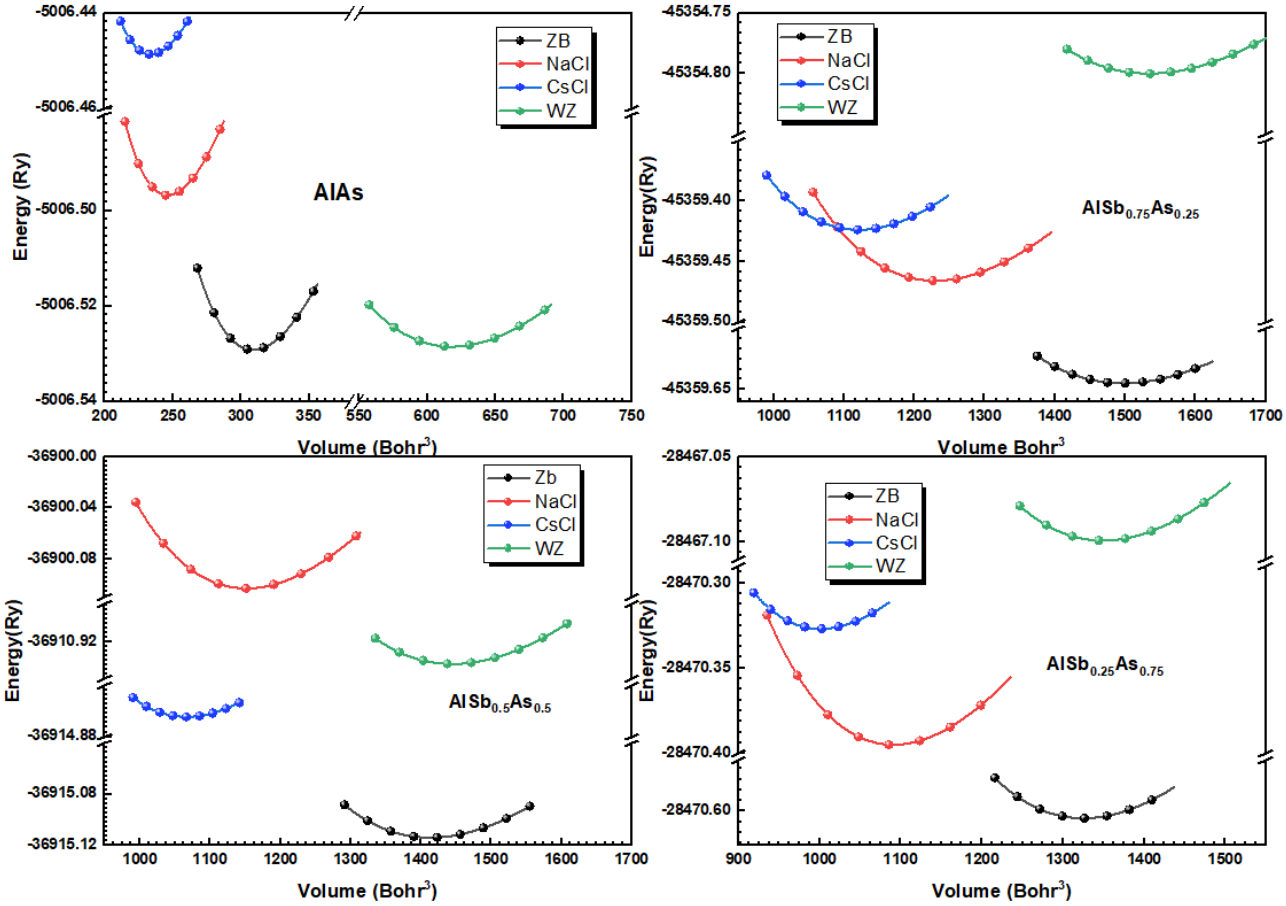


Figure. IV.4. Energy–volume points fitted with a Murnaghan EOS for the ZB, NaCl, CsCl, and WZ polymorphs of $AlSb_{1-x}As_x$ alloys .

For $BaO_{1-x}S_x$ and $BaO_{1-x}Se_x$ (Figures IV.5 and IV.6 it is clear that rocksalt is the ambient ground stateat ambient conditions. Substituting O by S or Se increases V_0, so B_0 is expected to decrease with x. The CsCl (B2, Pm-3m) wells lie appreciably higher at zero pressure.

Overall, the EOS analysis yields a consistent structural picture at ambient pressure showing the most stable zinc-blende for both III–V series and rocksalt for both II–VI series; together with composition-dependent trends in V_0 and B_0 that align with chemical expectations. Where phase competitions tighten at the Bi-rich, the enthalpy curves will provide a transparent way to discuss potential pressure-induced transitions without leaving the E(V) framework.

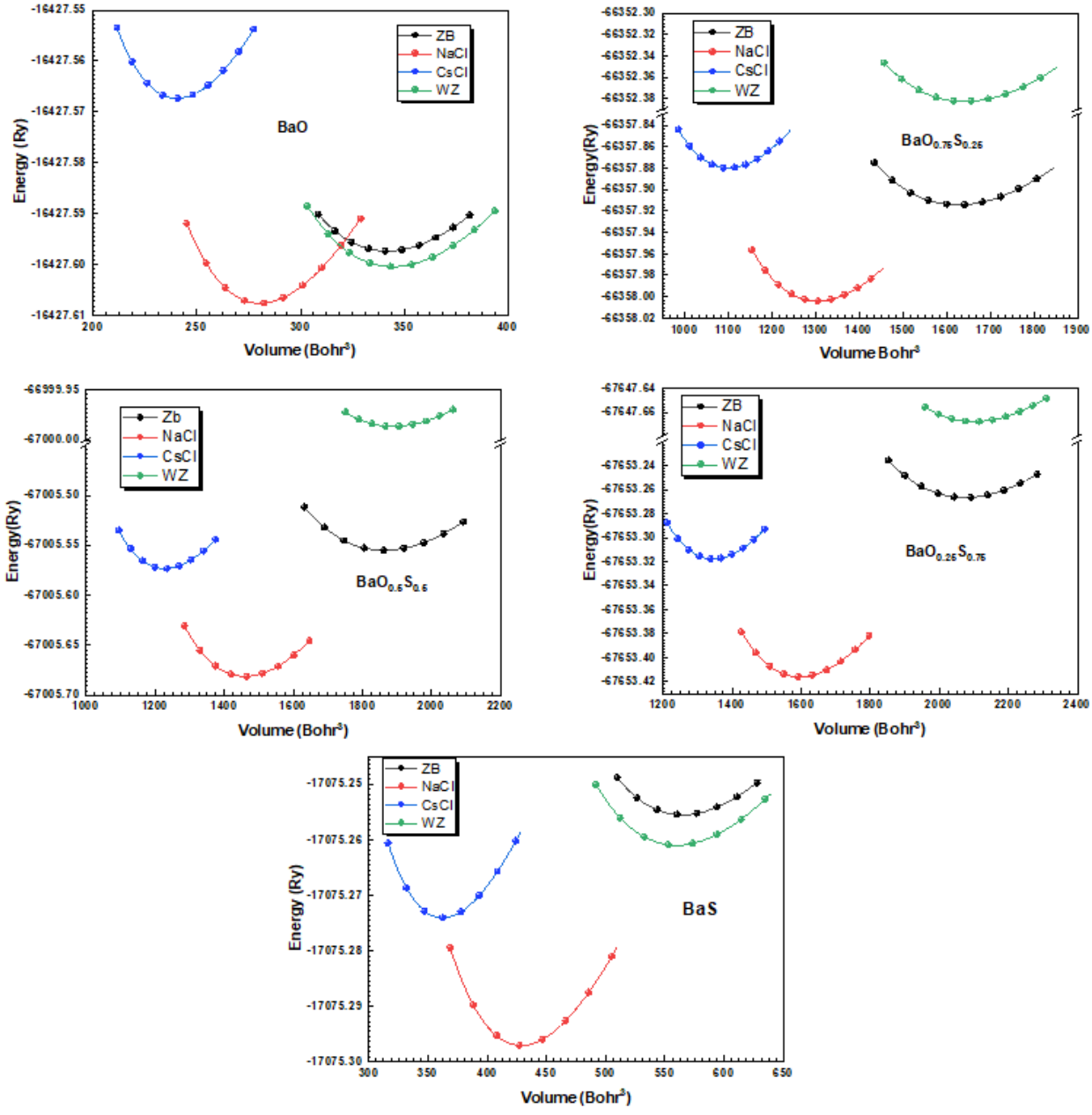


Figure. IV.5. Energy–volume points fitted with a Murnaghan EOS for the ZB, NaCl, CsCl, and WZ polymorphs for $BaO_{1-x}AS_x$ for $(x = 0,0.25,0.5,0.75and1)$ alloys .

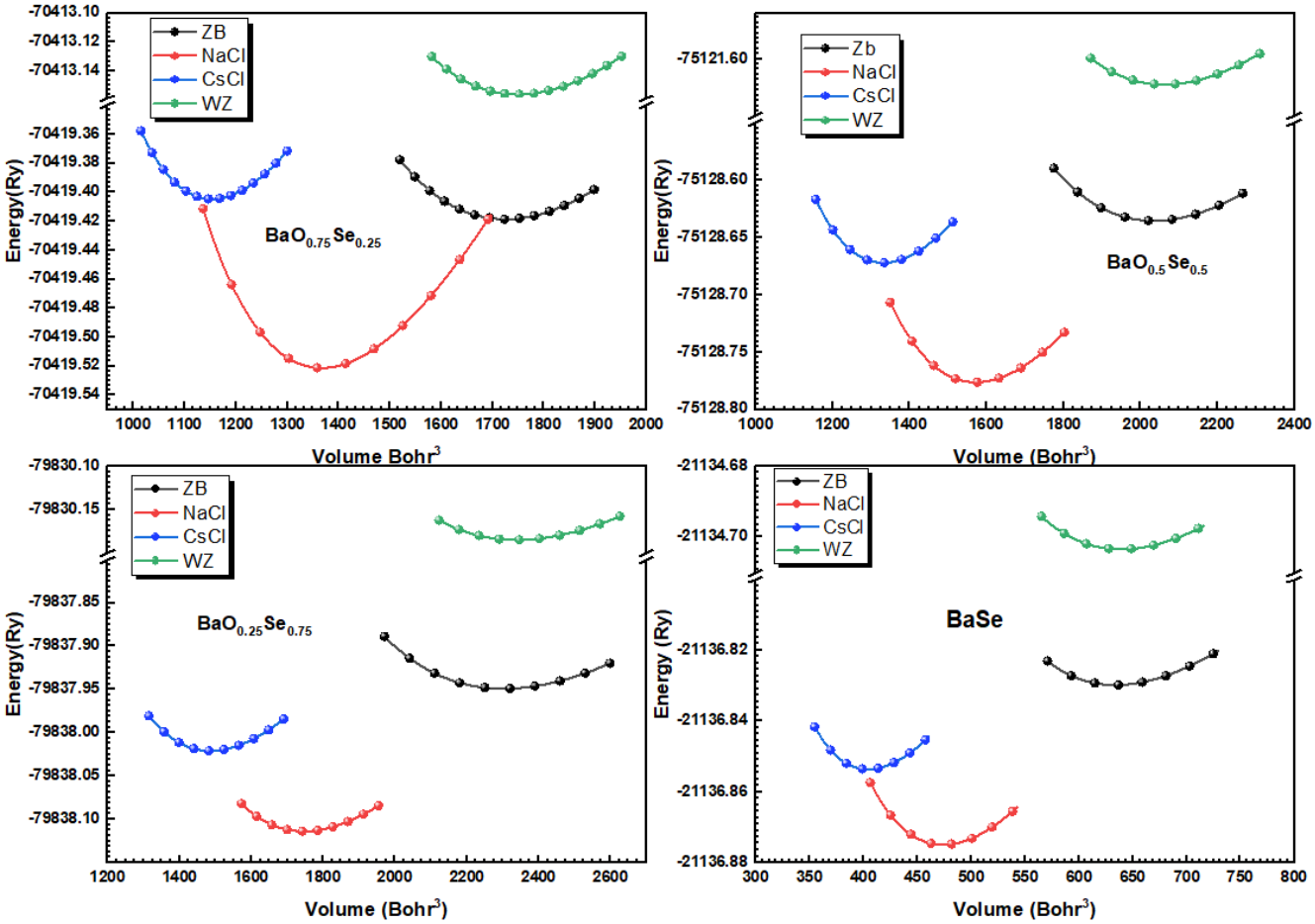


Figure. IV.6. Energy–volume points fitted with a Murnaghan EOS for the ZB, NaCl, CsCl, and WZ polymorphs of $BaO_{1-x}AS_x$ for($x = 0,0.25,0.5,0.75 and 1$) alloys using WC-GGA approximation.

The phase-stability analysis identifies zinc blende (F-43m) as the ground state at P=0 for all examined III–V alloys; accordingly, all electronic, optical, and elastic properties are calculated in zinc blende at each composition. For the group II–VI alloys, the rocksalt (NaCl) structure is the most stable, so all properties are reported in that phase as well.

IV.III.2. Pressure induced phase transitions

All transition pressures were evaluated strictly at zero temperature (T = 0 K) using static DFT energies for each candidate lattice (ZB, NaCl a CsCl,and WZ). At any external pressure P, the static enthalpy is defined as H(P) = E(V) + P·V; we therefore compute the equilibrium volume V(P) from the EOS (Eq. (4)) and substitute it into E(V) to obtain H(P) (Eq. **IV. 2**) for each phase. Phase

boundaries are identified where the enthalpy curves intersect (Eq. (IV. 3)). The precise definitions used are summarized in Eqs. (IV.2)–(IV.5) [6–9].

Static enthalpy used to rank phases at a given pressure (see text):

$$H(P) = E(V) + P \qquad (\mathbf{IV.2})$$

Pressure can equivalently be obtained from the slope of the E(V) curve (Eq. (VI.3)), which is consistent with the chosen EOS fit. We use this derivative primarily as a diagnostic for the smoothness and fidelity of the fitted curve.

Mechanical definition of pressure from the fitted E(V):

$$P = -\partial E/\partial V \qquad (\mathbf{IV.3})$$

The Murnaghan pressure–volume relation used for fitting is given by Eq. (**IV. 4**), parameterized by the equilibrium volume V_0, bulk modulus B_0, and its pressure derivative B_0'.

Murnaghan equation of state used to fit E(V) datasets:

$$P(V) = \frac{B_0}{B_0'}\left[(V_0/V)\, B_0' - 1\right] \qquad (\mathbf{IV.4})$$

For enthalpy evaluations via Eq. (1), we use the analytical inverse V(P) in Eq. (**IV. 5**), which avoids numerical noise from interpolation and ensures consistency across phases.

Closed-form inverse that provides the equilibrium volume at a given pressure:

$$V(P) = V_0\left[1 + \frac{B_0'}{B_0}P - 1/B_0'\right] \qquad (\mathbf{IV.5})$$

Finally, the critical pressure between two phases i and j is defined by the enthalpy crossing in Eq. (**IV.** 6). Operationally, we evaluate H(P) for all phases on a fine grid using Eqs. (**IV.** 2)and (IV. 5), then record the smallest P at which the minimum enthalpy changes identity.

The phase stability sequence was extracted by comparing H(P,T) among the candidate structures, and the transition pressure P_c for a pair (i,j)was identified by the crossing condition

$$H_i(P_c) = H_j(P_c) \qquad (\mathbf{IV.6}).$$

a) III-V alloys

Figures (IV.7 and IV.8) display the enthalpy H(P) at T ≈ 0K for the ZB, NaCl (B1), CsCl (B2), and WZ structures of the selected III–V alloys. According to Eq (**IV. 6**) the transition pressure between any two phases is identified from the point where their respective enthalpy–pressure curves intersect within the plotted range.

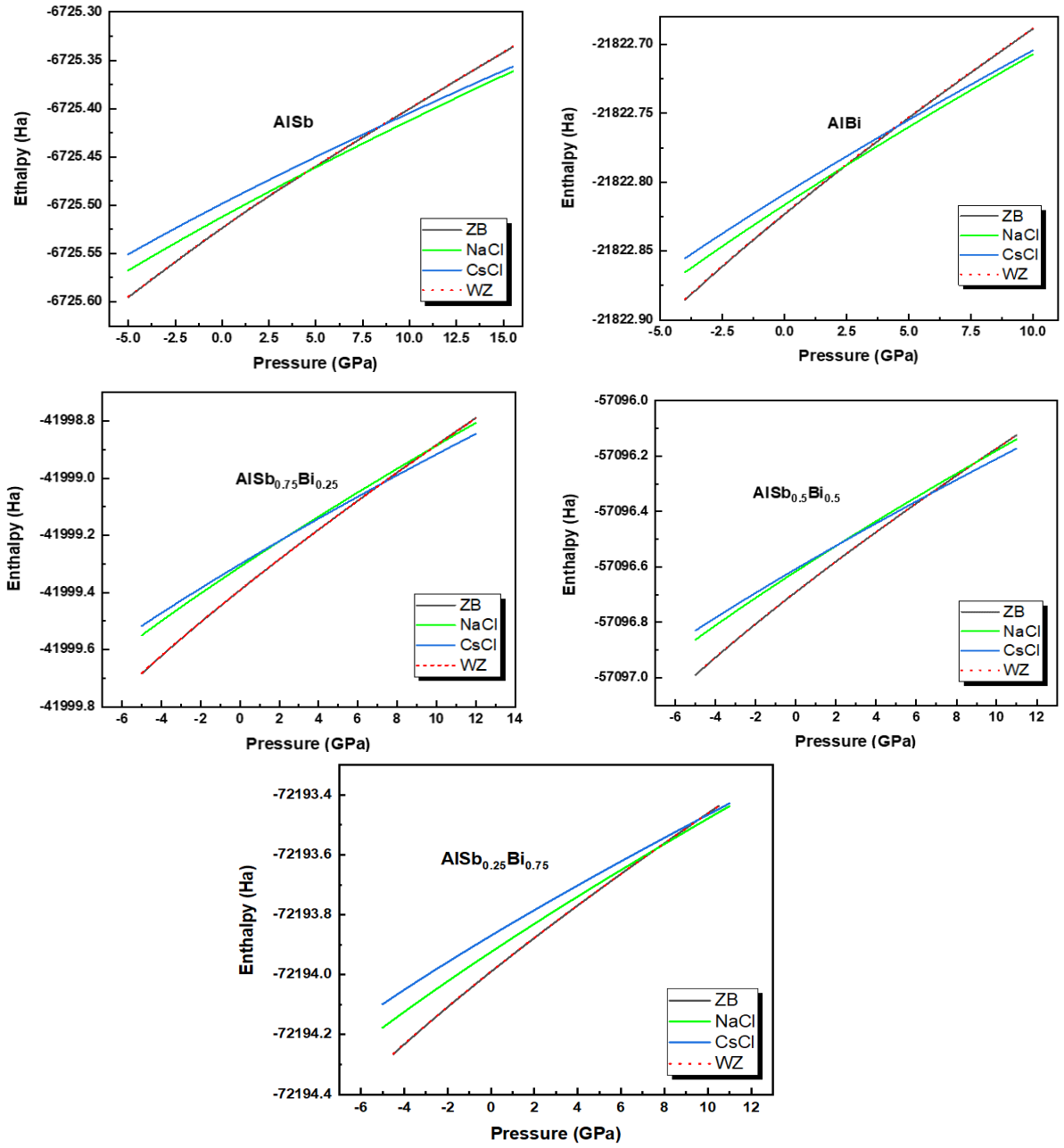


Figure IV.7. Calculated enthalpy versus pressure (0 K) for the ZB, NaCl, CsCl, and WZ (wurtzite) geometries for $AlSb_{1-x}Bi_x$ alloys.

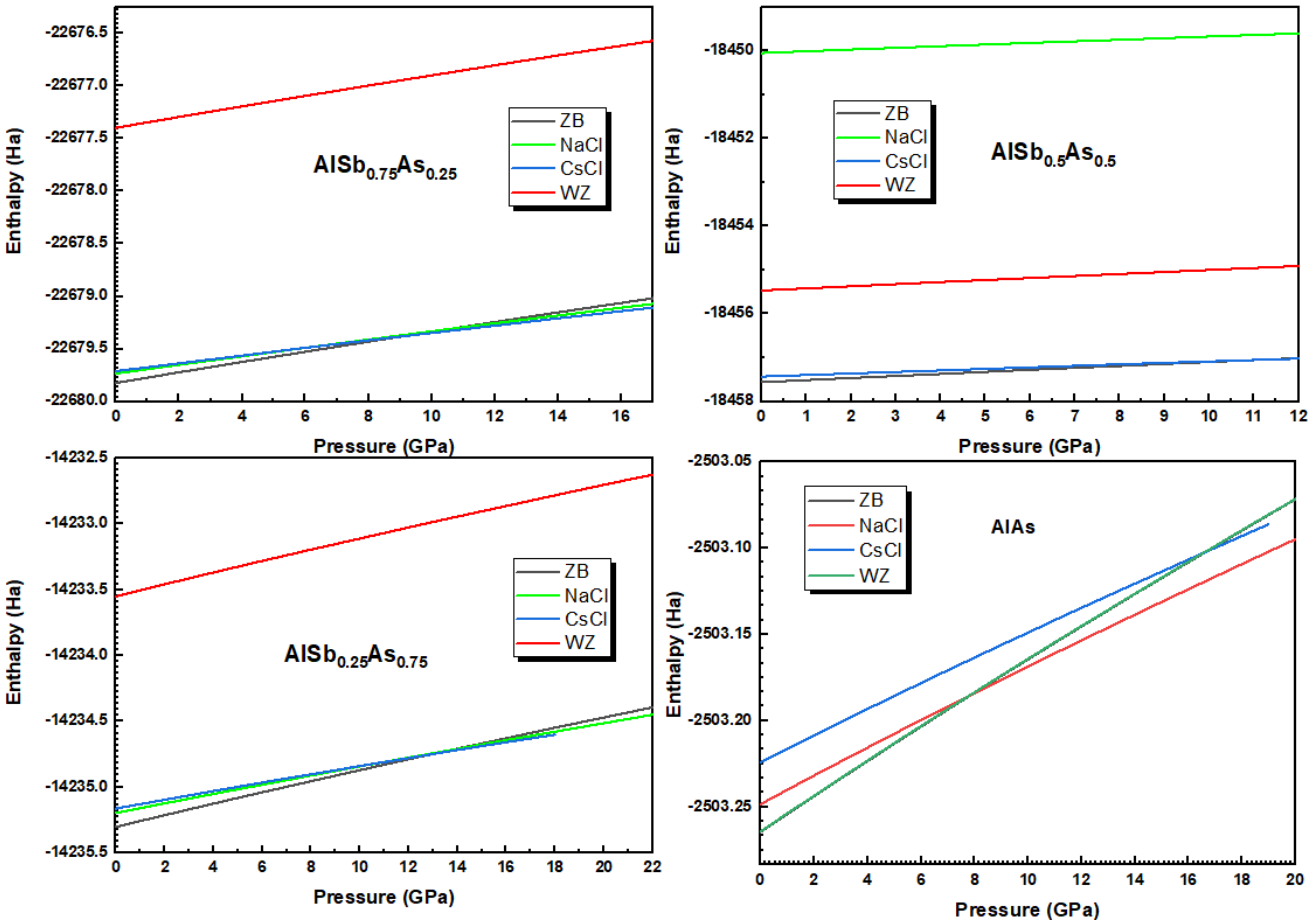


Figure IV.8. Computed enthalpies as a function of pressure at T=0K for the ZB, NaCl, CsCl, and WZ geometries for $AlSb_{1-x}As_x$ alloys for (x=0.25, 0.5, 0.75 and 1)

The extracted phase transitions pressures of the selected III-V alloys are tabulated in table IV.1 along with other available calculations and experimental data.

For $AlSb_{1-x}Bi_x$, the enthalpy crossings H(P)=E+PV reproduce the transitions in Table **IV**.1 . At x = 0 (AlSb), our ZB to NaCl pressure is 4.56 GPa, below the experimental range 6.2–8.3 GPa but close to a prior calculation (4.59 GPa) and lower than another report (~8 GPa). For the denser phase, our ZB to CsCl is 8.47 GPa, reasonably consistent with a reported theoretical value (7.81 GPa); WZ to CsCl (8.31 GPa) is also close to literature (8.24 GPa). Across the alloy, ZB remains the ground state at P = 0, and the enthalpy curves show direct ZB to CsCl transitions at x = 0.25 (7.18 GPa) and x = 0.5 (6.63 GPa), which occur before the corresponding ZB to NaCl crossings (9.69 and 8.95 GPa. At x = 0.75, the two-step sequence returns (ZB to NaCl 7.65 GPa, then NaCl to CsCl 9.57 GPa). The Bi-rich end (AlBi) compresses most readily, with ZB to NaCl at 2.42 GPa

and ZB to CsCl near 4.5 GPa. Overall, our absolute Pc for AlSb slightly underestimates experiment (a common GGA tendency), but the phase order and composition trends agree with prior calculations listed in the table.

Table IV.1. Calculated transition pressures P_c of the selected III-V alloys at 0K temperature

				P_c (GPa)			
$AlSb_{1-x}Bi_x$				$AlSb_{1-x}As_x$			
	Our results	Experiment	Other calc		Our results	Experiment	Other calc
X=0(AlSb)				**X=0.25**			
ZB to NaCl	4.56	6.2[10] , 8.3 [11]	8 [12],4.59 [11]	ZB to NaCl	9.12	–	–
ZB to CsCl	8.47	–	7.81[11]	ZB to CsCl	9.08	–	–
WZ to CsCl	8.31	–	8.24 [11]	NaCl to CsCl	5.88		
WZ to NaCl	4.34	–	–	**x=0.5**			–
				ZB to NaCl	11.14	–	
x=0.25				**x=0.75**			
ZB to NaCl	9.69	–	–	ZB to NaCl	13.92	–	–
ZB to CsCl	7.18	–	–	ZB to CsCl	12.93	–	–
WZ to CsCl	7.24	–	–	NaCl toCsCl	10.96	–	–
WZ to NaCl	9.50	–	–	**x=1(AlAs)**			
				ZB to NaCl	7.88	12	8.18[13], 7.4 [14]
x=0.5				ZB to CsCl	16.6		76.8[10], 77.9 [15]
ZB to NaCl	8.95	–	–				
ZB to CsCl	6.63	–	–	WZ to CsCl	16.5	–	–
WZ to CsCl	6.65	–	–	WZ to NaCl	7.73	–	–
WZ to NaCl	9.02	–	–				
x=0.75							
ZB to NaCl	7.65	–	–				
ZB to CsCl	9.57	–	–				
WZ to CsCl	9.62	–	–				
WZ to NaCl	7.68	–	–				
x=1							
ZB to NaCl	2.42	–	–				
ZB to CsCl	4.52	–	–				
WZ to CsCl	4.33	–	–				
WZ to NaCl	2.18	–	–				

For $AlSb_{1-x}As_x$, Fig. IV.4 shows ZB as the deepest E(V) well at P = 0 for all x, with V_0 decreasing as As replaces Sb. For AlAs, our ZB to NaCl is 7.88 GPa below the experimental ≈12 GPa, but within the spread of prior calculations (7.4–8.18 GPa). We obtain ZB to CsCl ≈16.6 GPa at the end member. For mixed compositions, the enthalpy curves explain the entries in Table IV.1: a direct ZB to CsCl switch at x = 0.25 (9.08 GPa, essentially at or just below ZB to NaCl 9.12 GPa) and again

at x = 0.75 (12.93 GPa before ZB to NaCl 13.92 GPa), while x = 0.5 ZB to NaCl occurs at 11.14 GPa and CsCl only at higher P). No experimental values are available for the mixed alloys.

b) II-VI alloys

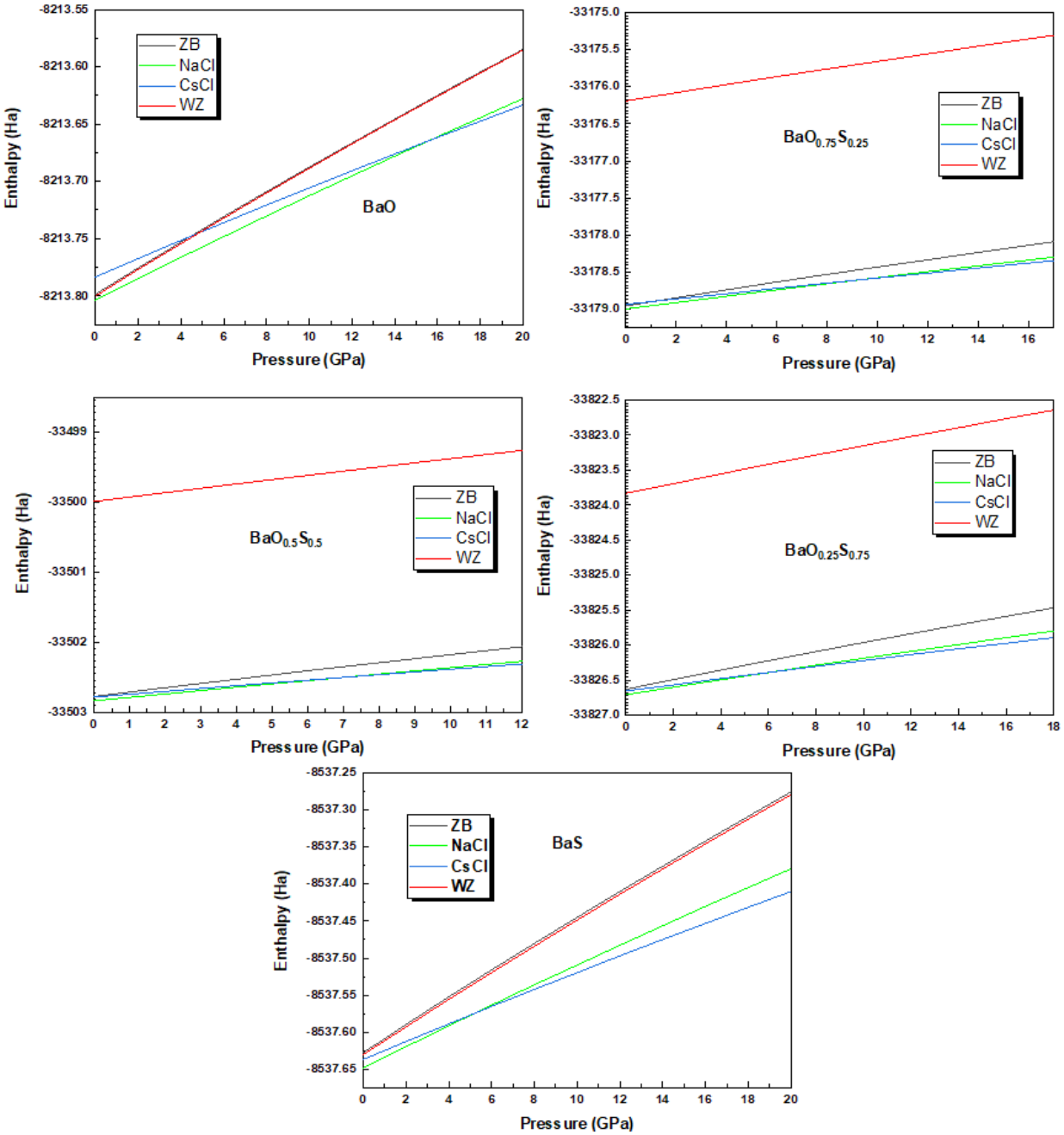


Figure IV.9. Computed enthalpies as a function of pressure at T=0K for the ZB, NaCl, CsCl, and WZ geometries for $BaO_{1-x}S_x$ alloys for (x=0, 0.25, 0.5, 0.75 and 1)

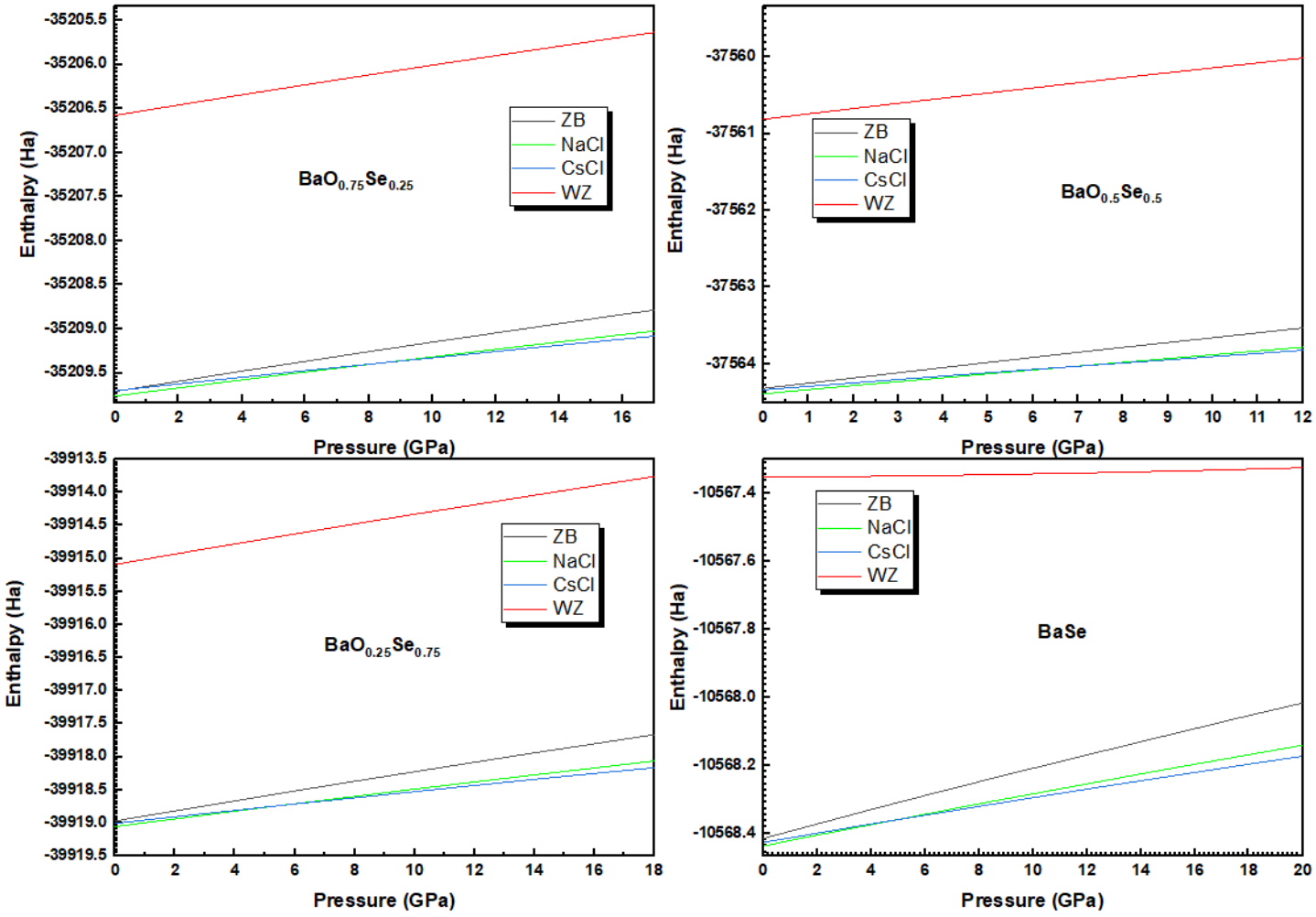


Figure IV.10. Computed enthalpies as a function of pressure at T=0K for the ZB, NaCl, CsCl, and WZ geometries for $BaO_{1-x}Se_x$ alloys for (x=0.25, 0.5, 0.75 and 1)

Figures IV.9 and IV.10 present the estimated enthalpy–pressure relations (T=0 K) in the ZB, NaCl, CsCl and WZ for the selected II-VI alloys $BaO_{1-x}S_x$ and $BaO_{1-x}Se_x$ respectively. The extracted phase transitions pressures of the selected alloys are tabulated in table VI.4 along with other calculations and available experimental data in literature.

$BaO_{1-x}S_x$. The calculated NaCl to CsCl pressure decreases rapidly with small sulfur additions and then tapers as x increases: 15.51 GPa at BaO, 9.30 GPa at x = 0.25, 7.03 GPa at x = 0.5, 5.90 GPa at x = 0.75, and 5.19 GPa at BaS. Relative to literature, our BaO endpoint is higher than the experimental entry (~10 GPa) yet below other prior 0-K DFT values (≈17.8–21 GPa). On the sulfur-rich side, our BaS value (5.19 GPa) lies ~1–1.5 GPa below the room-temperature experiment

(~6.5 GPa) and at the lower edge of reported DFT results (≈6.0–8.2 GPa). Overall, $P_c(x)$ shows a steep initial drop from x = 0 to 0.25 and a gentler decline thereafter.

For $BaO_{1-x}Se_x$. Selenium lowers the NaCl to CsCl pressure further at the same composition: 8.29 GPa at x = 0.25, 6.64 GPa at x = 0.5, 5.44 GPa at x = 0.75, and 4.65 GPa at BaSe. The BaSe endpoint agrees with published DFT values (≈5.2–6.0 GPa) and remains ≈1–1.5 GPa below the experimental ~6 GPa. As with sulfur, $P_c(x)$ decreases smoothly with x, but the absolute pressures are lower across the Se series.

At matched compositions, $BaO_{1-x}Se_x$ consistently requires less pressure than $BaO_{1-x}S_x$ to reach CsCl (e.g., 8.29 vs 9.30 GPa at x = 0.25; 6.64 vs 7.03 GPa at x = 0.5; 5.44 vs 5.90 GPa at x = 0.75; 4.65 vs 5.19 GPa at the endpoints). Thus, Se is the more effective anion for reducing P_c, and the reduction grows modestly toward the chalcogen-rich end.

Table IV.2. Calculated transition pressures P_c of the selected II-VI alloys at 0K temperature

P_c (GPa)							
$BaO_{1-x}S_x$				$BaO_{1-x}Se_x$			
	Our results	Exp	Other calc		Our results	Exp	Other calc
x=0(BaO)				**x=0.25**			
NaCl to CsCl	15.51	10 [16]	17.8[17], 21[18]	NaCl to CsCl	8.29		
x=0.25				**x=0.5**			
NaCl to CsCl	9.30			NaCl to CsCl	6.64		
x=0.5				**x=0.75**			
NaCl to CsCl	7.03			NaCl to CsCl	5.44		
x=0.75				**x=1(BaSe)**			
NaCl to CsCl	5.90			NaCl to CsCl	4.65	6.0[19]	5.2[20], 6.02[21]
x=1(BaS)							
NaCl to CsCl	5.19	6.5[16]	8.2[22],7.3[23]				

Unfortunately, We did not find composition resolved experimental Pc or prior DFT values for the intermediate alloys in either series, published data concentrate on binaries only. Thus, We strongly encourage further high-pressure experiments and complementary DFT calculations on the intermediate compositions (x = 0.25–0.75) in both III-V and II-VI alloys. Such work would help validate the predicted $P_c(x)$ trends, strengthen the end-member comparisons.

IV.III.3. Equilibrium Lattice Parameters (a_0) and Bulk Moduli (B_0)

a) III-V selected alloys

$AlSb_{1-x}Bi_x$: (Table IV.3) Over the span x (0 → 1) we find a net increase in the lattice parameter of +3.16% (6.1585 → 6.3532 Å) accompanied by a net decrease in the bulk modulus of −19.33% (53.54 → 43.19 GPa). In the equation-of-state view, the fitted equilibrium volume V_0 grows with x while the local curvature of E(V) at V_0 becomes shallower, so $B_0 = V_0 \frac{\partial^2 E}{\partial E^2}$ drops accordingly. These trends are consistent with independent calculations at matched compositions our (a_0) tends to be slightly larger and our B slightly smaller, which is typical of WC–GGA. For the endpoints: for AlSb we are within +0.38% in a and −2.83% in B of experiment; for AlBi our (a_0) is 0.26% below the measured value and our B aligns with other DFT results (≈43–44 GPa).

Table IV.3. Estimated computational values of lattice parameters *a* (in Å) and bulk modulus *B* (in GPa) of selected III-V ternary alloys in ZB phase via the Wu–Cohen (WC–GGA) approximation, compared with other calculations and experimental data.

$AlSb_{1-x}Bi_x$	Our work		Other Works		Experimental	
x	a (Å)	B (GPa)	a (Å)	B (GPa)	a (Å)	B (GPa)
AlSb (x=0)	6.1585	53.5403	6.1132[24], 6.16[25]	56.38[24] , 54.00[25]	6.1353[26]	55.1[27]
0.250	6.2104	51.1872	6.1616 [24]	53.5739[24]	–	–
0.500	6.2594	48.2488	6.2073[24]	51.054[24]	–	–
0.750	6.3092	45.8179	6.2621[24]	48.1380[24]	–	–
AlBi (x=1)	6.3532	43.1915	6.3562[28] ,6.361[29]	43.1684[28], 43.85[29]	6.37 [30]	–
$AlSb_{1-x}As_x$	Our work		Other Works		Experimental	
x	a (Å)	B (GPa)	a (Å)	B (GPa)	a (Å)	B (GPa)
AlSb (x=0)	6.1585	53.5403	6.1132[24], 6.16[25]	56.38[24] , 54.00[25]	6.1353[26]	55.1[27]
0.250	6.0539	56.8292	5.97[13],	59.92[13]	–	–
0.500	5.9391	60.6762	5.853[13],	64.03[13]	–	–
0.750	5.8128	65.7221	5.733[13],	69.04[13]	–	–
AlAs (x=1)	5.6740	72.5594	5.6280[31],5.6918[32]	71.855[33], 73.33[32]	5.66[34]	74[34]

$AlSb_{1-x}As_x$: (Table IV.3) Throughout the same interval we observe the corresponding response: a net contraction of −7.87% in a_0 (6.1585 → 5.6740 Å) with a net stiffening of +35.52% in B (53.54 → 72.56 GPa). Here V_0 decreases so B_0 rises.

Comparisons support this reading: at the AlAs endpoint our computed (a) sits +0.25% above experiment and within the DFT spread, while our B is −1.9% relative to experiment yet consistent with other calculations (≈72–73 GPa). At intermediate x, we show the usual WC–GGA pattern (slightly larger a, slightly smaller B than some supercell studies.

Across both series**,** increasing x in $AlSb_{1-x}Bi_x$ enlarges V_0 and lowers B_0; while increasing x in $AlSb_{1-x}As_x$ does the opposite, shrinking V_0 and higher B_0. The close endpoint agreement with experiment and the consistent tracking of other DFT indicate that the observed net percentage changes (Bi: a_0↑≈3%, B↓≈19%; As: a↓≈8%, B↑≈36%) arise from predictable shifts in equilibrium volume and local stiffness encoded by the EOS.

b) II-VI selected alloys

$BaO_{1-x}S_x$: The lattice constant increases smoothly from 5.4993 Å (BaO) to 6.3340 Å (BaS) (Δa = +0.835 Å, +15.2%),. Concomitantly, the bulk modulus drops from 79.04 to 46.49 GPa (ΔB = −32.55 GPa, −41.2%). Our obtained results agree well with available prior calculations and available experimental data.

$BaO_{1-x}Se_x$: Here the expansion is stronger: 5.4993 Å → 6.5508 Å (Δa = +1.052 Å, +19.1%), and bowing is more pronounced, with $b_a^{(Se)} \approx +0.519$ Å (≈ +2.15% at x = 0.5). The bulk modulus decreases from 79.04 to 39.92 GPa (ΔB = −39.11 GPa, −49.5%). Our results agree with available prior calculations and available experimental data.

Quantitatively, Se substitution yields ~26% greater total lattice expansion and ~20% stronger total softening than S over the same composition range, Within WC–GGA accuracy, endpoints match experiment to within ≲1% for (a_0) , indicating that the calculations reliably capture both systematic composition trends and the nonlinear alloying effects that govern compressibility in rock-salt BaO–S/Se.

Table IV.4. Estimated computational values of lattice parameters *a* (in Å) and bulk modulus *B* (in GPa) of selected II-VI ternary alloys in NaCl phase via the Wu–Cohen (WC–GGA) approximation, compared with other calculations and experimental data.

$BaO_{1-x}S_x$	Our work		Other Works		Experimental	
x	**a (Å)**	**B (GPa)**	**a (Å)**	**B (GPa)**	**a (Å)**	**B (GPa)**
BaO (x=0)	5.4993	79.0351	5.5200[35],5.478[36]	76.076[35],82.36[36]	5.5240[37]	75.6 [38]
0.250	5.7824	63.6189	5.839[39],5.8600[40]	55.55[40]	-	-
0.500	6.0037	54.7037	6.0090[40]	48.58[40]	-	-
0.750	6.1846	49.7187	6.245[39], 6.2700[40]	43.76[40]	-	-
BaS (x=1)	6.3340	46.4851	6.4400[40],6.4070[39]	40.93[40], 40.25[23]	6.3840[37]	39.42 [41]
$BaO_{1-x}Se_x$	Our work		Other Works		Experimental	
x	**a (Å)**	**B (GPa)**	**a (Å)**	**B (GPa)**	**a (Å)**	**B (GPa)**
BaO (x=0)	5.4993	79.0351	5.5200[35],5.478[36]	76.076[35],82.36[36]	5.524[37]	72.2
0.250	5.8732	58.5034	5.8790[35]	55.55[23], 58.560[35]	-	-
0.500	6.1544	48.6403	6.1590[35]	48.58[23], 52.461[35]	-	-
0.750	6.3723	43.8356	6.3730[35]	43.76[23], 44.693[35]	-	-
BaSe (x=1)	6.5508	39.9202	6.5820[35], 6.66[23]	34.00[23], 37.05[42]	6.6000[37]	43.4[43]

IV.IV. Electronic properties

Electronic properties (band structures and densities of states) are the core link between crystal structure and material behavior. They fix the band gap and band curvature, which set carrier concentrations, effective masses, mobility, and thus electrical conductivity and device performance. In practice, BS/DOS provide the quantitative baseline for comparing compositions and pressures, guiding which alloys are worth pursuing and how structural trends translate into functional outcomes [44–46] .

IV.IV.1. Band structure

a) III-V alloys

$AlSb_{1-x}As_x$ (ZB): Figure IV.11 shows that the two endpoints, AlSb (x = 0) and AlAs (x = 1), are indirect-gap semiconductors with VBM at Γ and CBM at X (Γ→X), whereas the intermediate alloys (x = 0.25, 0.50, 0.75) become direct at Γ–Γ. The band gap values in Table IV.5 quantify this evolution: Eg = 1.749 eV (Γ–X) → 1.4963 eV (Γ–Γ) → 1.6518 eV (Γ–Γ) → 1.8865 eV (Γ–Γ) → 2.145 eV (Γ–X). Overall, As substitution widens the gap but does so non-linearly as :

$$E_g(x) = (1-x)E_g(x)(AlSb) + xE_g(x)(AlAs) - b \cdot x(1-x) \qquad (\mathbf{IV.7})$$

Our obtained results agree well with other prior DFT works and available experimental bandgap values.

$AlSb_{1-x}Bi_x$ (ZB): Figure IV.12 begins with AlSb (x = 0) as indirect (Γ→X), but any Bi addition (x > 0) immediately stabilizes a direct Γ–Γ gap: the Γ conduction edge drops while the Γ valence top rises/flatten due to Bi-p hybridization and spin–orbit coupling, locking a direct gap across all Bi-containing alloys. The measured gaps (**Table IV.5)** decrease monotonically with x: 1.749 eV (Γ–X) → 1.376 eV (Γ–Γ) → 1.211 eV (Γ–Γ) → 0.774 eV (Γ–Γ) → 0.299 eV (Γ–Γ) at AlBi. Bi incorporation lowers the the band gap, driving a direct Γ–Γ character for all x > 0 . Our results agree well with other works ans available experimental bandgap values.

In summary, Starting from indirect-gap AlSb (Γ→X, 1.749 eV), As substitution creates a direct Γ–Γ window only at mid-compositions (x = 0.25–0.75) but ends indirect again at AlAs; the gap widens overall to ~2.145 eV . In contrast, Bi makes the alloy direct Γ–Γ for any x > 0 and the gap shrinks monotonically to ~0.299 eV at AlBi.

b) II-VI selected alloys

All calculations for the II–VI alloys were performed in the rocksalt (NaCl) phase using the Koller–Tran–Blaha modified Becke–Johnson (KTB-mBJ) potential at 0 K on the relaxed geometries. Band-structure trends and band gaps obtained here are compared directly with three representative

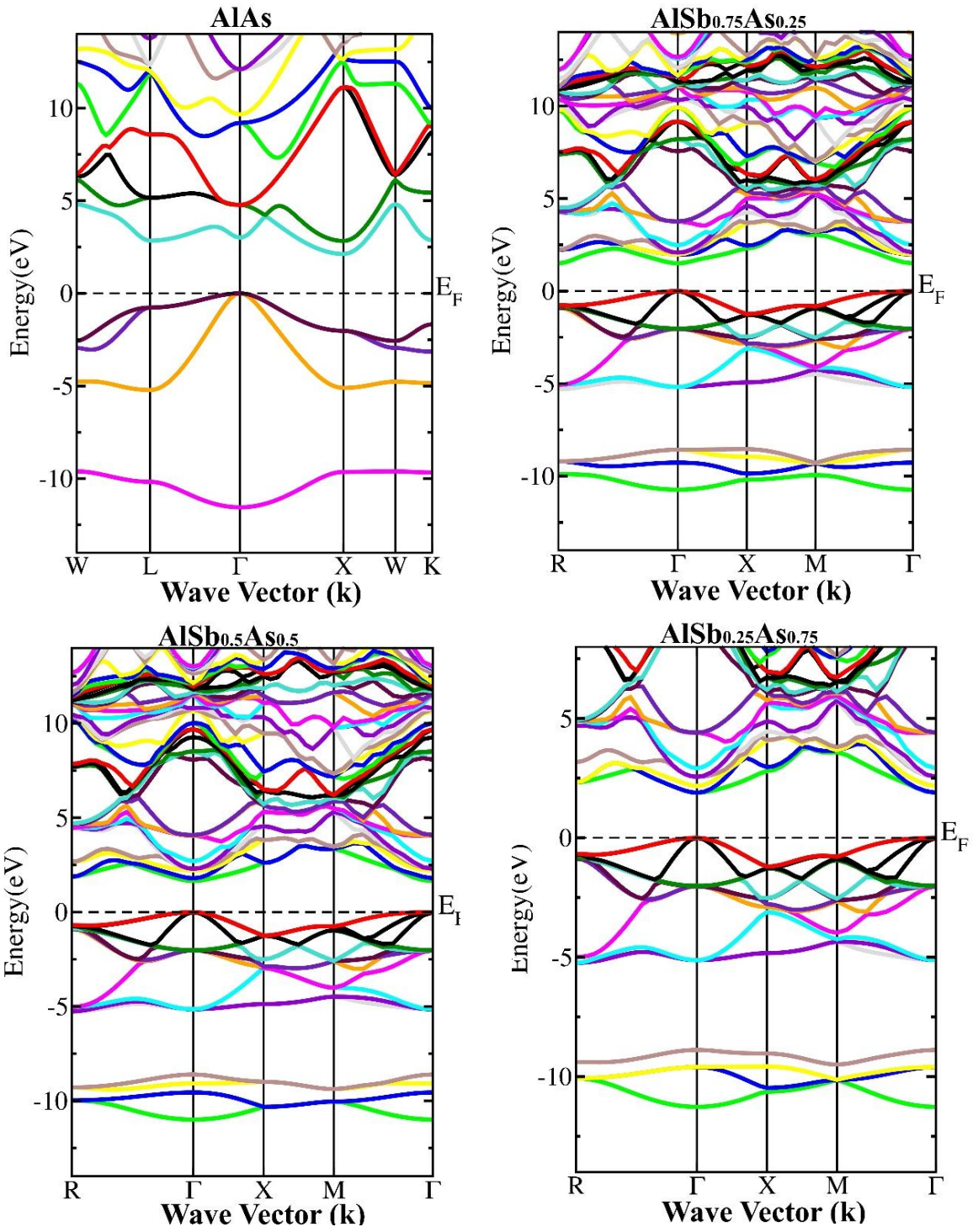


Figure IV.11. ZB $AlSb_{1-x}As_x$: Band structures (KTB-mBJ) (x=0.25,0.5,0.75 and 1)

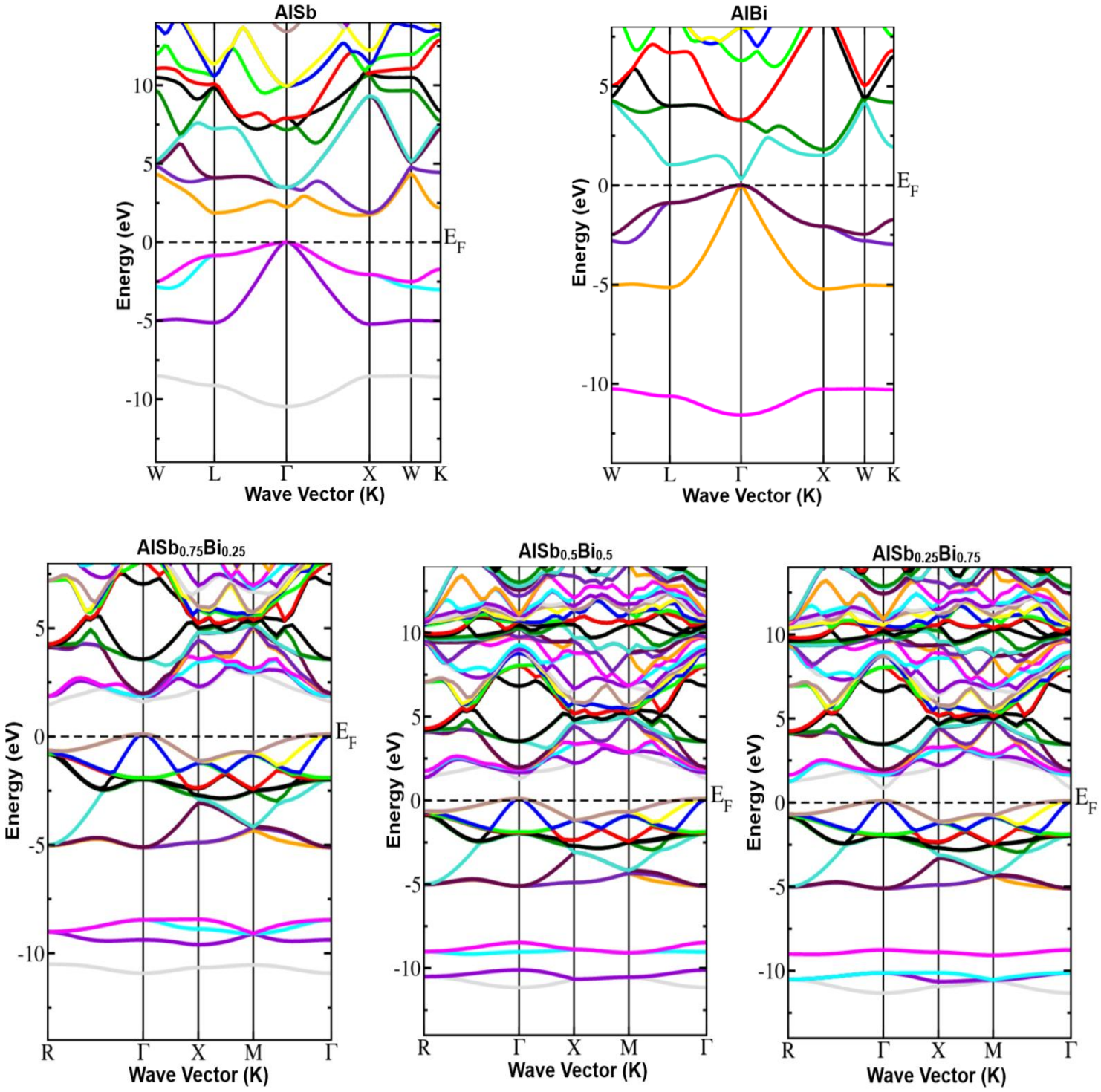


Figure IV.12. ZB $AlSb_{1-x}Bi_x$: Band structures (KTB-mBJ+SoC)

Table IV.5. Estimated computational values of Band Gaps $E_g(eV)$ of selected III-V ternary alloys in ZB phase via the PBE-KTB-mBJ+SoC approximation, compared with other calculations and experimental data.

$AlSb_{1-x}As_x$	Our work		Other Works	Experimental
x	$E_g(eV)$	Gap type	$E_g(eV)$	$E_g(eV)$
AlSb ($x = 0$)	1.749	$\Gamma - X$	1.775 [24], 1.79 [47], 1.767 [11]	1.68–1.70[48]
0.250	1.4963	$\Gamma - \Gamma$	-	-
0.500	1.6518	$\Gamma - \Gamma$	-	-
0.750	1.8865	$\Gamma - \Gamma$	-	-
AlAs (x=1)	2.145	$\Gamma - X$	2.146 [11] , 2.259 [33] , 2.18 [49]	2.15 [34] , 2.23 [48]
$AlSb_{1-x}Bi_x$	Our work		Other Works	Experimental
x	$E_g(eV)$	Gap type	$E_g(eV)$	$E_g(eV)$
AlSb ($x = 0$)	1.749	$\Gamma - X$	1.775 [24], 1.79 [47], 1.767 [11]	1.68–1.70[48]
0.250	1.376	$\Gamma - \Gamma$	1.598 [50]	-
0.500	1.211	$\Gamma - \Gamma$	1.280 [50]	-
0.750	0.774	$\Gamma - \Gamma$	0.817 [50]	-
AlBi (x=1)	0.299	$\Gamma - \Gamma$	0.373 [24], 0.426 [28], 0.000 [29]	-

methodologies reported in the literature: TB-mBJ (Ref. 40), EV-GGA (Ref. 35), and plain GGA (Ref. 51) (Table IV.6).

$BaO_{1-x}S_x$ (NaCl): The band structures in Figure. IV.13 shows BaO (x = 0) as an indirect-gap semiconductor with VBM near Γ and CBM at X (Γ→X). Introducing sulfur stabilizes the Γ valley so that the alloys at x = 0.25, 0.50, and 0.75 exhibit a direct Γ–Γ gap; at the S-rich limit (BaS, x = 1) the X valley again undercuts Γ and the indirect Γ→X character is recovered. The KTB-mBJ gaps in Table IV.6 follow a strongly concave composition curve with a pronounced mid-range minimum: 3.4092 eV (BaO, X–X) → 2.9240 eV (x = 0.25, Γ–Γ) → 2.3658 eV (x = 0.50, Γ–Γ) → 2.2040 eV (x = 0.75, Γ–Γ) → 3.1954 eV (BaS, Γ–X). In head-to-head comparisons, TB-mBJ (Ref. 40) tracks our results but tends to give slightly smaller mid-composition gaps (by a few tenths of an eV), while EV-GGA (Ref. 35) and GGA (Ref. 51) are systematically lower than both TB-mBJ and KTB-mBJ ,-EV-GGA typically by ~0.2–0.6 eV and GGA by ~0.5–1.0 eV in the middle of the

series- with all approaches converging within the usual spread at the two binaries. Relative to experiment, the BaO and BaS band gaps listed in the table exceed our 0-K KTB-mBJ values by

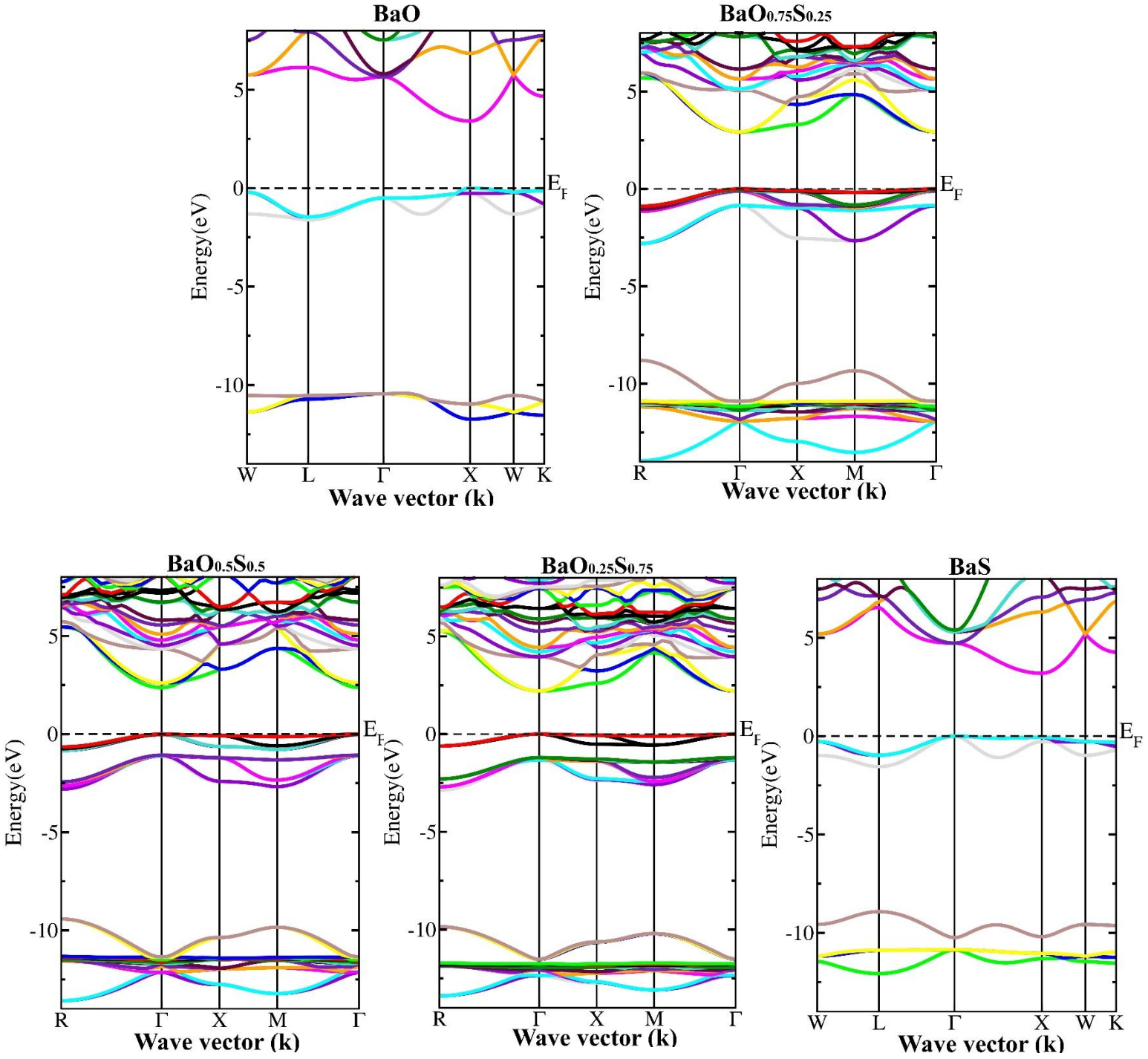


Figure IV.13. $BaO_{1-x}S_x$ (NaCl): Band structures (KTB-mBJ).

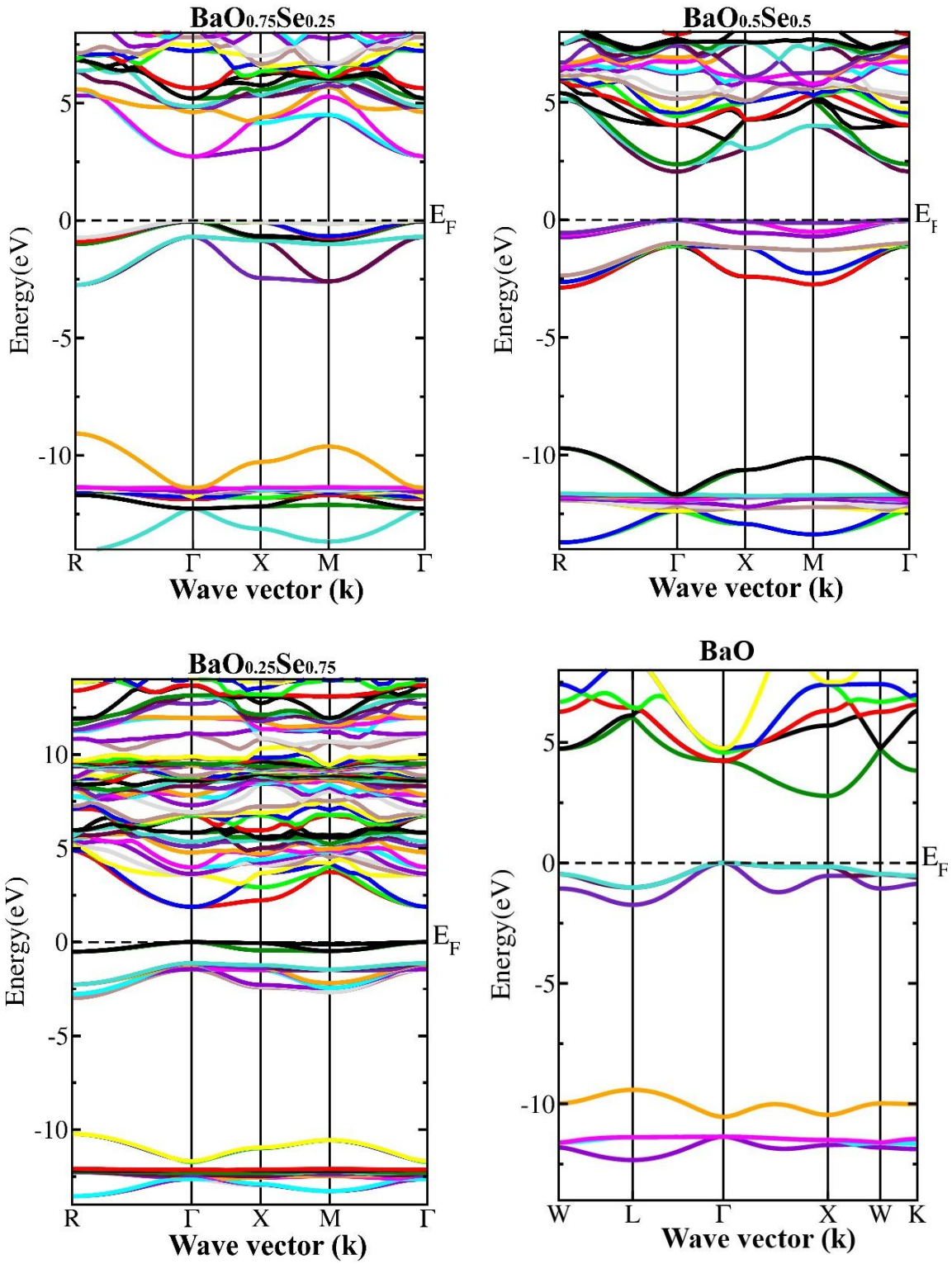


Figure IV.14. $BaO_{1-x}Se_x$ (NaCl): Band structures (KTB-mBJ).

Table IV.6. Estimated computational values of Band Gaps $E_g(eV)$ of selected II-VI ternary alloys in NaCl phase via the PBE-KTB-mBJ approximation, compared with other calculations and experimental data.

$BaO_{1-x}S_x$	Our work		Other Works	Experimental
x	$E_g(eV)$	Gap type	$E_g(eV)$	$E_g(eV)$
BaO ($x = 0$)	3.4092	$X - X$	2.76 [40] ,1.81 [51]	3.88 [52]
0.250	2.9240	$\Gamma - \Gamma$	2.50 [40]	-
0.500	2.3658	$\Gamma - \Gamma$	2.12 [40]	-
0.750	2.2040	$\Gamma - \Gamma$	2.01 [40]	-
BaS (x=1)	3.1954	$\Gamma - X$	3.00 [40], 1.97 [51]	3.90 [53]
$BaO_{1-x}Se_x$	Our work		Other Works	Experimental
x	$E_g(eV)$	Gap type	$E_g(eV)$	$E_g(eV)$
BaO ($x = 0$)	3.4092	$X - X$	3.486 [35], 1.81 [51]	3.88 [52]
0.250	2.7281	$\Gamma - \Gamma$	3.013 [35]	-
0.500	2.0482	$\Gamma - \Gamma$	2.264 [35]	-
0.750	1.8759	$\Gamma - \Gamma$	2.091 [35]	-
BaSe (x=1)	2.7790	$\Gamma - \Gamma$	2.903 [35], 2.75 [40], 1.89 [51]	3.58 [52]

a sub-eV margin, consistent with known finite-temperature and excitonic corrections not captured here (ground state).

$BaO_{1-x}Se_x$ (NaCl): Figure IV.14 again starts from an indirect Γ→X gap at BaO, but any selenium addition (x ≥ 0.25) pushes the Γ valley below X and it remains the conduction minimum all the way to BaSe; the series is therefore direct Γ–Γ for x ≥ 0.25. The KTB-mBJ gaps in Table IV.6 show a deeper concavity than in the sulfide: 3.4092 eV (BaO, X–X) → 2.7281 eV (x = 0.25, Γ–Γ) → 2.0482 eV (x = 0.50, Γ–Γ) → 1.8759 eV (x = 0.75, Γ–Γ) → 2.7790 eV (BaSe, Γ–Γ). Method-wise, TB-mBJ (Ref. 40) follows the same behaviour and is typically slightly below our KTB-mBJ values at mid-x; EV-GGA (Ref. 35) and GGA (Ref. 51) lie lower still, in the expected order. The BaSe endpoint from KTB-mBJ falls within the theoretical range reported in the table yet below the room-temperature experimental gap by ~sub-eV, again consistent with finite-T effects absent from static calculations.

In summary, The sulfide shows a direct Γ–Γ window only in the middle of the series and is indirect at both ends (X–X at BaO, Γ–X at BaS), whereas the selenide is direct Γ–Γ for all $x \geq 0.25$ and displays a deeper minimum with partial recovery at BaSe. Against the methods compared, KTB-mBJ (our work) sits within the established theoretical spread, typically above EV-GGA and GGA and slightly above TB-mBJ at mid-compositions where Γ is stabilized. Against experiment, the binaries are lower by the familiar sub-eV margin expected from 0-K band calculations without finite-T or excitonic corrections.

- **Application-Oriented Summary Based on Computed Band Gaps: III–V (ZB) and II–VI (NaCl) selected Alloys:**

$AlSb_{1-x}As_x$:The Γ–Γ window confined to intermediate compositions ($x \approx 0.25–0.75$) with band gaps around 1.50–1.89 eV (≈830–660 nm) makes these alloys attractive for red to deep-red optoelectronics. In this window, direct transitions enable thin-active-region light emitters and detectors; practical targets include red/deep-red LEDs and edge-emitting lasers for ~0.66–0.80 μm, and compact NIR photodiodes around 0.7–0.85 μm where the direct gap improves efficiency over the indirect endpoints. The same mid-x compositions, having wider gaps than GaSb, are also suitable as low-loss DBR/cladding materials for GaSb-platform lasers operating near 0.65–0.9 μm. At the binary limits (AlSb, AlAs), the indirect Γ→X character is less compatible with radiative emitters and favors passive/structural roles.

$AlSb_{1-x}Bi_x$: Any Bi incorporation ($x>0$) yields a direct Γ–Γ gap that can be tuned continuously from ≈1.38 eV down to ≈0.30 eV (≈0.9–4.1 μm). This enables a unified GaSb-lattice platform for telecom/NIR modulators and detectors at 1.0–1.6 μm ($x\approx0.5–0.75$), and extends to mid-wave infrared interband photodetectors or thermophotovoltaic cells in the 2–4 μm range as the gap approaches 0.3–0.6 eV.

The combination of Γ–Γ character and gap tunability across NIR–MWIR is the distinctive advantage of this alloy systems.

$BaO_{1-x}S_x$: The gap spans ≈2.20–3.41 eV (≈560–365 nm) with a direct Γ–Γ window at mid-compositions and indirect behavior at both endpoints (X–X at BaO, Γ–X at BaS). This profile

suits optical components whose functionality derives from a sharp absorption edge. Mid-x direct alloys are promising host matrices for visible phosphors (e.g., Eu^{2+}/Ce^{3+}) where a direct gap suppresses re-absorption, allowing host tuning toward green, cyan (~520–450 nm). More O-rich compositions, with wider gaps near 3.4 eV, serve as UV-pass, visible-blocking windows and robust wide-gap dielectrics for harsh-environment opto-MEMS.

$BaO_{1-x}Se_x$: With Γ–Γ direct gaps across all x ≥ 0.25 and Eg ≈1.88–3.41 eV (≈660–365 nm), the selenide series offers efficient radiative host behavior throughout much of the visible. Composition allows color-tunable emitters or down-converters from red to blue (660→450 nm) and supports spectrally selective photodetectors: Se-rich alloys (Eg≈1.9–2.8 eV) address the visible band, while O-rich alloys (Eg≈3.4 eV) provide UV-only response.

IV.IV.2. Density of states

The electronic density of states g(E) counts the number of single-particle states available per unit energy (and often per unit volume) in the interval [E, E + dE]. In a crystal it is obtained by summing over bands and integrating over the Brillouin zone [6,54] :

$$g(E) = \frac{2}{(2\pi)^3} \sum_n \int_{BZ} \delta\big(E - En(k)\big)\, dk^3 \quad \textbf{(IV.8)}$$

$$N(E) = \int_{-\infty}^{E} g(E')\, dE' \quad \textbf{(IV.9)}$$

$$g_{(free)}(E) = \frac{1}{2\pi^2} \left(\frac{2m}{\hbar^2}\right)^{3/2} . E^{1/2} \quad \textbf{(IV.10)}$$

$$n = \int g_c(E)\ f(E,\mu,T)\, dE, \quad p = \int g_v(E)\ [1 - f(E,\mu,T)]\, dE \quad \textbf{(IV. 11)}$$

Notes: g_c and g_v denote conduction- and valence-projected DOS; f is the Fermi–Dirac distribution which gives the probability that an electronic state of energy $E$is occupied by an electron at a temperature T. It is defined as:$f(E) = \frac{1}{e^{(E-\mu)/(k_B T)+1}}$

Where μ is the chemical potential, k_B is Boltzmann constant, and T is temperature.

The DOS determines carrier statistics (n, p via Fermi–Dirac), influences optical absorption through the joint DOS, and controls low-temperature electronic heat capacity and transport. In spectroscopy (tunneling, ARPES, XPS) peaks and gaps map directly to features of the total and projected DOS (PDOS), enabling chemical-bond and alloy-trend analysis [6,55] .

To keep the presentation rigorous yet compact, we analyze the DOS and PDOS using two representative compositions per alloy: one binary endpoint and one intermediate ternary composition. The binary case benchmarks the pristine parent lattice and serves as a reference for orbital character. The intermediate alloy then captures the essential alloy physics, possible valley reordering (direct/indirect changes), and the redistribution of cation/anion orbital weightswhich are most pronounced away from the endpoints. This two-sample strategy avoids redundant plots, preserves all key trends in bonding and band-edge topology, and provides a defensible basis for generalizing to the remaining concentrations.

a) III-V selected alloys

AlSb (binary, ZB) -Fig. IV.15: The total DOS separates into a lower valence band (LVB, -12…-8 eV), an upper valence band (UVB, ≈−5…0 eV), and the conduction band (CB) above the band gap (Valance band maximum is set to 0 eV). PDOS attribution matches the standard III–V bonding picture: sharp Sb-s features form the LVB; the UVB is dominated by Sb-p states with a minor Al-s admixture near the valence edge; and the CB onset is primarily cation-centred (Al-p with some Al-s) accompanied by weak, Sb-p tails. By combining this DOS/PDOS with the earlier band structures.

$AlSb_{0.5}As_{0.5}$ (alloy, ZB) - Fig. IV.16: Alloying yields two robust fingerprints. (i) In the LVB, the single anion-s manifold of the binary splits into As-s and Sb-s sub-manifolds, with the more electronegative As pushing its s-states . (ii) The UVB broadens and the VBM exhibits mixed Sb-p/As-p weight. On the CB side the onset remains cation-dominated (Al-p/Al-s).

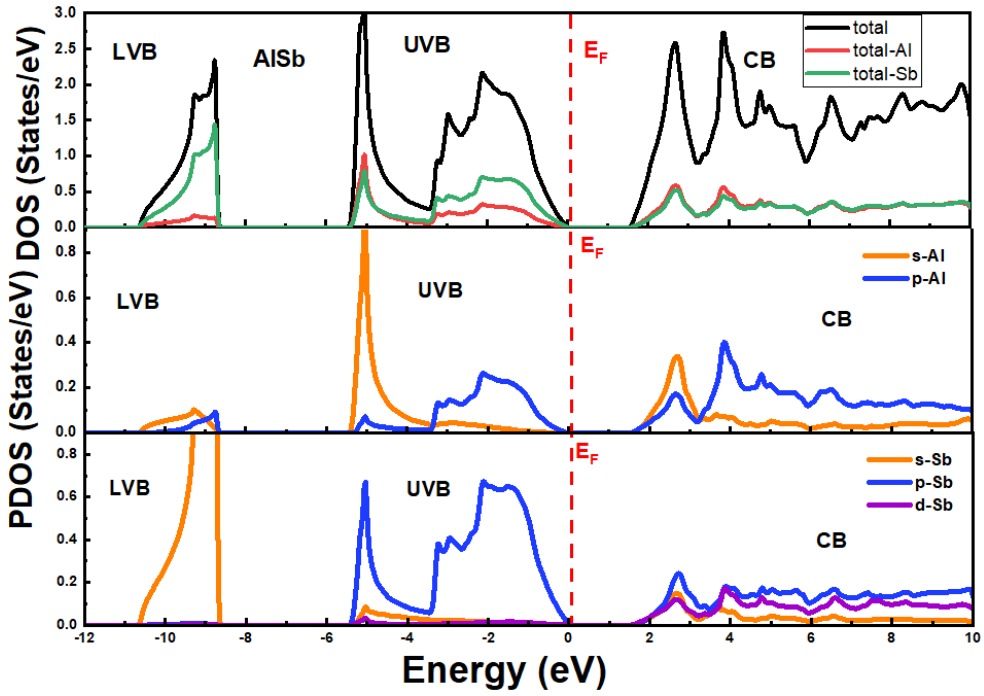


Figure IV.15. AlSb: Total DOS and PDOS vs energy (eV) (KTB-mBJ).

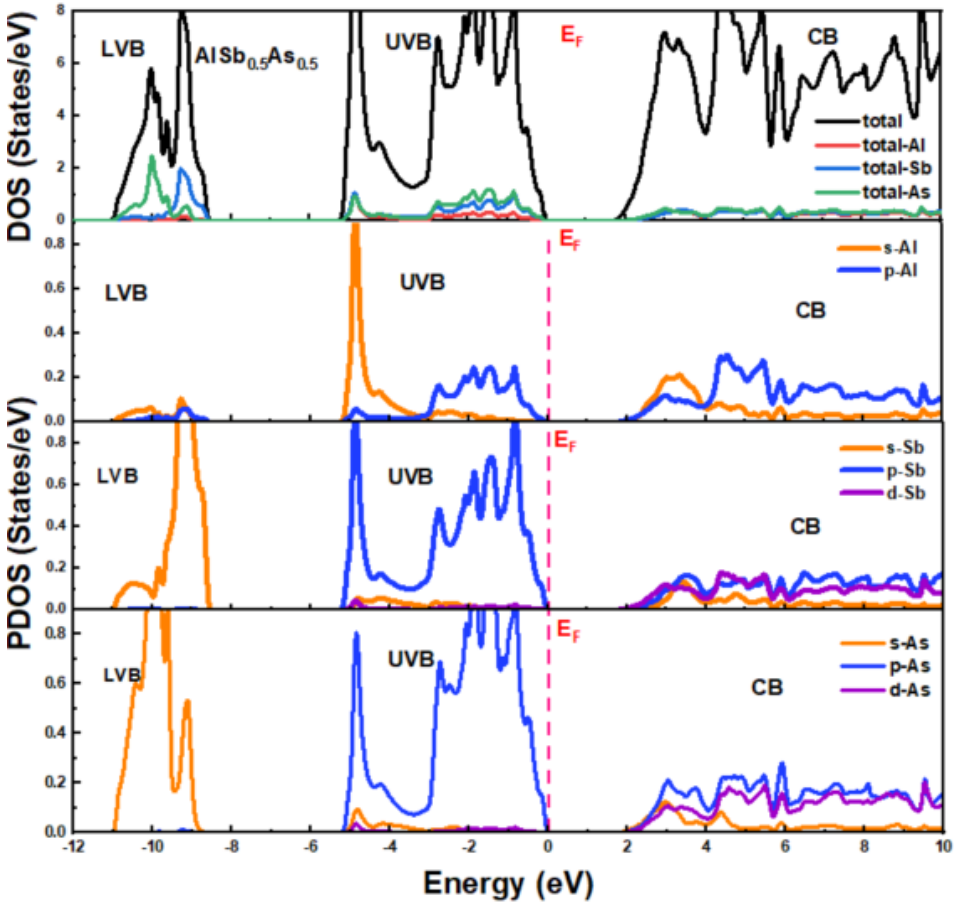


Figure IV.16. $AlSb_{0.5}As_{0.5}$: Total DOS and PDOS vs energy (eV) (KTB-mBJ).

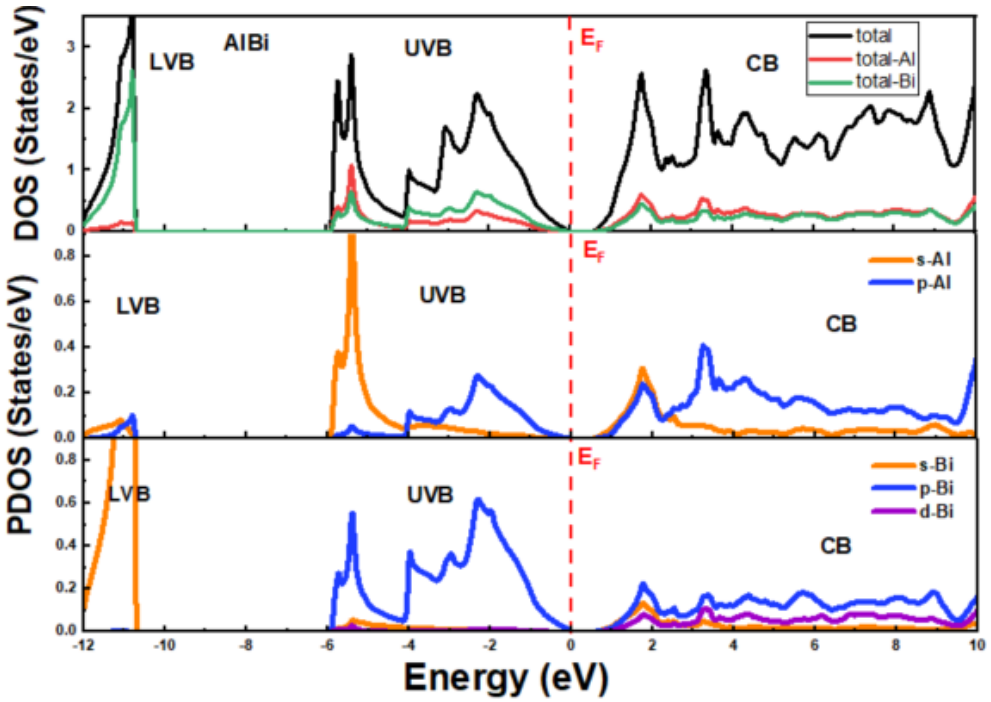


Figure IV.17. AlBi: Total DOS and PDOS vs energy (eV) (KTB-mBJ).

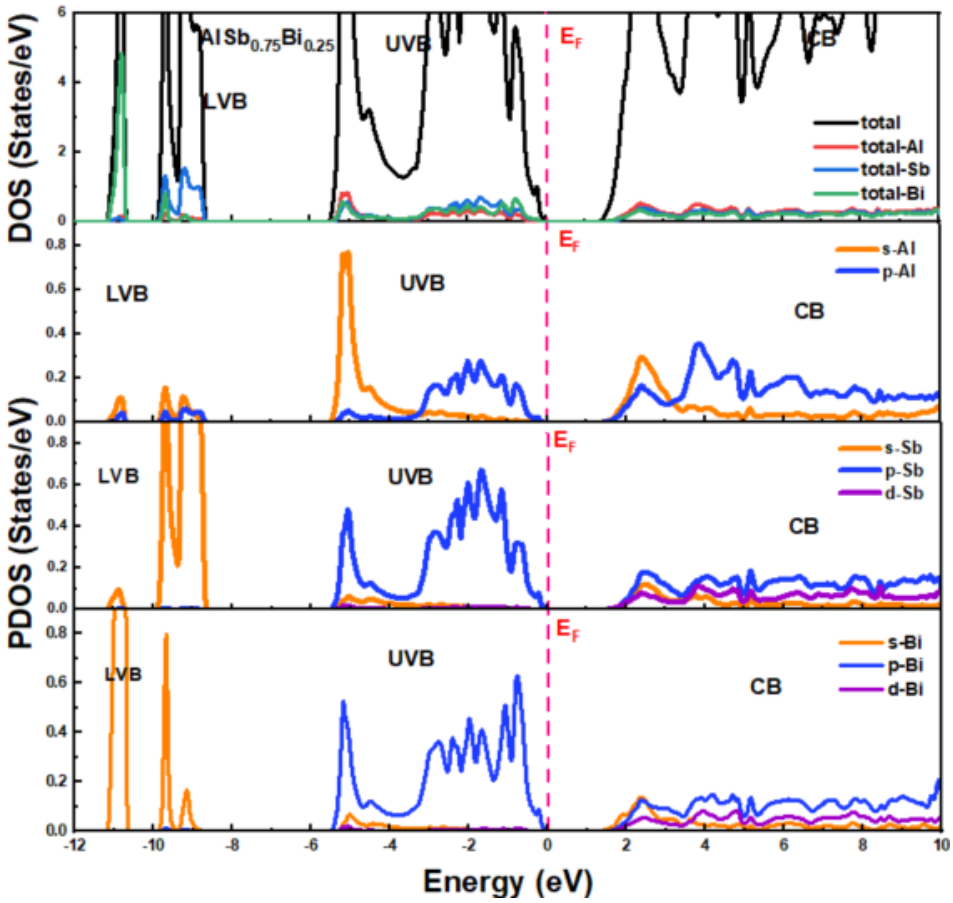


Figure IV.18. $AlSb_{0.75}Bi_{0.25}$: Total DOS and PDOS vs energy (eV) (KTB-mBJ).

The KTB-mBJ gap read from the panel (≈1.65 eV) appears clean, with no in-gap spectral weight attributable to numerical broadening or supercell artefacts.

AlBi (binary, ZB) -Fig. IV.17: The spectrum partitions into a deep lower valence band (LVB, ≈ −12 to −9 eV) formed mainly by Bi-s states, a broad upper valence band (UVB, ≈ −6 to 0 eV) dominated by Bi-p with modest Al-s admixture, and the conduction band (CB) above the Fermi-level reference where Al-p weight is prominent with small Bi-p/d tails. Relative to the antimonide, the UVB maximum sits closer to the CB onset and the total DOS rises quickly at the edge, consistent with the sub-eV fundamental gap obtained for AlBi (≈0.30 eV with KTB-mBJ).

$AlSb_{0.75}Bi_{0.25}$ (alloy, ZB) — Fig. IV.18: Alloying introduces two clear patterns. (i) In the LVB, the anion-s manifold splits into Sb-s and Bi-s sub-bands, with Bi-s appearing the LVB, the anion-s manifold splits into Sb-s and Bi-s sub-bands. (ii) In the UVB, the valence-edge region exhibits mixed p-character: Sb-p and Bi-p both contribute, with noticeable Bi-p weight approaching the top. On the CB side, the onset remains cation-centred (Al-p with some Al-s), while weak Bi-p/d tails track into the first antibonding features. Compared with the parent antimonide, the separation between the valence maximum and the conduction onset is reduced, consistent with the calculated gap near 1.38 eV for x = 0.25 (KTB-mBJ). The modest broadening/splitting across the UVB is the expected configurational fingerprint of a random alloy; importantly, the gap region remains clean, indicating that the supercell and smearing choices did not generate spurious in-gap states.

Across $AlSb_{1-x}Bi_x$, series, the DOS and PDOS patterns reflect the continuous band gap reduction. As the Bi content increases, more Bi-p character appears near the valence band edge, and the lowest conduction bands undergo slight reshaping, while the overall bonding scheme remains unchanged: the valence edge is dominated by anion p states, and the conduction edge by cation states.

In summary, Replacing Sb with As or Bi in zinc-blende AlSb leaves the bonding archetype intact anion-p–dominated valence edge and Al-centered conduction onset, but the DOS/PDOS fingerprints differ clearly. In both series the lower valence band splits into two anion-s submanifolds (Sb-s plus As-s or Bi-s). With As, the upper valence band (UVB) broadens and the valence edge shows a smooth mix of Sb-p/As-p weight, while the conduction onset remains sharp and predominantly Al-p/Al-s. With Bi, pronounced Bi-p intensity concentrates right at the valence edge and the UVB displays visible sub-structure (consistent with heavier-anion character), while

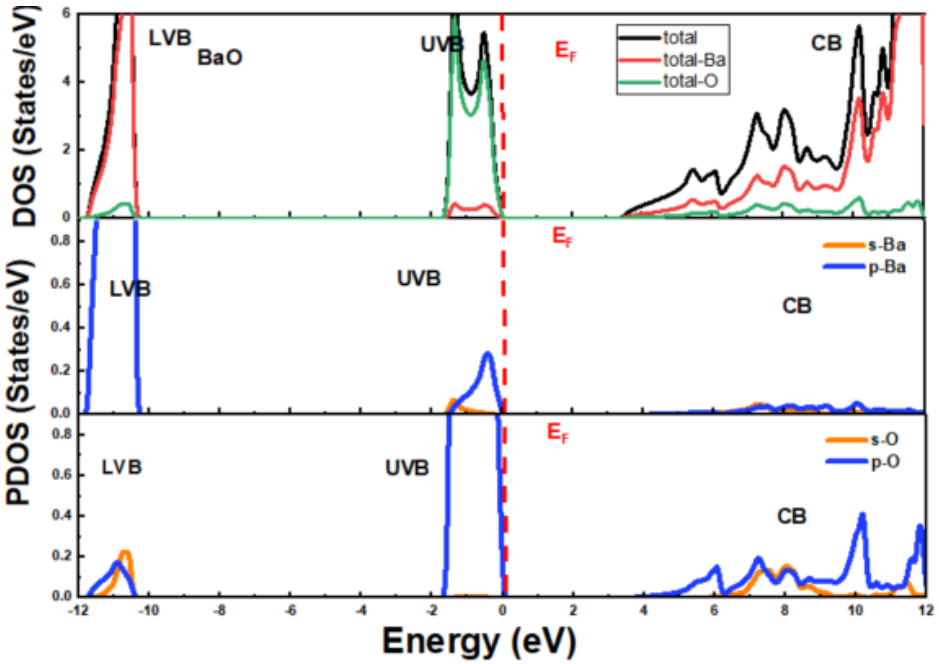
the conduction onset is still Al-centered but exhibits slightly stronger anion tailing into the first antibonding peaks. At comparable compositions the valence–conduction separation is smaller in the Bi series than in the As series, yet in all cases the gap window stays clean (no mid-gap spectral weight).

c) II-VI selected alloys

BaO (NaCl) — Fig. IV.19: The spectrum divides into three well-separated regions. (i) A deep lower-valence band (LVB) centered near −12 eV that is Ba-5p semicore–dominated (the sharp Ba-p spike in both the total-Ba trace and the Ba-p PDOS). Any O-2s intensity in this window is negligible. (ii) An upper-valence band (UVB) extending from roughly −3 eV up to the valence edge, where the O-2p manifold carries the spectral weight and a small Ba-s/p admixture appears as shoulders. (iii) Above the gap, the conduction band onset is Ba-centred, with the total-Ba channel rising first and only weak O-p tails following into the initial antibonding features. The gap window is clean: the total DOS drops to zero between the O-2p crest and the first Ba-centred antibonding peak, confirming numerically sharp edges with no spurious mid-gap states.

$BaO_{0.25}S_{0.75}$ (NaCl) — Fig. IV.20: Alloying leaves the overall ionic partitioning intact but introduces clear chemical fingerprints. In the deep LVB, the single Ba-5p spike of BaO is now accompanied by strong S-3s features (resolved as two closely spaced peaks), giving distinct Ba-5p and S-3s sub-manifolds and evidencing true substitution rather than a rigid spectral shift. In the UVB, two anion-p clusters appear: a deeper O-2p group and a shallower S-3p group; both contribute at the valence edge, with S-3p weight becoming prominent immediately below 0 eV. The conduction onset remains Ba-centred (rise of the total-Ba channel), but compared with BaO the first antibonding structure carries slightly stronger anion-p tailing.

Relative to the binary, the separation between the UVB crest and the conduction onset is visibly smaller, consistent with the reduced band gap reported for S-rich compositions. As in BaO, the gap region stays state-free, indicating that the supercell and smearing choices did not introduce in-gap artefacts.



igure IV.19. BaO: Total DOS and PDOS vs energy (eV) (KTB-mBJ).

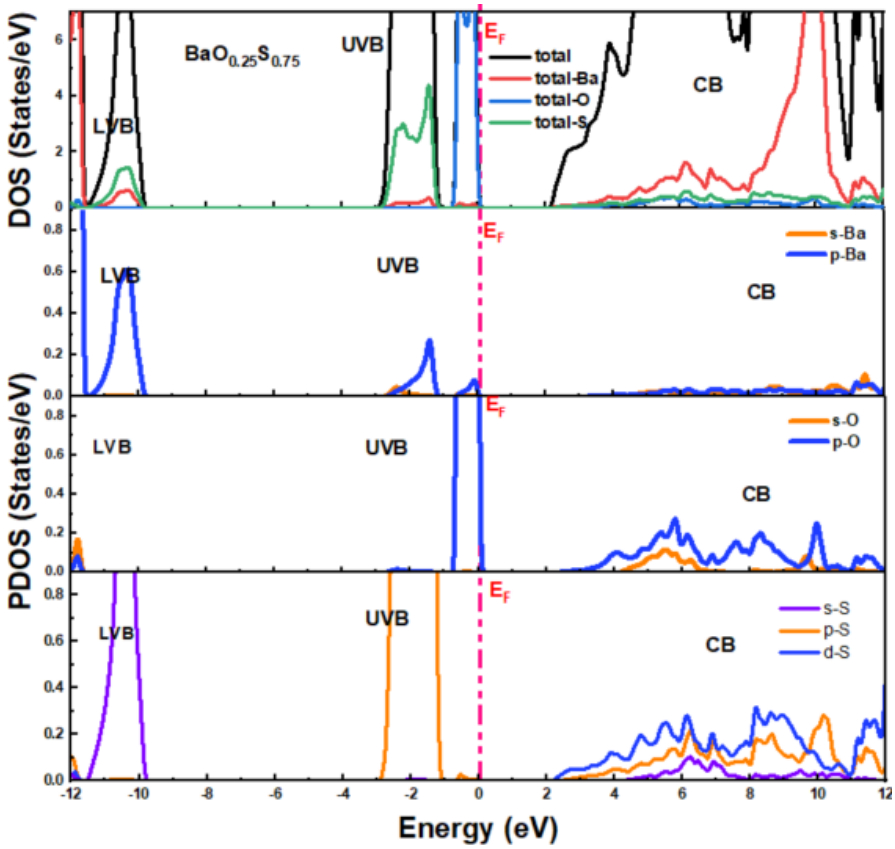


Figure IV.20. $BaO_{0.25}S_{0.75}$: Total DOS and PDOS vs energy (eV) (KTB-mBJ).

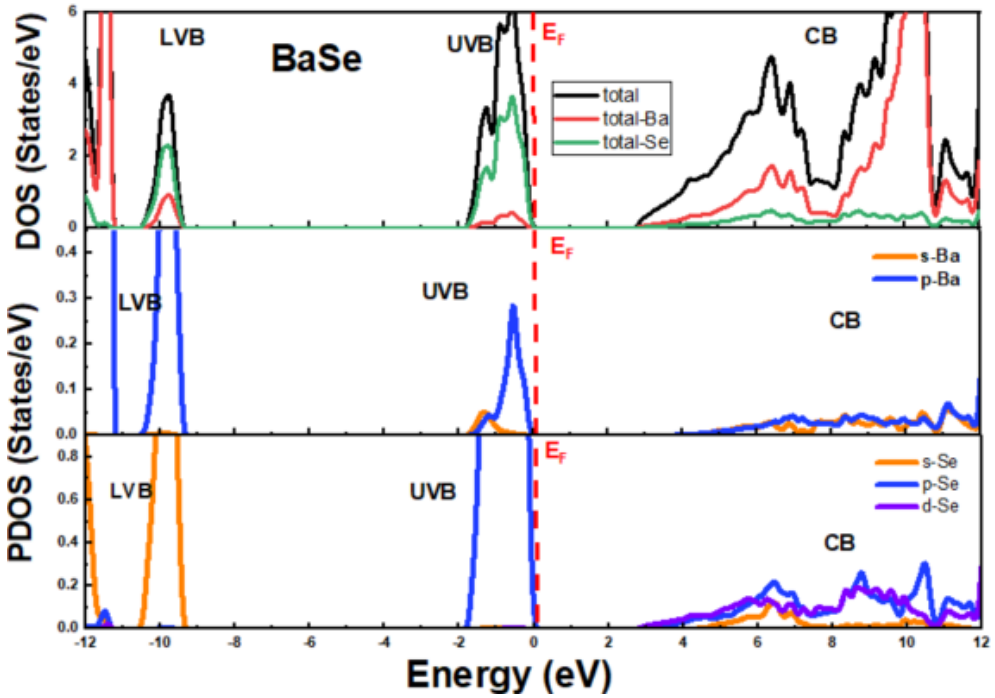


Fig IV.21. BaSe: Total DOS and PDOS vs energy (eV) (KTB-mBJ).

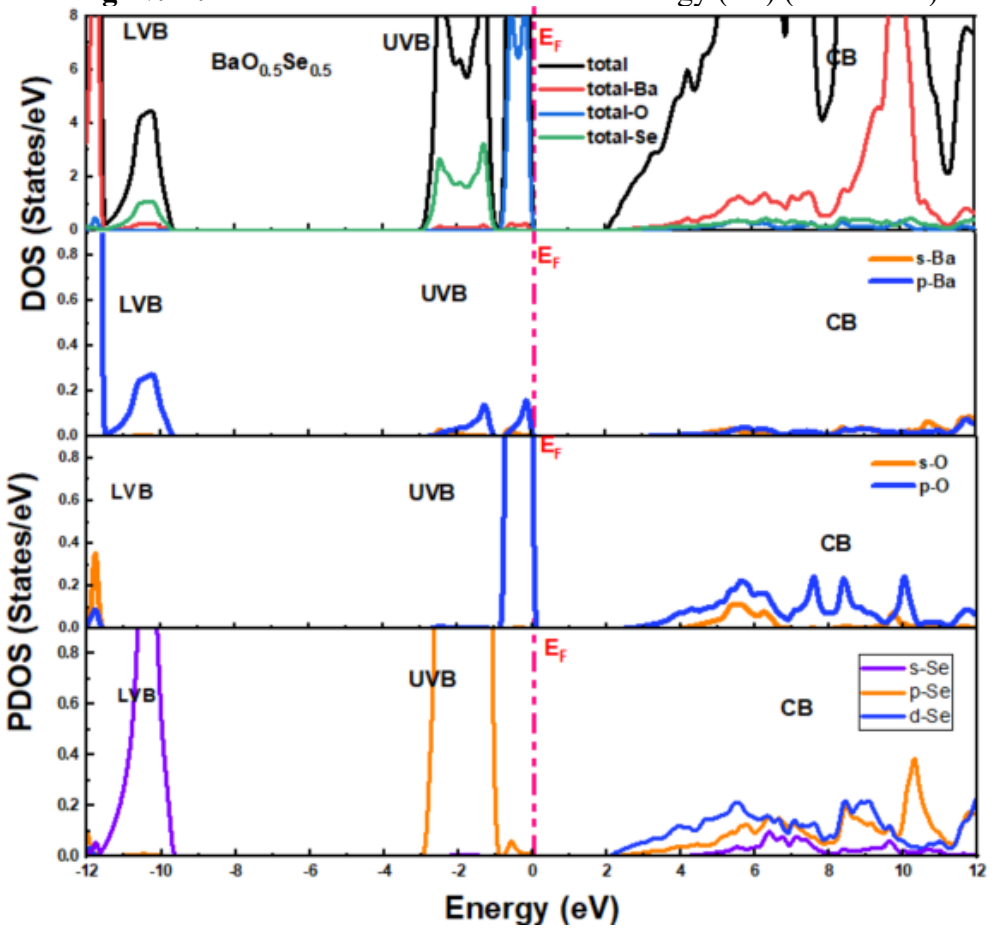


Figure IV.22. $BaO_{0.5}Se_{0.5}$: Total DOS and PDOS vs energy (eV) (KTB-mBJ).

Taken together, these DOS/PDOS signatures give a coherent chemistry-based picture. BaO exhibits the classic ionic partition Ba-5p semicore deep, O-2p at the valence edge, and a Ba-centred conduction onset. Introducing S splits the deep manifold (Ba-5p vs S-3s), broadens and elevates the anion-p UVB (now a mixture of O-2p and S-3p at the edge), and adds modest anion tailing to the first conduction antibonding peak. These changes rationalize the gap reduction with S incorporation while preserving clean band edges and the overall anion-p / cation-centered partitioning characteristic of the rock-salt II–VI family.

BaSe (NaCl) — Fig. IV.21: The spectrum splits into: (i) a deep LVB near −12 eV in which the sharp Ba-5p semicore peak dominates and a smaller Se-4s contribution appears; (ii) an upper valence band (UVB) from ≈−3 eV to the edge that is Se-4p dominated with only minor Ba s/p admixture textbook for an ionic Ba–Se bond where the anion-p manifold sets the valence edge; and (iii) the conduction side, where the rise is Ba-centred in the "total-Ba" trace. The gap window is clean, i.e., no residual spectral weight between the Se-p crest and the first Ba-centred peak.

$BaO_{0.5}Se_{0.5}$ (NaCl) — Fig. IV.22

Alloying preserves the ionic partitioning but introduces clear chemical fingerprints. In the deep LVB, Ba-5p persists and is now accompanied by O-2s and Se-4s peaks ; three distinct semicore/s sub-manifolds that confirm genuine substitution rather than a rigid shift. In the UVB, two anion-p clusters are resolved: a deeper Se-4p group and a shallower O-2p group; both contribute at the valence edge, and the overall envelope is broader than in BaSe, reflecting the distribution of local environments in the random alloy. On the conduction side, the onset remains Ba-centred (strong total-Ba rise), while O-2p and Se-4p/d tails are more evident in the first antibonding features than in the binary. The valence-to-conduction separation is clearly smaller than in BaSe, consistent with reported smaller mBJ gap at x = 0.5, and the gap region remains state-free, indicating that the calculations did not introduce spurious in-gap weight.

IV.IV.3. Cross-Family Comparison of Electronic Structure (Bands & DOS)

All band gaps are obtained with the same KTB-mBJ workflow; all DOS/PDOS are aligned at VBM = 0 eV and reported per formula unit. The comparison emphasizes a composition-dependent band-gap trends and an orbital make-up of the band edges as read from the DOS/PDOS.

III–V (zinc-blende) alloys: In $AlSb_{1-x}As_x$ the gap increases overall from AlSb to AlAs, but shows a dip at mid-x (where a direct window appears in the bands); in $AlSb_{1-x}Bi_x$ any Bi addition yields a direct gap and the magnitude decreases monotonically toward AlBi. This behavior is consistent with established III–V systematics: stronger, shorter Al–As bonds raise the gap, while heavier Bi brings high-lying p states. DOS/PDOS confirm the expected bonding archetype -anion-p–dominated valence edge and Al-centered conduction onset with substantial Al-p character- which is the textbook picture for III–V semiconductors [34,48] .

II–VI (rock-salt) alloys: Across $BaO_{1-x}S_x$ and $BaO_{1-x}Se_x$ the DOS shows a clean separation: the upper valence band is anion-p (O-2p, S-3p, Se-4p) and the conduction onset is Ba-centered. A sharp Ba-5p semicore peak sits near −12 eV; alloying introduces distinct anion-s features (O-2s, S-3s, Se-4s) and mixes O/S/Se-p weight at the valence edge ; signatures of ionic bonding in alkaline-earth chalcogenides. These edge characters and the evolution toward smaller gaps as O→S→Se (and at mid-x) agree with first-principles and spectroscopic studies of MgO/CaO/SrO/BaO and with standard data compilations for II–VI compounds [56–59].Putting the two families side-by-side: the III–V alloys express covalent-leaning hybridization (anion-p VBM / Al-p conduction edge) and show opposite composition responses for As vs Bi; the II–VI alloys exhibit ionic partitioning (anion-p VBM / Ba-centered conduction edge with strong Ba weight). In every series the DOS shows clean gap windows without mid-gap spectral weight, consistent with well-behaved band structures and with the qualitative trends summarized in reference handbooks and parameter compilations [34,56–59] . This comparative analysis highlights a clear consistency across bands and DOS between the two families.

IV.V. Optical properties

Optical properties dielectric function ε(ω), refractive index n(ω), extinction k(ω), absorption α(ω), and reflectance are the experimental bridge between electronic structure and device performance. In semiconductors and their alloys, these spectra encode the band gap and joint density of states, reveal critical-point transitions and excitonic effects, and set figures of merit for emitters, detectors, photovoltaics, and waveguides. Practically, n and k follow from ε via Fresnel relations and are obtained by reflectance/transmittance or ellipsometry; tabulated optical constants and dispersion

models are therefore essential both for optical design and for validating first-principles bands/DOS. This framing and methodology are standard in the literature [58,60–62].

a) III-V selected alloys

a.1) The dielectric functions of III-V alloys.

As described in chapter I , the dielectric function is a material's frequency-dependent optical "fingerprint" that describes how its electrons polarize in response to an electromagnetic field. Its real part sets how light slows and bends in the medium (refractive behavior), and its imaginary part captures how light is attenuated (absorption and loss). Together they determine refractive index, extinction, reflectivity, and the positions/intensities of interband transitions seen in optical spectra.

Table IV.7. III-V Selected alloys' Critical-Point Energies of $\varepsilon_2(\omega)$ and Static Dielectric Constant $\varepsilon_1(0)$

$AlSb_{1-x}As_x$												
	Present calculations					Other theoretical calculations					Exp	
x	P_0	P_1	P_2	P_3	$\varepsilon_1(0)$	P_0	P_1	P_2	P_3	$\varepsilon_1(0)$	$\varepsilon_1(0)$	P_0
0	1.78	3.11	4.01	4.94	9.12	1.775 [24]	3.15 [24]	4.03 [24]	-	9.13[24] 9.36[47]	12.04 [63]	-
0.25	1.48	3.29	3.97	5.11	8.95	-	-	-	-	-	-	-
0.5	1.64	3.52	4.15	5.21	8.53	-	-	-	-	5.99[64]	-	-
0.75	1.89	3.74	4.43	5.47	8.04	-	-	-	-	-	-	-
1	2.96	4.09	4.78	5.89	7.632	3.10[31] 2.75[65]	–	–	–	9.42[66] 9.77[67]	8.20 [68]	3.02 [69]
$AlSb_{1-x}Bi_x$												
	Present calculations					Other theoretical calculations					Exp	
x	P_0	P_1	P_2	P_3	$\varepsilon_1(0)$	P_0	P_1	P_2	P_3	$\varepsilon_1(0)$	$\varepsilon_1(0)$	P_0
0	1.78	3.11	4.01	4.94	9.12	1.775 [24]	3.15 [24]	4.03 [24]	-	9.13[24] 9.36[47]	12.04 [63]	-
0.25	1.38	2.83	3.83	4.84	9.88	1.59 [24]	2.89 [24]	3.96 [24]	-	10.01 [24]	-	-
0.5	1.22	2.59	3.80	4.59	10.56	1.28 [24]	2.62 [24]	3.88 [24]	-	10.75 [24]	-	-
0.75	0.78	2.52	3.61	4.54	11.83	0.817 [24]	2.54 [24]	3.78 [24]	-	11.67 [24]	-	-
1	0.30	2.17	3.70	4.5	13.24	0.373 [24]	2.45 [24]	3.75 [24]	-	12.67 [24]	-	-

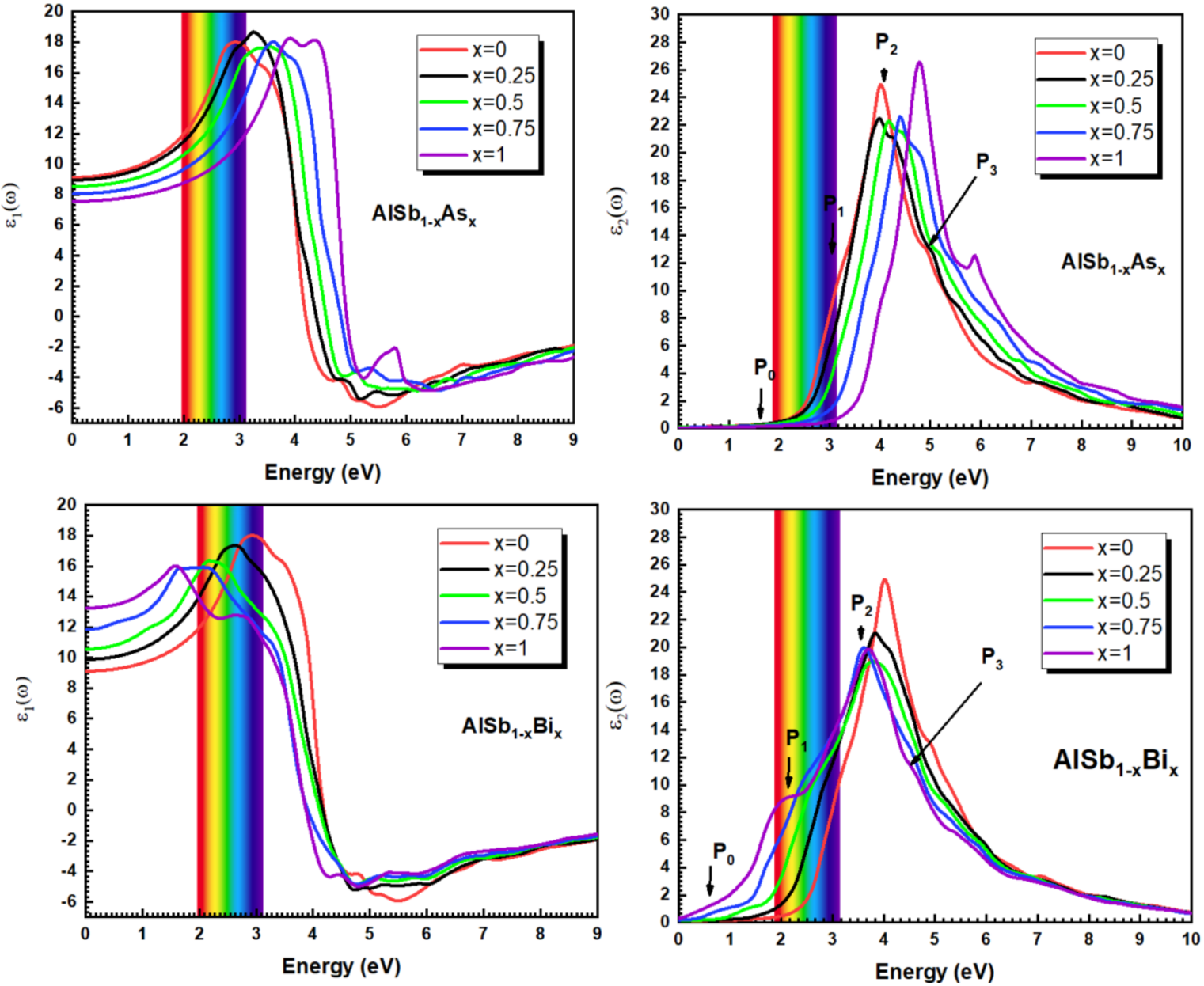


Figure IV.23. III-V Selected alloys' $\varepsilon_1(\omega)$ and $\varepsilon_2(\omega)$ spectra

Figure IV.23 depicts optical response of III–V selected Alloys ($\varepsilon_1(\omega)$, $\varepsilon_2(\omega)$):

For $AlSb_{1-x}As_x$, The $\varepsilon_2(\omega)$ onsets and peaks blue-shift with increasing As, mirroring the gap widening. From Table IV.7, the first critical point P_0 rises monotonically from 1.78 eV (x=0) to 2.96 eV (x=1), while higher features shift similarly (P_1: 3.11→4.09 eV, P_2: 4.01→4.78 eV, P_3: 4.94→5.89 eV). The ε_2 envelopes keep similar shapes while moving to higher energies,. In $\varepsilon_1(\omega)$, the static limit decreases with As ($\varepsilon_1(0)$: 9.12 → 7.632), consistent with the Penn-type

anticorrelation of $\varepsilon_1(0)$ with E_g. At the endpoints, our P_0 agrees closely with TB-mBJ data for AlSb (1.775 eV) and lies within the spread reported for AlAs (present 2.96 eV vs 3.10 eV [31] and 2.75 eV [65]). For $\varepsilon_1(0)$, our AlSb value (9.12) matches TB-mBJ entries (9.13, 9.36) [24, 47] but is below the room-temperature experiment (12.04) [63]; for AlAs, our $\varepsilon_1(0)$=7.632 is close to experiment (8.20) [68] and lower than some TB-mBJ reports (9.42, 9.77) [66, 67].

For $AlSb_{1-x}Bi_x$, The Bi series (Figure IV.23) exhibits the opposite trend. In $\varepsilon_2(\omega)$, the onset and principal peaks red-shift and gain low-energy weight with x. Table IV.6 quantifies this: P_0 decreases from 1.78 eV (x=0) to 0.30 eV (x=1), with P_1: 3.11→2.17 eV, P_2: 4.01→3.70 eV, and P_3: 4.94→4.50 eV. Concomitantly, $\varepsilon_1(0)$ increases monotonically (9.12 → 9.88 → 10.56 → 11.83 → 13.24), reflecting the narrowed gap and enhanced low-energy interband strength. End-member comparisons are favorable: our AlSb P_0 matches TB-mBJ (1.775 eV) [24], while for AlBi we obtain P_0=0.30 eV vs 0.373 eV [24]; higher-energy features are also close (our P_1=2.17 eV vs 2.45 eV, P_2=3.70 eV vs 3.75 eV [24]). Our $\varepsilon_1(0)$ for AlBi (13.24) is slightly above the TB-mBJ value (12.67) [24], consistent with somewhat larger low-energy ε_2 weight in our spectra. Mechanistically, Bi-p states and stronger spin–orbit interaction pull thresholds downward and concentrate p-character at the valence edge, thus red-shifting ε_2 peaks and raising $\varepsilon_1(0)$.

Sb→As vs Sb→Bi:

Sb→As substitution produces a systematic blue-shift of all critical points ($\Delta P_0 \approx +1.2$ eV) and a decrease in $\varepsilon_1(0)$, whereas Sb→Bi yields a red-shift ($\Delta P_0 \approx -1.5$ eV) with $\varepsilon_1(0)$ increasing. These trends are coherent with our mBJ band-gap evolution and are consistent with the ranges reported by the TB-mBJ studies and other results cited in the table [24, 47, 66, 67, 31, 65] and with room-temperature experimental $\varepsilon_1(0)$ values where available [63, 68].

a.2) The absorption coefficients of III-V alloys.

Figure IV.24 presents the calculated absorption spectra $\alpha(\omega)$ for the $AlSb_{1-x}As_x$ and $AlSb_{1-x}Bi_x$ alloys across the studied compositions. In both systems, the absorption onset follows the fundamental bandgap energy (E_g), in full agreement with the results obtained from the band structure and $\varepsilon_2(\omega)$ spectra. As expected, smaller E_g values correspond to a red-shift of the absorption edge, while larger E_g values yield a blue-shift.

For **$AlSb_{1-x}As_x$**, the absorption edge systematically shifts to higher photon energies with increasing As concentration, consistent with the bandgap widening observed in Table IV.5. The absorption magnitude remains high (~1.5–1.8 × 10^6 cm^{-1}), typical of direct-gap III–V semiconductors [60,61]. The strongest absorption occurs around 4–6 eV, corresponding to interband transitions that also manifest as P_2 and P_3 peaks in $\varepsilon_2(\omega)$. The progressive blue-shift reflects chemical pressure induced by the smaller and more electronegative As atoms, which shortens Al–As bonds and increases transition energies. This trend confirms the stronger interband optical response in As-rich alloys.

For **$AlSb_{1-x}Bi_x$**, the situation contrasts: the absorption edge moves steadily to lower photon energies as Bi is introduced, reflecting the monotonic decrease in E_g with x (Table IV.5). The spectra exhibit a red-shift of the absorption onset, and the main $\alpha(\omega)$ peaks gradually weaken at high Bi content. This reduction in absorption strength is attributable to both lattice expansion and strong

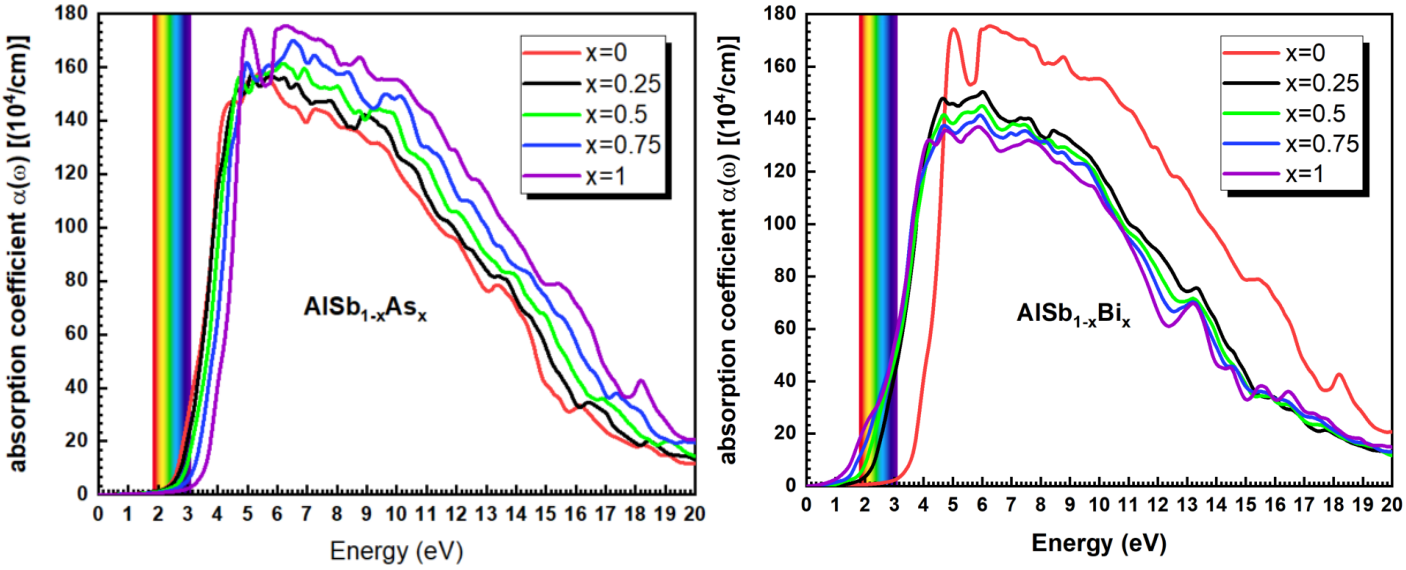


Figure IV.24. III-V Selected alloys' absorption coefficients

spin–orbit coupling from Bi-p states, which lower the Γ conduction band valley and compress the valence states. As a result, although Bi-alloyed systems still show strong absorption in the visible–UV range, the overall spectrum shifts toward lower energies with diminished magnitude compared to the As-series.

a.3) The refractive indices of III-V alloys.

Figure IV.25 shows III-V Selected alloys' Refractive indices.

$AlSb_{1-x}As_x$ (ZB): Static index follows $n(0) = \sqrt{\varepsilon_1(0)}$. From Table IV.8, n(0) decreases almost monotonically with x: 3.02 → 2.99 → 2.92 → 2.83 → 2.76 (for x = 0…1). This tracks the band-gap increase reported in Table IV.5 (AlSb → AlAs) and the blue-shift of P_0–P_3 in $\varepsilon_2(\omega)$. Spectral shape. In Fig. IV.25, the principal $n(\omega)$ hump lies near 3–4.5 eV and moves to higher energy as x increases; the slope below the hump becomes slightly gentler, indicating less low-energy oscillator strength.

Table IV.8. Estimated static refractive index *n(0)* of III–V selected alloys in ZB phase via KTB-mBJ, compared with other theoretical calculations and available experimental data.

Alloy (x)	Our work (n(0))	Other theoretical (n(0))	Experimental (n(0))
$AlSb_{1-x}As_x$			
x = 0.0 (AlSb)	3.02	3.02 [24], 3.06 [47]	3.05 [63]
x = 0.25	2.99	–	–
x = 0.5	2.92	–	–
x = 0.75	2.83	–	–
x = 1.0 (AlAs)	2.76	3.06 [66], 3.12 [67]	2.86 [68]
$AlSb_{1-x}Bi_x$			
x = 0.0 (AlSb)	3.02	3.02 [24], 3.06 [47]	3.05 [63]
x = 0.25	3.14	–	–
x = 0.5	3.25	–	–
x = 0.75	3.44	–	–
x = 1.0 (AlBi)	3.64	3.56 [24], 4.02 [70]	–

The absorption plots (Fig. IV.24) confirm a bluer onset and higher-energy maxima, which—via Kramers–Kronig—produce the observed drop in n(0) and the blue-shift of the dispersion maximum.

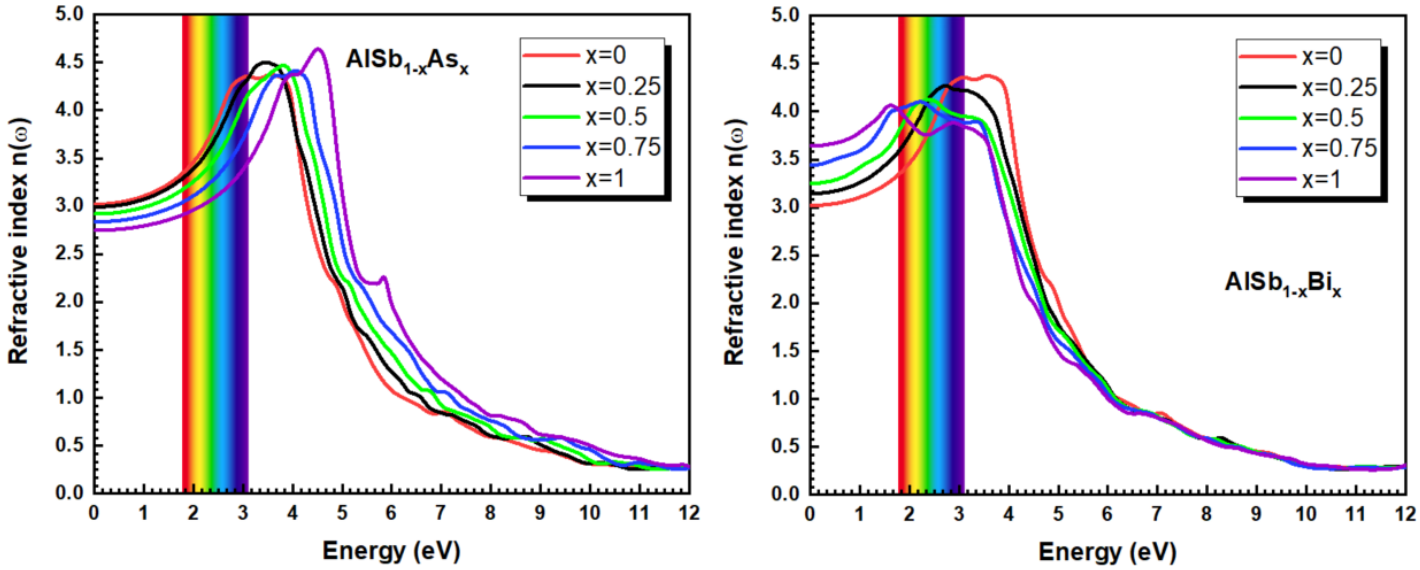


Figure IV.25. III-V Selected alloys' Refractive indices

For $AlSb_{1-x}Bi_x$, Static index. Table IV.8 shows n(0) increases with x: 3.02 → 3.14 → 3.25 → 3.44 → 3.64. This mirrors the gap reduction in Table IV.5. Spectral shape. In Fig. IV.25, the main n(ω) hump remains in the ~3–4 eV window but shifts to lower energy and gains weight at lower ω, consistent with $\varepsilon_2(\omega)$ moving oscillator strength toward the visible/near-IR and with α(ω) onsets sliding to smaller photon energy

Both series obey the expected trend n(0)↓ when Eg↑ (As-rich) and n(0)↑ when Eg↓ (Bi-rich) (Penn-type anticorrelation). The magnitudes (≈2.7–3.6) are typical for III–V's and match $\sqrt{\varepsilon_1(0)}$ from Table IV.7. The blue-shift of n(ω) in $AlSb_{1-x}As_x$ and the red-shift in $AlSb_{1-x}Bi_x$ are consistent with the shifts of P_1–P_3 in $\varepsilon_2(\omega)$ and the edges in α(ω).

Inflection points in n(ω) line up with the strong ε_2 peaks because both derive from the same interband critical points. As-rich alloys offer lower index , while Bi-rich alloys provide higher index at lower photon energies.

a.4) The reflectivities of III-V alloys.

Reflectivity is the fraction of incident light power that is bounced back from the surface of a material at a given photon energy. In practice it is governed by the complex refractive index: the

larger the refractive index and/or the stronger the absorption at a given energy, the larger the reflected fraction.

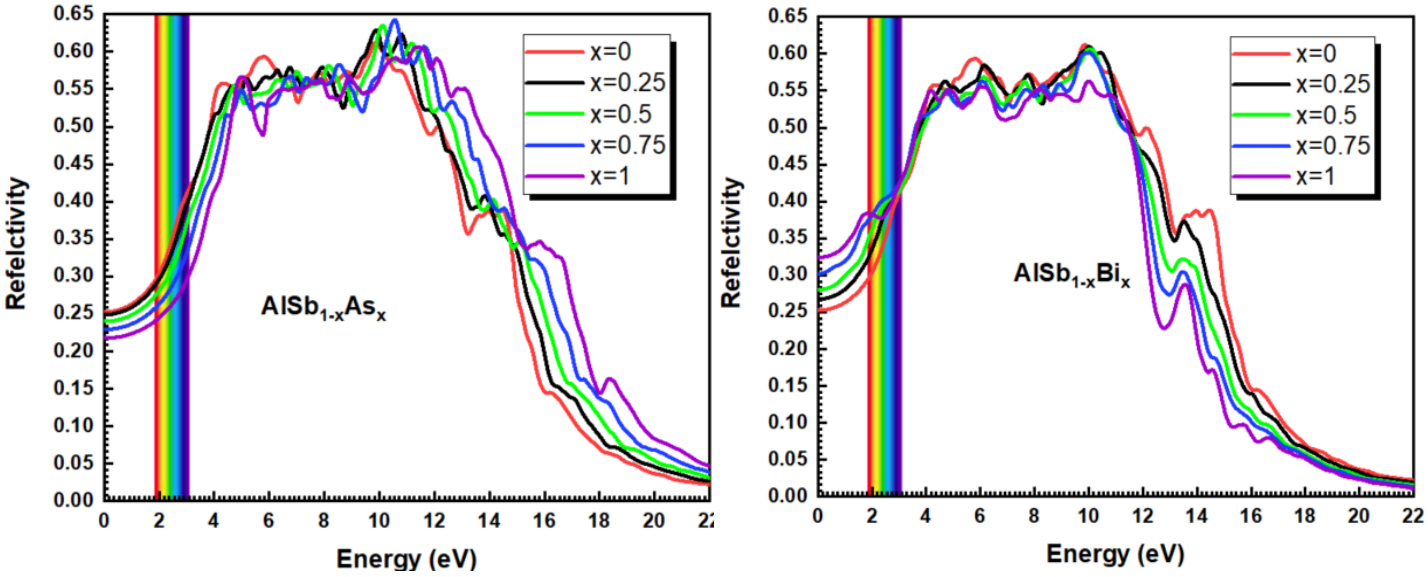


Figure IV.26. Reflectivities of selected III-V alloys

For **$AlSb_{1-x}As_x$**, The As series shows a progressive drop of the low-energy reflectivity as x increases, consistent with the measured decrease of n(0) in Table IV.7 (3.02 → 2.76 from AlSb to AlAs). Because a lower refractive index reduces the impedance mismatch with air, the surface returns a smaller fraction of the incident light. In Fig. IV.26 all compositions develop a broad reflectivity plateau around 0.50–0.62 in the near-UV to deep-UV; its onset and the position of the maxima shift to higher photon energy with increasing As. This blue-shift mirrors the movement of the critical points in $\varepsilon_2(\omega)$ and the higher-energy absorption peaks in $\alpha(\omega)$. The high-energy falloff of $R(\omega)$ likewise moves to higher energies at As-rich compositions, completing a consistent blue-shift across all optical observables.

For **$AlSb_{1-x}Bi_x$**, The Bi series exhibits the opposite trend. The low-energy reflectivity increases steadily with x, tracking the increase of n(0) reported in Table IV.7 (3.02 → 3.64 from AlSb to AlBi). A higher index means a stronger impedance mismatch and therefore a larger reflected fraction even before interband absorption sets in. In the UV, the main reflectivity band remains strong (again around 0.50–0.62),.As Bi is added, both the onset and the peaks of **R(ω)** shift to lower energies. This red-shift mirrors the behavior of **ε2(ω)** and the absorption edge, which also move to

smaller photon energies due to the increased polarizability brought by Bi and the consequent lowering of interband transition thresholds. Correspondingly, the high **R(ω)** occurs at lower energies in Bi-rich alloys.

Consistency with band gaps. Across both families the low-energy reflectivity anticorrelates with the fundamental gap: larger gaps (As-rich) give smaller n(0) and lower reflectivity, whereas smaller gaps (Bi-rich) give larger n(0) and higher reflectivity. Spectral shifts tied to interband structure. The broad UV features of R(ω) blue-shift in the As series and red-shift in the Bi series, exactly as do the critical-point peaks in $\varepsilon_2(\omega)$ and the maxima of α(ω). This one-to-one correspondence confirms that the same interband transitions control all three spectra.

In sum, the reflectivity data form a coherent picture with the refractive-index dispersion, the dielectric spectra, and the absorption: Sb→As drives a blue-shift and reduces the surface reflectance; Sb→Bi drives a red-shift and raises it. This is the expected optical fingerprint of band-gap engineering across the two alloy families.

a.5) Optics-Guided Device Design for $AlSb_{1-x}As_x$ and $AlSb_{1-x}Bi_x$

For the III–V alloys on the AlSb lattice, our electronic and optical results point to two complementary application tracks. In $AlSb_{1-x}As_x$, a direct Γ–Γ window confined to x ≈ 0.25–0.75 with Eg ≈ 1.50–1.89 eV (≈830–660 nm) supports red to deep-red emitters and detectors: thin active-region LEDs/edge-emitters around 0.66–0.80 μm and compact photodiodes in the 0.70–0.85 μm band, as corroborated by the steep α(ω) onsets and $\varepsilon_2(\omega)$ peaks in this range. Toward the As-rich end, the larger gap and lower refractive index (n(0) ≈ 2.76) reduce baseline reflectance R(0), making AlAs-lean compositions suitable as low-loss claddings/AR windows/DBR partners for GaSb-platform lasers operating near 0.65–0.9 μm; by contrast, the indirect binaries (AlSb, AlAs) are best reserved for passive/structural roles. In $AlSb_{1-x}Bi_x$, any Bi addition (x>0) yields a direct Γ–Γ gap that is continuously tunable from ≈1.38 eV to ≈0.30 eV (≈0.9–4.1 μm), enabling telecom/NIR modulators and detectors at 1.0–1.6 μm for x ≈ 0.5–0.75, and extending to SWIR/MWIR interband photodetectors or thermophotovoltaic cells in the 2–4 μm window as the gap narrows; the robust α(ω) in this region and red-shifted $\varepsilon_2(\omega)$ features confirm efficient interband coupling. Bi-rich alloys also exhibit higher index (n(0) → ~3.6) and higher R(0), advantageous for high-contrast

DBRs, gratings, and compact IR photonic resonators, while mid-x direct wells with compatible Al(Sb,Bi) barriers provide a practical route to interband-cascade/quantum-well gain media with reduced thresholds relative to indirect counterparts.

b) II-VI selected alloys

b.1) The dielectric functions of II-VI alloys.

Method notes: Present optical spectra and $\varepsilon_1(0)$ are computed with KTB-mBJ. Literature datasets used for benchmarking are plain GGA: [51] and [40]. Experimental static dielectric constants are from [71]. Our values, other calculations and exp values of Critical-Point Energies of $\varepsilon_2(\omega)$ and Static Dielectric Constant $\varepsilon_1(0)$ are tabulated in table IV.9.

$BaO_{1-x}S_x$ (rock-salt, KTB-mBJ optics): Figure IV.27 (top) shows a clear red-shift and strengthening of $\varepsilon_2(\omega)$ with increasing S content. Critical-point (CP) energies from Table IV.7 evolve as P_0: 3.59 → 2.83 eV, P_1: 5.86 → 4.84 eV, P_2: 7.87 → 6.62 eV, P_3: 8.43 → 7.24 eV for x: 0 → 1. Through Kramers–Kronig, this migration raises the static dielectric constant from $\varepsilon_1(0)$=3.34 (BaO) to 4.26 (BaS).

Compared with GGA optics, [51]/[40] place the first strong CP near ≈2.6 eV and generally lower all CPs by ≈0.6–1.0 eV, and they yield $\varepsilon_1(0)$=4.45/4.11 (BaO) and 5.58/5.08 (BaS) systematically too large because GGA underestimates the gap. Our KTB-mBJ values correct the gap and pull $\varepsilon_1(0)$ down toward experiment: BaO 3.34 vs 3.68 [71] (−9%), BaS 4.26 vs 4.26 [71] (exact).

$BaO_{1-x}Se_x$ (rock-salt, KTB-mBJ optics): For the Se series (Fig. IV.27 bottom), the same trends are present but more pronounced. Table IV.7 gives P_0: 3.59 → 3.22 eV, P_1: 5.86 → 4.28 eV, P_2: 7.85 → 6.11 eV, P_3: 8.44 → 6.73 eV for x: 0 → 1.

The stronger red-shift and growth of P_1/P_2 reflect h. The integrated consequence is $\varepsilon_1(0)$=3.34 → 4.71 from BaO to BaSe. As in the S series, GGA [51]/[40] puts near-edge CPs too low and overestimates the static dielectric response ($\varepsilon_1(0)$=6.07/5.55 for BaSe).

Our KTB-mBJ value 4.71 lies much closer to experiment 4.48 [71] (+5%), confirming that the mBJ-calibrated dispersion removes spurious near-gap strength and yields a more faithful $\varepsilon_1(0)$.

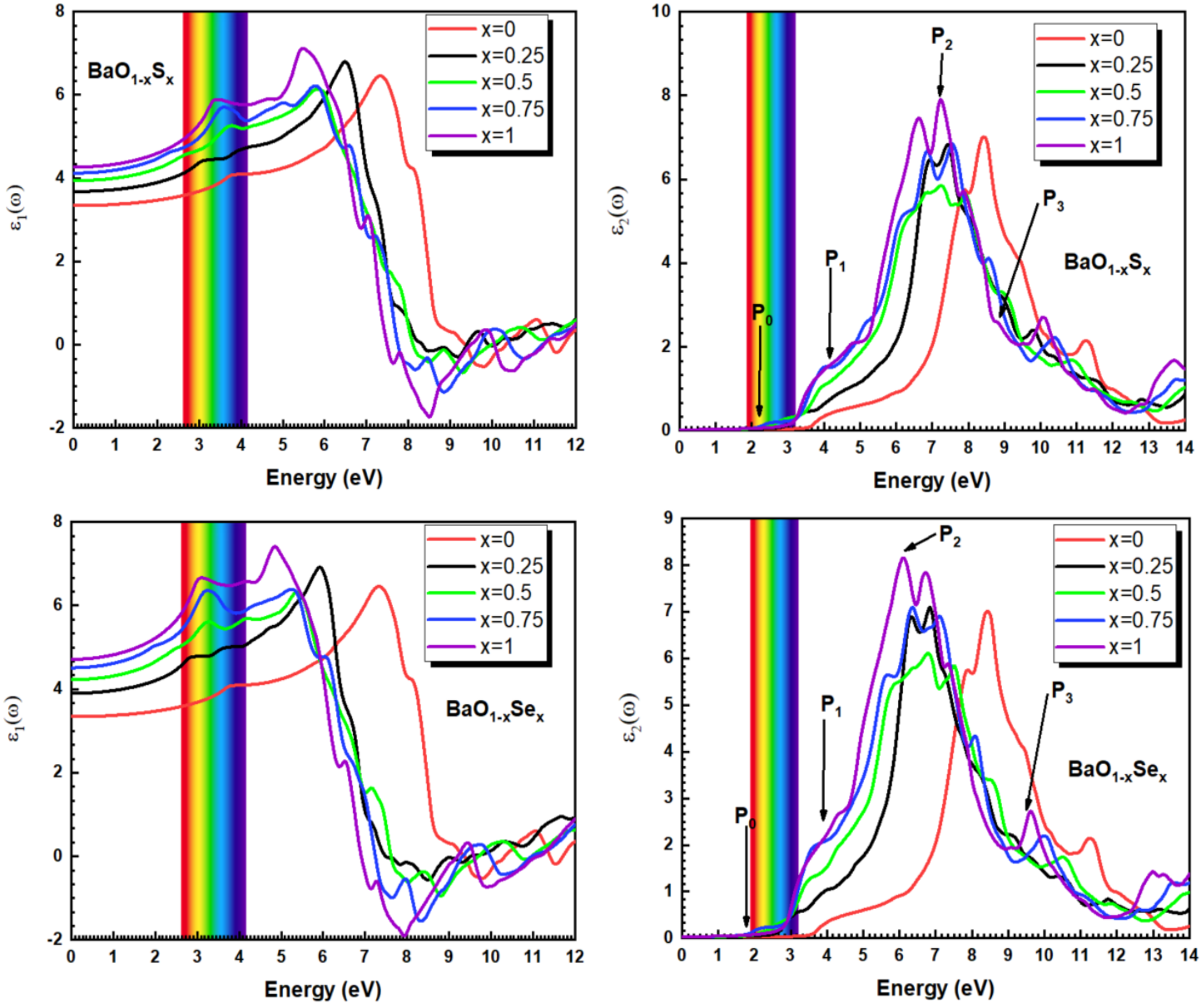


Figure IV.27. The dielectric functions of II-VI selected alloys

Table IV.9. II-VI Selected alloys' Critical-Point Energies of $\varepsilon_2(\omega)$ and Static Dielectric Constant $\varepsilon_1(0)$

$BaO_{1-x}S_x$												
	Present calculations					Other theoretical calculations					Exp	
x	P_0	P_1	P_2	P_3	$\varepsilon_1(0)$	P_0	P_1	P_2	P_3	$\varepsilon_1(0)$	$\varepsilon_1(0)$	P_0
0	3.59	5.86	7.87	8.43	3.34	–	2.62 [51]	–	–	4.45[51] 4.11[40]	3.68 [71]	–
0.25	2.93	4.69	6.93	7.43	3.68	–		–	–	4.39 [40]	–	–
0.5	2.38	3.85	6.83	7.91	3.94	–		–	–	4.6 [40]	–	–
0.75	2.21	3.98	6.87	7.25	4.12	–		–	–	4.97 [40]	–	–
1	2.83	4.84	6.62	7.24	4.26	–	2.59 [51]	–	–	5.58[51] 5.08[40]	4.26 [71]	–
$BaO_{1-x}Se_x$												
	Present calculations					Other theoretical calculations					Exp	
x	P_0	P_1	P_2	P_3	$\varepsilon_1(0)$	P_0	P_1	P_2	P_3	$\varepsilon_1(0)$	$\varepsilon_1(0)$	P_0
0	3.59	5.86	7.85	8.44	3.34		2.62 [51]	–	–	4.45[51] 4.11[40]	3.68 [71]	–
0.25	2.78	3.94	6.32	6.84	3.90	2.89[35]	–	–	–	3.17[35]	–	–
0.5	2.11	3.66	6.84	7.51	4.23	2.51[35]	–	–	–	3.57[35]	–	–
0.75	1.89	3.59	6.36	7.13	4.5	2.08[35]	–	–	–	3.87[35]	–	–
1	3.22	4.28	6.11	6.73	4.71	–	2.27 [51]	–	–	6.07 [51] 5.55[40]	4.48 [71]	–

Comparing both alloy families at matched x shows that $BaO_{1-x}Se_x$ undergoes a larger red-shift of P_1–P_3 and reaches a higher $\varepsilon_1(0)$ than $BaO_{1-x}S_x$. Across both systems, our KTB-mBJ spectra are blue-shifted relative to GGA ([51],[40]) by ≈0.6–1.0 eV for the first CP and deliver $\varepsilon_1(0)$ values systematically closer to experiment [71] hence they constitute enhanced (mBJ-calibrated) optics.

b.2) The absorption coefficients of II-VI alloys.

$BaO_{1-x}S_x$: The absorption edge red-shifts with x, consistent with the $\varepsilon_2(\omega)$ P_0 trend (Table IV.7: P_0 ≈ 3.59 → 2.83 eV for x:0→1). Taking a practical threshold $\alpha \approx 3.10^4 cm^{-1}$, the onset moves from 3.4–3.6 eV (BaO) toward ≈3.0 eV (BaS). The first broad band associated with p(VB)→Ba-d(CB) transitions (linked to P_1/P_2) rises rapidly across 5–8 eV and peaks around $(1.3–1.5)\times10^6$ cm^{-1}. A second band appears near 9–11 eV.

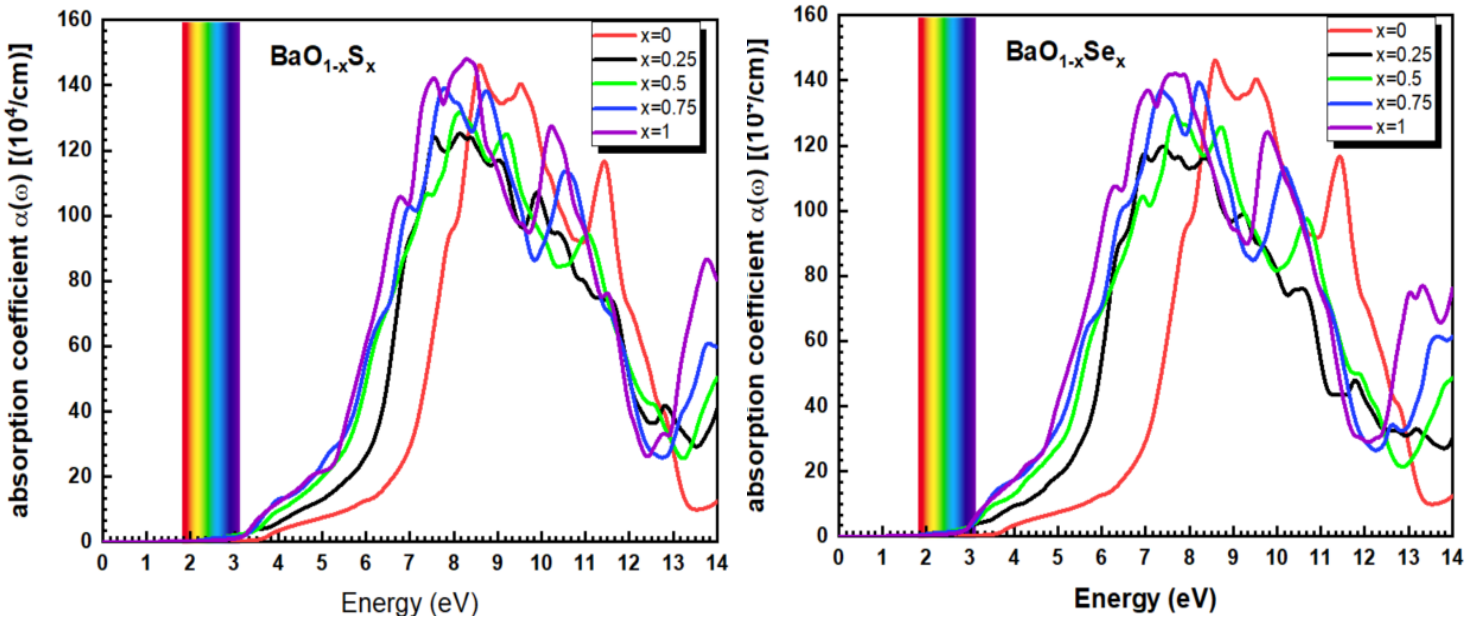


Figure IV.28. The absorption coefficients of II-VI alloys.

$BaO_{1-x}Se_x$: The edge also red-shifts with x but somewhat less than in the S series (Table IV.7: P_0 ≈ 3.59 → 3.22 eV for x:0→1). Beyond ≈5 eV the absorption strengthens more markedly than in $BaO_{1-x}S_x$, producing a dominant band in the 6–8 eV window with peaks up to ≈(1.4–1.5)×10^6 cm^{-1}, followed by a composition-dependent band near 9–11 eV.

At identical x, $BaO_{1-x}S_x$ tends to exhibit a slightly lower absorption threshold (earlier edge), while $BaO_{1-x}Se_x$ yields a steeper rise and larger α(ω) once above ≈5 eV. Thus S-rich alloys are favorable when a lower UV cut-off is desired, whereas Se-rich alloys provide stronger absorption in the near-/mid-UV (≈6–8 eV). Across both families, mBJ yields edges and band positions ~0.6–1.0 eV higher than plain GGA [51],[40], consistent with our $\varepsilon_1(0)$ benchmarking against experiment [71] and supporting the view that these are enhanced (mBJ-calibrated) absorption predictions.

b.3) The refractive indices of II-VI alloys.

We analyze the refractive-index dispersion n(ω) and static indices $n(0)=\sqrt{\varepsilon_1(0)}$ for $BaO_{1-x}S_x$ and $BaO_{1-x}Se_x$ alloys. Optical properties are obtained using the KTB-mBJ potential. We benchmark

n(0) against experiment [71] and prior GGA calculations [51],[40], with additional TB-mBJ values [35] where available. The computed n(0) values are tabulated in table IV.10.

$BaO_{1-x}S_x$: Dispersion shows normal behavior up to about 6 eV, with n(ω) increasing from roughly 1.9 near the edge to a broad maximum around 5–6 eV before declining above 7–8 eV as $\varepsilon_1(\omega)$ decreases after the main $\varepsilon_2(\omega)$ band. Increasing S content red-shifts the underlying ε_2 critical points (P_0–P_2) and lifts n through the visible/near-UV. Static indices evolve monotonically with composition: n(0) = 1.83 (x=0), 1.92 (0.25), 1.98 (0.5), 2.03 (0.75), 2.06 (1).

Table IV.10. n(0) computed values II–VI selected alloys in NaCl phase via KTB-mBJ along With Benchmarks (Exp [71], GGA [51],[40], TB-mBJ[35])

Series	x	Present	Exp [71]	GGA [51]	GGA [40]	TB-mBJ[35]
$BaO_{1-x}S_x$	0	1.83	1.92	2.11	2.03	—
	0.25	1.92	—	—	2.09	—
	0.5	1.98	—	—	2.14	—
	0.75	2.03	—	—	2.23	—
	1	2.06	2.06	2.36	2.25	—
$BaO_{1-x}Se_x$	0	1.83	1.92	2.11	2.03	—
	0.25	1.97	—	—	—	1.78
	0.5	2.06	—	—	—	1.89
	0.75	2.12	—	—	—	1.97
	1	2.17	2.12	2.46	2.36	—

$BaO_{1-x}Se_x$: The Se series exhibits the same overall shape but with a slightly higher plateau and a stronger maximum in the 5–7 eV window. Static indices are consistently higher than in the S series at matched x: n(0) = 1.83 (x=0), 1.97 (0.25), 2.06 (0.5), 2.12 (0.75), 2.17 (1). At high energies (≥10 eV), both series approach n≈1.

$BaO_{1-x}Se_x$ delivers a higher index across the visible/near-UV. S-rich alloys retain a marginally earlier absorption edge (lower UV cutoff), whereas Se-rich alloys provide stronger n in the 5–7 eV band. Because mBJ corrects the band gap, our n(0) values sit closer to experimental endpoints than

GGA's, which typically overestimates n(0).While for (x=0.25, 0.5, 0.75) our results (n(0)) are to some extent lower than those of GGA's (ref [40]) for $BaO_{1-x}Se_x$, and closely agree with the results obtained using TB-mBJ in ref [35].

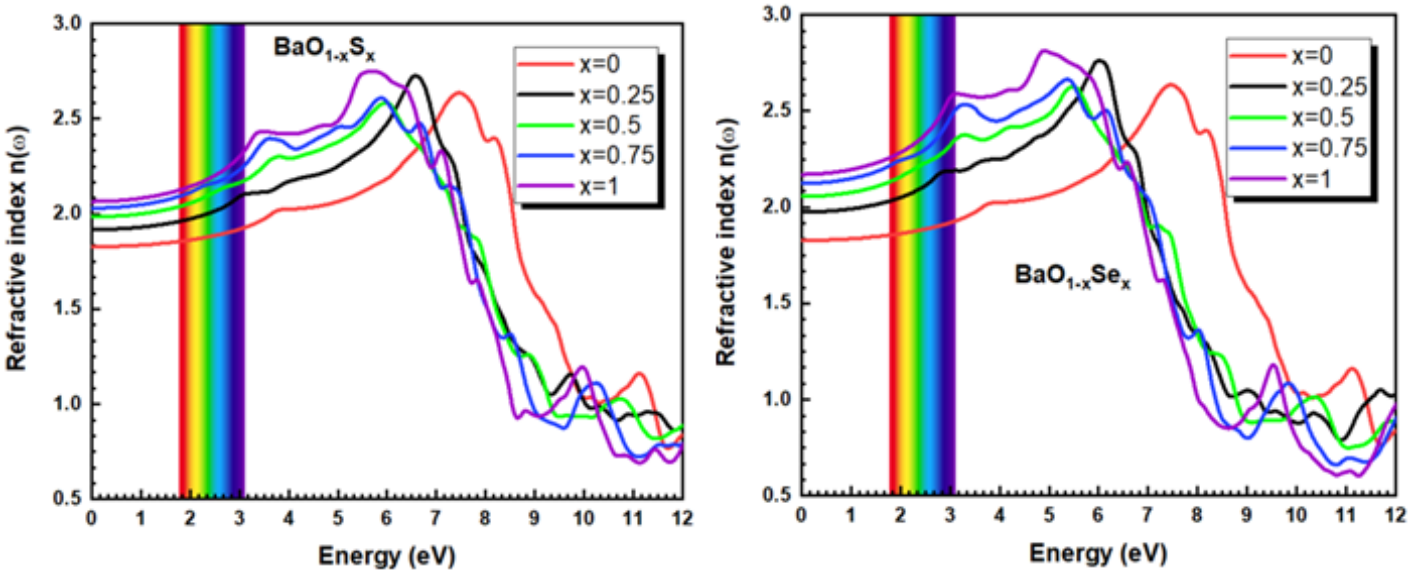


Figure IV.29. The refractive indices of selected II-VI alloys.

b.4) The reflectivities of II-VI selected alloys.

$BaO_{1-x}S_x$: Below ≈3–3.5 eV (pre-edge, k≈0) the spectra sit on a slowly rising Fresnel baseline governed by n(0). Using n(0) ≈ 1.83, 1.92, 1.98, 2.03, 2.06 for x = 0, 0.25, 0.5, 0.75, 1 ; hence R(0) increases monotonically across the series from ≈0.086 to ≈1.121 . Once interband transitions turn on (≈3–4 eV), R climbs into a broad maximum centered at ~6.5–8.5 eV. This peak tracks the $\varepsilon_2(\omega)$ critical points P_1/P_2; their red-shift with x pushes the reflectivity maximum to lower energies while also raising it .Above ≈11 eV, $\varepsilon_1(\omega)$ falls toward unity , producing a sharp minimum around 11.5–12.5 eV followed by a low-R high-energy window. Subtle shoulders beyond 12 eV correlate with the higher ε_2 feature P_3.

$BaO_{1-x}Se_x$: The Se series preserves the same structure but is slightly more reflective in the 5–8 eV region. The baseline rises from R≈0.08 at x=0 to ≈0.13–0.14 at x=1, consistent with n(0)=1.83→2.17. After the onset, R grows more steeply than in the S series and peaks around 6.5–8.5 eV at R≈0.34–0.40 for Se-rich alloys.

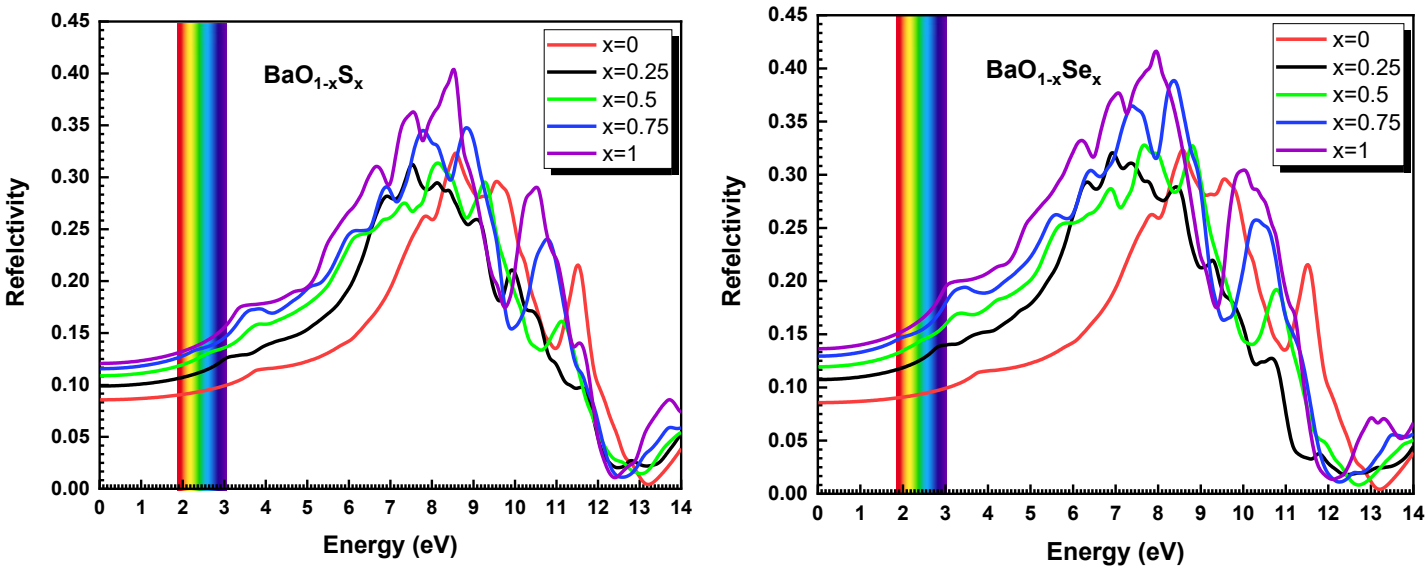


Fig 30. The reflectivities of II-VI selected alloys.

At the same composition, $BaO_{1-x}Se_x$ exhibits a slightly higher reflectivity peak and a marginally steeper rise, whereas $BaO_{1-x}S_x$ maintains a slightly earlier UV onset. For deep-UV coatings (≈6–8 eV; 200–155 nm), Se-rich alloys are preferable for stronger R, while S-rich alloys offer an earlier cut-off with still-moderate peaks. Because KTB-mBJ corrects the fundamental gap relative to GGA, these peaks are blue-shifted compared with plain-GGA predictions.

b.5) Optics-Guided Device Design for $BaO_{1-x}S_x$ /$BaO_{1-x}Se_x$

$BaO_{1-x}S_x$: The pre-edge region is transparent across ≈3.2–3.6 eV, and the static index increases monotonically with sulfur content (n(0)≈1.83→2.06 for x:0→1), which lifts the Fresnel baseline reflectivity from about 0.086 (BaO) to 0.120 (BaS). In practice this makes S-rich films reliable, moderate-index building blocks for anti-reflection coatings in the near-UV and visible (λ≳390–400 nm). Because the absorption onset P_0 red-shifts toward ~3.0–3.2 eV as x→1 and α(ω) rises steeply after the edge, S-rich alloys are well suited to edge-selective UV-A photodetectors and UV cut-off filters placed near ~3.1 eV. All recommendations rely on our KTB-mBJ optics ($\varepsilon_2 \rightarrow \varepsilon_1 \rightarrow$n,k and R), which correct plain-GGA tendencies and keep n(0) aligned with experiment.

$BaO_{1-x}Se_x$: The selenium series keeps a slightly higher band-edge window (P_0≈3.2–3.6 eV) but carries a consistently larger static index (n(0)≈1.83→2.17), yielding a higher below-edge

reflectance baseline (up to 0.136 for BaSe). Mid-range compositions (x≈0.3–0.7) place the photo response cutoff in the violet/near-UV (≈3.3–3.5 eV) for edge-tuned photodetection, whereas pushing to x→1 maximizes index and reflectivity for mirror or blocking roles. As with the sulfur series, the strong absorption tied to the P_1–P_2 band makes these films unsuitable for deep-UV transmission.

All previous applications suggestions rely on our KTB-mBJ calculations and further experimental studies are required to address the feasibility of these applications.

c) Cross-family fomparison of optical properties

Across our two families, the selected III–V alloys behave as low-gap, high-index semiconductors with $\varepsilon_2(\omega)$ turning on in the NIR/visible (sub-eV to ~2 eV depending on composition) and most oscillator strength packed below ~5–6 eV (classic E_1/E_2 region), which yields large n (typically ~3–3.5), a high Fresnel baseline R (~0.20–0.30) even below the edge, and strong dispersion tailor-made for emit/detect functions (LEDs, lasers, photodiodes) and very-high-n interference optics across the visible/NIR; in contrast, our II–VI rocksalt alloys $BaO_{1-x}S_x$/$BaO_{1-x}Se_x$ are wide-gap, visible-transparent materials whose ε_2 onset (P_0) lies near 3.6→~3.0 eV as x increases, with their strongest optical band (P_1–P_2) pushed into the deep-UV (~6–8 eV), giving moderate static indices that rise monotonically with x (n(0)≈1.83→2.06 for BaO→BaS and →2.17 for BaO→BaSe) and a correspondingly modest sub-edge reflectivity (~0.10–0.14). Practically, the III–V set is the go-to when you need high n and early absorption/emission in the NIR/visible or interband gain, whereas the II–VI set shines when you want clean UV-A cut-offs (earlier for S-rich; slightly later but higher-n for Se-rich), strong deep-UV blocking/reflecting around 6–8 eV.

IV.VI. Elastic Properties

a) III-V selected alloys

$AlSb_{1-x}As_x$: The $AlSb_{1-x}As_x$ alloys were treated in the cubic phase, for which only C_{11}, C_{12} and C_{44} are independent. Elastic tensors were obtained with IRelast in WIEN2k at the WC–GGA level, then Voigt–Reuss–Hill (VRH) averages were used to derive polycrystalline moduli and secondary indicators (Pugh ratio, Poisson's ratio, Cauchy pressure, and anisotropy indices).

For context, the study labeled Ref. [13] in Table IV.11 used the Hamann et al. finite-strain elastic-constants method, whereas the other cited works employed IRelast (GGA).

For every composition the ordering $C_{11} > C_{44} > C_{12}$ is preserved and the Born stability criteria for a cubic lattice are satisfied ($C_{11}-C_{12} > 0$, $C_{44} > 0$, $C_{11}+2C_{12} > 0$), confirming mechanical stability. At the Sb-rich end (x = 0) we obtain C_{11} = 82.31 GPa, C_{12} = 42.43 GPa and C_{44} = 51.11 GPa towards AlAs (x = 1) the three constants increase to 105.25, 53.33 and 68.48 GPa, respectively.

Table IV.11 Single-Crystal Stiffness (C_{11}, C_{12}, C_{44}) and Polycrystalline Bulk Modulus (GPa), Shear Modulus (GPa), Young's Modulus (GPa), Poisson's Ratio, Vickers Hardness (GPa), Pugh Ratio, and Cauchy Pressure (GPa) for $AlSb_{1-x}As_x$ via WC-GGA with available other calculations and existing experimental values

x	C_{11}	C_{12}	C_{44}	*B*	*Y*	*G*	*v*	H_v	*B/G*	C_p
0										
Our	82.31	42.43	51.108	55.721	86.91	35.04	0.24	6.61	1.59	-8.67
Other	84.97[47]	42.39[47]	1.74[47]	56.09[47]	82.23	32.70[47]	0.25[74]	-	-	-
	89.69[72]	38.67[72]	6.26[72]	55.68[72]	66.16	22.10[48]	0.25[75]	-	-	-
	85.32[13]	41.51[13]	39.80[13]	56.10[13]	-	25.42[74]	-	-	-	-
EXP	87.69[73]	43.41[73]	40.76[73]	55.10[73]	-	-	-	-	-	-
0.25	86.00	44.31	60.95	58.21	96.99	39.68	0.22	8.06	1.47	-16.6
	91.04[13]	44.36[13]	42.58[13]							
	89.09[13]	43.39[13]	41.82[13]							
0.5	91.85	47.60	65.51	65.51	103.76	42.43	0.22	8.43	1.47	-17.9
0.75	99.18	51.22	69.86	67.21	111.45	45.54	0.22	8.83	1.48	-18.6
1.0										
Our	105.25	53.33	68.48	70.64	114.24	46.42	0.23	8.48	1.52	-15.2
Other	101.30[76]	50.97[78]	54.58[78]	66.07[76]	95.67[76]	38.00[76]	0.26[76]	7.13[78]	1.74	-
	112.36[77]	48.40[76]	48.4[76]	-	-	-	-	-	[76]	-
	105.43[78]	57.07[77]	53.16[77]	-	-	-	-	-	-	-
EXP	119.90[79]	57.50[79]	56.60[79]	74.00[34]	-	-	0.32[79]	-	-	-

Thus, replacing Sb with As systematically stiffens the single-crystal response. The bulk modulus extracted from the elastic set evolves from 55.7 GPa (x = 0) to 70.6 GPa (x = 1), indicating reduced compressibility with As incorporation. At the binaries our AlSb set lies within reported ranges, while C_{44} is somewhat higher than several experimental/DFT values; for AlAs our C_{11}–C_{12} pair is

below the highest experimental numbers but C_{44} remains on the high side overall within the literature spread. VRH averages: the shear modulus increases from 35.0 to 46.4 GPa and Young's modulus from 86.9 to 114.2 GPa as x goes from 0 to 1. The Poisson ratio stays low and nearly composition-independent (≈0.22–0.23), which is characteristic of a directional, weakly metallic bonding network.

Two independent metrics classify the whole series as brittle at ambient conditions: the Pugh ratio remains below 1.75 (≈1.47–1.59) and ν remains below 0.26. The Cauchy pressure $C' = C_{12} - C_{44}$ is negative at all x (about −9 to −19 GPa), reinforcing a predominantly covalent, directional bonding picture that strengthens through the mid-As range and relaxes slightly at AlAs. In line with the increase of G, the Vickers hardness estimated from the elastic moduli grows from ~6.6 GPa (x = 0) to ~8.5 GPa (x = 1), peaking near x ≈ 0.75.

Elastic anisotropy (Table IV.12) : The Zener factor is well above unity from x = 0 to 0.75 (A ≈ 2.5–3.0), implying greater rigidity along ⟨111⟩ than along ⟨100⟩; at x = 1 it drops to 1.32, indicating reduced though still non-negligible anisotropy in AlAs. The percent anisotropy of the bulk modulus is zero at every composition, whereas the shear percent anisotropy is small but finite ($A_G \approx 0.10 - 0.14$), consistent with a modest directionality in shear response. The universal anisotropy index peaks around the mid-range (A^U ≈ 1.5–1.6 for x = 0.25–0.75) and declines to 1.22 at AlAs, mirroring the Zener trend.

Across $AlSb_{1-x}As_x$ (x = 0, 0.25, 0.50, 0.75, 1.0) our single-crystal elastic constants and VRH moduli evolve smoothly with composition, showing progressive stiffening as Sb is replaced by As. For

Table IV.12. Computational results of Zener anisotropic index A, percentage anisotropic indices (A_G) and (A_B) ,the universal anisotropic factor (A^U) are in GPa, of $AlSb_{1-x}As_x$ alloys via WC-GGA with other available calculations.

x	A	A_B	A_G	A^U
0	2.50	0.00	0.10	1.14
0.25	2.92	0.00	0.13	1.52
0.50	2.96	0.00	0.14	1.56
0.75	2.91	0.00	0.13	1.51
1 our work	1.32	0.00	0.11	1.22
1 other work	2.03[78]	-	-	0.63[78]

AlSb, our set (C_{11}, C_{12}, C_{44}) = (82.31, 42.43, 51.11) GPa compares well with the compiled ranges in Refs. [30, 36, 37, 9], with C_{11} a few gigapascals below typical 85–90 GPa values, C_{12} within the common 39–43 GPa interval, and C_{44} higher than many reports (often mid-30s to low-40s GPa); the bulk modulus from the elastic tensor, B ≈ 55.7 GPa, matches the ≈55–56 GPa benchmark. At x = 0.25, all three C_{ij} increase relative to AlSb and B rises to ≈58.2 GPa, while the VRH shear and Young's moduli reach ≈39.7 and ≈97.0 GPa; although composition-resolved literature values are not available at this x in our citation set, the trend conforms to the end-member ordering and the expected strengthening of Al–As bonding. At x = 0.50, the monotonic trajectory continues (B ≈ 65.5 GPa, G ≈ 42.4 GPa, Y ≈ 103.8 GPa) together with pronounced yet physically reasonable elastic anisotropy, a feature often observed near mid-series in III–V substitutions. At x = 0.75, B, G and Y rise further (≈67.2, 45.5 and 111.5 GPa, respectively) and the estimated Vickers hardness peaks (≈8.5 GPa), maintaining negative Cauchy pressure and low Poisson's ratio, both indicators of directional (covalent-leaning) bonding. At x = 1.0 (AlAs), our (C_{11}, C_{12}, C_{44}) = (105.25, 53.33, 68.48) GPa and B ≈ 70.6 GPa fall within modern DFT/empirical spreads; as for AlSb, our C_{44} is on the high side relative to several reports. Throughout the series, G increases from ≈35 to ≈46 GPa, Y from ≈86.9 to ≈114.2 GPa, Poisson's ratio remains low (≈0.22–0.23), B/G stays below 1.75 and Cauchy pressure remains negative, collectively supporting a consistent picture of increasing stiffness, persistent brittleness at ambient conditions, and covalent-leaning bonding as As content rises. Small deviations with Ref. [13] are attributable to methodological differences (finite-strain implementation and fit windows) rather than physics, and do not alter the composition-dependent trends summarized here.

In summary , As alloying tightens the lattice and monotonically raises B, G and Y while keeping ν low, B/G < 1.75 and $C' < 0$. The series therefore evolves toward a stiffer, harder yet still brittle and covalent-leaning solid, with anisotropy strongest at intermediate x and partially relieved at the AlAs endpoint. These mechanical trends are consistent with the structural picture of shorter, stronger Al–As bonds as Sb is replaced by the smaller, more electronegative As anion.

$AlSb_{1-x}Bi_x$: Across $AlSb_{1-x}Bi_x$ (x = 0, 0.25, 0.50, 0.75, 1.0) our elastic data in Table IV.13 show a clear, composition-driven softening as Sb is replaced by Bi, consistent with the larger size and higher polarizability of Bi. At x = 0 (AlSb) our single-crystal set (C_{11}, C_{12}, C_{44}) = (82.31, 42.43, 51.11) GPa lies within the binary literature spread: C_{11} sits a few GPa below common 85–90 GPa

values, C_{12} agrees with the 39–43 GPa bracket, and C_{44} is higher than many reports (often mid-30s to low-40s GPa); the bulk modulus B ≈ 55.7 GPa and VRH moduli (G ≈ 35.0 GPa, Y ≈ 86.9 GPa, ν≈ 0.24) are therefore reasonable against the experimental/theoretical ranges compiled for AlSb. From x = 0 to 0.25 and 0.50 we observe systematic decreases in C_{11} (≈82→76→73 GPa), C_{44} (≈51→48→46 GPa), and B (≈55.7→50.8→49.7 GPa), mirrored by declining polycrystalline stiffness (G ≈ 33.1 GPa and 31.1 GPa; Y ≈ 81.5 GPa and 77.2 GPa).

Table IV.13. Single-Crystal Stiffness (C_{11}, C_{12}, C_{44}) and Polycrystalline Bulk Modulus (GPa), Shear Modulus (GPa), Young's Modulus (GPa), Poisson's Ratio, Vickers Hardness (GPa), Pugh Ratio, and Cauchy Pressure (GPa) for $AlSb_{1-x}Bi_x$ via WC-GGA with available other calculations and existing experimental values

x	C_{11}	C_{12}	C_{44}	*B*	*Y*	*G*	*v*	H_v	*B/G*	C_p
0										
Our	82.31	42.43	51.108	55.721	86.91	35.04	0.24	6.61	1.59	-8.67
Other	84.97[47]	42.39[47]	1.74[47]	56.09[47]	82.2	32.70[47]	0.25[74]	-	-	-
	89.69[72]	38.67[72]	6.26[72]	55.68[72]	[47]	22.1[48]	0.25[75]	-	-	-
	85.32[13]	41.51[13]	39.80[13]	56.10[13]	66.2	25.42[74]	-	-	-	-
					[72]	-	-	-	-	-
EXP	87.69[73]	43.41[73]	40.76[73]	55.10[73]	-	-	-	-	-	-
0.25	75.75	38.38	48.43	50.83	81.512	33.061	0.233	6.87	1.54	-10.1
0.5	72.92	38.16	45.88	49.74	77.196	31.094	0.241	6.57	1.60	-07.72
0.75	67.83	35.47	37.54	46.26	67.346	26.781	0.257	6.02	1.73	-02.10
1.0										
Our	64.59	34.17	40.11	44.31	67.73	27.19	0.25	6.44	1.62	-05.97
Other	89.17 [29]	24.26[29]	4.90[29]	45.87[29]	144.06	49.17	0.105	15.4	0.93	−40.71
	48.49 [67]	29.00[67]	14.5[67]	38.75[67]	[29]	[29]	[29]	[29]	[29]	[29]

Poisson's ratio increases slightly (≈0.233→0.241), and the Pugh ratio rises (≈1.54→1.60) yet remains below the brittle–ductile threshold, while the Vickers hardness drops mildly (≈6.87→6.57 GPa). At x = 0.75 the softening is most pronounced (C_{11} ≈ 67.8 GPa, C_{44} ≈ 37.5 GPa, B ≈ 46.3 GPa, G ≈ 26.8 GPa, Y ≈ 67.3 GPa), with ν peaking near 0.257 and B/G approaching 1.73; the hardness shows the lowest value (~6.02 GPa) and the Cauchy pressure becomes least negative (≈ −2.1 GPa),indicating reduced bond directionality compared with Sb-rich compositions but still a covalent-leaning character. At the Bi-rich end x = 1 (AlBi) our (C_{11}, C_{12}, C_{44}) = (64.59, 34.17, 40.11)

GPa and derived B, G, Y (≈44.3, 27.2, 67.7 GPa) continue the softening trend relative to AlSb, with ν ≈ 0.25, B/G ≈ 1.62 and H_v ≈ 6.44 GPa. In head-to-head comparisons, our AlBi lies between the two most disparate literature sets: Ref. [29] (Thomas-Charpin) predicts a much stiffer crystal (C_{11} ≈ 89 GPa, G ≈ 49 GPa, Y ≈ 144 GPa, ν ≈ 0.105, H_v ≈ 15.4 GPa), whereas Ref. [67] reports substantially smaller constants (C_{11} ≈ 48 GPa, C_{44} ≈ 14.5 GPa, B ≈ 38.8 GPa). Methodology and strain-fit choices therefore account for most of the discrepancy, and our values sit in the middle of the published spread while remaining internally smooth across x.

The anisotropy analysis confirms these trends (Table IV.14): the Zener factor stays well above unity throughout (A ≈ 2.5 at x = 0, rising to ≈2.99 at x = 0.25), indicating stronger rigidity along ⟨111⟩ than ⟨100⟩; A then diminishes toward x = 0.75 (≈2.32), in line with the observed softening and the slight rise in ν, before recovering to ≈2.64 at AlBi. The shear percent anisotropy remains small (A_G ≈ 0.08–0.11) and the universal anisotropy index sits near unity (A^U ≈ 0.9–1.22), with our AlBi more anisotropic than the value quoted in Ref. [67] (A^U ≈ 0.60). Overall, the AlSb→AlBi substitution produces a monotonic reduction in single-crystal and polycrystalline stiffness with modest increases in ν and B/G, a slight decline in hardness toward x ≈ 0.75, and persistent though composition-dependent elastic anisotropy..

Table IV.14. Computational results of Zener anisotropic index A, percentage anisotropic indices (A_G) and (A_B) ,the universal anisotropic factor (A^U) in GPa of $AlSb_{1-x}Bi_x$ alloys via WC-GGA with other available calculations.

x	A	A_B	A_G	A^U
0	2.50	0.00	0.10	1.14
0.25	2.99	0.00	0.11	1.17
0.50	2.64	0.00	0.11	1.22
0.75	2.32	0.00	0.08	0.9
1 our work	2.64	0.00	0.11	1.22
1 other work	2.00	0.00	0.06	0.60

Replacing Sb by As drives a systematic stiffening of $AlSb_{1-x}As_x$ across all moduli, whereas replacing Sb by Bi produces the opposite, a systematic softening in $AlSb_{1-x}Bi_x$. In our data, the As series raises the polycrystalline set from B ≈ 55.7, G ≈ 35.0, Y ≈ 86.9 GPa at x=0 to B ≈ 70.6, G ≈

46.4, Y ≈ 114.2 GPa at x=1, with ν ≈ 0.22–0.23 and B/G ≈ 1.47–1.52 remaining low; hardness peaks near mid-range (H_v ≈ 8.5–8.8 GPa). Cauchy pressure becomes more negative and the anisotropy indices (e.g., Zener A ≈ 2.5→≈3) stay well above unity, indicating strong, direction-dependent rigidity with maximum stiffness along ⟨111⟩. By contrast, in the Bi series the moduli fall from B ≈ 55.7, G ≈ 35.0, Y ≈ 86.9 GPa at x=0 to about B ≈ 44.3, G ≈ 27.2, Y ≈ 67.7 GPa at x=1, ν rises slightly toward ≈0.25, B/G grows to ≈1.62 (still <1.75), and H_v dips around x≈0.75 (≈6.0 GPa). Correspondingly, the Cauchy pressure becomes less negative (approaching zero near x≈0.75) and the anisotropy weakens modestly before recovering at the Bi-rich end (Zener A ≳2 throughout). Put succinctly: As-alloying hardens and stiffens the lattice with enhanced covalent/anisotropic signatures, while Bi-alloying softens and slightly increases ductility propensity without crossing the brittle–ductile threshold; both families remain elastically anisotropic..

c) II-VI selected alloys

$BaO_{1-x}S_x$ (NaCl) : Table IV.15 illustrates Single-Crystal Stiffness (C_{11}, C_{12}, C_{44}) and Polycrystalline moduli .Our WC–GGA results show a clear, composition-driven softening as O is replaced by S. From BaO (x = 0) to BaS (x = 1) the single-crystal stiffnesses fall nearly monotonically: C11 ≈ 151 → 107 GPa, C44 ≈ 37.2 → 20.8 GPa, accompanied by decreases in the polycrystalline moduli B ≈ 82.2 → 46.1 GPa, G ≈ 42.4 → 28.7 GPa, and Y ≈ 108.6 → 71.2 GPa. This tracks the structural expansion and increasing anion polarizability along O→S. End-member checks are reasonable against literature: for BaO, our (C11, C12, C44) = (151.0, 47.8, 37.2) GPa lie close to other calculations (≈147.7, 47, 36.3 GPa)[80] and above the room-temperature experiment (≈126, 50.0, 33.7 GPa), while B = 82.2 GPa sits between prior theory (≈79.6 GPa)[80] and experiment (≈75.6 GPa)[38]. For BaS, our (C11, C12, C44) = (107.0, 15.7, 20.8) GPa fall within the spread of recent calculations (≈101–115, 9.7–17, 9–18 GPa)[21,42] and give B = 46.1 GPa, somewhat higher than the lowest experimental estimate (~39.4 GPa)[41] .

Table IV.15. Single-Crystal Stiffness (C_{11}, C_{12}, C_{44}) and Polycrystalline Bulk Modulus (GPa), Shear Modulus (GPa), Young's Modulus (GPa), Poisson's Ratio, Vickers Hardness (GPa), Pugh Ratio, and Cauchy Pressure (GPa) for $BaO_{1-x}S_x$ via WC-GGA with available other calculations and existing experimental values

x	C_{11}	C_{12}	C_{44}	*B*	*Y*	*G*	*v*	H_v	*B/G*	C_p
0										
Our	151.03	47.76	37.16	82.18	108.55	42.405	0.28	6.16	1.94	10.6
Other	147.7[80]	47[80]	36.3[80]	79.6[80]	-	-	-	-	-	-
EXP	126[63]	50.03[63]	33.68[63]	75.6[38]	-	-	-	-	-	-
0.25	126.27	32.13	27.65	63.51	87.13	34.27	0.27	5.57	1.85	4.47
0.5	114.86	19.98	23.71	51.61	78.360	31.42	0.246	6.00	1.64	-3.7
0.75	109.72	21.34	20.2	50.79	70.59	27.83	0.27	4.89	1.83	1.10
1.0										
Our	107	15.66	20.77	46.11	71.198	28.65	0.24	5.76	1.61	-5.1
Other	101.05[42]	9.67[42]	9.24[42]	40.28[42]	68.4[82]	27.5[82]	0.25[82]	5.51[82]	1.63	-
	115[21]	17[21]	18[21]	42.36[21]	-	-	-	-	[82]	-
EXP	124[81]	48.69[81]	33.68[81]	39.42[41]	-	-	-	-	-	-

Table IV.16. Computational results of Zener anisotropic index A, percentage anisotropic indices (A_G) and (A_B) ,the universal anisotropic factor (A^U) are in GPa, of $BaO_{1-x}S_x$ alloys via WC-GGA with other available calculations.

x	A	A_B	A_G	A^U
0	0.72	0.00	0.013	0.13
0.25	0.59	0.00	0.034	0.35
0.50	0.50	0.00	0.057	0.60
0.75	0.46	0.00	0.071	0.77
1	0.46	0.00	0.073	0.79

Ductility metrics evolve in a physically consistent way: Pugh's ratio B/G moves from 1.94 (BaO, ductile) → 1.85 (x = 0.25, ductile) → 1.64 (x = 0.5, brittle) → 1.83 (x = 0.75, ductile) → 1.61 (BaS, non-monotonic (≈6.2, 5.6, 6.0, 4.9, 5.8 GPa for x = 0→1). Cauchy pressure C′ = C12 − C44 is positive for BaO and x = 0.25 (≈ +10.6, +4.5 GPa), turns negative at x = 0.5 (≈ −3.7 GPa), returns

slightly positive at x = 0.75 (≈ +1.1 GPa), and is negative again for BaS (≈ −5.1 GPa); this sign change indicates an increasing directional (covalent-like) component in the bonding as S content grows. Elastic anisotropy (table IV.16) is modest but increases with x: the Zener factor A drops away from unity (0.72 → 0.46 from BaO→BaS), while the shear percent anisotropy A_G (0.013 → 0.073) and the universal anisotropy A^U (0.13 → 0.79) both rise, showing that the shear response becomes more direction-dependent toward BaS with an isotropic Bulk moduli for all compositions. Slightly reduced ν, intermittent ductile–brittle crossovers around mid-x by Pugh's criterion (see Chapter I), and a gradual enhancement of elastic anisotropy while our end-member numbers sit within the experimental/theoretical ranges compiled in the table.

All elastic tensors were obtained with IRelast in WIEN2k using WC–GGA, dense k-meshes, and stringent convergence thresholds. Polycrystalline moduli (B, G, Y), Poisson's ratio, hardness, and anisotropy indices were derived from Voigt–Reuss–Hill averages. Agreement of BaO and BaS end-members with published 0 K DFT and room-temperature measurements supports the quantitative reliability of the full composition trend.

$BaO_{1-x}Se_x$ (NaCl) : Elastic tensors were obtained with IRelast in WIEN2k using the WC–GGA functional for the cubic NaCl phase. For all compositions the cubic Born criteria are satisfied, confirming mechanical stability at 0 K and 0 GPa. Below, we discuss each composition (x = 0.25, 0.50, 0.75, 1.0) (x=0 (BaO) is already discussed) using our C_{11}, C_{12}, C_{44} and derived polycrystalline moduli and anisotropy indices with comparisons to other calculations and, where available, experiment (values as in Tables IV.17–IV.18).

For x=0.25 , With 25% Se, all stiffnesses decrease as the larger, more polarizable Se^{2-} lengthens and softens the Ba–X bonds: $C_{11}/C_{12}/C_{44}$ ≈ 114/33.8/26.7 GPa, B ≈ 60.4 GPa, G ≈ 31.4 GPa, Y ≈ 80.2 GPa. ν remains ≈0.28 and B/G ≈ 1.92, keeping the alloy on the ductile side of Pugh's criterion, and C′ stays positive (≈ +7.1 GPa), consistent with a still-dominant ionic character. Anisotropy increases slightly (A ≈ 0.67, A^U ≈ 0.20), reflecting a stronger orientation dependence of shear response than in BaO. At equiatomic composition (x=0.5) the softening continues ($C_{11}/C_{12}/C_{44}$ ≈ 105/18.2/21.2 GPa; B ≈47.2 GPa; G ≈ 28.4 GPa; Y ≈ 71.0 GPa).

Table IV.17. Single-Crystal Stiffness (C_{11}, C_{12}, C_{44}) and Polycrystalline Bulk Modulus (GPa), Shear Modulus (GPa), Young's Modulus (GPa), Poisson's Ratio, Vickers Hardness (GPa), Pugh Ratio, and Cauchy Pressure (GPa) for $BaO_{1-x}Se_x$ via WC-GGA with available other calculations and existing experimental values

x	C_{11}	C_{12}	C_{44}	*B*	*Y*	*G*	*v*	H_v	*B/G*	C_p
0										
Our	151.03	47.76	37.16	82.18	108.55	42.405	0.28	6.16	1.94	10.6
Other	147.7[80]	47[80]	36.3[80]	79.6[80]	-	-	-	-	-	-
EXP	126[63]	50.03[63]	33.68[63]	75.6[38]	-	-	-	-	-	-
0.25	113.53	33.79	26.71	60.37	80.23	31.38	0.28	5.01	1.92	7.1
0.5	105.23	18.24	21.21	47.24	70.98	28.40	0.24	5.51	1.66	-2.9
0.75	99.75	15.56	16.83	43.62	61.99	24.54	0.25	4.61	1.77	-1.3
1.0										
Our	92.6	13.40	16.43	39.80	59.10	23.58	0.25	4.75	1.69	-3
Other	113.95[42]	12.44 [42]	11.82[42]	37.05[42]	-	-	-	-	-	-
	112.67[83]	14.15[83]	15.25[83]	-	-	-	-	-	-	-
	95.48[84]	13.48[84]	16.70[84]	40.81[84]	-	24.16	0.252	3.98	1.69	-3.2
	-	-	-	-	-	[84]	[84]	[84]	[84]	[84]
EXP	-	-	-	43.4[43]	-	-	-	-	-	-

The bonding descriptor C′ becomes negative (≈ −2.9 GPa), signaling a transition toward more directional/covalent Ba–(O,Se) interactions. Both ν ≈ 0.24 and B/G ≈ 1.66 now fall in the brittle regime, while H_v shows a mild maximum (~5.5 GPa), consistent with reduced compressibility but stronger directionality. Elastic anisotropy strengthens markedly (A ≈ 0.49; A_G ≈ 0.061; A^U ≈ 0.65). Further Se addition lowers the stiffnesses ($C_{11}/C_{12}/C_{44}$ ≈ 100/15.6/16.8 GPa; B ≈ 43.6 GPa; G ≈ 24.5 GPa; Y ≈ 62.0 GPa). ν recovers slightly to ≈0.25 and B/G rises to ≈1.77, i.e., marginally on the ductile side of 1.75, but C′ remains negative (≈ −1.3 GPa), so the bonding retains a strong directional/covalent component. From Table IV.18 Anisotropy continues to grow (A ≈ 0.40; A^U ≈ 1.08), dominated by the shear channel (A_B ≈ 0, A_G ≈ 0.10). The hardness drops to ~4.6 GPa as the network softens. BaSe is the softest endpoint ($C_{11}/C_{12}/C_{44}$ ≈ 92.6/13.4/16.4 GPa; B ≈ 39.8 GPa; G ≈ 23.6 GPa; Y ≈ 59.1 GPa; ν ≈ 0.25; H_v ≈ 4.75 GPa). B/G ≈ 1.69 and C′ ≈ −3.0 GPa indicate a brittle, covalent-leaning response relative to BaO. Our B agrees with reported 37–41 GPa calculations and the ≈43 GPa experiment, while our single-crystal constants fall within the spread of prior DFT results, lending confidence to the endpoint calibration.

Table IV.18. Computational results of Zener anisotropic index A, percentage anisotropic indices (A_G) and (A_B) ,the universal anisotropic factor (A^U) are in GPa, of $BaO_{1-x}Se_x$ alloys via WC-GGA with other available calculations.

x	A	A_B	A_G	A^U
0	0.72	0.00	0.013	0.130
0.25	0.67	0.00	0.019	0.195
0.50	0.49	0.00	0.061	0.650
0.75	0.40	0.00	0.100	1.08
1	0.415	0.00	0.09	0.989

Across the series, O→Se substitution drives a near-monotonic reduction in C_{11}, C_{12}, C_{44} and the aggregate moduli (B, G, Y). Ductility metrics evolve coherently: BaO and x=0.25 are clearly ductile (B/G≈1.9, ν≈0.28), the alloy becomes brittle at x≈0.5 (B/G≈1.66, ν≈0.24) and remains borderline to brittle toward BaSe (B/G≈1.69, ν≈0.25). C′ changes sign near mid-composition, marking a crossover from predominantly ionic (positive C′) to directional/covalent (negative C′) bonding, which also explains the rise of shear anisotropy (A trending from ~0.7 to ~0.4; A^U rising from ~0.13 to ~1.0). Where comparison data exist, our values match prior DFT within a few GPa and sit above room-temperature experiments by the expected margin, supporting the fidelity of the predicted composition dependence. The WC–GGA/IRelast workflow reproduces literature values at both binaries (BaO and BaSe) within typical GGA accuracy and captures the known 0 K vs 300 K offsets seen in experiments. Agreement with multiple independent calculations for B and the single-crystal constants, together with internally consistent trends in ν, B/G and C′, argues that the predicted stiffening/softening, ductility crossover near x≈0.5 and the growth of shear anisotropy are robust. Remaining discrepancies at the few-GPa level are expected from functional choice and temperature effects; nevertheless, the end-member agreement and smooth compositional evolution indicate that the present dataset provides a reliable reference where measurements are not yet available.

Replacing O by sulfur produces a moderate softening of the BaO lattice: the single-crystal and polycrystalline stiffnesses (C_{11}, C_{12}, C_{44}; B, G, Y) all decrease smoothly with x, but a broader near-ductile window is retained toward the S-rich side. In $BaO_{1-x}S_x$ the Pugh ratio and Poisson's ratio

remain relatively high away from mid-composition (e.g., B/G ≈ 1.8 and ν ≈ 0.26–0.27 around x ≈ 0.75), and the Cauchy pressure $C' = C_{12} - C_{44}$, while turning negative near mid-x, can rebound slightly positive at x ≈ 0.75 signaling a mixed ionic/directional response. Elastic anisotropy grows with x but remains modest (e.g., universal anisotropy $A^U \lesssim 0.8$ near BaS). By contrast, substituting selenium causes a stronger softening at every matched composition: at x = 0.50, for example, B, G and Y are all lower in $BaO_{0.5}Se_{0.5}$ than in $BaO_{0.5}S_{0.5}$ (≈47.2 vs ≈51.6 GPa; ≈28.4 vs ≈31.4 GPa; ≈71.0 vs ≈78.4 GPa, respectively). The Se series also moves earlier and more persistently toward brittle metrics ; both alloys drop below B/G = 1.75 near mid-x, but Se-containing compositions hover closer to the brittle side and maintain lower ν (≈0.24–0.25). Crucially, C′ becomes negative by mid-x and stays negative to BaSe. The shear anisotropy is likewise enhanced in $BaO_{1-x}Se_x$ (A^U ~ 1.0 near BaSe vs ~0.8 near BaS), and the Vickers hardness is systematically lower in Se-containing alloys at the same x (tracking the reduced G). In short: S < Se in softening impact—S preserves a wider near-ductile regime and a more ionic signature at high x, while Se drives deeper softening, earlier and persistent C′ < 0, higher shear anisotropy, and lower hardness across the composition range.

c) **Cross-family comparison of elastic properties**

At the binaries, the II–VI O-rich compound (BaO) is among the stiffest materials in our set, with B ≈ 82 GPa, G ≈ 42 GPa, Y ≈ 109 GPa (ν ≈ 0.28), while AlAs the stiffest III–V endpoint reaches B ≈ 71 GPa, G ≈ 46 GPa, Y ≈ 114 GPa (ν ≈ 0.23). Thus, compression stiffness (B) is generally higher in the ionic rocksalt oxide (BaO) than in the III–V binaries, whereas shear and Young's moduli are comparable across AlAs and BaO. On the soft side, BaSe (B ≈ 40 GPa, G ≈ 24 GPa, Y ≈ 59 GPa, ν ≈ 0.25) and AlBi (B ≈ 44 GPa, G ≈ 27 GPa, Y ≈ 68 GPa, ν ≈ 0.25) set similar lower bounds for the two families. In the III–V alloys, replacing Sb by As causes a monotonic hardening across all moduli (B, G, Y increase from AlSb to AlAs), while replacing Sb by Bi causes the opposite; a monotonic softening toward AlBi. In the II–VI alloys, both S and Se substitutions soften BaO, with Se producing the stronger reduction at any matched composition (e.g., at x = 0.5, B, G, Y are all lower in $BaO_{0.5}Se_{0.5}$ than in $BaO_{0.5}S_{0.5}$). Hence, the dominant compositional trends are: As → stiffening, Bi/S/Se → softening, with Se > S in softening strength. The III–V alloys remain on the brittle side by Pugh's criterion across the composition range: B/G stays below ~1.75 for both

$AlSb_{1-x}As_x$ (≈1.47–1.52) and $AlSb_{1-x}Bi_x$ (up to ≈1.62), and ν remains low (≈0.22–0.25), indicative of directional bonding. By contrast, the II–VI alloys traverse a broader ductility landscape: BaO and the O-rich alloys are clearly ductile (B/G ≈ 1.9; ν ≈ 0.28), the mid-compositions approach or cross into brittle metrics (B/G ≈ 1.64–1.70; ν ≈ 0.24–0.25), and S-rich compositions can partially recover toward ductile values (e.g., B/G ≈ 1.83 at x ≈ 0.75 in $BaO_{1-x}S_x$), a recovery that is weaker along the Se track. The Cauchy pressure $C' = C_{12} - C_{44}$ is a sensitive probe of bonding character. In the III–V alloys, C′ is negative throughout (becoming less negative toward Bi-rich compositions). In the II–VI series, C′ is positive at the O-rich side (BaO and x ≈ 0.25), turns negative near mid-composition, and remains negative or weakly negative to the chalcogen-rich endpoints more persistently so for Se than for S. Rocksalt BaO is initially more ionic/central-force dominated but acquires increasing bond directionality as O is replaced by S or Se.

IV.VII. Thermal Properties

Thermal behavior sets practical limits on performance and reliability by governing how materials store heat, expand with temperature, and resist compression at operating conditions well beyond ambient. For the III–V (zinc-blende) and II–VI (rock-salt) alloys studied here, alloying alters bond lengths, bonding character, density, and elastic stiffness; consequently, the key thermal responses are composition-dependent and cannot be inferred from binaries alone. Because high-temperature and high-pressure measurements are difficult and often narrow in scope, we use a first-principles, equation-of-state–based workflow consistent with our structural, electronic, and elastic analysis to predict four core quantities across temperature: constant-volume heat capacity $C_v(T)$, Debye temperature $\theta_D(T)$, linear thermal expansion α(T), and the temperature-dependent bulk modulus B(T). These curves provide actionable inputs for thermal management and thermo-mechanical design (e.g., stress budgeting during cooldown, layer-stack selection) and allow direct cross-checks against available reference data at 300 K. Where relevant, we highlight composition trends (x=0, mid-x, x=1) and note how high-pressure conditions shift α(T) and B(T), thereby linking the thermal responses to the structural and elastic trends established earlier.

a) Thermal properties of III-V selected alloys

a.1) Constant-volume heat capacity $C_v(T)$

Figure IV.31 shows Cv(T) for the two zinc-blende series $AlSb_{1-x}As_x$ (left) and $AlSb_{1-x}Bi_x$ (right) at x = 0, 0.25, 0.50, 0.75, and 1. Each curve exhibits the expected Debye-like T^3 rise below ~100 K and then rolls over toward a composition-dependent plateau at higher temperature. The dashed horizontal line in each panel is the Dulong–Petit guide; curves that sit lower at a given T indicate a larger Debye temperature $\theta_D(T)$ (stiffer/lighter lattice), whereas curves that approach the guide sooner reflect a smaller $\theta_D(T)$ (softer/heavier lattice).

$AlSb_{1-x}As_x$: Across the As series, C_v increases rapidly up to ~200–300 K and then saturates. For x = 0–0.75 the high-T values cluster close to the Dulong–Petit line, whereas the AlAs end member (x = 1) remains markedly lower over the full temperature range. This suppression is consistent with a higher Debye temperature for AlAs caused by its lighter anion mass and larger stiffness (higher bulk modulus) relative to AlSb. Mixing Sb with As (x ≈ 0.25–0.75) lowers $\theta_D(T)$, so at a fixed temperature C_v is enhanced and approaches the classical limit more quickly.

$AlSb_{1-x}Bi_x$: By replacing Sb with the heavier, C_v(T) rises more steeply at low T and reaches its plateau at lower temperature than in AlSb. At any fixed temperature (e.g., 300–500 K), C_v grows monotonically with x, reflecting the concurrent mass increase and elastic softening we reported for this series (decreasing bulk modulus with Bi content). The Bi-rich compositions therefore store more heat per mole at operational temperatures.

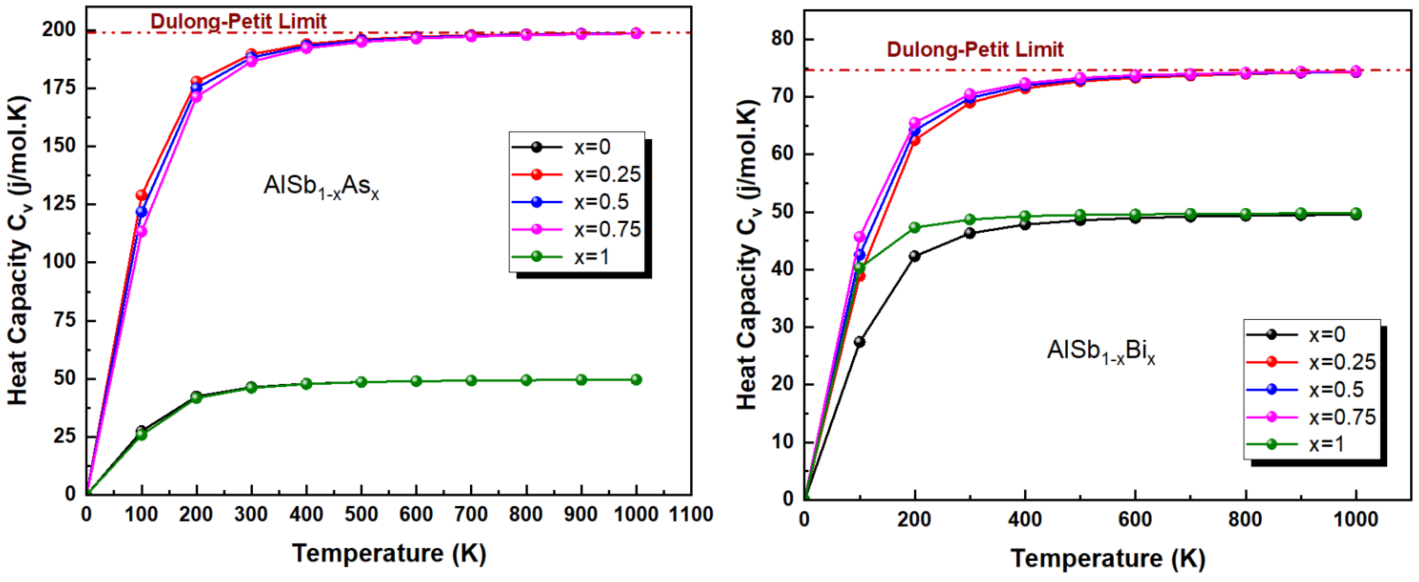


Figure IV.31. Constant-volume heat capacity $C_v(T)$ of III-V selected alloys

a.2) Debye temperature $\theta_D(T)$

The Debye temperature is a compact measure of lattice stiffness and the characteristic scale of acoustic phonons. Larger θ_D implies stronger average force constants and higher sound velocity; smaller θ_D signals heavier masses/softer bonding. In real crystals $\theta_D(T)$ falls gently with temperature.

$AlSb_{1-x}As_x$ (Figure IV.32-left panel): All compositions show a mild, nearly linear decrease of θ_D between ~100 and 1000 K, indicating moderate anharmonicity. Compositionally, the series trends upward as Sb→As: the As-rich end has the highest θ_D (≈390 K at low T, decaying to ≈345 K), then x≈0.75 (≈360→≈325 K), x≈0.50 (≈330→≈300 K) and x≈0.25 (≈310→≈275 K). AlSb itself sits high (≈365→≈360 K). θ_D increases with x. This matches the elastic dataset: C_{11}, G and B rise as As replaces Sb. The θ_D ordering is also consistent with the $C_v(T)$ curves: higher θ_D alloys (As-rich) delay approach to the Dulong–Petit limit.

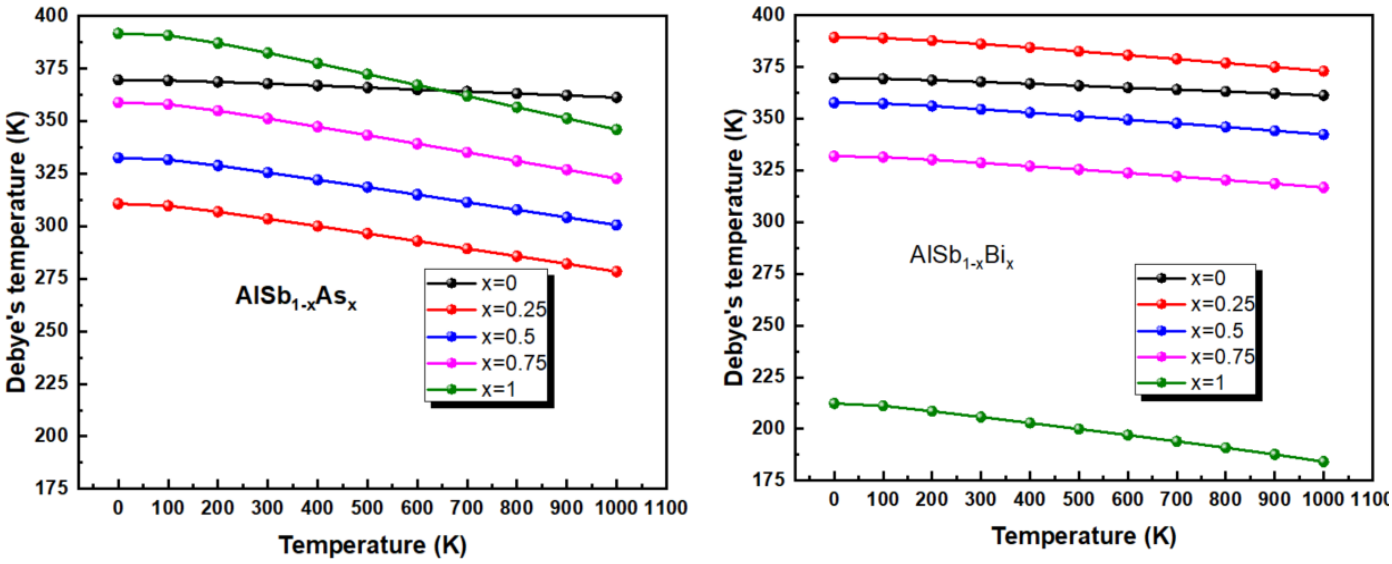


Figure IV.32. Debye temperature $\theta_D(T)$ versus temperature of III-V selected alloys

$AlSb_{1-x}Bi_x$ (Figure IV.32-right panel): The temperature slope is again gently negative, but the composition effect is much stronger. Adding Bi drives a pronounced softening: from AlSb (≈365→≈360 K) down to AlBi (≈212→≈185 K) over 0–1000 K. Intermediate compositions follow the expected sequence x=0.75 < 0.50 < 0.25 (≲ x=0), i.e., θ_D falls as Bi increases. The global trend is a clear decrease of θ_D with Bi, fully consistent with the elastic results (C_{11}, G, B all drop with Bi

content) and with the earlier $C_v(T)$ behavior (Bi-rich alloys reach the Dulong–Petit plateau at lower temperatures).

a.3) The temperature-dependent bulk modulus B(T)

Figure IV.33 compares the temperature dependence of the bulk modulus, B(T), for the $AlSb_{1-x}As_x$ and $AlSb_{1-x}Bi_x$ series. In both alloy families B decreases smoothly as temperature rises,. Throughout the measured range the composition ranking is preserved: in the AlSb–AlAs series the As-rich alloys remain the stiffest at any given T, whereas in the AlSb–AlBi series any Bi addition softens the lattice relative to AlSb.

For $AlSb_{1-x}As_x$, the curves show a systematic increase of the low-temperature stiffness with x, from roughly 53 GPa for AlSb to about 72 GPa for AlAs near 100 K. With increasing temperature, each

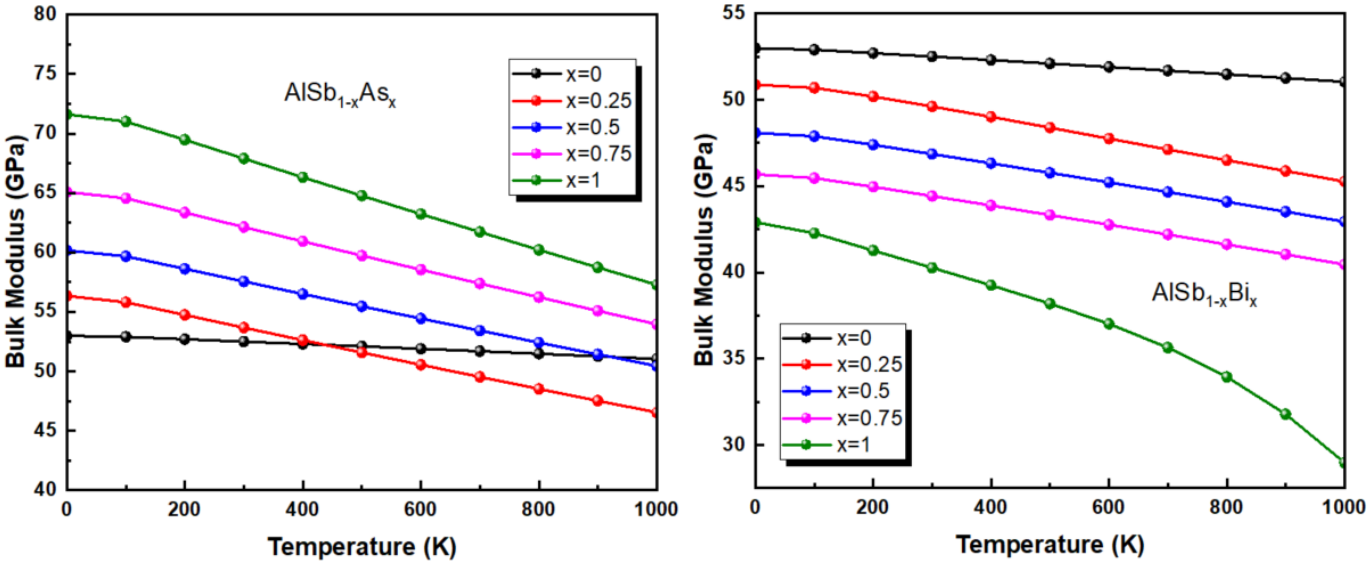


Figure IV.33. The temperature-dependent bulk modulus B(T) of our III-V selected alloys

composition exhibits a nearly linear reduction of B; by 1000 K the moduli have fallen to approximately 51–58 GPa. The fractional softening is modest for AlSb (a few percent) and grows toward the As-rich end (≈15–20% for $x \gtrsim 0.5$. The overall trend is consistent with the 0 K equation-of-state results, where As substitution contracted the lattice giving larger B_0 that is retained at finite T.

For $AlSb_{1-x}Bi_x$, the opposite behavior is observed. At low temperature the bulk modulus already declines with Bi content from about 53–54 GPa for AlSb down to roughly 43 GPa for AlBi and the

thermal softening is more pronounced on the Bi-rich side. Alloys with x ≤ 0.75 decrease approximately linearly with T, whereas the AlBi curve develops a visible downward curvature above ~700 K, reaching near 28 GPa by 1000 K.

a.4) Linear thermal expansion α(T)

Figure IV.34 summarizes the temperature dependence of the linear thermal expansion coefficients α(T) for the $AlSb_{1-x}As_x$ and $AlSb_{1-x}Bi_x$ series. Across all compositions, α rises steeply from 0 K to ≈150–250 K, then evolves toward a broad plateau by room temperature and above. Once the specific heat approaches its high-T limit, the rate of increase of α(T) diminishes.

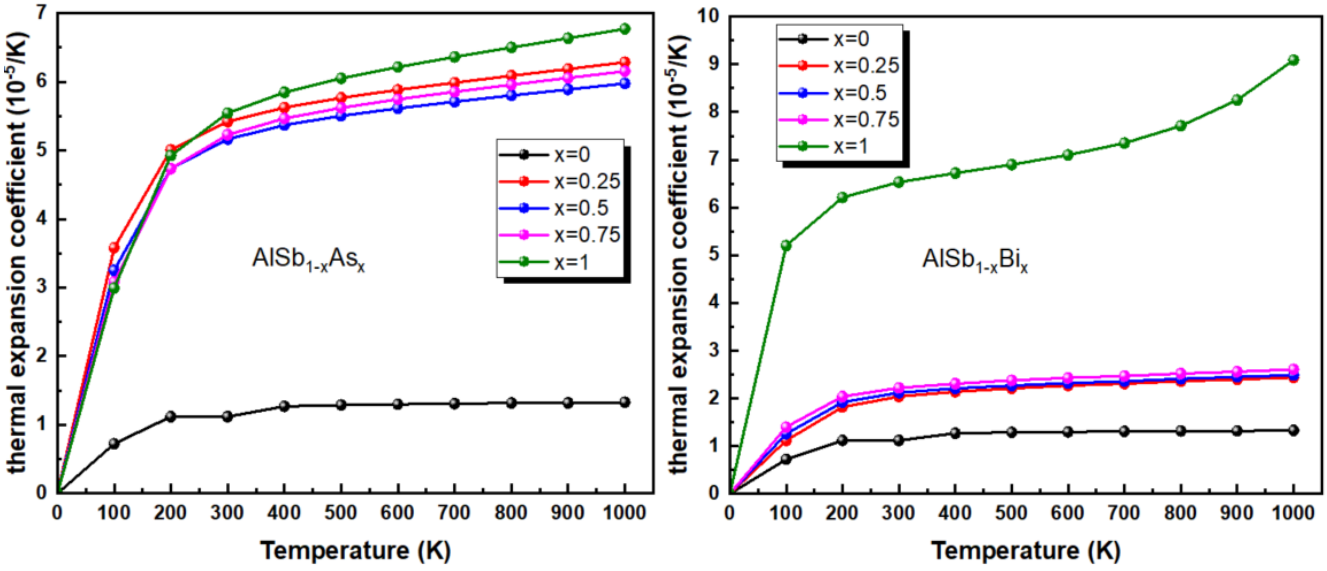


Figure IV.34. Linear thermal expansion α(T) of our III-V selected alloys

For the As-alloyed series, α(T) increases monotonically with arsenic content at all temperatures. Relative to AlSb (x = 0), even modest As substitution (x ≈ 0.25–0.75) produces a clearly larger thermal expansivity, and AlAs (x = 1) exhibits the highest α over the full temperature window.

In the Bi-alloyed series the behavior is bifurcated. For low and intermediate Bi contents (x ≈ 0.25–0.75) α(T) exceeds that of AlSb but remains in a narrow band that saturates by ≈300–400 K, consistent with modest increases in anharmonicity. By contrast, the Bi-rich limit AlBi (x = 1)

displays a much stronger α(T) larger at all temperatures and continuing to rise across the plotted range. This pronounced enhancement is consistent with the marked softening of the lattice (lower bulk modulus B(T) and lower Debye temperature $\theta_D(T)$ reported previously.

Comparing the two families at a fixed temperature, As substitution generally yields a moderate, nearly linear increase of α with x, while Bi substitution produces a modest increase at small x and a sharp growth toward the Bi-rich side. This contrast mirrors the electronic/elastic trends established earlier: $AlSb_{1-x}As_x$ stiffens with x and maintains higher Debye temperatures; $AlSb_{1-x}Bi_x$, on the other hand, softens structurally and shows depressed θ_D. Overall, Fig. IV.33 is internally consistent with our Debye-temperature and bulk-modulus trends: higher α correlates with lower θ_D and lower B.

a.5) 300 K Thermal Properties of III–V Selected Alloys

This note analyzes the constant-volume heat capacity C_v(T), Debye temperature $\theta_D(T)$, bulk modulus B(T), and linear thermal-expansion coefficient α(T) at T = 300 K for two zinc-blende alloy families. Table IV.19 shows computational results of thermal properties of III-V Selected alloys at 300 K.

$AlSb_{1-x}As_x$: For AlSb (x = 0), our values are C_v = 46.33 J·mol^{-1}·K^{-1}, θ_D = 367.8 K, B = 52.5 GPa, and α = 1.12×10^{-5} K^{-1}. Relative to other calculations (C_v = 47.68 J·mol^{-1}·K^{-1}, θ_D ≈ 340 K, B ≈ 53 GPa) our θ_D is higher by ≈8% and B is within 1%. The experimental θ_D ≈ 370 K places our value within 1% of measurement [58, 90].For AlAs (x = 1), we obtain C_v = 47.73 J·mol^{-1}·K^{-1}, θ_D = 382.4 K, B = 67.9 GPa, and α = 5.54×10^{-5} K^{-1}. Other calculations quote θ_D ≈ 490 K and B ≈ 74 GPa, while experiments report θ_D ≈ 450 K and B ≈ 74 GPa [58, 69, 90]. Thus θ_D is ≈−15% vs experiment (≈−22% vs the higher computed estimate) and B is ≈−8% vs both theory and experiment a level of underestimation typical of GGA-level treatments at room temperature. Heat capacity agrees with other work (∼46–48 J·mol^{-1}·K^{-1}).

Intermediate compositions. The ternaries show a chemically sensible stiffening as As replaces Sb: B(T) increases from 53.7 → 57.6 → 62.1 GPa for x = 0.25, 0.50, 0.75, while θ_D grows from 303.5 → 325.5 → 351.2 K. The corresponding α(T) remains clustered near (5.2±0.2)×10^{-5} K^{-1}. The C_v values tabulated for the mixed alloys (∼186–190 J·mol^{-1}·K^{-1}); their relative ordering still mirrors the θ_D trend (larger θ_D ↔ slightly smaller C_v at a fixed T).

$AlSb_{1-x}As_x$: Trend with Bi content. At 300 K we find a monotonic softening as Bi replaces Sb: B(T) declines from 52.5 → 49.6 → 46.9 → 44.4 → 40.3 GPa for x = 0, 0.25, 0.50, 0.75, 1, while θ_D drops from 367.8 → 386.1 → 354.6 → 328.7 → 205.8 K.

Heat capacity increases from ≈46 to ≈70 J·mol^{-1}·K^{-1} across the mid-range, then returns to ≈49 J·mol^{-1}·K^{-1} for AlBi as the classical limit is approached. The thermal-expansion coefficient rises with Bi, from 1.12×10^{-5} K^{-1} (AlSb) to ≈(2.0–2.2)×10^{-5} K^{-1} at x ≈ 0.25–0.75 and further to 6.53×10^{-5} K^{-1} for AlBi.

Table IV.19. Computational results of thermal properties of III-V Selected alloys at 300 K

$AlSb_{1-x}As_x$				
x	$C_v(T)(J/mol.K)$	$\theta_D(T)(K)$	$\boldsymbol{B(T)(GPa)}$	α(T) 10^{-5} K^{-1}
0 (Our)	46.33	367.77	52.5	1.12
other	47.68[85]	340[86]	53[86]	0.5[86]
EXP	-	370	-	-
0.25	189.70	303.51	53.7	5.42
0.50	188.28	325.53	57.6	5.16
0.75	186.52	351.21	62.1	5.22
1 (Our)	47.73	382.40	67.9	5.54
Other	46[86]	490[86]	74[86]	-
EXP		450[58]	74[69]	-
$AlSb_{1-x}Bi_x$				
0	46.33	367.77	52.5	1.12
0.25	69.00	386.09	49.6	2.04
0.50	69.85	354.57	46.9	2.12
0.75	70.50	328.66	44.4	2.22
1	48.70	205.75	40.3	6.53
Other	48.03[29]	261.65[29]	-	-

Our AlSb values match closely the independent calculation (C_v ≈ 48 J·mol^{-1}·K^{-1}) and canonical θ_D ≈ 370 K. For AlBi, an available calculation reports θ_D ≈ 262 K [29], whereas we obtain 206 K

(≈−21%). Direct room-temperature bulk-modulus measurements for the intermediate alloys are scarce; nevertheless, the observed B(T) decrease with Bi content is expected from both mass and bonding arguments.

b) Thermal properties of II-VI selected alloys

b.1) Constant-volume heat capacity $C_v(T)$

Figure VI.35 illustrates the temperature dependence of the constant-volume heat capacity $C_v(T)$ of our II-VI alloys.

$BaO_{1-x}S_x$ (NaCl). Across the series, $C_v(T)$ exhibits the expected Debye-like rise at low temperature (steeper than linear below ~100 K) and then saturates toward the classical high-temperature Dulong–Petit limit shown in the figure. As S replaces O, the low-T heat capacity increases and the curve flattens earlier which is an evidence of a decreasing effective θ_D with x. Compositions x≈0.25–0.75 bunch closely above ~150–200 K, BaO (x=0) rises slowest , and S-rich alloys approach the plateau first; all converge to the same classical limit at high T.

$BaO_{1-x}Se_x$ (NaCl). The Se series mirrors the S trends but with a more pronounced low-T enhancement: for the same x, $C_v(T)$ is slightly larger below ~150 K and reaches its plateau earlier.

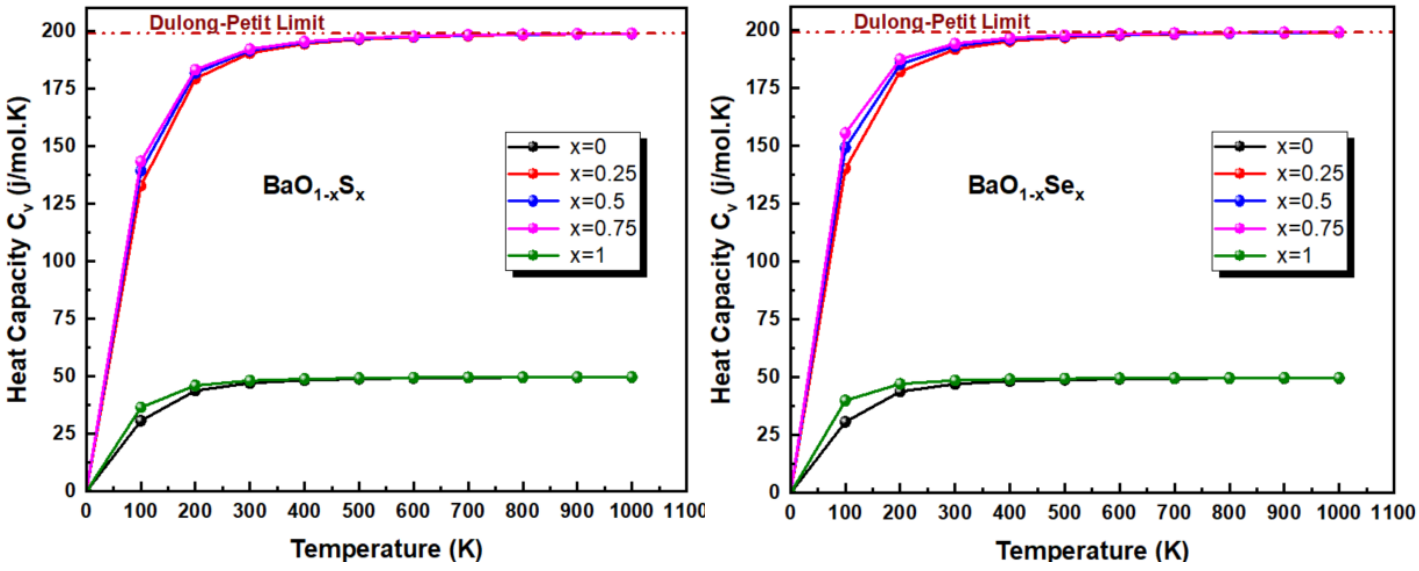


Figure IV.35. Constant-volume heat capacity $C_v(T)$ of our II-VI alloys.

This indicates a further reduction of sound velocities (lower θ_D) when substituting the heavier, more polarizable Se for O. the low-T ordering follows the stiffness hierarchy from our elastic analysis: BaO (stiffest) < $BaO_{1-x}S_x$ < $BaO_{1-x}Se_x$ (softest).

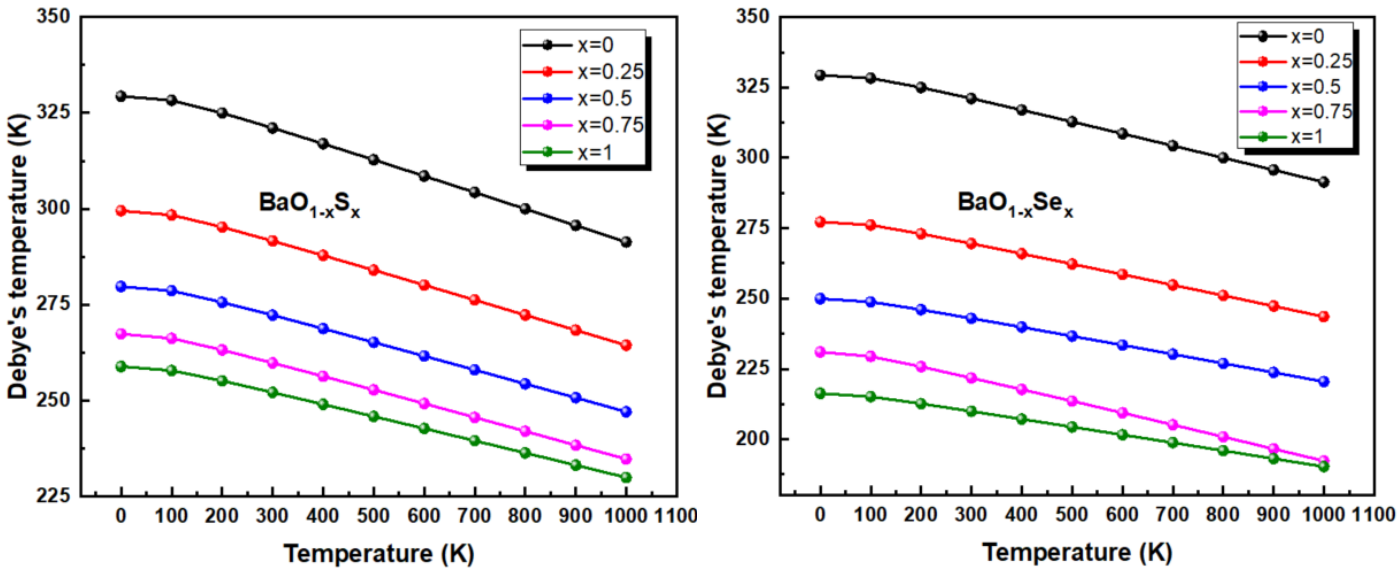


Figure IV.36. Debye temperature $\theta_D(T)$ versus temperature of II-VI selected alloys

b.2) Debye temperature $\theta_D(T)$

Figure IV.36 shows Debye temperature θ_D versus temperature of II-VI selected alloys.

$BaO_{1-x}S_x$ (NaCl). Across the sulfur series, the Debye temperature θ_D decreases monotonically with both temperature and sulfur content. At x = 0 (BaO) θ_D is ≈330 K at the lowest plotted T and falls nearly linearly by ~35–40 K up to 1000 K. Introducing S lowers θ_D roughly uniformly: for x ≈ 0.25, 0.50, 0.75 and 1.0 the curves are successively shifted downward by about 20–70 K relative to BaO. The near-parallel nature of the curves indicates a similar temperature-softening rate across compositions.

$BaO_{1-x}Se_x$ (NaCl). The selenium series shows the same qualitative behavior but with systematically slightly lower Debye temperatures at matched composition. From x = 0.25 to 1.0, θ_D in $BaO_{1-x}Se_x$ lies ≈15–25 K below $BaO_{1-x}S_x$ and exhibits a slightly stronger linear decrease with T. The hierarchy θ_D(BaO) > θ_D(S-rich) > θ_D(Se-rich) mirrors the hierarchy in our calculated moduli (B, C11, C44)

and the lattice-dynamical picture in which θ_D scales with acoustic velocity and effective bond rigidity.

The observed trends θ_D decreasing with T, with chalcogen content, and being lower for Se than for S are internally consistent with our EOS/elastic results and with standard Debye–quasi-harmonic expectations. Lower θ_D signals softer bonds and lower sound speeds, which we independently inferred from the composition-driven decline of B and Cij. These findings provide a coherent thermal-elastic picture for the II–VI alloys studied.

b.3) The temperature-dependent bulk modulus B(T)

Figure IV.37 shows Temperature-dependent bulk modulus B(T) of $BaO_{1-x}S_x$ and $BaO_{1-x}Se_x$. Both alloy families show a clear, nearly linear decrease of B with temperature from 0–1000 K and a systematic decrease with increasing chalcogen content x.

$BaO_{1-x}S_x$: At low temperature the moduli rank as BaO (≈78 GPa) > x = 0.25 (≈62 GPa) > 0.50 (≈54 GPa) > 0.75 (≈49 GPa) > BaS (≈46 GPa). Each composition softens smoothly with T; approximate drops from 0→1000 K are ~15 GPa (BaO), ~11 GPa (x = 0.25–0.50), ~10 GPa (x = 0.75), and ~8 GPa (BaS). The near-parallel slopes indicate a similar anharmonic response across x, while the vertical offsets reflect bond-stiffness reduction with O→S replacement. The ordering and magnitudes are consistent with the higher θ_D and larger 0 K elastic constants (C_{11}, C_{44}) of the O-richer members.

$BaO_{1-x}Se_x$: The same trends hold but at uniformly lower B for every matched x, e.g., ≈57→46 GPa (x = 0.25), ≈48→40 GPa (x = 0.50), ≈44→34 GPa (x = 0.75), and ≈40→31 GPa (BaSe) from 0→1000 K. Softening slopes are comparable to, or slightly steeper than, those in the sulfide series. The systematic reduction relative to $BaO_{1-x}S_x$ reflects weaker Ba–Se bonding), which also produced lower Debye temperatures in Fig. IV.35 and smaller room-temperature moduli.

b.4) Linear thermal expansion α(T) (Figure IV.38)

$BaO_{1-x}S_x$ (NaCl): The α(T) curves show the textbook rise from near-zero at cryogenic T to a rapid growth below ~200–300 K, followed by a slow, almost linear increase toward a broad high-T

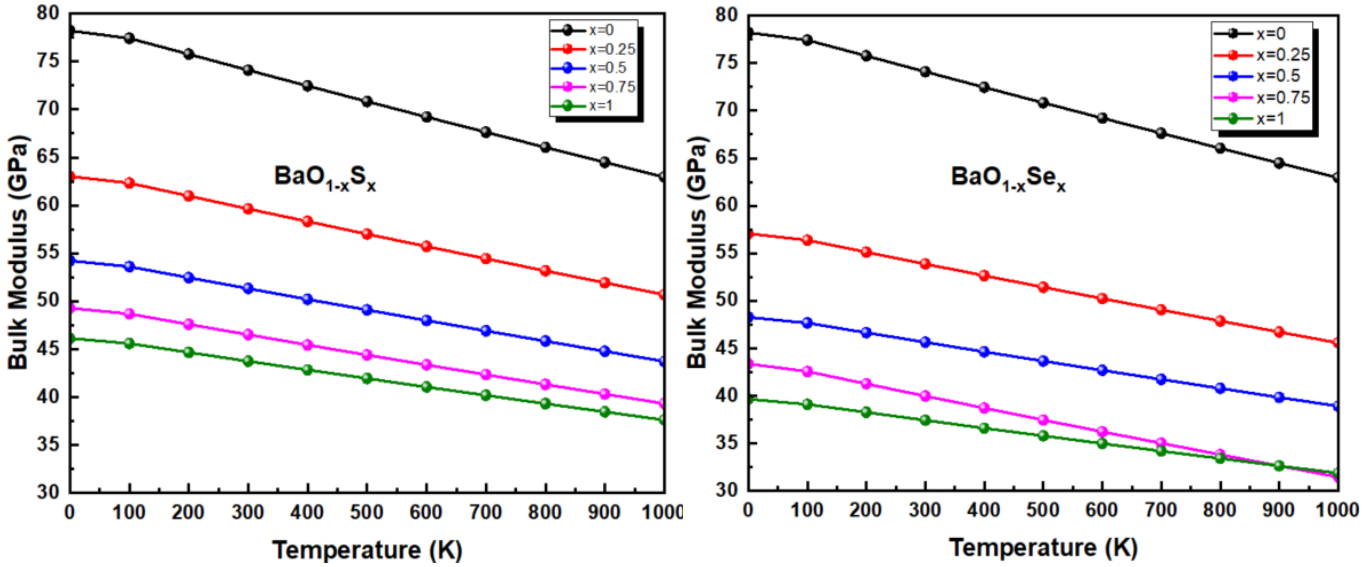


Figure IV.37. The temperature-dependent bulk modulus B(T) of our II-VI selected alloys.

shoulder. By 1000 K, α clusters around ≈6.4–7.1 × 10^{-5} K^{-1}, with a consistent order: x≈0.75 is largest, then 0.50 ≳ 0.25 ≳ 1.0, while BaO (x = 0) is smallest.

$BaO_{1-x}Se_x$ (NaCl): The temperature evolution is the same (steep low-T rise, gentle high-T drift), but absolute α values are systematically larger than in the sulfides. At 1000 K the series spans ≈6.3–9.3 × 10^{-5} K^{-1}, again peaking at x≈0.75, with x=0.50/0.25/1.0 forming a mid-band and x=0 the lowest. The higher α across this family is fully consistent with its lower θ_D (T) and smaller B(T) (heavier anion, softer bonds).

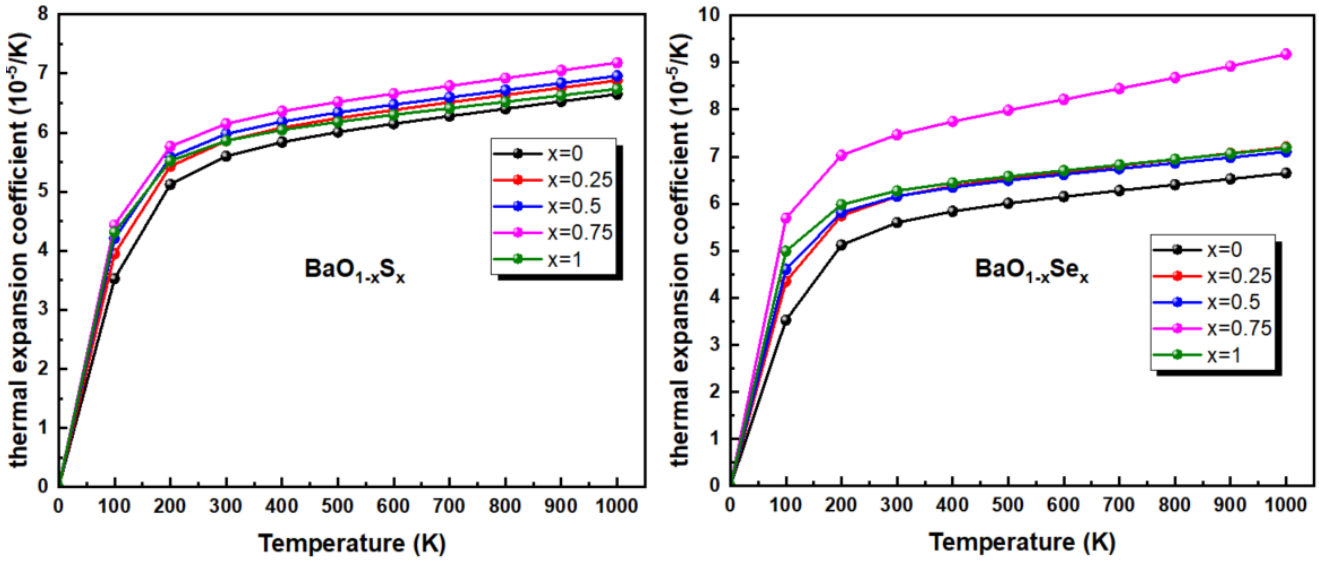


Figure IV.38. Linear thermal expansion coefficients α(T) of II-VI selected alloys

For matched composition and temperature, $BaO_{1-x}Se_x$ expands more than $BaO_{1-x}S_x$, and in both families the maximum expansion occurs near x≈0.75, the same composition range where B(T) is most reduced. Conversely, BaO-rich alloys minimize α(T), making them better suited for roles where thermal-mismatch strains must be controlled (as they are more stable when heated or cooled), while x≈0.75 compositions demand more care under thermal cycling due to their larger expansion (larger α(T), leading to higher thermal stresses under heating–cooling cycles, which may increase the risk of mechanical degradation and thus require careful thermal management and strain-engineering strategies).

b.5) 300 K Thermal Properties of III–V Selected Alloys

Table IV.20. Computational results of thermal properties of II-VI Selected alloys at 300 K

		$BaO_{1-x}S_x$		
x	$C_v(T)(J/mol.K)$	$\theta_D(T)(K)$	$\boldsymbol{B(T)(GPa)}$	α(T) 10^{-5} K^{-1}
0 (Our)	47.14	321.08	74.11	5.59
other	-	305[86]	-	-
0.25	190.43	291.64	59.65	5.86
0.50	195.11	272.28	51.33	5.97
0.75	192.26	259.85	46.52	6.15
1	48.17	252.15	43.76	5.86
		$BaO_{1-x}Se_x$		
0	47.14	321.08	74.11	5.59
0.25	191.72	269.51	53.88	6.15
0.50	193.15	242.97	45.65	6.16
0.75	194.62	221.77	39.99	7.46
1	48.69	209.91	37.44	6.27

Table IV.20 shows Computational results of thermal properties of II-VI Selected alloys at 300 K

$BaO_{1-x}S_x$ (NaCl): Heat capacity C_v(300 K) is ~47 $J\cdot mol^{-1}\cdot K^{-1}$ at the binary limits (x = 0, 1) and ~190–195 $J\cdot mol^{-1}\cdot K^{-1}$ for the alloy supercells (x = 0.25–0.75), consistent with the Debye-like saturation seen in Fig. IV.34. The Debye temperature decreases monotonically with sulfur

replacement of oxygen: θ_D falls from 321 K (x = 0) → 292 K (0.25) → 272 K (0.5) → 260 K (0.75) → 252 K (x = 1). This softening tracks a concurrent drop in the 300 K bulk modulus: B ≈ 74.1 → 59.7 → 51.3 → 46.5 → 43.8 GPa, signalling a more compressible lattice at higher S content. The linear thermal expansion shows a mild rise with alloying, peaking near x = 0.75 ($\alpha \approx 6.15 \times 10^{-5}$ K^{-1}) and then slightly decreasing at BaS ($\alpha \approx 5.86 \times 10^{-5}$ K^{-1}). Where external benchmarks exist, our θ_D for BaO (321 K) is close to an independent calculation (≈305 K [90]), indicating that the overall stiffness scale is reasonable.

$BaO_{1-x}Se_x$ (NaCl): The same internal consistency holds for C_v: binaries give ~47–49 $J \cdot mol^{-1} \cdot K^{-1}$, and alloys with 8-atom cells give ~192–195 $J \cdot mol^{-1} \cdot K^{-1}$ at 300 K. Compared to the S series, selenium causes a stronger softening: θ_D drops from 321 K (x = 0) to 270 K (0.25), 243 K (0.5), 222 K (0.75) and 210 K (x = 1). Bulk modulus decreases in parallel, B ≈ 74.1 → 53.9 → 45.7 → 40.0 → 37.4 GPa. The thermal expansion coefficient rises across the series (≈5.6 → 6.2–6.3 $\times 10^{-5}$ K^{-1}), with a somewhat larger increase than in $BaO_{1-x}S_x$.

Chapter IV References

[1] D. Singh, L. Nordström, Planewaves, Pseudopotentials and the LAPW Method, Second Edition, 2005. https://doi.org/10.1007/978-0-387-29684-5.
[2] P. Blaha, K. Schwarz, F. Tran, R. Laskowski, G.K.H. Madsen, L.D. Marks, WIEN2k: An APW+lo program for calculating the properties of solids, The Journal of Chemical Physics 152 (2020) 074101. https://doi.org/10.1063/1.5143061.
[3] Z. Wu, R.E. Cohen, More accurate generalized gradient approximation for solids, Phys. Rev. B 73 (2006) 235116. https://doi.org/10.1103/PhysRevB.73.235116.
[4] D. Koller, F. Tran, P. Blaha, Improving the modified Becke-Johnson exchange potential, Phys. Rev. B 85 (2012) 155109. https://doi.org/10.1103/PhysRevB.85.155109.
[5] M.A. Blanco, E. Francisco, V. Luaña, GIBBS: isothermal-isobaric thermodynamics of solids from energy curves using a quasi-harmonic Debye model, Computer Physics Communications 158 (2004) 57–72. https://doi.org/10.1016/j.comphy.2003.12.001.
[6] C. Kittel, Introduction to solid state physics, 8. ed., [repr.], Wiley, Hoboken, NJ, 20.
[7] A. Otero-de-la-Roza, D. Abbasi-Pérez, V. Luaña, Gibbs2: A new version of the quasiharmonic model code. II. Models for solid-state thermodynamics, features and implementation, Computer Physics Communications 182 (2011) 2232–2248. https://doi.org/10.1016/j.cpc.2011.05.009.
[8] Landau, L. D., and E. M. Lifshitz. Statistical Physics: Volume 5. 3rd ed. Amsterdam: Elsevier, (2013).
[9] L. Stixrude, C. Lithgow-Bertelloni, Thermodynamics of mantle minerals-II. Phase equilibria, Geophysical Journal International 184 (2011) 1180–1213.
[10] R.K. Singh, S. Singh, High-pressure phase transition and elastic behavior of aluminum compound semiconductors, Phys. Rev. B 45 (1992) 1019–1022. https://doi.org/10.1103/PhysRevB.45.1019.
[11] L. Salmi, H. Meradji, S. Ghemid, O. Nemiri, F. Oumelaz, R. Khenata, Phase stability, pressure-induced phase transition and electronic properties of AlX (X = P, As and Sb) compounds from first principle calculations., Phase Transitions 93 (2020) 843–855. https://doi.org/10.1080/01411594.2020.1795858.
[12] D. Varshney, G. Joshi, M. Varshney, S. Shriya, Pressure induced structural phase transition and elastic properties in BSb, AlSb, GaSb and InSb compounds, Physica B: Condensed Matter 405 (2010) 1663–1676. https://doi.org/10.1016/j.physb.2009.12.064.
[13] K. Daoud, Kh. Bouamama, P. Djemia, S.M. Chérif, *Ab initio* calculation of the elastic properties and the lattice dynamics of the $AlAs_{x}Sb_{1-x}$ alloy under pressure, High Pressure Research 31 (2011) 310–324. https://doi.org/10.1080/08957959.2010.545406.
[14] G.C. Liu, Z.W. Lu, B.M. Klein, Pressure-induced phase transformations in AlAs: Comparison between *ab initio* theory and experiment, Phys. Rev. B 51 (1995) 5678–5681. https://doi.org/10.1103/PhysRevB.51.5678.
[15] D.C. Gupta, S. Kulshrestha, Effect of high pressure on polymorphic phase transition and electronic structure of XAs (X=Al, Ga, In), Phase Transitions 82 (2009) 850–865. https://doi.org/10.1080/01411590903326628.
[16] S.T. Weir, Y.K. Vohra, A.L. Ruoff, High-pressure phase transitions and the equations of state of BaS and BaO, Phys. Rev. B 33 (1986) 4221–4226. https://doi.org/10.1103/PhysRevB.33.4221.

[17] A. Aguado, L. Bernasconi, P.A. Madden, Interionic potentials from *ab initio* molecular dynamics: The alkaline earth oxides CaO, SrO, and BaO, The Journal of Chemical Physics 118 (2003) 5704–5717. https://doi.org/10.1063/1.1556074.
[18] M.J. Mehl, R.J. Hemley, L.L. Boyer, Potential-induced breathing model for the elastic moduli and high-pressure behavior of the cubic alkaline-earth oxides, Phys. Rev. B 33 (1986) 8685–8696. https://doi.org/10.1103/PhysRevB.33.8685.
[19] T.A. Grzybowski, A.L. Ruoff, High-pressure phase transition in BaSe, Phys. Rev. B 27 (1983) 6502–6503. https://doi.org/10.1103/PhysRevB.27.6502.
[20] G. Kalpana, B. Palanivel, M. Rajagopalan, Electronic structure and structural phase stability in BaS, BaSe, and BaTe, Phys. Rev. B 50 (1994) 12318–12325. https://doi.org/10.1103/PhysRevB.50.12318.
[21] A. Bouhemadou, R. Khenata, F. Zegrar, M. Sahnoun, H. Baltache, A.H. Reshak, Ab initio study of structural, electronic, elastic and high pressure properties of barium chalcogenides, Computational Materials Science 38 (2006) 263–270. https://doi.org/10.1016/j.commatsci.2006.03.001.
[22] M. Teng, X. Hong, Phase transition and thermodynamic properties of BaS: An Ab initio study, Wuhan Univ. J. Nat. Sci. 16 (2011) 33–37. https://doi.org/10.1007/s11859-011-0707-1.
[23] R. Khenata, M. Sahnoun, H. Baltache, M. Rérat, D. Rached, M. Driz, B. Bouhafs, Structural, electronic, elastic and high-pressure properties of some alkaline-earth chalcogenides: An ab initio study, Physica B: Condensed Matter 371 (2006) 12–19. https://doi.org/10.1016/j.physb.2005.08.046.
[24] M. Benchehima, H. Abid, A. Sadoun, A. Chabane Chaouche, Optoelectronic properties of aluminum bismuth antimony ternary alloys for optical telecommunication applications: First principles calculation, Computational Materials Science 155 (2018) 224–234. https://doi.org/10.1016/j.commatsci.2018.08.050.
[25] K. Boubendira, S. Bendaif, O. Nemiri, A. Boumaza, H. Meradji, S. Ghemid, F.E.H. Hassan, Fundamental properties of zinc-blende AlSb, BSb and their Al1-xBxSb ternary alloys, Chinese Journal of Physics 55 (2017) 1092–1102. https://doi.org/10.1016/j.cjph.2017.05.021.
[26] C. Bocchi, A. Bosacchi, C. Ferrari, S. Franchi, P. Franzosi, R. Magnanini, L. Nasi, Determination of lattice parameters in the epitaxial AlSbGaSb system by high resolution X-ray diffraction, Journal of Crystal Growth 165 (1996) 8–14. https://doi.org/10.1016/0022-0248(96)00148-0.
[27] S. Ves, K. Strössner, M. Cardona, Pressure dependence of the optical phonon frequencies and the transverse effective charge in AlSb, Solid State Communications 57 (1986) 483–486. https://doi.org/10.1016/0038-1098(86)90613-7.
[28] M. Benchehima, M. Hicham Hachemi, H. Abid, Theoretical studies of optoelectronic properties of AlP1xBix ternaries: Promising light sources for fiber optic communications, Radiation Physics and Chemistry 202 (2023) 110591. https://doi.org/10.1016/j.radphyschem.2022.110591.
[29] F. Oumelaz, O. Nemiri, A. Boumaza, H. Meradji, S. Ghemid, R. Khenata, S. Bin-Omran, R. Ahmed, S.A. Tahir, First-principle investigations of structural, electronic, thermal, and mechanical properties of AlP1−xBix alloys, J Mol Model 29 (2023) 124. https://doi.org/10.1007/s00894-023-05497-5.

[30] X. Zhang, Y. Zhang, L. Yue, H. Liang, C. Chi, Y. Wu, X. Ou, S. Wang, Growth and properties of AlSbBi thin films by molecular beam epitaxy, Journal of Alloys and Compounds 801 (2019) 239–242. https://doi.org/10.1016/j.jallcom.2019.05.300.
[31] R. Alaya, M. Mbarki, A. Rebey, A.V. Postnikov, Ab initio predictions of structure preferences and band gap character in ordered AlAs1−xBix alloys, Current Applied Physics 16 (2016) 288–293. https://doi.org/10.1016/j.cap.2015.11.019.
[32] B. Mohamed, A. Boucheta, C. Yassine, L. Djoudi, M. Merabet, S. Benalia, R. Belghit, First principles study of stacking periodicity effects on structural, electronic and magnetic properties of MnAs/AlAs superlattice, Physica B: Condensed Matter 670 (2023) 415340. https://doi.org/10.1016/j.physb.2023.415340.
[33] S. Bouchareb, Structure, electronic properties of AlAs using first-principles calculations, in: 2023: pp. 204–211. https://doi.org/10.21741/9781644902592-22.
[34] S. Adachi, Properties of semiconductor alloys: group-IV, III-V and II-VI semiconductors, 1. ed, Wiley, Chichester, 2009.
[35] B. Khalfallah, F.Z.D. Khodja, N. Marbouh, Y. Saidi, Predictive Study of Structural, Electronic and Optical Properties of the Ternary Alloys BaO1-xSex (x=0.25, 0.50 and 0.75), 3 (n.d.).
[36] J.A. Santana, J.T. Krogel, P.R.C. Kent, F.A. Reboredo, Cohesive energy and structural parameters of binary oxides of groups IIA and IIIB from diffusion quantum Monte Carlo, The Journal of Chemical Physics 144 (2016) 174707. https://doi.org/10.1063/1.4947569.
[37] Y. Kaneko, K. Morimoto, T. Koda, Optical Properties of Alkaline-Earth Chalcogenides. I. Single Crystal Growth and Infrared Reflection Spectra Due to Optical Phonons, J. Phys. Soc. Jpn. 51 (1982) 2247–2254. https://doi.org/10.1143/JPSJ.51.2247.
[38] K. Park, J.M. Sivertsen, Temperature Dependence of the Bulk Modulus of BaO Single Crystals, Journal of the American Ceramic Society 60 (1977) 537–538. https://doi.org/10.1111/j.1151-2916.1977.tb14101.x.
[39] G.Q. Lin, H. Gong, P. Wu, Electronic properties of barium chalcogenides from first-principles calculations: Tailoring wide-band-gap II-VI semiconductors, Phys. Rev. B 71 (2005) 085203. https://doi.org/10.1103/PhysRevB.71.085203.
[40] S. Drablia, H. Meradji, S. Ghemid, G. Nouet, F. El Haj Hassan, First principles investigation of barium chalcogenide ternary alloys, Computational Materials Science 46 (2009) 376–382. https://doi.org/10.1016/j.commatsci.2009.03.013.
[41] S. Yamaoka, O. Shimomura, H. Nakazawa, O. Fukunaga, Pressure-induced phase transformation in BaS, Solid State Communications 33 (1980) 87–89. https://doi.org/10.1016/0038-1098(80)90702-4.
[42] F. El Haj Hassan, H. Akbarzadeh, First-principles elastic and bonding properties of barium chalcogenides, Computational Materials Science 38 (2006) 362–368. https://doi.org/10.1016/j.commatsci.2005.09.012.
[43] A.L. Ruoff, T.A. Grzybowski, Solid state physics under pressure, Terra Scientific, Tokyo (1985).
[44] P. Hohenberg, W. Kohn, Inhomogeneous Electron Gas, Phys. Rev. 136 (1964) B864–B871. https://doi.org/10.1103/PhysRev.136.B864.
[45] W. Kohn, L.J. Sham, Self-Consistent Equations Including Exchange and Correlation Effects, Phys. Rev. 140 (1965) A1133–A1138. https://doi.org/10.1103/PhysRev.140.A1133.
[46] S.M. Sze, K.K. Ng, LEDs and lasers, Physics of Semiconductor Devices 3 (2006) 601–657.

[47] R. Moussa, A. Abdiche, R. Khenata, F. Soyalp, First principles calculation of the structural, electronic, optical and elastic properties of the cubic Al Ga1-Sb ternary alloy, Optical Materials 113 (2021) 110850. https://doi.org/10.1016/j.optmat.2021.110850.
[48] I. Vurgaftman, J. Meyer, L.R. Ram-Mohan, Band parameters for III–V compound semiconductors and their alloys, Journal of Applied Physics 89 (2001) 5815–5875.
[49] K.A. Johnson, N.W. Ashcroft, Corrections to density-functional theory band gaps, Phys. Rev. B 58 (1998) 15548–15556. https://doi.org/10.1103/PhysRevB.58.15548.
[50] B. Ul Haq, R. Ahmed, S. AlFaify, F.K. Butt, A. Shaari, A. Laref, Exploring thermoelectric materials for renewable energy applications: The case of highly mismatched alloys based on AlBi1-xSbx and InBi1-xSbx, Intermetallics 93 (2018) 235–243. https://doi.org/10.1016/j.intermet.2017.09.017.
[51] S. Drablia, H. Meradji, S. Ghemid, N. Boukhris, B. Bouhafs, G. Nouet, ELECTRONIC AND OPTICAL PROPERTIES OF BaO , BaS , BaSe , BaTe AND BaPo COMPOUNDS UNDER HYDROSTATIC PRESSURE, Mod. Phys. Lett. B 23 (2009) 3065–3079. https://doi.org/10.1142/S0217984909021235.
[52] R.J. Zollweg, Optical Absorption and Photoemission of Barium and Strontium Oxides, Sulfides, Selenides, and Tellurides, Phys. Rev. 111 (1958) 113–119. https://doi.org/10.1103/PhysRev.111.113.
[53] G.A. Saum, E.B. Hensley, Fundamental Optical Absorption in the IIA-VIB Compounds, Phys. Rev. 113 (1959) 1019–1022. https://doi.org/10.1103/PhysRev.113.1019.
[54] N.W. Ashcroft, N.D. Mermin, Solid state physics Brooks, Cole, Cengage Learning 10 (1976).
[55] Marder, Michael P. Condensed matter physics. John Wiley & Sons, 2010.
[56] V.S. Stepanyuk, A. Szasz, A.A. Katsnelson, A.A. Grigorenko, O.V. Farberovich, Electronic Structure of MgO and SrS Compounds under Pressure, Physica Status Solidi (b) 171 (1992). https://doi.org/10.1002/pssb.2221710137.
[57] J.A. McLeod, R.G. Wilks, N.A. Skorikov, L.D. Finkelstein, M. Abu-Samak, E.Z. Kurmaev, A. Moewes, Band gaps and electronic structure of alkaline-earth and post-transition-metal oxides, Phys. Rev. B 81 (2010) 245123. https://doi.org/10.1103/PhysRevB.81.245123.
[58] S. Adachi, Optical Properties of Crystalline and Amorphous Semiconductors: Materials and Fundamental Principles. Berlin, Germany: Springer Science & Business Media, 2012.
[59] H. Warlimont, W. Martienssen, eds., Springer Handbook of Materials Data, Springer International Publishing, Cham, 2018. https://doi.org/10.1007/978-3-319-69743-7.
[60] M. Fox, Optical properties of solids, 2nd ed, Oxford University Press, Oxford ; New York, 2010.
[61] P. YU, M. Cardona, Fundamentals of Semiconductors: Physics and Materials Properties, Springer Science & Business Media, 2010.
[62] E. D. Palik, Handbook of Optical Constants of Solids. San Diego, CA: Academic Press, 1998.
[63] O. Madelung, Semiconductors: Data Handbook, Springer, Berlin, Heidelberg, 2004. https://doi.org/10.1007/978-3-642-18865-7.
[64] R.K. Jhakal, M.D. Sharma, Structural and Optical Properties of AlAsxSb1-x, Journal of Condensed Matter 3 (2025) 46–48. https://doi.org/10.61343/jcm.v3i01.90.

[65] R. Mamindla, M.K. Niranjan, Temperature-dependent electronic, optical, and solar cell device properties of AlAs and AlSb semiconductors and their p-n homojunctions, Journal of Physics and Chemistry of Solids 189 (2024) 111971. https://doi.org/10.1016/j.jpcs.2024.111971.
[66] M.S. Ali, R. Parvin, Investigation of pressure effect on structural, mechanical, electrical and optical properties of AlAs for optoelectronic applications, Physica B: Condensed Matter 673 (2024) 415491. https://doi.org/10.1016/j.physb.2023.415491.
[67] B. Amrani, First-principles investigation of AlAs at high pressure, Superlattices and Microstructures 40 (2006) 65–76. https://doi.org/10.1016/j.spmi.2006.05.005.
[68] L. Pavesi, M. Guzzi, Photoluminescence of AlxGa1−xAs alloys, Journal of Applied Physics 75 (1994) 4779–4842. https://doi.org/10.1063/1.355769.
[69] O. Madelung, Semiconductors: Data Handbook, Springer, Berlin, Heidelberg, 2004. https://doi.org/10.1007/978-3-642-18865-7.
[70] B.G. Yalcin, S. Bagci, M. Ustundag, M. Aslan, Electronic and optical properties of BBi and AlBi: Hybrid (YS-PBE0) function, Computational Materials Science 98 (2015) 136–141. https://doi.org/10.1016/j.commatsci.2014.11.010.
[71] M.E. Lines, Bond-orbital theory of linear and nonlinear electronic response in ionic crystals. I. Linear response, Phys. Rev. B 41 (1990) 3372–3382. https://doi.org/10.1103/PhysRevB.41.3372.
[72] E.B. Elkenany, Theoretical investigations of electronic, optical and mechanical properties for GaSb and AlSb semiconductors under the influence of temperature, Spectrochimica Acta Part A: Molecular and Biomolecular Spectroscopy 150 (2015) 15–20. https://doi.org/10.1016/j.saa.2015.05.033.
[73] D.I. Bolef, M. Menes, Elastic Constants of Single-Crystal Aluminum Antimonide, Journal of Applied Physics 31 (1960) 1426–1427. https://doi.org/10.1063/1.1735857.
[74] E.B. Elkenany, Theoretical investigations of electronic, optical and mechanical properties for GaSb and AlSb semiconductors under the influence of temperature, Spectrochimica Acta Part A: Molecular and Biomolecular Spectroscopy 150 (2015) 15–20. https://doi.org/10.1016/j.saa.2015.05.033.
[75] G. Gökoğlu, Theoretical investigation of zincblende AlSb and GaSb compounds, Journal of Alloys and Compounds 478 (2009) 653–656. https://doi.org/10.1016/j.jallcom.2008.11.097.
[76] C. Zhu, R. Yang, Q. Wei, D. Zhang, Theoretical investigations of phases of AlAs by first-principles, Chinese Journal of Physics 56 (2018) 2119–2128. https://doi.org/10.1016/j.cjph.2018.09.010.
[77] Y. Claveau, M. Vallet, H. Tang, N. Combe, A. Ponchet, Elastic properties of AlAs-like and InSb-like strained interfaces in [InAs/AlSb] heterostructures, Applied Physics Letters 109 (2016) 041903. https://doi.org/10.1063/1.4959843.
[78] E.E. Gregory, S.A. Ekong, J.B. Emah, Ab-initio Assessment of the Electronic, Mechanical, Thermal, Optical and Phonon Properties of B3-AlAs, Researchers Journal of Science and Technology 4 (2024) 69–93.
[79] M. Krieger, H. Sigg, N. Herres, K. Bachem, K. Köhler, Elastic constants and Poisson ratio in the system AlAs–GaAs, Applied Physics Letters 66 (1995) 682–684. https://doi.org/10.1063/1.114098.
[80] Y. Duan, L. Qin, G. Tang, L. Shi, First-principles study of ground- and metastable-state properties of XO (X = Be, Mg, Ca, Sr, Ba, Zn and Cd), Eur. Phys. J. B 66 (2008) 201–209. https://doi.org/10.1140/epjb/e2008-00415-3.

[81] Z.P. Chang, E.K. Graham, Elastic properties of oxides in the NaCl-structure, Journal of Physics and Chemistry of Solids 38 (1977) 1355–1362. https://doi.org/10.1016/0022-3697(77)90007-5.
[82] D. Zagorac, J. Zagorac, K. Doll, M. Cebela, B. Matovic, Extreme pressure conditions of bas based materials: Detailed study of structural changes, band gap engineering, elastic constants and mechanical properties, PAC 13 (2019) 401–410. https://doi.org/10.2298/PAC1904401Z.
[83] A. Benamrani, K. Kassali, Kh. Bouamama, Pseudopotential study of barium chalcogenides under hydrostatic pressure, High Pressure Research 30 (2010) 207–218. https://doi.org/10.1080/08957950903461301.
[84] B. Khalfallah, F.-Z. Driss-Khodja, F. Saadaoui, M. Driss-Khodja, A. Boudali, H. Bendaoud, B. Bouhafs, A first-principles study of the structural, elastic, electronic, vibrational, and optical properties of BaSe1−xTex, J Comput Electron 17 (2018) 1478–1491. https://doi.org/10.1007/s10825-018-1249-y.
[85] S. Gagui, S. Ghemid, H. Meradji, M.A. Javed, B. Ul Haq, R. Ahmed, N. Baki, Aluminium doping effects on physical properties of semiconductors InSb for optoelectronic devices: a computational insight, Opt Quant Electron 56 (2024) 87. https://doi.org/10.1007/s11082-023-05637-4.
[86] C. Toher, C. Oses, J.J. Plata, D. Hicks, F. Rose, O. Levy, M. de Jong, M. Asta, M. Fornari, M. Buongiorno Nardelli, S. Curtarolo, Combining the AFLOW GIBBS and elastic libraries to efficiently and robustly screen thermomechanical properties of solids, Phys. Rev. Mater. 1 (2017) 015401. https://doi.org/10.1103/PhysRevMaterials.1.015401.

Conclusions

Conclusions

Across the four alloy families studied $AlSb_{1-x}As_x$ and $AlSb_{1-x}Bi_x$ found stable in zinc-blende and $BaO_{1-x}S_x$ and $BaO_{1-x}Se_x$ found stable in rock-salt ; our first-principles results provide a coherent, composition-resolved picture that links structure and bonding to electronic, optical, elastic and thermal behavior. All compositions satisfy the Born mechanical stability conditions at ambient pressure. Chemical pressure governs the trends: substituting Sb→As contracts Al–anion bonds and strengthens them, while Sb→Bi expands the lattice and softens the bonds; in the II–VI series the anion sequence O→S→Se increases cell size and polarizability and progressively weakens average bond strength. Electronic structures and DOS are mutually consistent with these structural changes.

In $AlSb_{1-x}As_x$, the endpoints AlSb and AlAs are indirect, but intermediate alloys ($x\approx0.25–0.75$) open a direct Γ–Γ window; DOS shows compact anion-p-dominated valence bands and Γ-edge conduction states whose relative ordering with X flips only in the mid-range. In $AlSb_{1-x}Bi_x$ any Bi incorporation stabilizes a direct Γ–Γ gap that decreases monotonically to AlBi, mirrored in a denser p-manifold and lowered conduction edge in the DOS. For $BaO_{1-x}S_x$ and $BaO_{1-x}Se_x$ the gap narrows with heavier anions and the band edges remain direct; the upper valence is chalcogen-p, deep valence carries Ba-p character, and the conduction band mixes Ba-d/Ba-p with growing anion-p weight from O to Se.

Optical responses follow the band edges: $\varepsilon_2(\omega)$ critical points shift to higher energy with As and to lower energy with Bi/Se; $\varepsilon_1(0)$ and the static refractive index $n(0)$ inversely track Eg (lower n at the wider-gap As-rich end, higher n as Bi or Se narrows Eg). The absorption coefficient $\alpha(\omega)$ turns on at the calculated gaps and rises steeply across the near-UV, while reflectivity exhibits a broad plateau whose onset shifts in lockstep with composition.

Elastic trends are chemically intuitive. In $AlSb_{1-x}As_x$, C_{11}, C_{44} and derived polycrystalline moduli (B, E, G) increase with As stiffer, more resistant to shear whereas in $AlSb_{1-x}Bi_x$ they decrease softer with Bi. Both III–V series are elastically anisotropic with Zener $A\approx2–3$ (stronger rigidity along ⟨111⟩). In $BaO_{1-x}S_x$ and $BaO_{1-x}Se_x$ all moduli fall with S/Se content; Zener $A<1$ and decreases with x, indicating greater relative rigidity along ⟨100⟩. Pugh ratios and Poisson's ratios keep the III–V

alloys on the brittle side at ambient conditions, with only a slight drift toward ductility at intermediate Bi; the II–VI alloys remain comparatively compliant yet still brittle-leaning.

Thermal behavior closes the loop between mass, bonding and stiffness. C_v(T) shows the expected Debye rise at low T and saturation near the Dulong–Petit limit; $\Theta_D(T)$ mirrors stiffness (rising with As, falling with Bi; decreasing from O→S→Se), B(T) decreases quasi-linearly with T for every composition, and the linear expansion α(T) grows with T and is largest in Se-rich alloys and smallest in As-rich alloys.

Taken together, the III–V family offers strong electronic tunability (an indirect-to-direct window in $AlSb_{1-x}As_x$ and continuous direct-gap control from NIR to MWIR in $AlSb_{1-x}Bi_x$), while the II–VI family provides wide-gap dielectrics with predictable softening and expansion as O→S→Se—attributes valuable for high-temperature optics and substrate/encapsulation roles. Novel contributions of this work include a single, internally consistent dataset that spans bands/DOS, full optical spectra, complete elastic tensors with anisotropy metrics, and temperature-dependent thermal functions for interior compositions that are sparsely documented in the literature; the direct-gap window in $AlSb_{1-x}As_x$ and the direct-gap persistence across $AlSb_{1-x}Bi_x$ are quantified and tied to clear DOS/bonding signatures; and composition-dependent elastic/thermal tables provide reference predictions.

Reliability is supported by agreement with reported endpoint data (gaps, dielectric constants, elastic constants, Debye temperatures) within typical ab-initio uncertainty and by cross-property consistency structural trends, moduli, θ_D, α(T), optical onsets and DOS all tell the same physical story so the principal outcome of the thesis is a robust map from chemistry to function that can guide device-oriented material selection and future experimental validation.